UNIVERSITAT POLITÈCNICA DE CATALUNYA BARCELONATECH

Modelling time-dependent plastic behaviour of geomaterials

Fei Song

Doctoral thesis

Modelling time-dependent plastic behaviour of geomaterials

A thesis submitted in partial fulfilment of the requirements for the degree of

Doctor of Philosophy

Division of Geotechnical Engineering and Geosciences,

Department of Civil and Environmental Engineering,

Technical University of Catalonia (UPC-BarcelonaTech)

Author: Fei Song

Supervised by: Alfonso Rodriguez-Dono, Antonio Gens Solé

Barcelona, Spain

April 2021

Abstract

Representing the time-dependent plastic behaviour of geomaterials is a critical issue in the correct application of tunnelling design techniques such as the convergence-confinement method or numerical modelling. Furthermore, during underground excavations below the water table, the effect of seepage flow cannot be ignored, and the behaviour of the tunnel must be analysed in a coupled hydro-mechanical framework.

The main objective of this thesis is to analyse the response of tunnels excavated in saturated time-dependent plastic rock masses. For this purpose, a time-dependent plastic constitutive model has been developed and implemented in the software CODE_BRIGHT to simulate the time-dependent, strain-softening and creep-induced failure behaviour of geomaterials. Moreover, a coupled hydro-mechanical model is utilised to simulate the interaction between solid deformations and fluid flows. The obtained results provide relevant insights into the response of tunnels excavated in saturated time-dependent plastic rock masses. However, numerical difficulties might occur when modelling multi-stage excavations problems, when considering multi-physics coupled processes or non-linear mechanical material models, especially if the layers or pieces of the excavated material are relatively coarse. In order to mitigate these numerical difficulties, a smoothed excavation (SE) method has been proposed and implemented in the software CODE_BRIGHT, which can improve numerical efficiency and mitigate non-convergence issues.

Subsequently, to analyse the stability of tunnels with a combined support system, numerical solutions have been developed for tunnels excavated in strain-softening rock masses, considering the whole process of tunnel advancement, and the sequential installation of primary and secondary support systems. For this purpose, the actual compatibility conditions at both the rock-support interface and the support-support interface are considered. This method provides a convenient alternative method for the preliminary design of supported tunnels.

Keywords: Plasticity; Creep; Hydro-mechanical modelling; Tunnelling; Excavation; strain-softening; Viscoelasticity; Viscoplasticity; CODE_BRIGHT

Resumen

La adecuada representación del comportamiento plástico y dependiente del tiempo de los geomateriales es una cuestión crítica en la correcta aplicación de técnicas de diseño de túneles como el método de convergencia-confinamiento o el modelado numérico. Por otro lado, durante las excavaciones subterráneas por debajo del nivel freático no se puede ignorar el efecto del flujo de filtración y, por tanto, el comportamiento del túnel debe analizarse en un marco hidromecánico acoplado.

El principal objetivo de esta tesis es analizar la respuesta de túneles excavados en macizos rocosos plásticos saturados y dependientes del tiempo. Para este propósito, se ha desarrollado e implementado un modelo constitutivo plástico dependiente del tiempo en el software CODE_BRIGHT, que permite simular el comportamiento dependiente del tiempo, el de reblandecimiento por deformación y el inducido por fluencia de los geomateriales. Además, se ha utilizado un modelo hidromecánico acoplado para simular la interacción entre la deformación del sólido y el flujo de fluido. Los resultados obtenidos proporcionan información relevante sobre la respuesta de los túneles excavados en macizos rocosos plásticos, saturados y dependientes del tiempo. Sin embargo, pueden surgir dificultades numéricas al modelar problemas de excavaciones en varias etapas, al considerar procesos multifísicos acoplados o modelos de materiales mecánicos no lineales, especialmente si las capas o piezas de material excavado son relativamente gruesas. Para mitigar estas dificultades numéricas, se ha propuesto e implementado un método de excavación suavizada (SE) en el software CODE_BRIGHT, que puede mejorar la eficiencia numérica y mitigar los problemas de no convergencia.

Posteriormente, para analizar la estabilidad de túneles con sistemas de sostenimiento combinado, se han desarrollado soluciones numéricas para túneles excavados en macizos con reblandecimiento por deformación, considerando todo el proceso de avance del túnel y la instalación secuencial de los sistemas de sostenimiento primario y secundario. Con este propósito, se han considerado las condiciones reales de compatibilidad tanto en la interfaz roca-sostenimiento como en la interfaz sostenimiento-sostenimiento. Este método proporciona un método alternativo conveniente para el diseño preliminar de túneles con sostenimiento.

Palabras clave: Plasticidad; Fluencia; Modelado hidromecánico; Túneles; Excavación; Reblandecimiento; Viscoelasticidad; Viscoplasticidad; CODE_BRIGHT.

Acknowledgements

The author would like to acknowledge the following support, organizations and people for making this thesis possible.

First of all, the research work described in this thesis has been carried out in the framework of the CODE_BRIGHT project (International Centre for Numerical Methods in Engineering). Additionally, I greatly acknowledge the China Scholarship Council for the grant (NO. 201706260240).

I sincerely thanks my supervisors Antonio Gens and Alfonso Rodriguez-Dono. Professor Antonio Gens is a great and excellent scientist. I still remember the exciting moment when I received the offer for doing a Ph.D. candidate in his excellent lab. I will always be grateful for his unconditional support and encouragement in every aspect related to my research and life in Technical University of Catalonia (UPC). I sincerely thanks Professor Alfonso Rodriguez-Dono, for his continuous assistant and suggestions in my thesis. He is an outstanding researcher in rock mechanics and guides my research step by step. He encourages me to do exploratory research and respects all my research ideas. He worked together with me to timely solve all problems that I have met. He treats me sincerely like a friend. He provides me with unconditional support in every aspect related to my research and my daily life in Spain.

I would like to make a special thanks to Professor Sebastia Olivella from our department. He helps me to be familiar with the source code in CODE_BRIGHT and provides valuable comments to my research. The numerical implementation in CODE_BRIGHT could not be completed without his assistant. Also, special thanks to Professor Jean Vaunat and Dr. Miguel Manica, for their suggestions in programming codes and theoretical background of rock mechanics. Another special thanks is given to Professor Huaning Wang from Tongji University, China. She is the supervisor of my Master's thesis. She helps me to know how to do research, and provides me with generous support and continuous encouragement all over the years. A special thank is given to Professor Mingjing Jiang from Tianjin University, China, for his encouragement in my research.

Special thanks are given to all the friends and colleagues I met in UPC and in my daily life. I cannot list all the names herein, but I believe that we have always remembered our wonderful

experience. Finally, I would like to make a special thanks to my family: my parents, my wife -Junhui Zhang-, and my son -Mige Song-. In my mind, Junhui Zhang is a great human being, who can excellently balance our family and her research projects. Without their unconditional support and encouragement, I would never have completed this thesis.

Contents

List of Publications

This is an extensive list of all the work published, submitted or to be submitted, related to this doctoral thesis.

Articles in peer-reviewed journals:

[1] Fei Song, Alfonso Rodriguez-Dono, Sebastia Olivella, Zhen Zhong. Analysis and modelling of longitudinal deformation profiles of tunnels excavated in strain-softening time-dependent rock masses [J]. Computers and Geotechnics, 2020, 125: 103643.

https://doi.org/10.1016/j.compgeo.2020.103643

[2] Fei Song, Alfonso Rodriguez-Dono. Numerical solutions for tunnels excavated in strain-softening rock masses considering a combined support system [J]. Applied Mathematical Modelling, 2021, 92: 905-930. https://doi.org/10.1016/j.apm.2020.11.042

[3] Fei Song, Alfonso Rodriguez-Dono, Sebastia Olivella. Hydro-mechanical modelling and analysis of multi-stage tunnel excavations using a smoothed excavation method. Computers and geotechnics [J]. Computers and Geotechnics, 2021, 135: 104150.

https://doi.org/10.1016/j.compgeo.2021.104150

[4] Fei Song, Alfonso Rodriguez-Dono, Sebastia Olivella, Antonio Gens. Hydro-mechanical analyses of longitudinal deformation profiles for tunnels excavated in saturated Burgers-viscoplastic strain-softening rock masses. Submitted to the journal of <Applied Mathematical Modelling>.

Conference abstract

[1] Fei Song, Alfonso Rodriguez-Dono, Sebastia Olivella. A viscoplastic damage model combined with strain softening failure criterions for rock mass. 11th Workshop of CODE_BRIGHT Users: 16th May 2019, Barcelona, Spain.

https://deca.upc.edu/en/projects/code_bright/workshop/doc/abstract

[2] Fei Song, Alfonso Rodriguez-Dono. An anisotropic time-dependent model for rocks. 14th Euroconference on Rock Physics and Rock Mechanics. <Submitted>.

List of Figures

List of Tables

Chapter 1. Introduction and literature review

1.1. Research background

In the field of geotechnical engineering, the socio-economic and technological development of several countries in the world has led to the need to increase the construction of underground structures (Rodriguez-Dono, 2011; Song and Rodriguez-Dono, 2021; Song et al., 2020; Wang et al., 2020a). This increase in exploitation and construction has created some social concerns related to both work accidents and environmental contamination, which should be dealt with not only during the exploitation and construction phases, but also during the operational and long-term service phases of these engineering works, according to the application of the principles of sustainable development economy and the current environmental awareness and protection trends.

From a purely economic point of view, many of these accidents result in collapses, hence stopping the works for a significant amount of time, at a great cost to the exploitation or construction company and delayed implementation for the use of the society (Rodriguez-Dono, 2011). If all these observations are extended to a global scale is found that a large number of significant casualties, environmental issues and economic losses have been and will continue to be produced (Rodriguez-Dono, 2011).

In a geomechanics framework, accidents are frequently related to fractures. The complexity of the different geomaterials makes the study of these fractures a critical topic for understanding their behaviour and, hence such a study constitutes a significant step in the mitigation of all these accidents that may occur in the working projects (Rodriguez-Dono, 2011; Song et al., 2020; Zhang et al., 2015).

Besides, geomaterials undergo long-term time-dependency and progressive damage evolution during excavation and operation phases. Some underground structures show large delayed deformations that could lead to failure, *i.e.* creep-induced failure response, which may be relevant for many engineering cases, such as for some tunnels that do not fail during excavation but ultimately fail after a long-term operation (Fabre and Pellet, 2006; Sandrone and Labiouse, 2010; Song et al., 2020).

Furthermore, many multi-physical processes, such as mechanical, hydraulic or even thermal, affect the behaviour of the geomaterials in a coupled way. During tunnelling below the water table, there may be some seepage flowing towards the tunnel, affecting the response of underground structures (Lee and Nam, 2004; Nam and Bobet, 2007; Nogueira et al., 2011). Consequently, the tunnelling below the water table should be analysed in a coupled hydro-mechanical framework, considering the coupled interaction between solid deformations and fluid flows. There are still many aspects of interest in coupled behaviour to study, which will require more detailed investigations.

In addition, the complexity in the estimation of underground structures behaviour is also tricky because, geomaterials have a marked effect of scale, so that frequently the behaviour observed in the laboratory cannot be extrapolated to the scale of the work. Thus a standard application of the scientific method is not valid for this field of engineering, in which heuristic methods, case studies and numerical modelling techniques are all necessary (Rodriguez-Dono, 2011; Starfield and Cundall, 1988).

1.2. State-of-art

The support structures are usually needed to be constructed, in order to maintain the stability of tunnels (Dong, 2020; Song and Rodriguez-Dono, 2021; Song et al., 2020; Song et al., 2018a and 2018b; Wang et al., 2020b). The art of tunnel design is to find right stiffness and right installation time of the support systems (Alonso et al., 2003). Too early installation time or too lower stiffness of support systems, may lead to uncontrolled convergences or over-stressing on the support system, which may result in collapse (Alonso et al., 2003; Song and Rodriguez-Dono, 2021; Song et al., 2018a and 2018b). The design of supported tunnels can be tackled by various methods, such as theoretical approaches, numerical simulations, the convergence-confinement method (CCM) or field monitoring.

1.2.1. Theoretical solutions for supported tunnels

Theoretical solution provides an efficient and quick approach to gain insights into the nature of the problem (Carranza-Torres and Fairhurst, 1999). Concerning the ground-support interaction, many researchers developed solutions for mechanical as well as hydro-mechanical problems. However, solutions for tunnels with more complex models (such as poromechanics, rock instabilities or non-linear constitutive models of geomaterials) are not easy to be developed (Dong et al., 2019; Song and Rodriguez-Dono, 2021).

1.2.1.1. Solutions for mechanical problems

Using the complex variable method, Li and Wang (2008) presented plane-strain elastic solutions for supported tunnels under isotropic initial stresses, accounting for the relative radius misfit and interaction between the circular tunnels and the support structures. Then, for plane-strain problems with anisotropic initial stresses, Wang and Li (2009) developed elastic solutions for stresses and displacements of supported circular tunnels due to ground loads and internal pressure.

Lu et al. (2011) developed stress solutions for supported circular tunnels, considering the delayed installation of the support structure, and the displacement release coefficient was determined according to the distance between the working face and the supported section. For lined vertical boreholes in a homogeneous ground under non-axisymmetric loads, Lu et al. (2013) developed plane-stress elastic solutions, and two extreme boundary conditions (pure-bond and a pure-slip) on the ground-support interface have been considered. Additionally, based on the complex variable method and the optimization theory, Lu et al. (2019) developed analytical stresses solutions for supported circular tunnels, considering frictional-slip contact condition on the ground-support interface and the delayed installation of support. Theoretical elastic solutions were developed by Carranza-Torres et al. (2013) for more complex conditions, considering longitudinal excavation progress, the delayed installation of support structures and two different types of ground-support interface conditions. Besides, for non-circular supported tunnels, some researchers (Kargar et al., 2014; Lu et al., 2014a; Lu et al., 2014b; Lu et al., 2015) developed

analytical or semi-analytical solutions using the complex variable method and the conformal transformation method.

In all above mentioned references, the surrounding rock masses are assumed as elastic materials. However, elastic material behaviour is quite different from that in real projects in which the rock masses exhibit strong time-dependency or plastic response (Alejano et al., 2010; Alejano et al., 2009; Alejano et al., 2012; Wang et al., 2020b). Actually, unlike linear elastic materials with constitutive algebraic equations, time-dependent viscoelastic materials have their constitutive relations expressed by a set of operator equations (Song et al., 2018a and 2018b; Wang et al., 2020b).

Sulem et al. (1987) developed time-dependent solutions for tunnel wall displacements and support forces, and the Kelvin-Voigt viscoelastic model was utilized to describe the time-dependent properties of geomaterials. Fahimifar et al. (2010) presented analytical solutions for circular tunnels excavated in time-dependent Burgers geomaterials under axisymmetric initial stresses, accounting for the longitudinal tunnelling advancement. By using Burgers viscoelastic model to predict ground behaviours, Nomikos et al. (2011) developed analytical solutions for circular tunnels with single support system under isotropic initial stresses, taking into account the stiffness and installation time of the support system. After that, Wang et al. (2013 and 2014a) presented analytical solutions for circular tunnels with two/n-support systems, considering the sequential excavation process of cross-section, sequential installation of the support systems, and viscoelastic properties of the surrounding rock masses.

All above viscoelastic solutions were derived under isotropic initial stresses. For tunnels subjected to anisotropic initial stresses, Lo and Yuen (1981) developed closed-form solutions for time-dependent stresses and displacements of the surrounding rock masses and the support, considering two types of ground-support interface conditions, time-dependent properties of the surrounding rock masses and support, as well as the delayed installation of support. Wang et al. (2020b) presented time-dependent solutions of tunnels excavated in viscoelastic rock masses under non-hydrostatic initial stresses, two types of ground-support interface conditions (full-slip and no-slip) have been analysed. Using the complex variable method, the Laplace transformation technique and extension of the correspondence principle, Song et al (2018a and 2018b) developed

analytical solutions for tunnels excavated in time-dependent viscoelastic rock masses, and the sequential installation of the primary and the secondary support systems were accounted for.

Furthermore, elastic-plastic, viscoplastic and viscoelastic-viscoplastic models have been utilized to predict the plastic response of geomaterials (Alejano et al., 2009; Alonso et al., 2003; Cui et al., 2019; Kabwe et al., 2020b and 2020c; Kargar, 2019; Wang et al., 2010; Zhang et al., 2016; Zhang et al., 2012a; Zhang et al., 2019b; Zou et al., 2017a; Zou et al., 2017b; Zou et al., 2017c). When considered plastic response of geomaterials, the design of supported tunnels usually tackled by the convergence-confinement method (CCM) or numerical simulations, as described in sections 1.2.2 and 1.2.3. Actually, some researchers developed plastic solutions for circular openings, which can be assumed as a type of ground reaction curves (GRC) in the CCM.

1.2.1.2. Solutions for hydro-mechanical problems

During underground excavations below the water table, there may be some seepage flow towards the tunnel, affecting its behaviour (Arjnoi et al., 2009; El Tani, 2003; Lee and Nam, 2004; Ming et al., 2010; Nam and Bobet, 2007; Nogueira et al., 2011; Park et al., 2008a). Consequently, the effect of seepage flow cannot be ignored, and the tunnelling responses must be analysed in a coupled hydro-mechanical (HM) framework (Nam and Bobet, 2007; Yuan and Harrison, 2005). Therefore, a proper simulation of the coupled HM behaviour and the entire excavation and operation phases is crucial to achieve an optimal design of tunnels.

Regarding the ground-support interaction, Dong et al. (2019) presented analytical elastic solutions for stress distribution around deeply supported tunnels under the water table, using the complex variable method and the conformal mapping technique. Based on a generalized effective stress principle, Zareifard (2018) developed analytical elastic solutions for analysing and designing of pressure tunnels, covering various types of pressure tunnels, such as unlined, shotcrete lined, concrete lined, reinforced concrete lined and prestressed concrete lined pressure tunnels.

Considering the plastic response of geomaterials, Carranza-Torres and Zhao (2009) investigated the effect of water pressure on the mechanical response of cylindrical lined tunnels

in the elastic and elastic-plastic porous ground that obeys Terzaghi's effective stress principle. Li et al. (2014) presented plane-strain elastic-plastic solutions of the stress and displacements distributions around deeply circular tunnels in the isotropic saturated ground due to uniform ground loads and seepage forces, considering a gap between the ground and the support.

1.2.2. The convergence-confinement method

The convergence-confinement method (CCM) is an analytical-graphical procedure for designing support structures. The CCM developed in the 1930s (Fenner, 1938), and later refined by other researchers (Alejano et al., 2010; Alejano et al., 2012; Carranza-Torres and Fairhurst, 2000; Corbetta et al., 1991; Cui et al., 2015; Paraskevopoulou, 2016; Vlachopoulos and Diederichs, 2009). It provides an efficient way to determine support forces by considering the ground-support interaction (Alejano et al., 2010 and 2012).

As shown in Figure 1.1, the CCM consists of three basic components in the form of graphs: (1) the ground reaction curve (GRC) establishes the relationship between the decreasing inner pressure and the increasing radial displacements of the tunnel wall; (2) the longitudinal deformation profile (LDP) relates the radial displacements of an unsupported tunnel section with its longitudinal distance to the tunnel face; and (3) the support characteristic curve (SCC) represents the stress-strain relationship of a support system (Alejano et al., 2010; Alejano et al., 2012; Cui et al., 2015).

1.2.2.1. The ground reaction curves

In practice, elastic-perfectly-plastic (EPP) behaviour models are often used to obtain the GRC (Carranza-Torres, 1998; Carranza-Torres and Fairhurst, 1999; Carranza-Torres and Fairhurst, 2000). However, unless the rock mass is of very poor quality, the EPP models do not adequately represent the real post-failure behaviour of rock masses (Alejano et al., 2009; Hoek and Brown, 1997). Some researchers (Jiang et al., 2019; Serrano et al., 2011; Wang et al., 2012a; Wang and Yin, 2011; Wang, 1996; Zhang et al., 2012b) presented solutions for circular openings excavated in elastic-brittle (EB) rock masses. Indeed, strain-softening (SS) models are more suitable for

simulating ground behaviour accurately, especially for average-quality rock masses (Alejano et al., 2009 and 2012). Moreover, both the EPP and the EB models are special cases of the SS model (Song and Rodriguez-Dono, 2021).

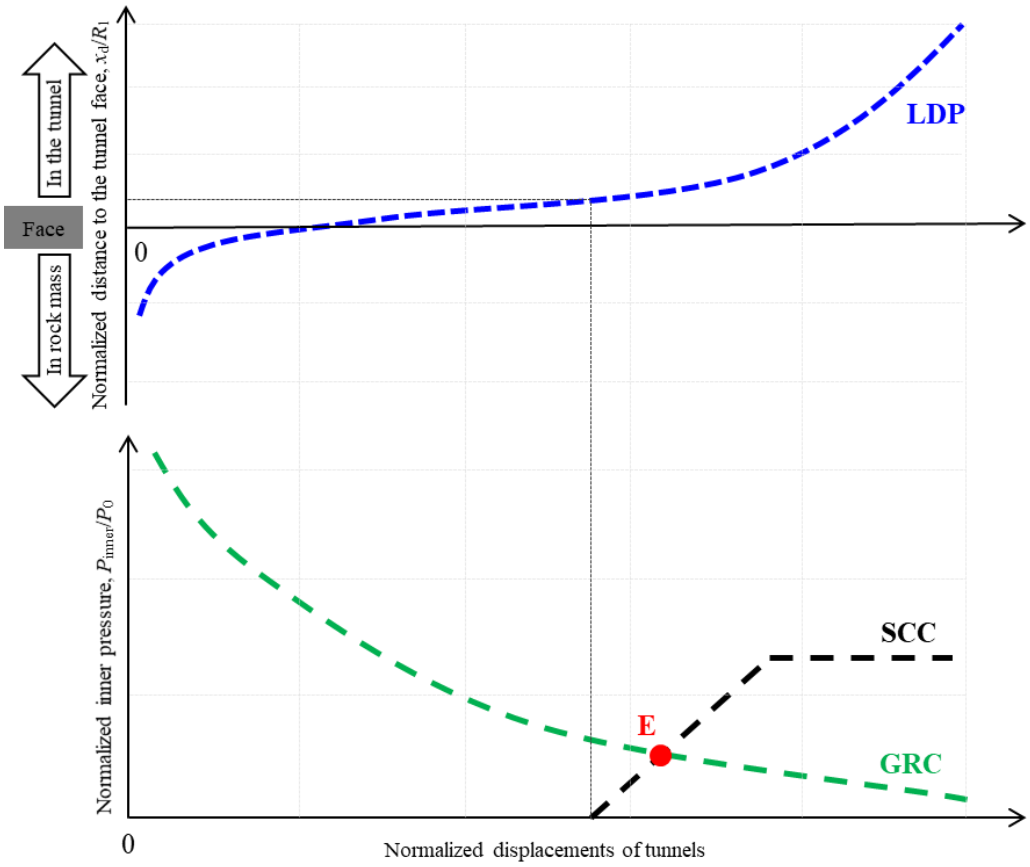

Figure 1.1. Main elements of the convergence-confinement method (CCM). Typical graphs obtained for the longitudinal deformation profile (LDP) –above–, and for the ground reaction curve (GRC) and the support characteristic curve (SCC) –below. Based on the work of Alejano et al. (2009, 2010 and 2012), Song et al. (2020) and Song and Rodriguez-Dono (2021).

Regarding rock masses exhibiting strain-softening (SS) behaviour, through defining a fictitious 'time' variable and re-scaling some variables, Carranza-Torres (1998a) and Alonso et al. (2003) presented self-similarity solutions of circular openings excavated in strain-softening geomaterials. Later, based on those solutions that developed in Alonso et al. (2003), Alejano et al.

(2009) presented the improved ground reaction curves, considering EPP, EB and SS behaviour models and increasingly realistic parameters. Furthermore, by using a simple stepwise procedure that successively determines the stresses and strains on the boundaries of a number of the annuli into which the plastic zone is divided, some researchers (Brown et al., 1983; Lee and Pietruszczak, 2008; Park et al., 2008b; Wang et al., 2012b; Wang et al., 2010; Zhang et al., 2012a; Zhang et al., 2018; Zou et al., 2017a) presented solutions for tunnelling in rock masses that exhibit strain-softening behaviour. Moreover, some researchers extended the application of the ground reaction curves to design non-circular tunnels (Kabwe et al., 2020b and 2020c), or viscoplastic problems (Kabwe et al., 2020c; Kargar, 2019; Ladanyi and Gill, 1988).

Based on the framework of the ground reaction curves, many researchers developed hydro-mechanical solutions for circular tunnels. Fahimifar and Zareifard (2013) developed analytical solutions for plane-strain and axial symmetry conditions of circular openings, considering elastic behaviour of ground and steady-state flow. Considering the effect of seepage forces, some researchers presented solutions for circular openings excavated in elastic-perfectly-plastic (Shin et al., 2010) or elastic-brittle (Lee et al., 2007; Zareifard and Fahimifar, 2014 and 2015) rock masses. Using the so-called stepwise procedure, some researchers (Fahimifar et al., 2015; Fahimifar and Zareifard, 2014; Yang and Huang, 2010; Zou and Li, 2015) developed solutions for circular openings considering seepage flow and strain-softening behaviour of surrounding rock masses.

However, most of these studies only considered the completely steady-state drained conditions of the grounds. When considering a fully coupled hydro-mechanical model, Zhang et al. (2020a) and Zhang et al. (2020b) developed solutions for circular openings excavated in the elastic-brittle and the strain-softening rock masses, respectively. Additionally, Fang et al. (2015) developed stress solutions of an underwater tunnel in an elastic half-plane, using the complex variable method and conformal mapping method. Combining these obtained ground reaction curves with the CCM, the above solutions can be used for designing supported tunnels.

1.2.2.2. The longitudinal deformation profiles

Regarding the longitudinal deformation profiles (LDP), many researchers developed solutions based on field measurements or numerical simulations. Corbeta et al. (1991) and Panet (1995) presented elastic solutions for the relationship between radial displacements and the distance to the tunnel face. Using numerical simulations, Unlu and Gercek (2003) proposed empirical equations for predicting normalized radial displacements ahead and behind the tunnel face, considering the effect of Poisson's ratio. Additionally, based on field-measured data from a tunnel in the Mingtam Power cavern project (Chern et al., 1998), an empirical best-fit relationship of the LDP was presented for the elastic-plastic problems. After that, Vlachopoulos and Diederichs (2009) presented a robust formulation for the calculation of the LDP for plastic problems, which takes into account the significant influence of the ultimate plastic radius.

Considering post-failure behaviour, Alejano et al. (2012) extended that approach from Vlachopoulos and Diederichs (2009) to the case of strain-softening rock masses, representing a wider range of rock masses, which can be used to obtain a more realistic approach to calculate the LDP. Considering time-dependent properties of rock masses, Paraskevopoulou (2016) and Paraskevopoulou and Diederichs (2018) presented LDP simulations for viscoelastic rock masses, based on the Burgers-creep viscous (CVISC) model introduced by Itasca (2007 and 2008). As a result of this review of the LDP, it turns out that there is still not a satisfactory general result considering the LDP for time-dependent plastic problems and, thus *in this thesis, analysis and modelling of the LDP for tunnels excavated in time-dependent plastic rock masses are carried out, considering Mohr-Coulomb and Hoek-Brown strain-softening models*.

Nonetheless, the previously mentioned researches about the LDP were carried out without considering the coupled hydro-mechanical (HM) interactions. When tunnels excavated in saturated ground, the HM response of geomaterials is significantly important for estimating tunnelling responses (Guayacan-Carrillo et al., 2017; Nam and Bobet, 2007; Prassetyo and Gutierrez, 2018a and 2018b). Nam and Bobet (2007) proposed the empirical best-fit elastic solutions for the LDP for both dry and saturated ground with drained steady-state water flow condition. Considering coupled interactions between solid deformations and fluid flows that affect the HM response, Prassetyo and Gutierrez (2018b) proposed elastic solutions of the LDP

for predicting transient radial displacements along the tunnel axis under a fully coupled hydro-mechanical framework. However, the surrounding rock masses were assumed as linear elastic materials in their research for HM problems (Prassetyo and Gutierrez, 2018b). By revising the references, it turns out that there is still not a satisfactory general result for the hydro-mechanical LDP solutions with more complex behaviour models. Therefore, *the HM modelling of tunnels excavated in elastic-plastic and time-dependent plastic surrounding rock masses are carried out in this thesis. Moreover, the empirical best-fit solutions of the LDP are proposed for the elastic-plastic saturated ground with drained steady-state seepage flow.*

1.2.2.3. The support characteristic curves

Obtaining the support characteristic curves (SCC) for support system involves solving a structural load-displacement problem (Carranza-Torres and Engen, 2017). Closed circular type of supports is the most common type of support systems in the application of the CCM, and the analytical elastic or elastic-plastic stress-strain relationship of the SCC was usually utilized (Carranza-Torres and Fairhurst, 2000; Song and Rodriguez-Dono, 2021; Timoshenko and Goodier, 1970; Wang et al., 2013; Wang et al., 2014). Furthermore, some researchers presented analytical expressions of the SCC for different types of supports, including rockbolts and cables and, steel sets used with and without wood blocks (Brady and Brown, 1993; Carranza-Torres and Fairhurst, 2000; Hoek and Brown, 1980). Carranza-Torres and Engen (2017) developed the SCC for a combined support system consisting of closed circular steel sets linked to the periphery of the tunnel by equally spaced prismatic wood blocks. Lu and Sun (2020) developed the expressions of the SCC of concrete filled steel tubular arch with and without blocks.

On the other hand, Oreste (2003) proposed the SCC for a compound support system, which extended the CCM in the application of tunnels with several different supports (Alejano et al., 2009; Oreste, 2015; Oreste, 2003). However, in order to make more correct design of the secondary support system, the modified ground reaction curves (GRC) due to the influence of the primary support system is needed; research on this topic is a residual until now. To do that, the compatibility conditions at the rock-support and support-support interfaces should be considered. Therefore, at this point, the CCM meets one of its limitations. *In the current research, solutions*

for tunnels with two different support systems are developed, considering the real compatibility conditions on the rock-support and support-support interfaces, as well as the strain-softening post-failure behaviour of rock masses.

1.2.3. Numerical modelling

Numerical simulations have been widely used in the analysis of underground engineering projects, considering more complex geological conditions (Song and Rodriguez-Dono, 2021), due to the increasingly successful use of numerical techniques, such as Finite Element Method (FEM), Finite Difference Method (FDM), Discrete Element Method (DEM), Material Point Method (MPM), Smoothed Particle Hydrodynamics (SPH), and Particle Finite Element Method (PFEM), etc.

Zhu et al. (2003) investigated the effect of the construction process mechanics principle on the stability of tunnels using the FEM and, analysed the deformation and failure of surrounding rock masses. Using an axisymmetric two-dimensional model in a FEM code, Bernaud et al. (1995) simulated the advancement of a bolt-supported tunnel and calculated its convergence as the excavation proceeds. Maghous et al. (2012) described a three-dimensional FEM theoretical and numerical model for the behaviour of tunnels reinforced by bolts. Funatsu et al. (2008) carried out numerical simulations using the DEM and, analysed the effect of supports and reinforcements on tunnel stability. Boon et al. (2015) illustrated a systematic approach of using the DEM to provide useful insights for tunnels support in moderately jointed rock masses.

In order to simulate time-dependent behaviours of surrounding rock masses, Paraskevopoulou (2016) carried out modelling of tunnels excavated in viscoelastic rock masses, using the FDM software FLAC. Some other researchers investigated tunnelling response using viscoplastic model (Bonini et al., 2009; Careglio et al., 2016; Debernardi and Barla, 2009; Sterpi and Gioda, 2009; Zhu et al., 2013), three-stage creep model (Barla et al., 2011), Burger-creep visco-plastic model (CVISC) (Barla et al., 2011; Bonini et al., 2009; Debernardi and Barla, 2009), Burgers-MC deterioration rheological model (Guan et al., 2009; Guan et al., 2008), viscoelastic viscoplastic with isotropic damage model (Kabwe et al., 2020a), or stress hardening

elastic viscous plastic model (SHELVIP) (Barla et al., 2011; Debernardi and Barla, 2009), etc. However, the tunnelling responses are not easy to be anticipated due to the use of inadequate geomaterial models, which is one of the largest limiting factors in numerical analyses (Lade, 1993; Paraskevopoulou, 2016). Thus, in the current study, *the coupled time-dependent plastic model is proposed, to simulate the mechanical behaviour of geomaterials*.

Considering hydro-mechanical coupling, tunnelling response would be more complex. Some researchers carried out hydro-mechanical modelling of tunnelling problems (Armand et al., 2014; Chen et al., 2015; Guayacan-Carrillo et al., 2017; Lisjak et al., 2015; Mánica, 2018; Moon and Fernandez, 2010; Seyedi et al., 2017; Shin et al., 2002). Although numerical simulations can provide some useful results, but without the benefit of the insight that can be gained from examining the relationship between the parameters (Alejano et al., 2010). Moreover, numerical simulations are usually carried out for some special projects, which may lead to difficulties in engineering applications. Additionally, few of these numerical simulations were used to estimate the LDP, which is critical to the design of tunnels based on the CCM.

In this research, numerical approach is adopted to simulate longitudinal excavation of tunnels. Both the finite element method and the multi-stage excavation method (Gharti et al., 2012; Zienkiewicz and Taylor, 2000; Zienkiewicz and Taylor, 2005) have been adopted to obtain the LDP. Revising the literature so far on existing solutions for the LDP, research has mainly focused on purely mechanical problems or on HM problems but with linear elastic materials (as discussed in section 1.2.2). To overcome these limitations, in this thesis, *the hydro-mechanical modelling of tunnels excavated in elastic-plastic and time-dependent plastic surrounding rock masses are carried out.*

However, numerical solutions for coupled non-linear problems may require high computational effort. Load application or construction of geotechnical structures can be easily smoothed by ramping in time the loads or the weight layers to be constructed. Excavation is more challenging because it is difficult to smooth the removal of pieces of soil or rock that occur instantaneously. Removal of very thin pieces of material can be a solution as it can avoid the sharp changes in stresses and fluid fluxes; however, it can lead to too refined meshes. To solve these numerical problems, in this thesis, *a smoothed excavation (SE) method is proposed to simulate excavation so it takes place in a smooth way even for relatively coarse layers or pieces*

of soil or rock, which can improve the numerical efficiency and the convergence of the numerical calculation.

1.3. Research objectives and methodology

The general objective of this doctoral thesis is to analyse the stability of tunnels and thus, improving the design ability of underground workings. The following aspects are addressed:

- Propose a coupled time-dependent plastic mechanical model. In the proposed model, a viscous dashpot and the strain-softening model are coupled to simulate the progressive damage process and creep-induced failure behaviour of geomaterials.
- Propose a smoothed excavation (SE) method and programme the SE method in the finite element method software CODE_BRIGHT. The SE method can improve the numerical efficiency and the convergence of the numerical calculation for multi-stage excavation problems.
- Hydro-mechanical modelling of tunnels excavated in saturated rock masses with plastic or time-dependent plastic models. Meanwhile, propose the empirical plastic solutions of the longitudinal deformation profiles (LDP) for steady-state saturated problems.
- Develop numerical solutions for supported tunnels constructed in strain-softening rock masses, considering longitudinal tunnelling advancement and sequential installation of the primary and secondary support systems, which can improve the design ability of supported tunnels.

The finite element method and multi-stage excavation method are utilized to carry out numerical simulations of longitudinal tunnelling problems. The finite difference method is adopted to develop numerical solutions for supported tunnels constructed in strain-softening rock masses, considering longitudinal tunnelling advancement and sequential installation of different support systems.

1.4. Thesis outline

This thesis is prepared as a compendium of publications, consisting of six chapters. It consists of four international journal articles and a conference abstract. Chapter 1 summarizes the research background, state-of-art, research objectives and research methodology. In chapter 6, the general conclusions of the thesis are presented, and the further works are recommended. Each chapter in chapters 2-5 corresponds to a journal article (published or to be submitted) and, thus each chapter can be read dependently. However, because of this, there will inevitably be some duplication. The contents of each chapter are briefly described in the following paragraphs.

In **chapter 2**, a coupled time-dependent plastic mechanical model has been proposed, and the creep response and strain-softening model are coupled. Thus, the proposed mechanical model can simulate the progressive damage process and the creep-induced failure behaviour of geomaterials. Then, the time-dependent plastic model is utilized in analysing of the longitudinal deformation profiles (LDP). Parametric analyses are carried out, to analyse the sensitivity of the longitudinal deformation profiles to excavation rates, rock behaviour models selection, viscoelasticity and viscoplasticity.

In **chapter 3**, a smoothed excavation (SE) method is proposed and programmed in the finite element method software CODE_BRIGHT, which can improve numerical efficiency and can eliminate numerical difficulties for excavation problems to some degree. The proposed SE method is then utilized in hydro-mechanical modelling of tunnels excavated in saturated rock masses with plastic response. Finally, the best-fitted empirical plastic solutions of the longitudinal deformation profiles for steady-state problems have developed, by fitting non-linear curves for the normalized radial displacements that occur ahead and behind the tunnel face.

In **chapter 4**, considering a coupled solid-fluid interaction and a time-dependent plastic behaviour of rock masses, finite element analyses are performed to analyse tunnelling problems. To do that, the proposed mechanical model in chapter 2 is extended to a Burgers-viscoplastic strain-softening (BVSS) model, and the BVSS model can simulate the primary, secondary and creep-induced failure behaviour of geomaterials. Then, a coupled solid-fluid model is utilised, to simulate the interaction between solid deformations and fluid flows. Parametric analyses are

performed to analyse the influence on the tunnelling response of different time-dependent models, different standstill times and different excavation rates.

In **chapter 5**, numerical solutions for supported tunnels excavated in strain-softening rocks are developed, considering the sequential construction of different support systems and longitudinal tunnelling process. Finite difference method is employed in the derivation, and the real compatibility conditions at rock-support and support-support interfaces are considered. Compared with the convergence-confinement method, the proposed method provides a safer design of tunnels with combined support systems. Finally, the application of the proposed solutions in the design of tunnels is presented, which provides a convenient alternative method for the preliminary design of tunnels.

Chapter 2. Analysis and modelling of longitudinal deformation profiles of tunnels excavated in strain-softening time-dependent rock masses

Based on the published manuscripts of the following article and a conference abstract:

Fei Song, Alfonso Rodriguez-Dono, Sebastia Olivella, Zhen Zhong. Analysis and modelling of longitudinal deformation profiles of tunnels excavated in strain-softening time-dependent rock masses [J]. Computers and Geotechnics, 2020, 125: 103643.

https://doi.org/10.1016/j.compgeo.2020.103643

Fei Song, Alfonso Rodriguez-Dono, Sebastia Olivella. A viscoplastic damage model combined with strain softening failure criterions for rock mass. 11th Workshop of CODE_BRIGHT Users: 16th May 2019, Barcelona, Spain.

https://deca.upc.edu/en/projects/code_bright/workshop/doc/abstracts

Abstract

Rock mass behaviour model selection, in particular, to represent the post-failure behaviour and time-dependent behaviour of rock masses, are critical issues in the correct application of tunnelling design techniques such as the convergence-confinement method or numerical modelling. This study provides a general numerical approach for predicting longitudinal deformation profiles using a coupled ViscoElastic-ViscoPlastic Strain-Softening (VEVP-SS) model. A viscous dashpot and the strain-softening model are coupled to simulate the progressive damage process and creep failure behaviour of rock masses. Different failure criteria are considered to simulate the post-failure behaviour. As a verification step, numerical creep tests are carried out to analyse the coupled behaviour, and the basic viscoelastic and strain-softening results of the VEVP-SS model are compared with analytical solutions and numerical results. The proposed method is able to consider the coupling between post-failure behaviour and time-dependent behaviour, thus providing a new alternative method for preliminary tunnel design.

Parametric analyses are then carried out to investigate the influence of different aspects on the longitudinal deformation profiles. The tunnel deformation based on the VEVP-SS model is larger than the corresponding elastic-plastic results due to the contribution of the creep behaviour, and the excavation rate becomes relevant when considering time-dependent behaviour.

2.1. Introduction

In a geomechanics framework, accidents are frequently related to fractures. The complexity of different geomaterials makes the study of these fractures a critical topic for the understanding of their behaviour; such a study constitutes a very important step in the mitigation of accidents that may occur in mining or civil engineering works such as tunnel excavation (Alejano et al., 2012; Zhao et al., 2015; Zhou et al., 2019). Rock masses undergo progressive damage and long-term viscous behaviour throughout excavation and construction. Some underground structures show large delayed displacements that could lead to failure (Fabre and Pellet, 2006). The effect of time on rock mass deformability and strength is a topic of considerable interest in rock mechanics (Damjanac and Fairhurst, 2010; Eberhardt et al., 1999). Therefore, a proper selection of rock mass behaviour models and a proper simulation of the entire process of excavation and construction are crucial to obtain a reliable tool to achieve the optimal design of tunnels.

Most tunnel designs are currently based on empirical, analytical or numerical methods (Alejano et al., 2010; Alejano et al., 2009; Alejano et al., 2012; Alonso et al., 2003; Barla and Borgna, 2000; Barla et al., 2011; Carranza-Torres and Fairhurst, 1999; Carranza-Torres and Fairhurst, 2000; Conte et al., 2013; Cui et al., 2019; Cui et al., 2015; de la Fuente et al., 2019; Debernardi and Barla, 2009; Deng and Liu, 2020; Doležalová, 2001; Fabre and Pellet, 2006; Galli et al., 2004; Kitagawa et al., 1991; Mánica, 2018; Paraskevopoulou, 2016; Paraskevopoulou and Diederichs, 2018; Sainoki et al., 2017; Song and Rodriguez-Dono, 2021; Song et al., 2020; Song et al., 2018a and 2018b; Sterpi and Gioda, 2009; Sulem et al., 1987; Vlachopoulos and Diederichs, 2009; Wang et al., 2018a; Wang et al., 2020a; Wang et al., 2017a; Wang et al., 2019; Wang et al., 2013; Wang et al., 2020b; Wang et al., 2014; Wang et al., 2015; Wang et al., 2018c; Wang et al., 2018d; Wang et al., 2018e; Wang et al., 2017b; Yi et al., 2019; Zhao et al., 2015; Zhu et al., 2013; Zou et al., 2017a). Among all these methods, the convergence-confinement

method (CCM) is an analytical method that was developed in the 1930s (Fenner, 1938) and later refined by other researchers (Alejano et al., 2010; Alejano et al., 2012; Carranza-Torres and Fairhurst, 2000; Corbetta et al., 1991; Cui et al., 2015; Paraskevopoulou, 2016; Vlachopoulos and Diederichs, 2009). It provides an efficient way to determine supporting forces by considering the rock-support interactions (Alejano et al., 2010; Alejano et al., 2012). The CCM consists of three basic components in the form of graphs:

1. The longitudinal deformation profile (LDP) relates the radial displacements of an unsupported tunnel section with its longitudinal distance to the tunnel face.
2. The ground reaction curve (GRC) establishes the relationship between the decreasing inner pressure and the increasing radial displacements of the tunnel wall.
3. The support characteristic curve (SCC) represents the stress-strain relationship of the support system (Alejano et al., 2010; Alejano et al., 2012; Cui et al., 2015). Then, an adequate design of the required support system can be achieved by taking into account the distance from the tunnel face at which the support will be installed and the supporting forces to which the support will be subjected, which can be obtained by the intersection of the GRC and the SCC, as shown in Figure 2.1.

The GRC has been studied by various researchers (Alejano et al., 2009; Alonso et al., 2003; Cui et al., 2019; Kabwe et al., 2020b; Wang et al., 2010; Zhang et al., 2012a; Zhang et al., 2019b; Zou et al., 2017a). Hoek and Brown initially presented the SCC for different types of support structures (Hoek and Brown, 1980), and then further research on the topic was carried out by other researchers (Carranza-Torres and Fairhurst, 2000; Oreste, 2008; Oreste, 2003).

However, the main focus of this study also includes the longitudinal deformation profile (LDP). Many researchers have derived solutions for the LDP, most of which are based on the elastic (Corbetta et al., 1991; Panet, 1993; Panet, 1995; Unlu and Gercek, 2003) and elastic-perfectly plastic (EPP) behaviour of rock masses (Carranza-Torres and Fairhurst, 1999; Carranza-Torres and Fairhurst, 2000; Vlachopoulos and Diederichs, 2009). These models, nonetheless, do not seem to properly model the behaviour for average-quality rock masses (Alejano et al., 2012; Hoek and Brown, 1997). The response of rock masses will differ depending on the selected model. Considering post-failure behaviour, Alejano et al. (2012) extended the Vlachopoulos and Diederichs (2009) approach to the case of strain-softening rock masses, representing a wider

range of rock masses, which can be used to obtain a more realistic approach to calculate the LDP. In fact, the LDP and the GRC heavily depend on the behaviour model chosen for the rock mass (Alejano et al., 2012).

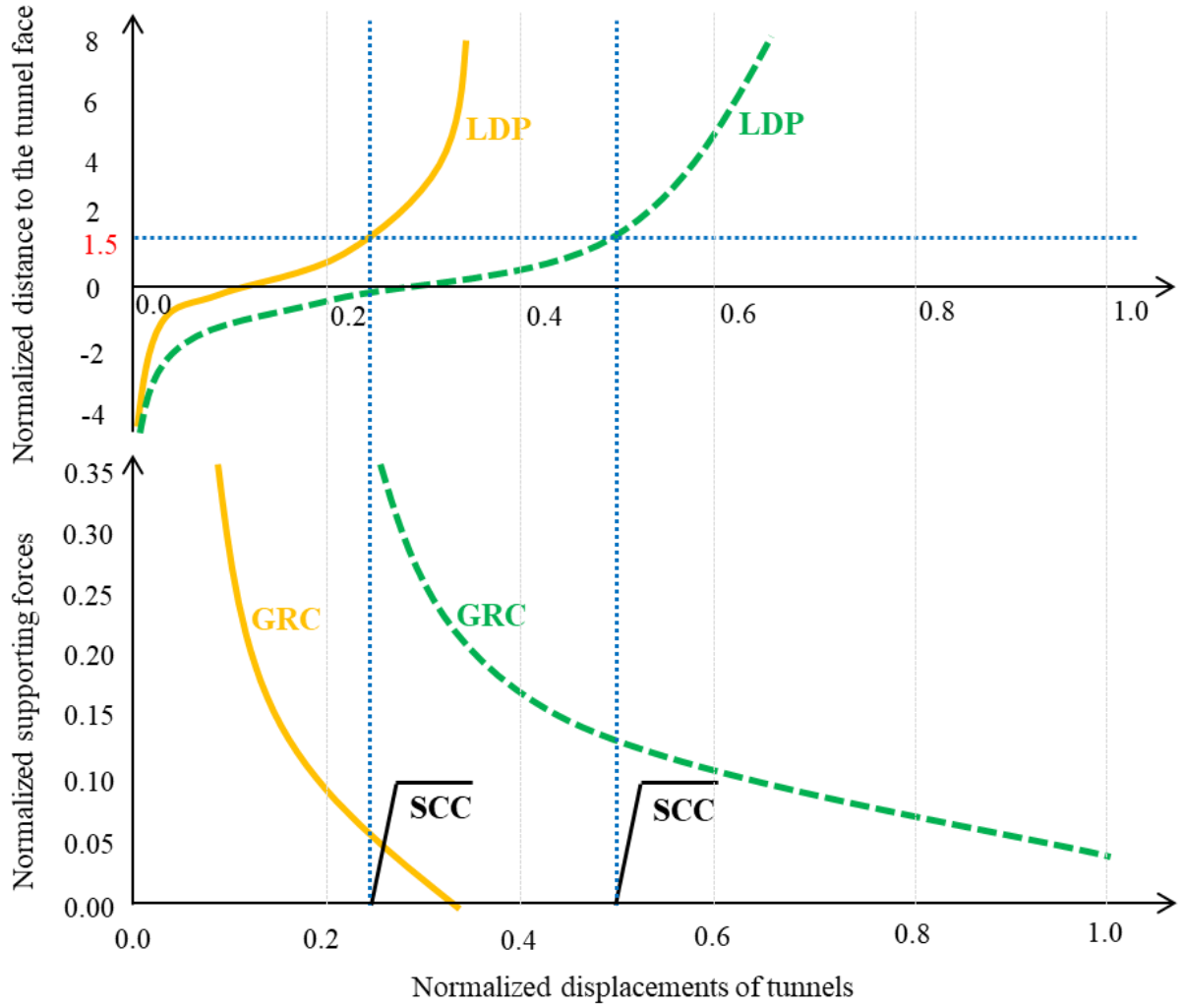

Figure 2.1. Main elements of the convergence-confinement method (CCM). Typical graphs obtained for the longitudinal deformation profile (LDP) above and for the ground reaction curve (GRC) and the supporting characteristic curve (SCC) below. Different lines indicate different rock mass behaviour models: elastic-perfectly plastic (EPP) in the solid yellow line and strain-softening (SS) in the dashed green line. Based on the work of Alejano et al. (2012).

In Figure 2.1, the support design of a tunnel is estimated using CCM. For instance, if the support system is installed at a distance of 1.5 times the tunnel radius from the tunnel face, the support strength is enough to withstand the load when considering an EPP approach for the calculation of both the LDP and the GRC. However, at the same distance from the tunnel face, the support will collapse if the GRC and the LDP are calculated according to a strain-softening approach. Therefore, if the rock mass model cannot reproduce the actual behaviour of the rock mass, the resulting design may be unsafe. In the current research, a strain-softening model will be adopted to simulate the post-failure behaviour of rock masses.

Nevertheless, the solutions mentioned above do not consider the time-dependent properties of rock masses. Most types of rock masses exhibit significant time-dependent characteristics (de la Fuente et al., 2019; Malan, 2002; Sainoki et al., 2017), which are known to induce gradual deformations over time that occur even after the completion of underground excavations. Some researchers presented solutions for tunnels excavated in viscoelastic geomaterials (Song et al., 2018a and 2018b; Wang and Nie, 2010; Wang et al., 2015), but plastic behaviour cannot be accounted for in viscoelastic models. On the other hand, many researchers proposed elastic-viscoplastic models (Conte et al., 2013; Debernardi and Barla, 2009; Desai and Zhang, 1987; Karim et al., 2013; Kutter and Sathialingam, 1992; Pellet et al., 2005; Sterpi and Gioda, 2009; Zhu et al., 2013), three-stage creep (3SC) model (Barla et al., 2011; Sterpi and Gioda, 2009) or Stress Hardening ELastic VIscous Plastic (SHELVIP) model (Barla et al., 2011; Debernardi and Barla, 2009) to simulate the creep and damage behaviour of geomaterials, but few of these models were used for the estimation of the LDP.

Moreover, few of these models consider a Mohr-Coulomb/Hoek-Brown strain-softening model, which may be important to model tunnel behaviour, especially in average-quality rock masses (Alejano et al., 2009 and 2012). Based on the Burgers-creep viscoplastic (CVISC) model introduced by Itasca (2007 and 2008), Paraskevopoulou (2016) and Paraskevopoulou and Diederichs (2018) presented LDP simulations for viscoelastic rock masses. However, in the CVISC model, the plastic slider is not coupled with viscous dashpot plastic yielding, which means that the model behaves similarly to a viscoelastic body if the stress states are below the yielding threshold (Paraskevopoulou et al., 2018). However, in many engineering cases, it is

essential to consider the coupling between the plastic behaviour and the creep behaviour of the rock mass.

In summary, research on this topic has been mostly concerned with elastic, plastic, viscoelastic, or viscoplastic problems. To overcome these limitations, in the current research, we present a new coupled ViscoElastic-ViscoPlastic Strain-Softening (VEVP-SS) model, which considers the following:

1. Time-dependent creep deformation.

2. Mohr-Coulomb and Hoek-Brown strain-softening models.

3. Progressive damage coupled with creep behaviour to simulate failure induced by creep and the subsequent progressive damage. This is the most significant part of the proposed model.

4. The existence of the 'limited stress level', which will be explained in section 2.2. Our approach intends to be a general numerical approach for obtaining the longitudinal deformation profile (LDP) of tunnels excavated in time-dependent strain-softening rock masses.

The coupled ViscoElastic-ViscoPlastic Strain-Softening (VEVP-SS) model is first introduced and implemented into the finite element software CODE_BRIGHT (Olivella et al., 2020). Numerical tests are carried out to calibrate the numerical implementation and to verify the coupled behaviour of viscous dashpot and strain-softening models. Then, the CODE_BRIGHT results are compared with analytical solutions and FLAC results to verify the viscoelastic and strain-softening behaviour in the VEVP-SS model, respectively. Finally, a comprehensive parameter analysis is provided to illustrate the sensitivity of the model to the excavation rate and rock mass behaviour model selection.

2.2. Theoretical background

2.2.1. Rock mass behaviour

In many practical engineering problems, the actual behaviour of rock masses is governed by plastic and viscous effects (Perzyna, 1966). Many creep tests on soft rocks show that the time-

dependent deformation generally accounts for a large amount of the total deformations (Chu et al., 2019; Sulem et al., 1987; Tomanovic, 2006). Time dependency (also known as creep) results in delayed deformations and displacements, which must be taken into account to design underground projects more accurately and avoid safety issues in the working area (Paraskevopoulou and Diederichs, 2018; Paraskevopoulou et al., 2018). Moreover, the post-peak stress-strain behaviour of the rock mass may play a non-negligible role when a deep underground excavation is made (Alejano et al., 2012). Hoek and Brown (1997) provided particularly relevant post-peak strength guidelines. These guidelines are based on the geotechnical quality of the rock mass described by the geotechnical strength index (GSI):

1. For high-quality rock masses (GSI > 70), the rock mass behaves in a purely brittle manner.

2. For average-quality rock masses (25 < GSI < 70), the rock mass presents strain-softening (SS) behaviour, *i.e.* after achieving a maximum stress, the rock mass can still withstand some load.

3. For very weak rock masses (GSI < 25), perfectly plastic behaviour is assumed, as shown in Figure 2.2a. Note that these ranges are just a reference and they may vary in some cases.

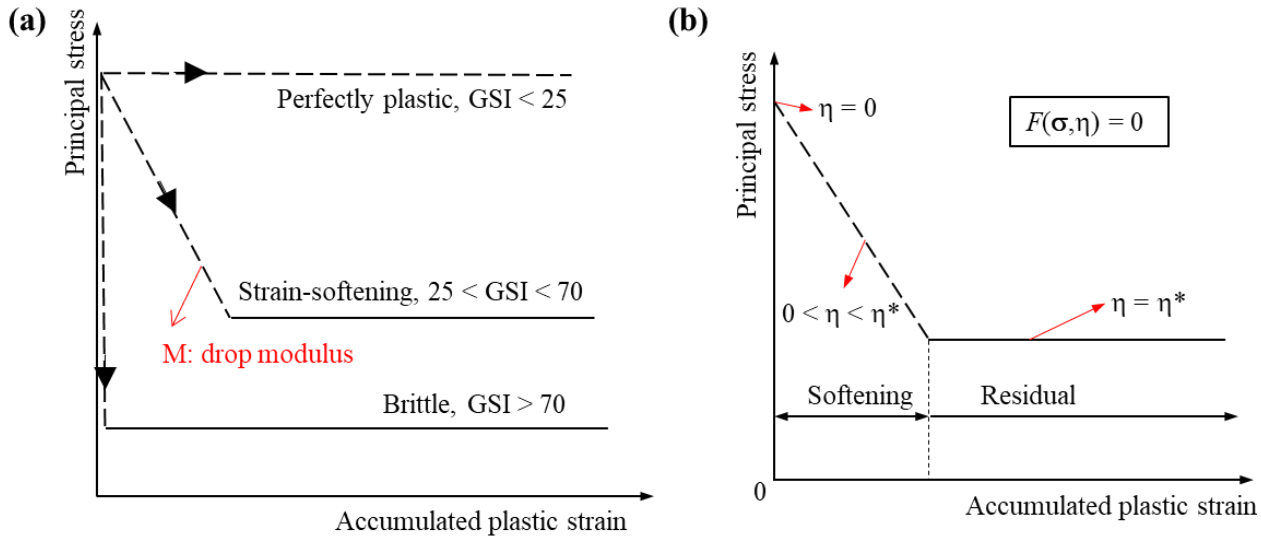

Figure 2.2. **(a)** Different post-failure behaviours of rock masses with different geological strength indexes (GSI); and **(b)** conceptual behaviour for a strain-softening model. Based on the work of Alejano et al. (2009) and Alejano et al. (2012).

Strain-softening behaviour can incorporate purely brittle behaviour (strain-softening with an infinite drop modulus, M, as shown in Figure 2.2a) and perfectly plastic behaviour (strain-softening with a drop modulus, M, equal to zero, as shown in Figure 2.2a). M represents the drop modulus of the strain-softening model, as shown in Figure 2.2(a). Thus, perfectly plastic and purely brittle behaviours are just two particular cases of strain-softening behaviour.

In this study, strain-softening models are adopted to simulate the post-failure behaviour of rock masses (Alejano et al., 2010). The yield surfaces $F(\boldsymbol{\sigma}, \eta)$ for strain-softening models depend not only on the stress tensor $\boldsymbol{\sigma}$ but also on the plastic or softening parameter η (Alejano et al., 2009; Alonso et al., 2003), as shown in Figure 2.2(b). Strain-softening behaviour is characterized by a gradual transition from the peak failure surface to the residual failure surface, which is governed by the plastic or softening parameter η. In a strain-softening model, a softening regime occurs whenever $0 < \eta < \eta^*$, and the residual regime takes place when $\eta \geq \eta^*$ (Alejano et al., 2009; Alonso et al., 2003). η^* is the value of the softening parameter at which the softening phase ends and the residual phase begins.

Figures 2.3(a) and 2.3(b) present the typical creep curves of a rock mass under a constant applied load based on experimental data (Ramírez Oyanguren, 1966) and a conceptual model, respectively. As shown in Figure 2.3(b), the typical creep curves can be characterized by three stages:

1. Elastic stage: the elastic strain appears instantaneously upon loading, and the associated strains are fully reversible and transient (Sterpi and Gioda, 2009).

2. Viscoelastic stage: the displacements are induced with time under a constant stress. In some research, the viscoelastic stage can also be divided into the primary creep stage (the strain rate decreases with time) and secondary creep stage (a constant strain rate with time). Note that although the load reversal would cause the specimen to return to the initial dimensions in the primary creep stage, the associated strain is irreversible in the secondary creep stage (Sterpi and Gioda, 2009). In this research, only secondary creep is considered, which is reasonable for some cases, such as rock salt (Günther et al., 2015; Olivella and Gens, 2002), rock masses under squeezing conditions (Sterpi and Gioda, 2009), tunnels excavated in weak or altered rock masses (Sainoki et al., 2017) or very deep excavations (Sterpi and Gioda, 2009).

3. Viscoelastic-viscoplastic stage (accelerated or tertiary creep stage): the strain rate starts to accelerate once the material starts to yield (damage). Viscoplastic strain occurs only when the stresses achieve a critical state, which can be defined by a yield surface $F = 0$. Hence, only elastic/viscoelastic deformations occur when $F < 0$, and viscoelastic-viscoplastic strains occur when $F \geq 0$ (Paraskevopoulou, 2016).

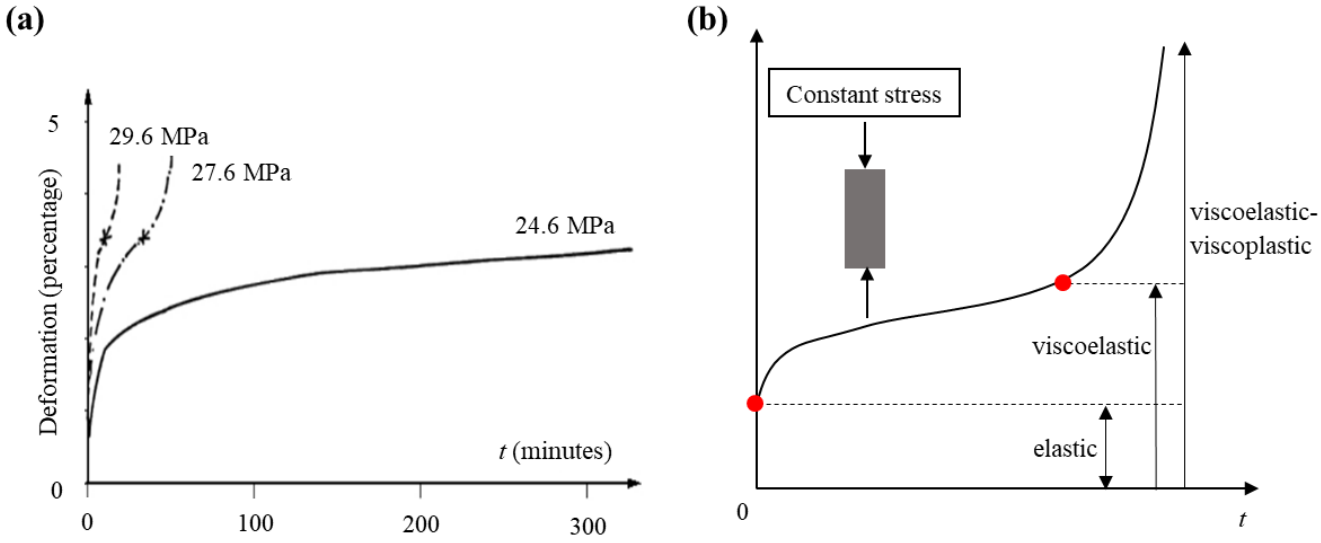

Figure 2.3. **(a)** Typical creep curve based on experimental data (Ramírez Oyanguren, 1966) and **(b)** the conceptual model of creep curves.

Figure 2.4(a) presents the typical stress-strain curves of creep tests (Paraskevopoulou, 2016): after some incremental stress $\Delta\sigma$ is applied (points A, C or E), the applied load is kept constant for a long period of time. Note that there exists a 'limited stress level': for stress values below the 'limited stress level', no failure occurs, even with sufficient time (see line 'A-B' in Figure 2.4a). However, for stress states above the 'limited stress level', the stress state will result in failure. This failure will occur at different values of accumulated strain. In fact, the higher the stress is, the lower the value of the accumulated strain that leads to failure (see lines 'C-D' and 'E-F' in Figure 2.4a) and the faster this failure occurs (Barla and Borgna, 2000; Damjanac and Fairhurst, 2010; Paraskevopoulou, 2016).

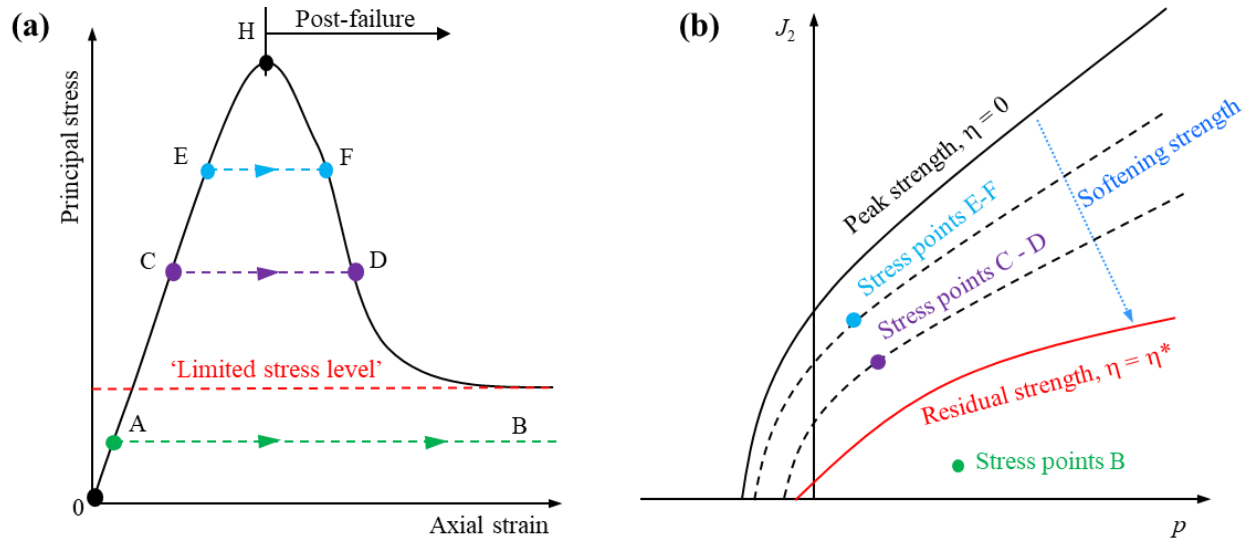

Figure 2.4. **(a)** Schematic representation of the long-term stress-strain response when subjected to constant stress conditions, and **(b)** yield surface evolution for a strain-softening rock mass.

In the present study, a coupled ViscoElastic-ViscoPlastic Strain-Softening (VEVP-SS) model combined with strain-softening failure criteria (Mohr-Coulomb and Hoek-Brown) is proposed. As shown in Figure 2.5, these tentative approaches are needed if, as recommended by Starfield and Cundall (1988), we follow heuristic approaches to study, analyse and understand rock mechanics problems.

2.2.2. A coupled ViscoElastic-ViscoPlastic Strain-Softening (VEVP-SS) model

In rock mechanics, Hookean elastic springs, Newtonian viscous dashpots, and plastic sliders are used to model a variety of rock mass behaviours (Wang et al., 2013). The coupled ViscoElastic-ViscoPlastic Strain-Softening (VEVP-SS) model consists of an elastic spring and a viscous dashpot in series with the Perzyna viscoplastic model.

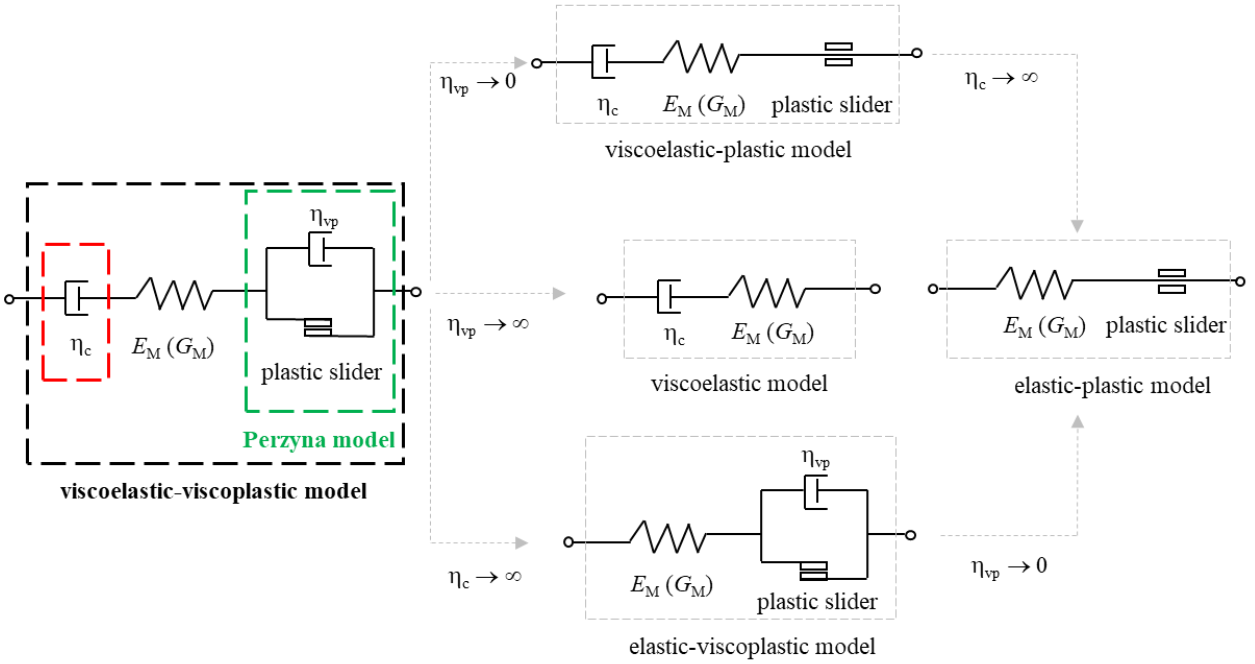

Figure 2.5. Comparison among five mechanical models for geomaterials.

Figure 2.5 shows five common typical mechanical models of a rock mass, where E_M (G_M) is the elastic (shear) modulus of the rock mass; η_c and η_{vp} represent the viscosities of the viscous dashpot and the Perzyna model, respectively; and the parameters for the plastic slider depend on the failure criteria chosen. As shown in Figure 2.5, four different models can be considered as particular cases of the VEVP-SS model: the viscoelastic model, by assigning a sufficiently large value to η_{vp}; the elastic-viscoplastic model, by assigning a sufficiently large value to η_c; the viscoelastic-plastic model, by assigning a sufficiently small value to η_{vp}; and the elastic-plastic model, by assigning a sufficiently large value to η_c and a sufficiently small value to η_{vp}. Note that the concepts of 'sufficiently large' and 'sufficiently small' denote infinite and zero, respectively, for practical numerical reasons that do not significantly affect the results.

The total strain rate tensor $\frac{d\boldsymbol{\varepsilon}}{dt}$ of the proposed VEVP-SS model can be decomposed into components describing the rock elasticity ($\frac{d\boldsymbol{\varepsilon}_e}{dt}$) and inelasticity ($\frac{d\boldsymbol{\varepsilon}_i}{dt}$), as shown in Eq. (2.1).

$$\frac{d\boldsymbol{\varepsilon}}{dt} = \frac{d\boldsymbol{\varepsilon}_{\mathrm{e}}}{dt} + \frac{d\boldsymbol{\varepsilon}_{\mathrm{i}}}{dt} \tag{2.1}$$

where $\boldsymbol{\varepsilon}_{\mathbf{e}}$ and $\boldsymbol{\varepsilon}_{\mathbf{i}}$ represent the elastic and inelastic strain tensors, respectively. The elastic strain rate can be expressed in Eq. (2.2).

$$\frac{d\boldsymbol{\varepsilon}_{\mathrm{e}}}{dt} = \frac{\mathbf{m}}{3K_{\mathrm{M}}}\frac{dp}{dt} + \frac{1}{2G_{\mathrm{M}}}\left(\frac{d\boldsymbol{\sigma}}{dt} - \frac{dp}{dt}\mathbf{m}\right) \tag{2.2}$$

where $K_{\mathrm{M}} = \dfrac{E_{\mathrm{M}}}{3(1-2\nu)}$ and $G_{\mathrm{M}} = \dfrac{E_{\mathrm{M}}}{2(1+\nu)}$ represent the volumetric stiffness and deviatoric stiffness, respectively; ν represents Poisson's ratio; and $\boldsymbol{\sigma} = p\mathbf{m} + \mathbf{s}$, in which $\boldsymbol{\sigma}$ (p) represents the stress (mean stress) matrix and $\mathbf{m} = [1\ 1\ 1\ 0\ 0\ 0]^{\mathrm{T}}$. The inelastic strain ($\boldsymbol{\varepsilon}_{\mathrm{i}}$) is the sum of the viscous (creep) strain $\boldsymbol{\varepsilon}_{\mathrm{c}}$ and the viscoplastic strain $\boldsymbol{\varepsilon}_{\mathrm{vp}}$, *i.e.*, $\boldsymbol{\varepsilon}_{\mathrm{i}} = \boldsymbol{\varepsilon}_{\mathrm{c}} + \boldsymbol{\varepsilon}_{\mathrm{vp}}$. As shown in Figure 2.5, the viscous dashpot is adopted to simulate the creep behaviour of rock masses. The Perzyna model, consisting of a viscous dashpot in parallel with a plastic slider, can simulate the viscoplastic behaviour of rock masses. Thus, the inelastic strain rate can be expressed by Eq. (2.3), where $\eta_{\mathrm{c}}^{\mathrm{v}}$ ($\eta_{\mathrm{c}}^{\mathrm{d}}$) represents the volumetric (deviatoric) viscosity of the viscous dashpot, η_{vp} represents the viscosity of the viscoplastic model and F and G represent the overstress function and the viscoplastic potential, respectively, of the viscoplastic model.

$$\frac{d\boldsymbol{\varepsilon}_{\mathrm{i}}}{dt} = \frac{d\boldsymbol{\varepsilon}_{\mathrm{c}}}{dt} + \frac{d\boldsymbol{\varepsilon}_{\mathrm{vp}}}{dt} = \frac{\mathbf{m}}{3\eta_{\mathrm{c}}^{\mathrm{v}}}p + \frac{1}{2\eta_{\mathrm{c}}^{\mathrm{d}}}(\boldsymbol{\sigma} - p\mathbf{m}) + \frac{1}{\eta_{\mathrm{vp}}}\langle\Phi(\mathrm{F})\rangle\frac{\partial G}{\partial \boldsymbol{\sigma}} \tag{2.3}$$

$$\langle\Phi(F)\rangle = \begin{cases} 0, & \text{for } F \le 0 \\ \Phi(F), & \text{for } F > 0 \end{cases} \tag{2.4}$$

The form of $\Phi(F)$ can be defined by experimental data (Perzyna, 1966). For simplicity, $\Phi(F) = F^{\mathrm{m}}$ ($\mathrm{m} \ge 1$) is adopted in this research. Overstress theory (Mánica, 2018; Perzyna, 1966) has been adopted for the Perzyna viscoplastic model and is different from purely plastic theory. Overstress theory allows the stress point to exceed the yield surface. As shown in Figure 2.6, the yield surface sets the limits of two different regimes in the stress space:

1. If the stress point is below the yield surface, the rock mass exhibits non-viscoplastic behaviour, *i.e.*, elastic or viscoelastic behaviour in the proposed model.

2. If the stress point is between the yield surface and the viscoplastic limit, the rock mass will exhibit viscoplastic properties. The viscoplastic limit is related to the viscosity of the Perzyna viscoplastic model, *i.e.*, η_{vp} in Eq. (2.3). As the viscosity η_{vp} is closer to zero, the viscoplastic limit will be closer to the yield surface *F*. It must be noted again that one can always ensure a viscoplastic solution as close as necessary to the 'true' purely plastic solution by sufficiently decreasing the viscosity η_{vp} of the viscoplastic formulation (Alonso et al., 2005).

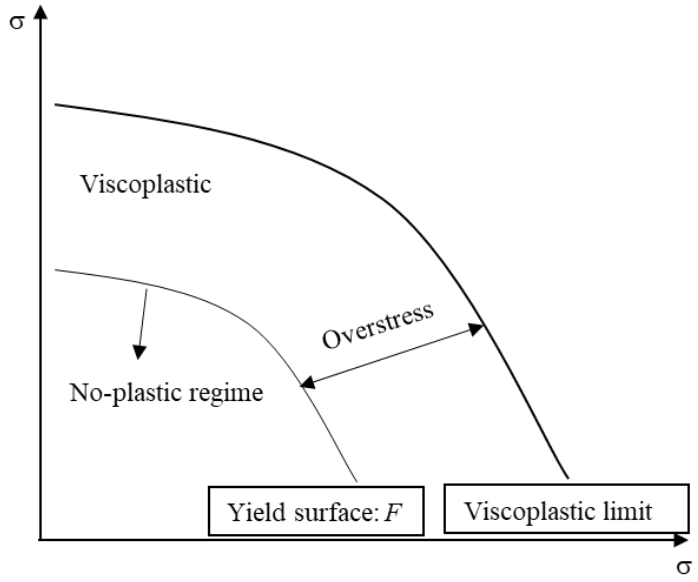

Figure 2.6. Overstress theory of the viscoplastic model.

In rock masses, deviatoric stress states cause deviatoric strain rates that may produce significant long-term deformations, while the volumetric strain is less significant (Sulem et al., 1987). Thus, only the deviatoric part of the viscosity (η_c^d) has been considered, and the volumetric viscosity (η_c^v) has not been considered. In the VEVP-SS model, the overstress function is assumed to be equal to the viscoplastic yield function (failure criterion). Thus, the total strain rate can be expressed by Eq. (2.5).

$$\frac{d\boldsymbol{\varepsilon}}{dt}=\frac{d\boldsymbol{\varepsilon}_{\mathrm{e}}}{dt}+\frac{d\boldsymbol{\varepsilon}_{\mathrm{c}}}{dt}+\frac{d\boldsymbol{\varepsilon}_{\mathrm{vp}}}{dt}=\frac{\mathbf{m}}{3K_{\mathrm{M}}}\frac{dp}{dt}+\frac{1}{2G_{\mathrm{M}}}\left(\frac{d\boldsymbol{\sigma}}{dt}-\frac{dp}{dt}\mathbf{m}\right)+\frac{1}{2\eta_{\mathrm{c}}^{\mathrm{d}}}(\boldsymbol{\sigma}-p\mathbf{m})+\frac{1}{\eta_{\mathrm{vp}}}\left\langle F^{\mathrm{m}}\right\rangle\frac{\partial G}{\partial\boldsymbol{\sigma}} \tag{2.5}$$

It should be noted that in our proposed VEVP-SS model, only the secondary creep stage is considered in the viscoelastic model; hence, the associated creep strain $\boldsymbol{\varepsilon}_{\mathrm{c}}$ is irreversible (Debernardi and Barla, 2009; Sterpi and Gioda, 2009). Then, it is reasonable to assume that failure may be reached by accumulated creep deformation (*e.g.*, from point E to point F in Figure 2.4). To make this failure depend on the stress history and the applied stress, the viscoplastic yield surface is assumed to evolve from a peak failure criterion to a residual one (which we refer to as softening). Furthermore, after failure, both creep strain $\boldsymbol{\varepsilon}_{\mathrm{c}}$ and viscoplastic strain $\boldsymbol{\varepsilon}_{\mathrm{vp}}$ accumulate in the proposed model to account for the strain-softening behaviour (*e.g.*, from point F to the residual stage in Figure 2.4). This coupling constitutes the most important part and the most significant novelty of the VEVP-SS model. Hence, the proposed VEVP-SS model can be used to simulate the creep-induced failure shown in Figure 2.4 and the coupled behaviour between creep deformation and damage evolution.

In the VEVP-SS model, as shown in Figure 2.4(b), the peak and residual yield surfaces define 3 different fields in the stress space:

1. The viscoelastic field below the residual yield surface, where the strain rates are $\frac{d\boldsymbol{\varepsilon}_{\mathrm{e}}}{dt}+\frac{d\boldsymbol{\varepsilon}_{\mathrm{c}}}{dt}$ (*e.g.*, stress point B in Figure 2.4b with a stress-strain behaviour represented by the line '0-A-B' in Figure 2.4a).

2. The field between the peak and residual yield surfaces, where the deformations are initially viscoelastic (*e.g.*, points C and E in Figure 2.4a) but will then become viscoelastic-viscoplastic when the yield surfaces eventually decrease to the stress point (e.g., points D and F in Figure 2.4a).

3. The viscoelastic-viscoplastic field on/above the peak yield surface (e.g., point H in Figure 2.4a), where the deformations can be divided into elastic, creep and viscoplastic parts, $\frac{d\boldsymbol{\varepsilon}_{\mathrm{e}}}{dt}+\frac{d\boldsymbol{\varepsilon}_{\mathrm{c}}}{dt}+\frac{d\boldsymbol{\varepsilon}_{\mathrm{vp}}}{dt}$.

In this study, a linearly decreasing function of the plastic parameters k(η) is adopted to represent the strain-softening behaviour (Alejano et al., 2009; Alonso et al., 2003), as shown in Eq. (2.6), where k_{peak} and k_{res} are the peak and residual values of k, respectively. If a Mohr-Coulomb failure surface is considered, k represents the cohesion c and friction angle φ, while k represents the m_{HB} and s_{HB} parameters when considering the Hoek-Brown failure surface.

$$\mathrm{k}(\eta)=\begin{cases}\mathrm{k}_{\mathrm{peak}}, & \text{for } \eta<0\\ \mathrm{k}_{\mathrm{peak}}+\left(\dfrac{\mathrm{k}_{\mathrm{res}}-\mathrm{k}_{\mathrm{peak}}}{\eta^{*}}\right)\eta, & \text{for } 0\le\eta<\eta^{*}\\ \mathrm{k}_{\mathrm{res}}, & \text{for } \eta\ge\eta^{*}\end{cases} \tag{2.6}$$

Note that when considering a Mohr-Coulomb failure criterion, the relationship between the friction angle φ and its tangent (tanφ) can be assumed to be approximately linear for the typical range of friction angle values for rock masses (< 30 deg). Nevertheless, we selected a linear decrease in the friction angle to represent softening, following the work of other researchers that used a linearly decreasing function for the friction angle (Alejano et al., 2009; Alejano et al., 2012; Alonso et al., 2003; Lee and Pietruszczak, 2008; Zhang et al., 2012a; Zou et al., 2017a).

The softening parameter η is defined as shown in Eq. (2.7), where $\boldsymbol{\varepsilon}^{\mathbf{p}}$ ($\boldsymbol{\gamma}^{\mathbf{p}}$) represents the accumulated plastic strain and $\varepsilon_{\mathrm{m}}^{\mathrm{p}}=\frac{1}{3}\left(\varepsilon_{\mathrm{x}}^{\mathrm{p}}+\varepsilon_{\mathrm{y}}^{\mathrm{p}}+\varepsilon_{\mathrm{z}}^{\mathrm{p}}\right)$.

$$\eta=\sqrt{\frac{3}{2}\left[\left(\varepsilon_{\mathrm{x}}^{\mathrm{p}}-\varepsilon_{\mathrm{m}}^{\mathrm{p}}\right)^{2}+\left(\varepsilon_{\mathrm{y}}^{\mathrm{p}}-\varepsilon_{\mathrm{m}}^{\mathrm{p}}\right)^{2}+\left(\varepsilon_{\mathrm{z}}^{\mathrm{p}}-\varepsilon_{\mathrm{m}}^{\mathrm{p}}\right)^{2}+\left(\frac{1}{2}\gamma_{\mathrm{xy}}^{\mathrm{p}}\right)^{2}+\left(\frac{1}{2}\gamma_{\mathrm{yz}}^{\mathrm{p}}\right)^{2}+\left(\frac{1}{2}\gamma_{\mathrm{zx}}^{\mathrm{p}}\right)^{2}\right]} \tag{2.7}$$

The expression of the Mohr-Coulomb strain-softening failure criterion is shown in Eq. (2.8), where c(η) and φ(η) are the plastic strain-dependent cohesion and the friction angle, respectively.

p, J_2 (J_3) and θ represent the mean stress, the second (third) invariable stress, and the Lode angle, respectively.

$$F_{\mathrm{MC}} = p\sin\varphi(\eta) + \sqrt{J_2}\left(\cos\theta - \frac{1}{\sqrt{3}}\cdot\sin\varphi(\eta)\cdot\sin\theta\right) - c(\eta)\cos\varphi(\eta) \tag{2.8}$$

The expression of the Hoek-Brown strain-softening failure criterion is shown in Eq. (2.9), where $m_{HB}(\eta)$ and $s_{HB}(\eta)$ are the plastic strain-dependent parameters of the Hoek-Brown failure criterion and σ_{ci} is the uniaxial compressive strength of the intact rock.

$$F_{\mathrm{HB}} = \left[\frac{4}{\sigma_{\mathrm{ci}}}\cos^2\theta\sqrt{J_2} + \frac{2}{\sqrt{3}}m_{\mathrm{HB}}(\eta)\cos\left(\theta + \frac{\pi}{6}\right)\right]\sqrt{J_2} - m_{\mathrm{HB}}(\eta)\left[-p + \frac{s_{\mathrm{HB}}(\eta)\sigma_{\mathrm{ci}}}{m_{\mathrm{HB}}(\eta)}\right] \tag{2.9}$$

The Mohr-Coulomb form of the potential has been considered in both the Mohr-Coulomb and Hoek-Brown strain-softening models (Alejano et al., 2009 and 2012), as expressed in Eq. (2.10), where α is a parameter for the potential ($0 \le \alpha \le 1$) and ψ is the dilatancy angle.

$$G = \alpha p\sin\psi + \sqrt{J_2}\left(\cos\theta - \frac{1}{\sqrt{3}}\sin\psi\sin\theta\right) \tag{2.10}$$

The total number of constitutive parameters of the ViscoElastic-ViscoPlastic Strain-Softening (VEVP-SS) model is 12, as shown in Table 2.1: 2 classical elastic parameters, 1 viscous (creep) parameter, and 9 viscoplastic parameters. The only clear disadvantage of the VEVP-SS model is the inability to simulate the primary creep stage; thus, the use of the VEVP-SS model should be limited to cases in which large deformation occurs due to secondary and accelerated creep and the primary creep-induced deformation is negligible, such as tunnelling excavation in weak, altered or hard rock masses or very deep tunnelling excavation (Sainoki et al., 2017; Sterpi and Gioda, 2009).

Table 2.1. Constitutive parameters of the VEVP-SS model.

Elastic	E_M (G_M)	Elastic (shear) modulus
	ν	Poisson's ratio
Viscous	η_c	The viscosity of the viscous dashpot
Viscoplastic	η_{vp}	The viscosity of the Perzyna model
	m	Stress power
	η^*	The critical softening parameter
	ψ	Dilatancy angle
	α	Associativity parameter
	c_{peak}, c_{res}, φ_{peak}, φ_{res}	Parameters for the Mohr-Coulomb strain-softening model
	m_{peak}, m_{res}, s_{peak}, s_{res}	Parameters for the Hoek-Brown strain-softening model

2.3. Numerical implementation

The proposed ViscoElastic-ViscoPlastic Strain-Softening (VEVP-SS) model was implemented into the finite element method software CODE_BRIGHT. CODE_BRIGHT (Olivella et al., 2020) was developed at the Department of Civil and Environmental Engineering of the Technical University of Catalonia (UPC) and works in combination with the pre-/post-processor GID (Coll et al., 2018), developed by the International Centre for Numerical Methods in Engineering (CIMNE). If another code is adopted, the same constitutive model presented in this study can be utilized. The implementation of the proposed VEVP-SS model should consider the following aspects: (1) the existence of corners in the yield (and potential) surfaces at which the gradients are not uniquely defined, and thus requiring smoothing methods; (2) the development of strain-softening and localization.

2.3.1. Smoothing method of the failure criteria and the potential

Due to the gradient discontinuities in both the Mohr-Coulomb and Hoek-Brown failure criteria, we found that the developed numerical implementations suffered from non-convergence issues as

well as excessive CPU time consumption. Therefore, to overcome these problems, smoothing methods have been adopted to round both yield surfaces and the potential function. Expressions of both the Mohr-Coulomb failure surface and the potential function were based on a smoothing method described in the scientific literature (Abbo et al., 2011; Abbo and Sloan, 1995). On the other hand, it should be noted that the smoothed Hoek-Brown failure surface was derived in this study.

The smoothed Mohr-Coulomb strain-softening yield surface (Abbo and Sloan, 1995) shown in Eq. (2.11) was adopted in the current research, where a = $m_{mc}c(\eta)\cot\varphi(\eta)$, and a is typically defined as 0.25.

$$F_{\mathrm{MC}} = \sqrt{J_2 K_{\mathrm{MC}}^2(\theta) + a^2 \sin^2\varphi(\eta)} + p\sin\varphi(\eta) - c(\eta)\cos\varphi(\eta) \tag{2.11}$$

As the value of the hyperbolic parameter m_{MC} approaches zero, the yield surface approaches a hyperbolic shape (Abbo and Sloan, 1995). In addition, an alternative form of $K_{MC}(\theta)$ in the vicinity of the singularities was defined to round the failure surface function *F* (Abbo and Sloan, 1995), as shown in Eq. (2.12), where θ_T is a specified transition angle, typically defined as 25 deg.

$$K_{\mathrm{MC}}(\theta,\eta) = \begin{cases} A_{\mathrm{MC}} + B_{\mathrm{MC}}\sin 3\theta, & \text{for } |\theta| > \theta_{\mathrm{T}} \\ \cos\theta - \dfrac{1}{\sqrt{3}}\sin\varphi(\eta)\sin\theta, & \text{for } |\theta| \le \theta_{\mathrm{T}} \end{cases} \tag{2.12}$$

where:

$$A_{\mathrm{MC}} = \frac{1}{3}\cos\theta_{\mathrm{T}}\left[3 + \tan\theta_{\mathrm{T}}\tan 3\theta_{\mathrm{T}} + \frac{1}{\sqrt{3}}\langle\theta\rangle\left(\tan 3\theta_{\mathrm{T}} - 3\tan\theta_{\mathrm{T}}\right)\sin\varphi(\eta)\right]$$

$$B_{\mathrm{MC}} = -\frac{1}{3\cos 3\theta_{\mathrm{T}}}\left[\langle\theta\rangle\sin\theta_{\mathrm{T}} + \frac{1}{\sqrt{3}}\sin\varphi(\eta)\cos\theta_{\mathrm{T}}\right]$$

$$\langle\theta\rangle = \begin{cases} +1, & \theta \ge 0 \\ -1, & \theta < 0 \end{cases}$$

Since the second derivative of the plastic potential should also be continuous, the C2 method (Abbo et al., 2011) was used to smooth the potential function. Following the method of Abbo et al. (2011), the smoothed potential was adopted, which can be expressed as shown in Eq. (2.13).

The alternative form of $K_G(\theta)$ in the vicinity of the singularities can be expressed as shown in Eq. (2.14), where θ_T is a specified transition angle, typically defined as 25 deg.

$$G = \alpha p \sin\psi + J_2 K_G^2(\theta) \tag{2.13}$$

$$K_G(\theta) = \begin{cases} D_G + E_G \sin 3\theta + F_G \sin^2 3\theta, & \text{for } |\theta| > \theta_T \\ \cos\theta - \frac{1}{\sqrt{3}} \sin\psi \sin\theta, & \text{for } |\theta| \le \theta_T \end{cases} \tag{2.14}$$

where

$$F_G = \frac{-\cos 3\theta_T \left(\cos\theta_T - \frac{1}{\sqrt{3}} \sin\psi \langle\theta\rangle \right) - 3\langle\theta\rangle \sin 3\theta_T \left(\langle\theta\rangle \sin\theta_T + \frac{1}{\sqrt{3}} \sin\psi \cos\theta_T \right)}{18\cos^3 3\theta_T}$$

$$E_G = \frac{\langle\theta\rangle \sin 6\theta_T \left(\cos\theta_T - \frac{1}{\sqrt{3}} \sin\psi \langle\theta\rangle \sin\theta_T \right) - 6\cos 6\theta_T \left(\langle\theta\rangle \sin\theta_T + \frac{1}{\sqrt{3}} \sin\psi \cos\theta_T \right)}{18\cos^3 3\theta_T}$$

$$D_G = -\frac{1}{\sqrt{3}} \sin\psi \langle\theta\rangle \sin\theta_T - E\langle\theta\rangle \sin 3\theta_T - F \sin^2 3\theta_T + \cos\theta_T$$

These equations were adapted from Abbo et al. (2011) and Abbo and Sloan (1995). The reader is referred to the original source for a detailed description of the smoothed approximation (C1 and C2) to the Mohr-Coulomb failure surface.

However, the smoothed approximation to the Hoek-Brown yield surface was derived in the current research and is presented in Eq. (2.15), and the alternative form of $K_{HB}(\theta, \eta)$ in the vicinity of the singularities can be expressed as Eq. (2.16), where θ_T is a specified transition angle, typically defined as 25 deg. The derivatives of $K_{HB}(\theta)$ with respect to θ are shown in Eq. (2.17).

$$F_{HB} = K_{HB}(\theta, \eta) \sqrt{J_2} - m_{HB}(\eta) \left[-p + \frac{s_{HB}(\eta) \sigma_{ci}}{m_{HB}(\eta)} \right] \tag{2.15}$$

$$K_{\mathrm{HB}}(\theta,\eta)=\begin{cases} A_{\mathrm{HB}}+B_{\mathrm{HB}}\sin 3\theta, & \text{for } \theta \geq \left|\theta_{\mathrm{T}}\right| \\ \dfrac{4}{\sigma_{\mathrm{ci}}}\cos^2\theta\sqrt{J_2}+\dfrac{2}{\sqrt{3}}m_{\mathrm{HB}}(\eta)\cos\left(\theta+\dfrac{\pi}{6}\right), & \text{for } \theta \leq \left|\theta_{\mathrm{T}}\right| \end{cases} \tag{2.16}$$

$$\frac{dK_{\mathrm{HB}}(\theta)}{d\theta}=\begin{cases} 3\mathrm{B}_{\mathrm{HB}}\cos 3\theta, & \theta \geq \left|\theta_{\mathrm{T}}\right| \\ -\dfrac{8}{\sigma_{\mathrm{ci}}}\cos\theta\sin\theta\sqrt{J_2}-\dfrac{2}{\sqrt{3}}m_{\mathrm{HB}}(\eta)\sin\left(\theta+\dfrac{\pi}{6}\right), & \theta \leq \left|\theta_{\mathrm{T}}\right| \end{cases} \tag{2.17}$$

Note that the expressions of $\mathrm{A_{HB}}$ and $\mathrm{B_{HB}}$ were obtained by matching the zero and first derivatives for the rounded surface to those for the Hoek-Brown surface at θ_{T} and $-\theta_{\mathrm{T}}$, providing two linear equations, as shown in Eqs. (2.18) and (2.19).

$$\mathrm{A_{HB}}+\mathrm{B_{HB}}\sin 3\theta_{\mathrm{T}}=\frac{4}{\sigma_{\mathrm{ci}}}\cos^2\theta_{\mathrm{T}}\sqrt{J_2}+\frac{2}{\sqrt{3}}m_{\mathrm{HB}}(\eta)\cos\left(\theta_{\mathrm{T}}+\frac{\pi}{6}\right) \tag{2.18}$$

$$3\mathrm{B_{HB}}\cos 3\theta_{\mathrm{T}}=-\frac{8}{\sigma_{\mathrm{ci}}}\cos\theta_{\mathrm{T}}\sin\theta\sqrt{J_2}-\frac{2}{\sqrt{3}}m_{\mathrm{HB}}(\eta)\sin\left(\theta_{\mathrm{T}}+\frac{\pi}{6}\right) \tag{2.19}$$

Finally, the coefficients of $\mathrm{A_{HB}}$ and $\mathrm{B_{HB}}$ can be determined, and the corresponding expressions are shown in Eqs. (2.20) and (2.21).

$$\begin{aligned}\mathrm{A_{HB}}=m_{\mathrm{HB}}(\eta)&\left[\left(\cos\theta_{\mathrm{T}}-\frac{\langle\theta\rangle\sin\theta_{\mathrm{T}}}{\sqrt{3}}\right)+\left(\frac{\cos\theta_{\mathrm{T}}}{3\sqrt{3}}+\frac{1}{3}\langle\theta\rangle\sin\theta_{\mathrm{T}}\right)\langle\theta\rangle\tan 3\theta_{\mathrm{T}}\right] \\ &+\sqrt{J_2}\left[\frac{4\cos^2\theta_{\mathrm{T}}}{\sigma_{\mathrm{ci}}}+\frac{8\sin\theta_{\mathrm{T}}\cos\theta_{\mathrm{T}}\tan 3\theta_{\mathrm{T}}}{3\sigma_{\mathrm{ci}}}\right]\end{aligned} \tag{2.20}$$

$$\mathrm{B_{HB}}=\sqrt{J_2}\left[-\frac{8\langle\theta\rangle\sin\theta_{\mathrm{T}}\cos\theta_{\mathrm{T}}}{3\sigma_{\mathrm{ci}}\cos 3\theta_{\mathrm{T}}}\right]-\frac{m_{\mathrm{HB}}(\eta)}{3\cos 3\theta_{\mathrm{T}}}\left[\langle\theta\rangle\sin\theta_{\mathrm{T}}+\frac{\cos\theta_{\mathrm{T}}}{\sqrt{3}}\right] \tag{2.21}$$

2.3.2. The gradients of the yield surface and potential

The gradients of the yield surface and the potential function with respect to the stresses play an essential role in the numerical implementation. The derivative of Eq. (2.1) with respect to the stress tensor can be expressed in Eq. (2.22), where the first derivative of the yield surface with respect to the stress, $\frac{\partial F}{\partial \boldsymbol{\sigma}}$, is expressed in Eq. (2.23); the first derivative of the potential with respect to the stress, $\frac{\partial G}{\partial \boldsymbol{\sigma}}$, is expressed in Eq. (2.24); and the second derivative of the potential with respect to the stress, $\frac{\partial^2 G}{\partial \boldsymbol{\sigma}^2}$, is expressed in Eq. (2.25).

$$\frac{d}{d\boldsymbol{\sigma}}\left(\frac{d\boldsymbol{\varepsilon}(t)}{dt}\right)=\frac{1}{3K_{\mathrm{M}}}\frac{d}{d\boldsymbol{\sigma}}(\frac{dp}{dt}\mathbf{m})+\frac{1}{2G_{\mathrm{M}}}\frac{d}{d\boldsymbol{\sigma}}\left(\frac{d\boldsymbol{\sigma}}{dt}-\frac{dp}{dt}\mathbf{m}\right)+\frac{1}{2\eta_{\mathrm{c}}^{\mathrm{d}}}\frac{d(\boldsymbol{\sigma}-\mathrm{p}\,\mathbf{m})}{d\boldsymbol{\sigma}}+\frac{1}{\eta_{\mathrm{vp}}}\mathrm{m}\left\langle F^{\mathrm{m\text{-}1}}\right\rangle\frac{\partial F}{\partial\boldsymbol{\sigma}}\frac{\partial G}{\partial\boldsymbol{\sigma}}+\frac{1}{\eta_{\mathrm{vp}}}\left\langle F^{\mathrm{m}}\right\rangle\frac{\partial^2 G}{\partial\boldsymbol{\sigma}^2} \tag{2.22}$$

$$\frac{\partial F}{\partial\boldsymbol{\sigma}}=\frac{\partial F}{\partial p}\frac{\partial p}{\partial\boldsymbol{\sigma}}+\frac{\partial F}{\partial\sqrt{J_2}}\frac{\partial\sqrt{J_2}}{\partial\boldsymbol{\sigma}}+\frac{\partial F}{\partial\theta}\frac{\partial\theta}{\partial\boldsymbol{\sigma}} \tag{2.23}$$

$$\frac{\partial G}{\partial\boldsymbol{\sigma}}=\frac{\partial G}{\partial p}\frac{\partial p}{\partial\boldsymbol{\sigma}}+\frac{\partial G}{\partial\sqrt{J_2}}\frac{\partial\sqrt{J_2}}{\partial\boldsymbol{\sigma}}+\frac{\partial G}{\partial\theta}\frac{\partial\theta}{\partial\boldsymbol{\sigma}} \tag{2.24}$$

$$\frac{\partial^2 G}{\partial\boldsymbol{\sigma}^2}=\left(\frac{\partial^2 G}{\partial\sqrt{J_2}^2}\frac{\partial\sqrt{J_2}}{\partial\boldsymbol{\sigma}}+\frac{\partial^2 G}{\partial\sqrt{J_2}\partial\theta}\frac{\partial\theta}{\partial\boldsymbol{\sigma}}\right)\frac{\partial\sqrt{J_2}}{\partial\boldsymbol{\sigma}}+\frac{\partial G}{\partial\sqrt{J_2}}\frac{\partial^2\sqrt{J_2}}{\partial\boldsymbol{\sigma}^2}+\left(\frac{\partial^2 G}{\partial\theta\partial\sqrt{J_2}}\frac{\partial\sqrt{J_2}}{\partial\boldsymbol{\sigma}}+\frac{\partial^2 G}{\partial\theta^2}\frac{\partial\theta}{\partial\boldsymbol{\sigma}}\right)\frac{\partial\theta}{\partial\boldsymbol{\sigma}}+\frac{\partial G}{\partial\theta}\frac{\partial^2\theta}{\partial\boldsymbol{\sigma}^2} \tag{2.25}$$

2.3.2.1. The first derivative expressions of the Mohr-Coulomb and Hoek-Brown failure criteria

The first derivative of the failure surface is shown in Eq. (2.26).

$$\frac{\partial F}{\partial \boldsymbol{\sigma}} = \frac{\partial F}{\partial p}\frac{\partial p}{\partial \boldsymbol{\sigma}} + \frac{\partial F}{\partial \sqrt{J_2}}\frac{\partial \sqrt{J_2}}{\partial \boldsymbol{\sigma}} + \frac{\partial F}{\partial \theta}\frac{\partial \theta}{\partial \boldsymbol{\sigma}} \tag{2.26}$$

For the Mohr-Coulomb failure criterion,

$$\frac{\partial F_{\mathrm{MC}}}{\partial p} = \sin\varphi \tag{2.27}$$

$$\frac{\partial F_{\mathrm{MC}}}{\partial \sqrt{J_2}} = \frac{K_{\mathrm{MC}}^2\sqrt{J_2}}{\sqrt{J_2 K_{\mathrm{MC}}^2 + a^2\sin^2\varphi}} \tag{2.28}$$

$$\frac{\partial F_{\mathrm{MC}}}{\partial \theta} = \frac{J_2 K_{\mathrm{MC}}}{\sqrt{J_2 K_{\mathrm{MC}}^2 + a^2\sin^2\varphi}}\frac{dK_{\mathrm{MC}}}{d\theta} \tag{2.29}$$

where

$$\frac{dK_{\mathrm{MC}}(\theta,\eta)}{d\theta} = \begin{cases} 3B_{\mathrm{MC}}\cos 3\theta, & |\theta| > \theta_{\mathrm{T}} \\ -\sin\theta - \dfrac{1}{\sqrt{3}}\sin\varphi(\eta)\cos\theta, & |\theta| \le \theta_{\mathrm{T}} \end{cases} \tag{2.30}$$

For the Hoek-Brown failure criterion,

$$\frac{\partial F_{\mathrm{HB}}}{\partial p} = m_{\mathrm{HB}}(\eta) \tag{2.31}$$

$$\frac{\partial F_{\mathrm{HB}}}{\partial \sqrt{J_2}} = \frac{dK_{\mathrm{HB}}(\theta,\eta)}{d\sqrt{J_2}}\sqrt{J_2} + K_{\mathrm{HB}}(\theta,\eta) \tag{2.32}$$

$$\frac{\partial F_{\mathrm{HB}}}{\partial \theta} = \frac{dK_{\mathrm{HB}}(\theta,\eta)}{d\theta}\sqrt{J_2} \tag{2.33}$$

where

$$\frac{dK_{\mathrm{HB}}(\theta,\eta)}{d\sqrt{J_2}}=\begin{cases}\dfrac{dA_{\mathrm{HB}}}{d\sqrt{J_2}}+\dfrac{dB_{\mathrm{HB}}}{d\sqrt{J_2}}\sin 3\theta, & \theta>\left|\theta_{\mathrm{T}}\right| \\ \dfrac{4}{\sigma_{\mathrm{ci}}}\cos^2\theta, & \theta\le\left|\theta_{\mathrm{T}}\right|\end{cases} \tag{2.34}$$

$$\frac{dK_{\mathrm{HB}}(\theta,\eta)}{d\theta}=\begin{cases}3B_{\mathrm{HB}}\cos 3\theta, & \theta>\left|\theta_{\mathrm{T}}\right| \\ -\dfrac{8}{\sigma_{\mathrm{ci}}}\cos\theta\sin\theta\sqrt{J_2}-\dfrac{2}{\sqrt{3}}m_{\mathrm{HB}}(\eta)\sin\left(\theta+\dfrac{\pi}{6}\right), & \theta\le\left|\theta_{\mathrm{T}}\right|\end{cases} \tag{2.35}$$

$$\frac{dA_{\mathrm{HB}}}{d\sqrt{J_2}}=\frac{4\cos^2\theta_{\mathrm{T}}}{\sigma_{\mathrm{ci}}}+\frac{8\sin\theta_{\mathrm{T}}\cos\theta_{\mathrm{T}}\tan 3\theta_{\mathrm{T}}}{3\sigma_{\mathrm{ci}}} \tag{2.36}$$

$$\frac{dB_{\mathrm{HB}}}{d\sqrt{J_2}}=-\frac{8\langle\theta\rangle\sin\theta_{\mathrm{T}}\cos\theta_{\mathrm{T}}}{3\sigma_{\mathrm{ci}}\cos 3\theta_{\mathrm{T}}} \tag{2.37}$$

2.3.2.2. The first and second derivative expressions of the potential function

The first derivative of the potential function is presented in Eq. (2.38).

$$\frac{\partial G}{\partial\boldsymbol{\sigma}}=\frac{\partial G}{\partial p}\frac{\partial p}{\partial\boldsymbol{\sigma}}+\frac{\partial G}{\partial\sqrt{J_2}}\frac{\partial\sqrt{J_2}}{\partial\boldsymbol{\sigma}}+\frac{\partial G}{\partial\theta}\frac{\partial\theta}{\partial\boldsymbol{\sigma}} \tag{2.38}$$

where

$$\frac{\partial G}{\partial p}=\alpha\sin\psi \tag{2.39}$$

$$\frac{\partial G}{\partial\sqrt{J_2}}=2K_{\mathrm{G}}^2(\theta)\sqrt{J_2} \tag{2.40}$$

$$\frac{\partial G}{\partial\theta}=2J_2K_{\mathrm{G}}\frac{dK_{\mathrm{G}}}{d\theta} \tag{2.41}$$

$$\frac{dK_{\mathrm{G}}(\theta)}{d\theta}=\begin{cases}3E_{\mathrm{G}}\cos 3\theta+6F_{\mathrm{G}}\sin 3\theta\cos 3\theta, & |\theta|>\theta_{\mathrm{T}}\\ -\sin\theta-\dfrac{1}{\sqrt{3}}\sin\psi\cos\theta, & |\theta|\le\theta_{\mathrm{T}}\end{cases} \tag{2.42}$$

The second derivative of plastic potential function is presented in Eq. (2.43).

$$\begin{aligned}\frac{\partial^2 G}{\partial\boldsymbol{\sigma}^2}=&\left(\frac{\partial^2 G}{\partial\sqrt{J_2}^2}\frac{\partial\sqrt{J_2}}{\partial\boldsymbol{\sigma}}+\frac{\partial^2 G}{\partial\sqrt{J_2}\partial\theta}\frac{\partial\theta}{\partial\boldsymbol{\sigma}}\right)\frac{\partial\sqrt{J_2}}{\partial\boldsymbol{\sigma}}+\frac{\partial G}{\partial\sqrt{J_2}}\frac{\partial^2\sqrt{J_2}}{\partial\boldsymbol{\sigma}^2}\\&+\left(\frac{\partial^2 G}{\partial\theta\partial\sqrt{J_2}}\frac{\partial\sqrt{J_2}}{\partial\boldsymbol{\sigma}}+\frac{\partial^2 G}{\partial\theta^2}\frac{\partial\theta}{\partial\boldsymbol{\sigma}}\right)\frac{\partial\theta}{\partial\boldsymbol{\sigma}}+\frac{\partial G}{\partial\theta}\frac{\partial^2\theta}{\partial\boldsymbol{\sigma}^2}\end{aligned} \tag{2.43}$$

where

$$\frac{\partial^2 G}{\partial\sqrt{J_2}^2}=2K_{\mathrm{G}}^2(\theta) \tag{2.44}$$

$$\frac{\partial^2 G}{\partial\sqrt{J_2}\partial\theta}=\frac{\partial^2 G}{\partial\theta\partial\sqrt{J_2}}=4K_{\mathrm{G}}(\theta)\sqrt{J_2}\frac{dK_{\mathrm{G}}(\theta)}{d\theta} \tag{2.45}$$

$$\frac{\partial^2 G}{\partial\theta^2}=2J_2\frac{dK_{\mathrm{G}}}{d\theta}\frac{dK_{\mathrm{G}}}{d\theta}+2J_2K_{\mathrm{G}}\frac{d^2K_{\mathrm{G}}}{d\theta^2} \tag{2.46}$$

$$\frac{d^2K_{\mathrm{G}}(\theta)}{d\theta^2}=\begin{cases}-9E_{\mathrm{G}}\sin 3\theta+18F_{\mathrm{G}}\cos 6\theta, & |\theta|>\theta_{\mathrm{T}}\\ -\cos\theta+\dfrac{1}{\sqrt{3}}\sin\psi\sin\theta, & |\theta|\le\theta_{\mathrm{T}}\end{cases} \tag{2.47}$$

2.3.3. Strength parameter update and strain localization

In the proposed VEVP-SS model, the strength parameters are the cohesion and friction angle if the Mohr-Coulomb failure surface is chosen or m_{HB} and s_{HB} if the Hoek-Brown failure surface is chosen. A specific implementation has been developed to compute the accumulated plastic (unrecoverable) strain $\boldsymbol{\varepsilon}^{\mathbf{p}}$, *i.e.*, the sum of the viscous strain $\boldsymbol{\varepsilon}_{\mathbf{c}}$ and viscoplastic strain $\boldsymbol{\varepsilon}_{\mathbf{vp}}$, in this

model. For the elements in the numerical model, the accumulated unrecoverable strain is updated, and then the softening parameter η is updated based on Eq. (2.7). Finally, the strength parameters are updated following the function of Eq. (2.6), and the failure surface is updated.

As shown in Figure 2.4(b), the peak residual strength surfaces divide the stress space into 3 fields:

1. For the elements where the stress state is below the residual strength, the accumulated unrecoverable strain ($\boldsymbol{\varepsilon}^p$) is equal to the viscous strain $\boldsymbol{\varepsilon}_c$, *i.e.*, $\boldsymbol{\varepsilon}^p = \boldsymbol{\varepsilon}_c$. Therefore, the response will be only viscoelastic in this case, even if the strength parameters are updated.

2. For the elements where the stress state is between the peak and residual strength surfaces, the accumulated strain is equal to the viscous (creep) strain at the beginning of the simulation, and the strength parameters are updated with the increase in the accumulated creep strain (as well as the softening parameter η). Thus, the failure surface shrinks with increasing η, and the stress state could then meet the failure surface if η is sufficiently large. After that, the accumulated unrecoverable strain is assumed to be a combination of viscous and viscoplastic strains ($\boldsymbol{\varepsilon}^p = \boldsymbol{\varepsilon}_c + \boldsymbol{\varepsilon}_{vp}$).

3. For the elements where the stress state is on/above the peak strength, the accumulated unrecoverable strain is assumed to be a combination of viscous and viscoplastic strains, *i.e.*, $\boldsymbol{\varepsilon}^p = \boldsymbol{\varepsilon}_c + \boldsymbol{\varepsilon}_{vp}$, and thus, their response would be viscoelastic-viscoplastic. The softening parameters can be updated based on Eq. (2.7), when the unrecoverable strain is obtained.

Nonetheless, softening behaviour may introduce numerical difficulties. In some cases, instability occurs because softening concentrates at isolated elements, while other elements in their vicinity experience stress relaxation. However, the viscoplastic approach that is adopted for our strain-softening model is capable of homogenizing the spatial distribution of softening strain, which benefits the control of the size of the localized zone and thus allows avoidance of the dependency on the employed mesh (Günther et al., 2015; Mánica, 2018). In addition, from an engineering point of view, strain localization effects are not relevant when considered on an appropriately large spatial scale (Alejano et al., 2010), as would be the case of the tunnel excavation model in this research. In section 2.4.2, an analysis of the effect of mesh on the resulting tunnel deformation is carried out.

2.4. Numerical verification

To verify the numerical implementation, an example of a creep test was first carried out to verify the coupled behaviour between the creep model and the strain-softening model. After that, a number of 2D axisymmetric numerical models were employed to assess the performance of the viscoplastic model in tunnel excavation, including a mesh-independence analysis. Finally, the viscoelastic part and the strain-softening part of the proposed VEVP-SS model were verified separately by comparison with analytical solutions (Wang et al., 2014; Wang et al., 2015) and FLAC numerical results (Alejano et al., 2012), respectively.

2.4.1. Verification of the coupled behaviour

As we explained in section 2.2, the most important novelty of the VEVP-SS model is the coupled behaviour between the creep model and the strain-softening model. Hence, a biaxial creep numerical test was carried out to analyse the coupled behaviour implemented in CODE_BRIGHT. Note that the analyses made do not represent any particular experiment, and the conditions and parameters adopted in the simulation were simply chosen to evaluate the key aspects of the coupled behaviour.

The model used here is 2D axisymmetric with dimensions of 0.01 m × 0.05 m. The normal displacements along the bottom and left boundaries were restrained, as shown in Figure 2.7(a). In addition, constant stresses were applied along the top boundary, with values of p_y = 20.0 MPa, respectively. A mesh with 2250 quadratic triangle elements was considered for the analysis, as shown in Figure 2.7(b). The calculation was stopped at 150 days. In this sub-section, the Mohr-Coulomb strain-softening model was adopted for this example, and the parameters input into the numerical simulations are listed in Table 2.2.

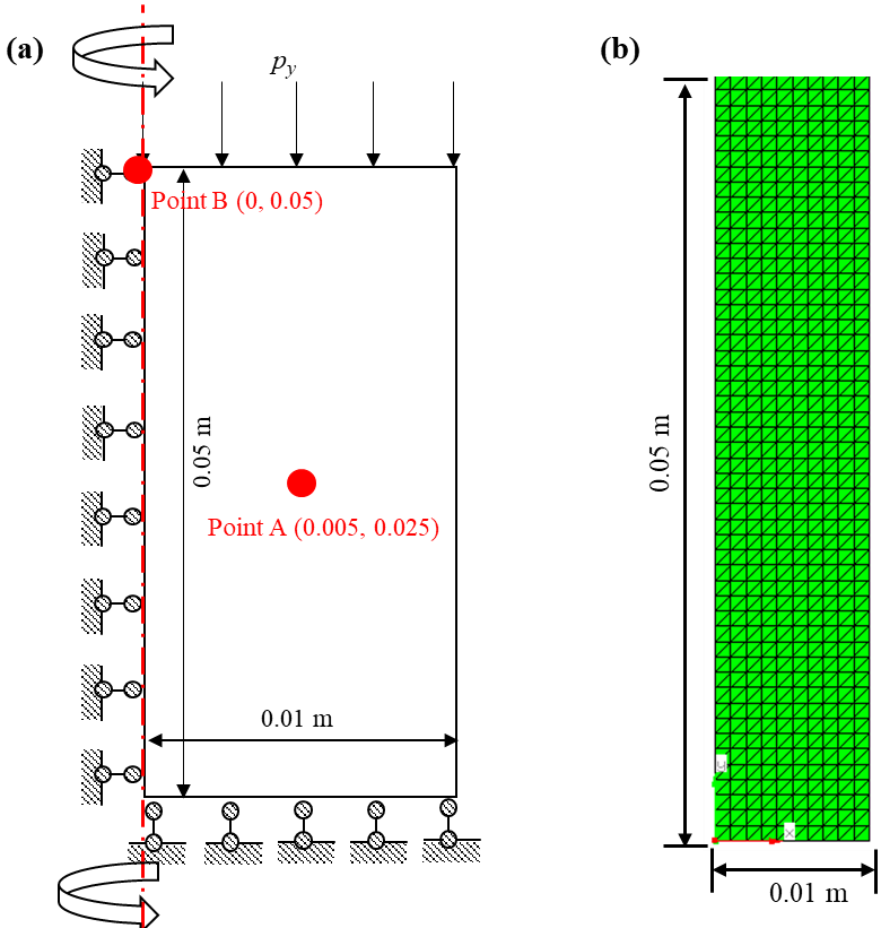

Figure 2.7. Creep numerical test: **(a)** basic features and boundary conditions (not real scale), and **(b)** mesh (real scale). A mesh with 2250 quadratic triangle elements.

In Figure 2.8, the results of the viscoelastic (VE) model and the ViscoElastic-ViscoPlastic Strain-Softening (VEVP-SS) model are compared. At the start of the simulation, stress point A (Figure 2.7a) is inside the viscoelastic domain, as shown in Figure 2.8(a), so only viscoelastic strain occurs. Hence, initially, a steady creep takes place under constant stress, with the viscoelastic strain in the *x* and *y* directions increasing similarly for both the VE and VEVP-SS models, with the chosen point A maintains a constant stress under the constant stress condition imposed.

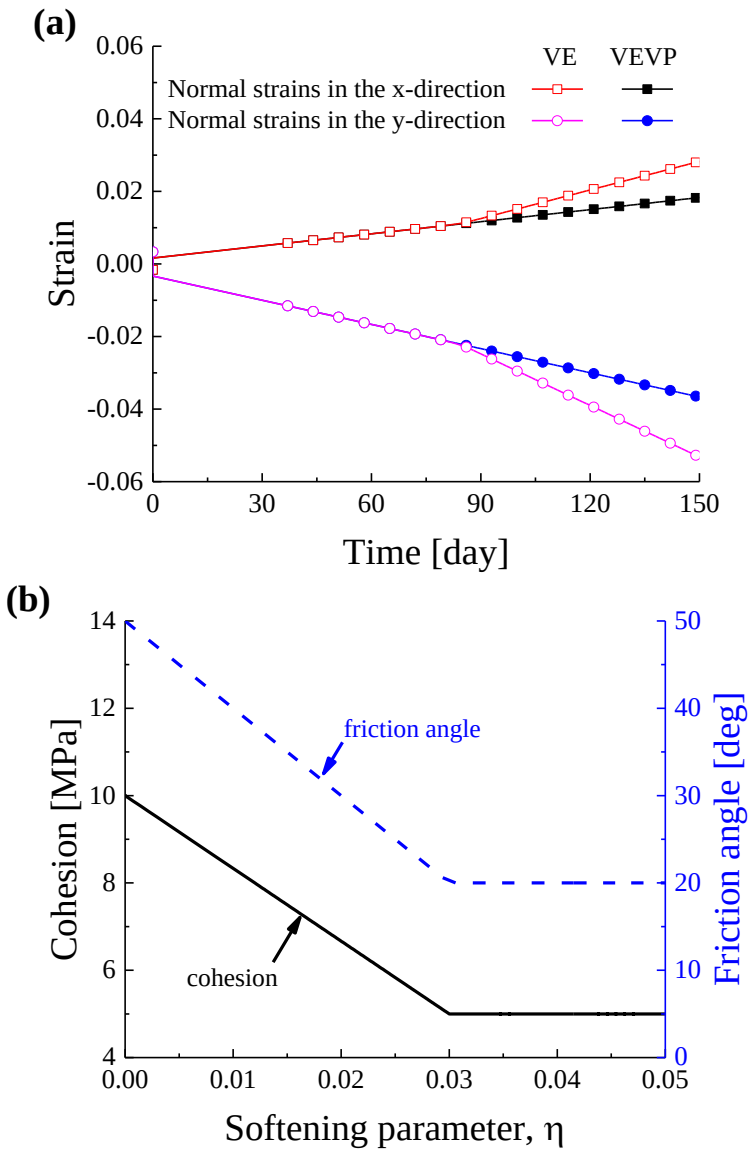

Figure 2.8. **(a)** Normal strain in the *x* and *y* directions for the viscoelastic (VE) and ViscoElastic-ViscoPlastic Strain-Softening (VEVP-SS) models at point A in Figure 2.7(a). **(b)** Strength parameters (cohesion and friction angle in the Mohr-Coulomb strain-softening model) versus the softening parameter (η) at point A in Figure 2.7(a).

However, as the accumulated plastic (unrecoverable) strain increases, the yield surface decreases due to softening induced by creep (*i.e.* the softening parameter η develops due to the accumulated viscoelastic strain $\boldsymbol{\varepsilon}_c$). Consequently, when the yield surface reaches the point of our analysis, the strain rate accelerates due to both the creep and viscoplastic contributions. Figure

2.8(b) presents the softening process in terms of the cohesion and friction angle. Based on the numerical analysis, it can be concluded that creep behaviour is coupled with plastic behaviour in the proposed VEVP-SS model.

Table 2.2. Mechanical properties of the rock mass in the numerical biaxial creep tests.

Input parameters for the ViscoElastic-ViscoPlastic Strain-Softening (VEVP-SS) model						
Peak cohesion, c_{peak} (MPa)	Residual cohesion, c_{res} (MPa)	Peak friction angle, φ_{peak} (deg)	Residual friction angle, φ_{res} (deg)	The critical softening parameter, η^*	Stress power, m	η_{vp} (MPa^{m}s)
10.0	5.0	50.0	20.0	0.03	5	10^{10}
Associativity parameter, α	Dilatancy angle, ψ (deg)	Elastic modulus, E_M (MPa)	Poisson's ratio, ν	η_c^d (MPa.s)	a in F_{MC}	θ_T (deg) for F and G
1.0	5.0	6000	0.49	2.592×10^9	0.25	25

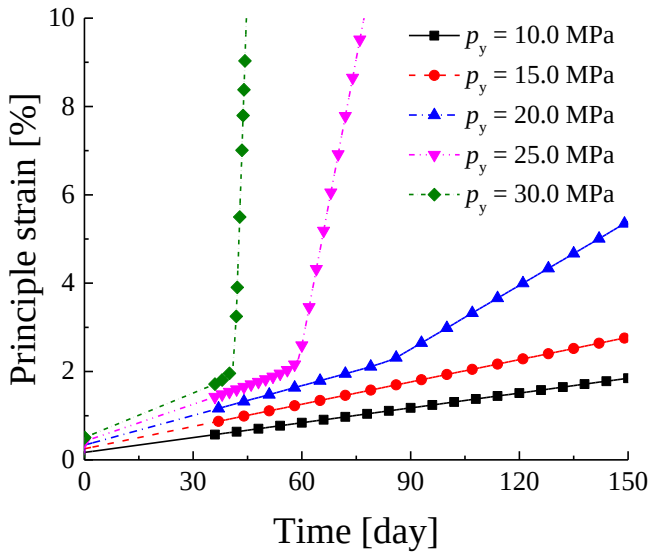

Figure 2.9. Numerical examples of creep tests for five different applied stresses.

For further calibration, a series of biaxial creep tests were carried out to analyse the relationship between the principal strain and the applied stress. The numerical geometry and mesh are the same as in the former example, as shown in Figure 2.7. In the biaxial creep tests,

five different applied stresses were considered, p_y = 10.0 MPa, 15.0 MPa, 20.0 MPa, 25.0 MPa, 30.0 MPa and 35.0 MPa. The calculation was stopped at 150 days. The input parameters of materials are the same as those in Table 2.2, and these parameters were estimated with the intent of matching experimental data from the scientific literature. Figure 2.9 shows the time-dependent strains of the point B (see Figure 2.7). In Figure 2.9, it shows that different stresses result in different strains, and a higher applied stress will result in larger deformation, which is consistent with the conclusion of laboratory tests (Cristescu and Hunsche, 1998; Sterpi and Gioda, 2009).

2.4.2. Mesh independency

As previously mentioned in section 2.3, numerical analysis involving softening problems may exhibit a marked dependency on the finite element mesh employed. In this section, a number of 2D axisymmetric models were developed to assess the performance of the viscoplastic approach in the simulation of softening problems. In these models, a deeply buried tunnel with a diameter of 5 m is excavated in an elastic-viscoplastic ($\eta_c \rightarrow \infty$) and low-quality rock mass (GSI_{peak} = 40, GSI_{res} = 27), exhibiting a strong strain-softening behaviour. The rock specific weight is 25 kN/m^3 and the rest of the input parameters concerning this low-quality rock mass are shown in Table 2.3. Moreover, two different values of viscosity were adopted ($\eta_{vp} = 10^2$ MPa^{5}s and $\eta_{vp} = 10^4$ MPa^{5}s) to assess the influence of viscoplastic viscosity on mesh independency.

Furthermore, the tunnel is presented as a rectangle with a length of 55 m (Figure 2.10) so that 22 excavation steps of 2.5 m in length can be performed. The tunnel is excavated at a depth of 1500 m, implying a field stress of 37.5 MPa. Hence, the normal displacements are fixed along the axisymmetric axis (x = 0) and on the bottom of the model (y = 0), and a pressure of 37.5 MPa is applied to the other boundaries of the model. As shown in Figure 2.11, four meshes with different qualities were adopted to analyse the effect of mesh on the resulting displacements. The meshes are composed of the following number of quadratic triangular elements (*i.e.*, triangles with 6 nodes): (a) 988, (b) 2016, (c) 3719, and (d) 6342.

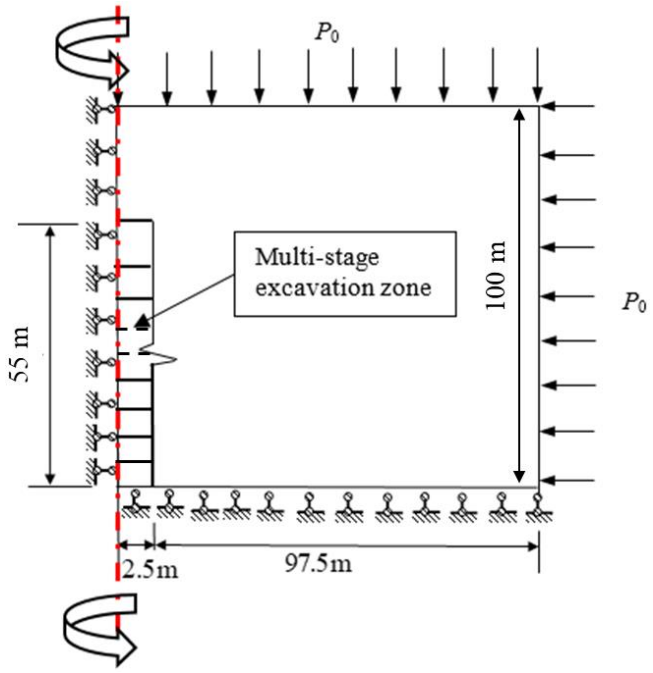

Figure 2.10. Basic features and boundary conditions for the 2D axisymmetric excavation model.

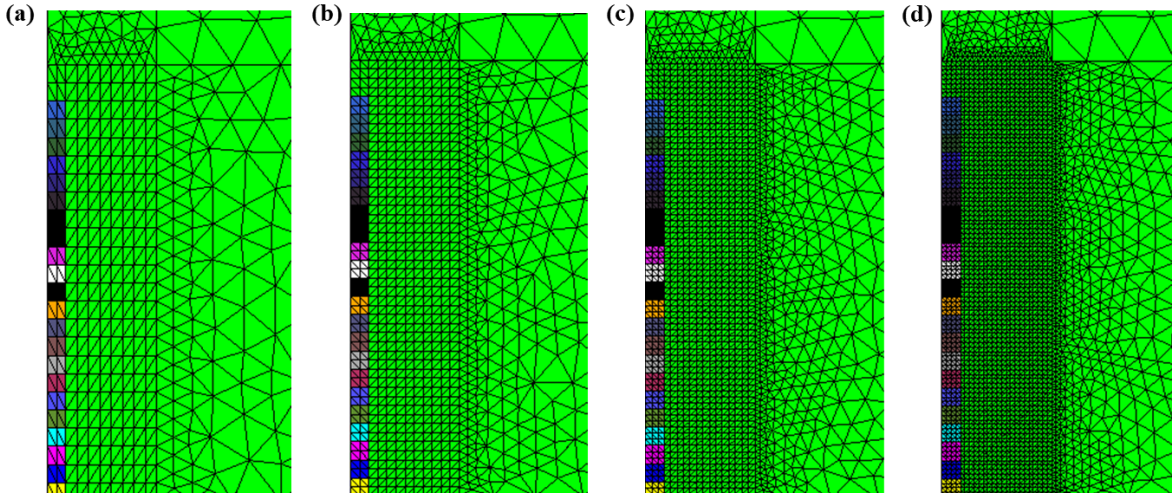

Figure 2.11. Four different mesh qualities used in the numerical analysis. The meshes are composed of the following number of quadratic triangular elements: **(a)** mesh_01: 988 elements, **(b)** mesh_02: 2016 elements, **(c)** mesh_03: 3719 elements, and **(d)** mesh_04: 6342 elements.

Table 2.3. Input parameters of the ViscoElastic-ViscoPlastic Strain-Softening (VEVP-SS) model.

Input parameters of the ViscoElastic-ViscoPlastic Strain-Softening (VEVP-SS) model							
Different quality of rock masses					High	Medium	Low
GSI			Peak		60	50	40
			Residual		35	30	27
Elastic parameters		Elastic modulus		E_M (MPa)	15400	8660	4870
		Poisson's Ratio		v	0.25	0.25	0.25
Viscoelastic parameters		Deviatoric viscosity		η_c^d (MPa s)	∞	∞	∞
Viscoplastic parameters	Stress power			m	5	5	5
	Viscosity of the Perzyna model			η_{vp} ($MPa^m s$)	10^2 (*)	10^2 (*)	10^2 (*)
	θ_T for *F* and *G*			θ_T (deg)	25	25	25
	Post-failure behaviour	Hoek-Brown	Peak values	m_{HB}	1.68	1.17	0.821
				s_{HB}	0.0110	0.0039	0.0013
			Residual values	m_{HB}	0.687	0.575	0.516
				s_{HB}	0.0007	0.0004	0.0003
		Mohr-Coulomb	Peak values	c (MPa)	2.67	2.24	1.88
				φ (deg)	25.7	23.1	20.6
			Residual values	c (MPa)	1.71	1.54	1.43
				φ (deg)	19.4	18.2	17.5
			Smoothing parameter	a	0.25	0.25	0.25
		Critical softening parameters		η^*	0.0062	0.0288	0.119
	Plastic potential	Associativity parameter		α	1.0	1.0	1.0
		Dilatancy angle		ψ (deg)	4.49	2.89	1.55

(*) A sufficiently small value of η_{vp} to make the solution comparable to the purely plastic case

Finally, Figure 2.12 presents the radial deformation versus the distance to the tunnel face for the aforementioned four meshes (mesh_01, mesh_02, mesh_03 and mesh_04) and for two different values of the viscoplastic viscosity η_{vp} ($\eta_{vp} = 10^2$ MPa^{5}s and $\eta_{vp} = 10^4$ MPa^{5}s). The good agreement shown among the results obtained with different mesh qualities verifies the mesh-independency of the proposed strain-softening model in tunnel design applications.

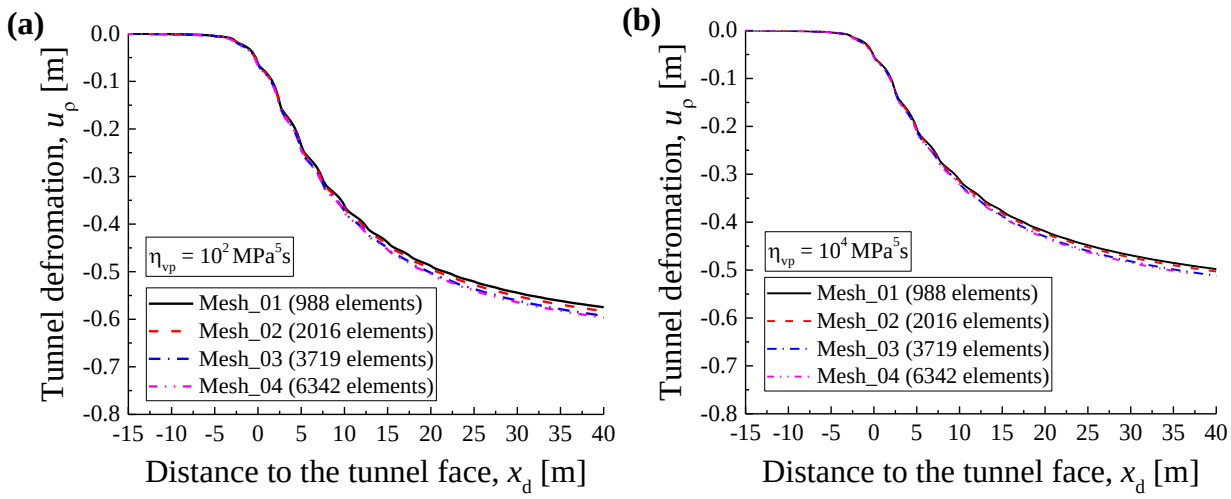

Figure 2.12. Radial deformation u_ρ versus the distance to the tunnel face x_d for **(a)** $\eta_{vp} = 10^2$ MPa^{5}s and **(b)** $\eta_{vp} = 10^4$ MPa^{5}s. Four different mesh qualities (mesh_01, mesh_02, mesh_03 and mesh_04) are adopted for each case.

2.4.3. Verification of the viscoelastic model

The VEVP-SS model can be simplified to a viscoelastic model, as shown in Figure 2.5. To verify the viscoelastic model, an example of a circular tunnel excavated in a viscoelastic rock mass is carried out in CODE_BRIGHT. The numerical results are compared with the analytical solutions of Wang et al. (2014a and 2015), who presented analytical solutions for circular tunnels with a time-dependent boundary. The expressions for tunnels excavated in Maxwell viscoelastic geomaterials under isotropic initial stresses are shown in Eq. (2.48), where G_M and η_c^d are the

deviatoric stiffness (shear modulus) and the deviatoric viscosity of the Maxwell viscoelastic model, respectively. *R* represents the time-dependent radius of the tunnel section; *t* represents time; p_0 represents the initial stress; u_ρ represents the incremental radial displacements that occurred during the excavation along the radial axis; and ρ represents the radial location in polar coordinates (ρ, θ), where ρ = 0 represents the location of the tunnel centre.

$$u_\rho(t) = -\frac{p_0}{2\rho}\int_0^t \left[\frac{1}{G_{\mathrm{M}}}\delta(t-\tau) + \frac{1}{\eta_{\mathrm{c}}^{\mathrm{d}}}\right] R^2(\tau)\, d\tau \tag{2.48}$$

The numerical model developed using CODE_BRIGHT is consistent with the hypothesis made in the analytical model, and both of them are calculated under plane-strain conditions with small deformation. Only a quarter of the tunnel structure is analysed in the numerical model (Figure 2.13) because of the double symmetry of the geometry and the boundary conditions on both the *x* and *y* axes. Moreover, the normal displacements along the bottom (*y* = 0) and the left (*x* = 0) boundaries are restrained. Figure 2.14 shows the mesh of the numerical model in the vicinity of the tunnel. A mesh of 764 quadratic triangular elements was adopted, with finer elements near the excavation. The initial stresses in the model are p_0 = 20 MPa.

For the rock mass, G_{M} = 2000 MPa, and $\eta_{\mathrm{c}}^{\mathrm{d}}$ = 8.64 × 10^8 MPa.s. The first section of the tunnel was instantaneously excavated at time equal to zero, *t* = 0 day. The following sections of the tunnel were excavated step by step, and the radius of the tunnel cross-section can be expressed by Eq. (2.49).

$$R(t) = \begin{cases} 2\,\mathrm{m}, & \text{for } 0 \le t < 5 \text{ days} \\ 4\,\mathrm{m}, & \text{for } 5 \text{ days} \le t < 10 \text{ days} \\ 6\,\mathrm{m}, & \text{for } 10 \text{ days} \le t < 15 \text{ days} \\ 8\,\mathrm{m}, & \text{for } t \ge 15 \text{ days} \end{cases} \tag{2.49}$$

After the completion of all excavation steps, the calculation was stopped at *t* = 30 days.

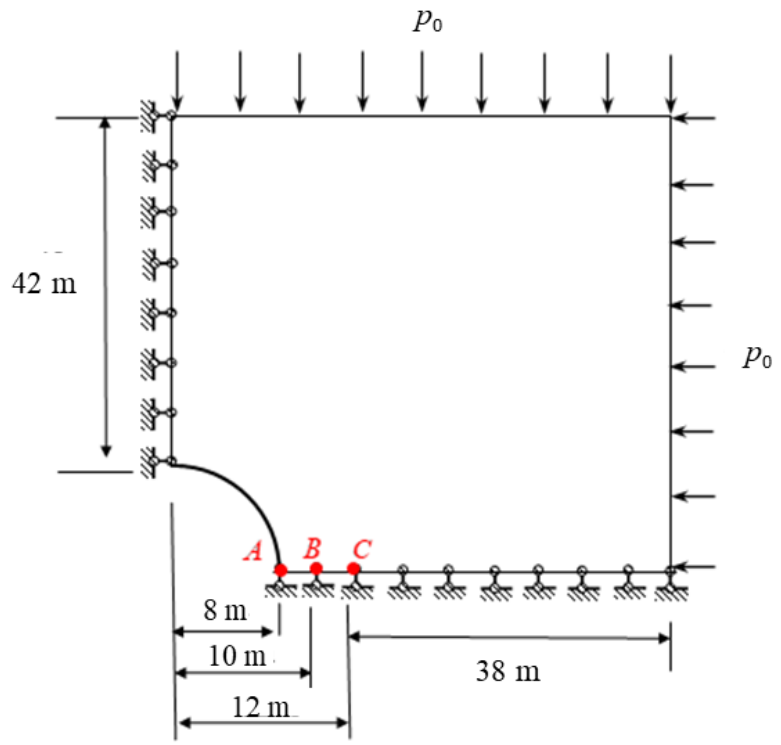

Figure 2.13. Basic features and boundary conditions for the plane-strain excavation model.

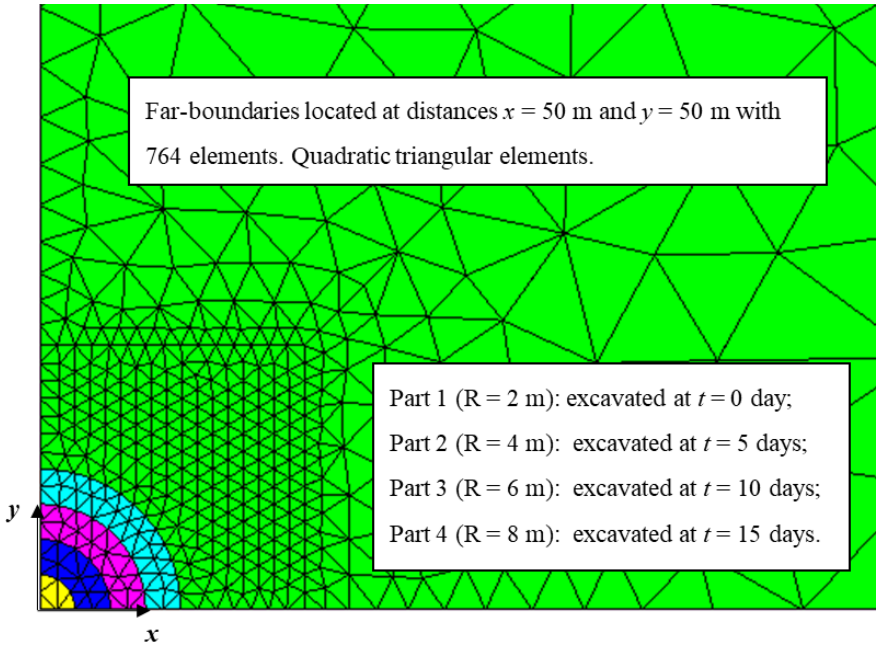

Figure 2.14. Mesh and geometry of the plane-strain excavation model.

A comparison of the time-dependent incremental radial displacements that occurred during the excavation along the radial axis (u_ρ) predicted by the analytical solutions and the numerical simulations is shown in Figure 2.15 for points A, B, and C (see Figure 2.13). A good agreement between the numerical and analytical results is observed, verifying the viscoelastic model in CODE_BRIGHT.

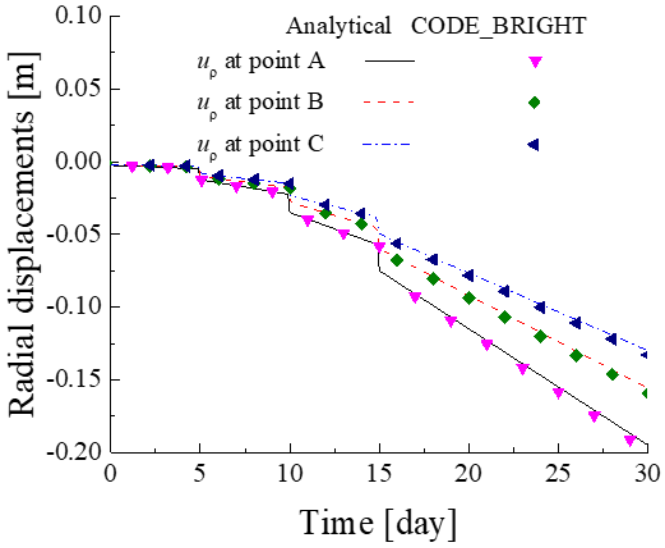

Figure 2.15. Comparison between analytical solutions (Wang et al., 2014a and 2015) and CODE_BRIGHT results for the incremental radial displacements u_ρ.

2.4.4. Verification of the strain-softening model

The VEVP-SS model can be simplified to the elastic-plastic strain-softening model by applying a sufficiently small η_{vp} and a sufficiently large η_c, as shown in Figure 2.5. To verify the theory and implementation of the strain-softening model, the results of the longitudinal deformation profile (LDP) obtained from CODE_BRIGHT are compared with the FLAC results from Alejano et al. (2012). The numerical model developed using CODE_BRIGHT is made to be consistent with the one described by Alejano et al. (2012) and both of the models are solved using the elastic-plastic strain-softening model.

In the simulation, the geometry, boundary conditions, initial field stress and excavation process are the same as those described in section 2.4.2. The rock masses were weak intact rock, with m_i = 7 and σ_{ci} = 35 MPa. Three rock masses with different geotechnical qualities (high, medium and low) were adopted in the comparison, and Table 2.3 shows the input parameters for these rock masses (Alejano et al., 2012). Considering the post-failure behaviour, simulations are performed using both perfectly plastic (PP) and strain-softening (SS) models. Moreover, both the Mohr-Coulomb and Hoek-Brown failure criteria are used. Mesh_02 (in Figure 2.11) is adopted in the following numerical analysis.

The FLAC2D and FLAC3D results from Alejano et al. (2012) were used for the comparison with the CODE_BRIGHT results. Neumann boundary conditions were adopted in the FLAC2D numerical models, and the discretised area was 70 m × 100 m (Alejano et al., 2012). Dirichlet boundary conditions were adopted in the FLAC3D numerical models, and the discretised domain was 60 m × 60 m × 60 m (Alejano et al., 2012). A more detailed description of the numerical models was provided by Alejano et al. (2012). In the comparison, the radial displacements u_ρ were normalized by the maximum radial displacements $u_\rho^{\max}$, and the distance to the tunnel face x_d were normalized by the radius of the tunnel R.

Figures 2.16 and 2.17 show good agreement of the longitudinal deformation profile (LDP) obeying the Mohr-Coulomb perfectly plastic (MC-PP), Mohr-Coulomb strain-softening (MC-SS), Hoek-Brown perfectly plastic (HB-PP), and Hoek-Brown strain-softening (HB-SS) models between CODE_BRIGHT, FLAC2D and FLAC3D, verifying the implementation of the strain-softening model. The slight differences in Figure 2.17 between the CODE_BRIGHT, FLAC2D and FLAC3D results when using the HB failure criterion may be caused by the different smoothing methods of the Hoek-Brown failure criterion (as shown in section 2.3) and the use of different types of boundary conditions (Dirichlet versus Neumann).

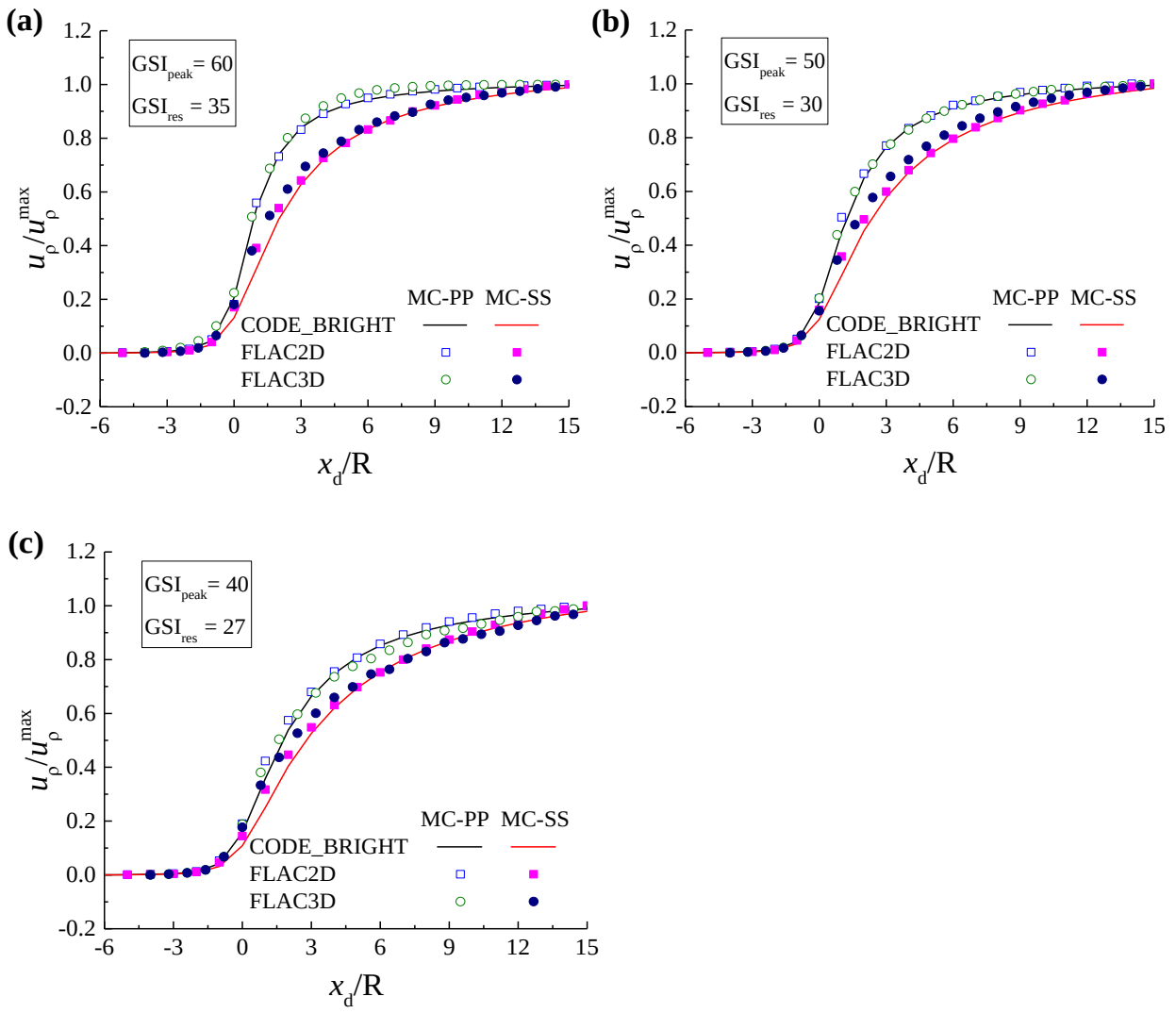

Figure 2.16. Comparison between FLAC results (Alejano et al., 2012) and CODE_BRIGHT results for the normalized longitudinal deformation profile for three different rock mass qualities, **(a)** high-quality rock mass (GSI_{peak} = 60, GSI_{res} = 35), **(b)** medium-quality rock mass (GSI_{peak} = 50, GSI_{res} = 30), and **(c)** low-quality rock mass (GSI_{peak} = 40, GSI_{res} = 27), considering the Mohr-Coulomb perfectly plastic (MC-PP) and the Mohr-Coulomb strain-softening (MC-SS) behaviour models.

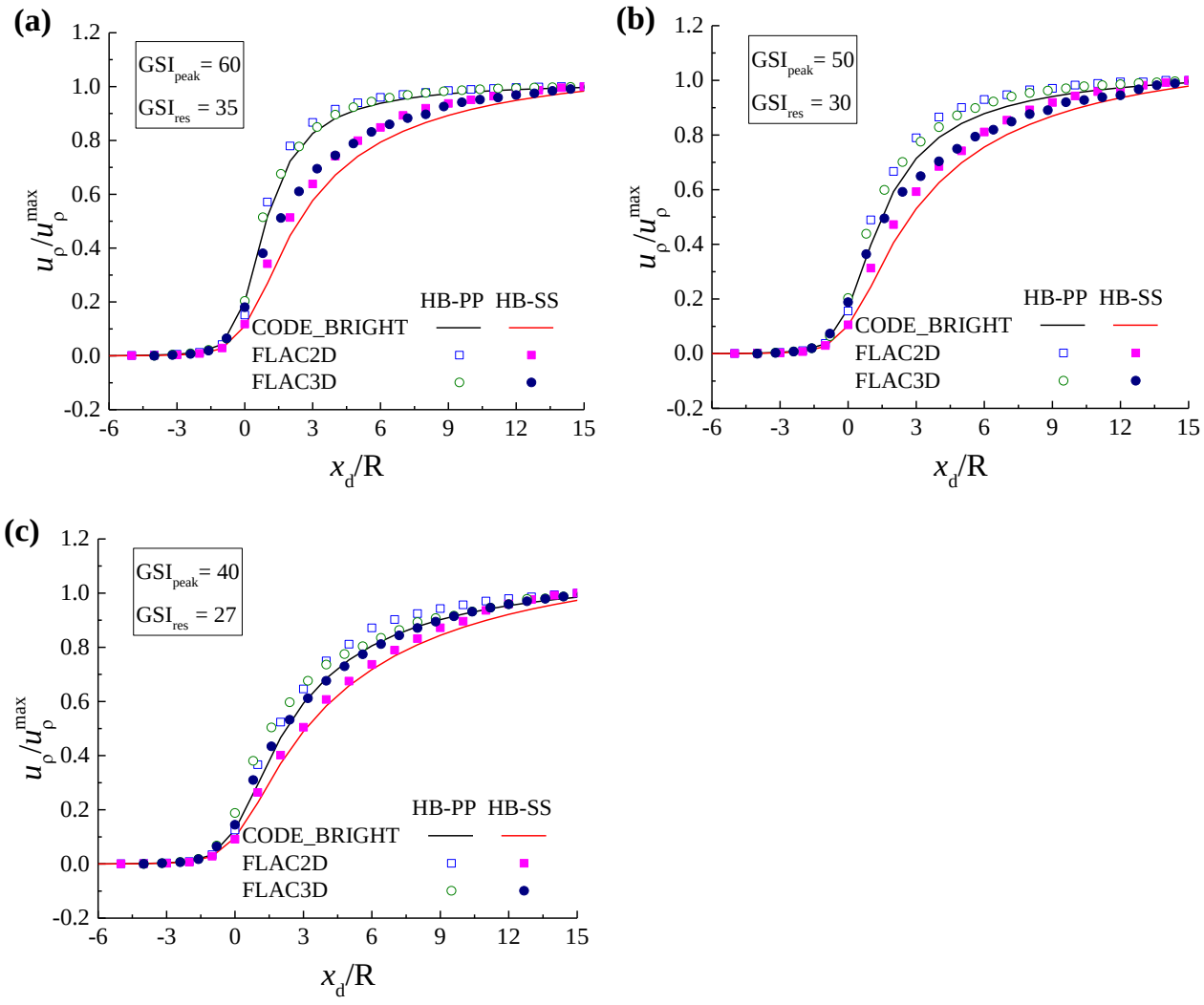

Figure 2.17. Comparison between FLAC results (Alejano et al., 2012) and CODE_BRIGHT results for the normalized longitudinal deformation profile for three different rock mass qualities: **(a)** high-quality rock mass (GSI_{peak} = 60, GSI_{res} = 35), **(b)** medium-quality rock mass (GSI_{peak} = 50, GSI_{res} = 30), and **(c)** low-quality rock mass (GSI_{peak} = 40, GSI_{res} = 27), considering the Hoek-Brown perfectly plastic (HB-PP) and the Hoek-Brown strain-softening (HB-SS) behaviour models.

2.5. The application of the VEVP-SS model in the design of tunnels

The creep-induced failure behaviour of rock may be relevant for many engineering cases, such as for some tunnels that do not fail during the process of tunnel excavation and support construction but ultimately fail after long-term operation (Fabre and Pellet, 2006; Sandrone and Labiouse, 2010). This phenomenon may be caused by the coupling between the creep behaviour and the strain-softening behaviour of rock masses, which can now be simulated by the proposed ViscoElastic-ViscoPlastic Strain-Softening (VEVP-SS) model.

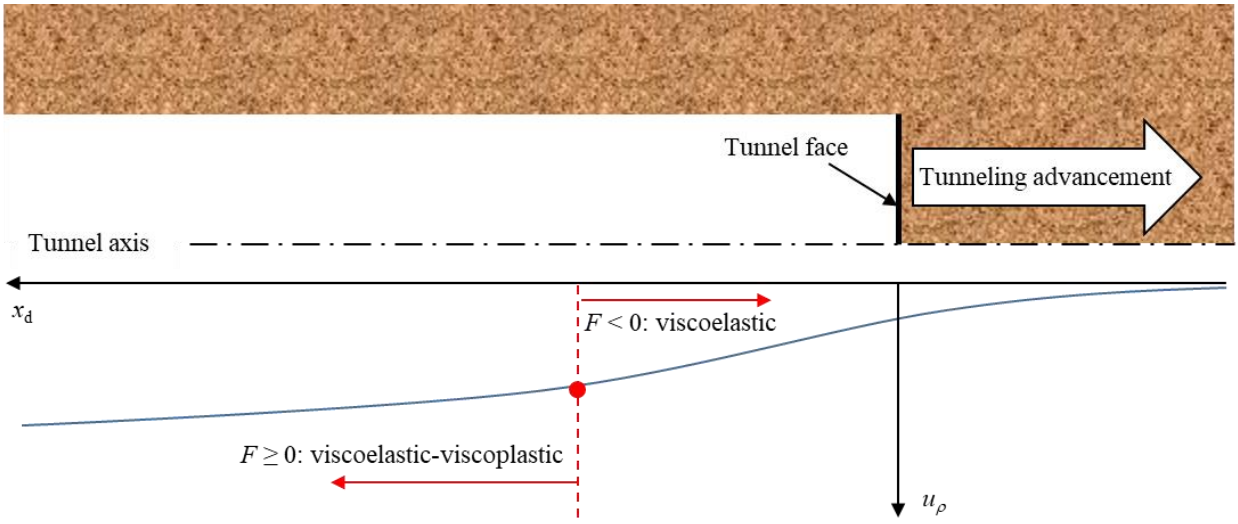

Figure 2.18. The longitudinal deformation profile (LDP) in a ViscoElastic-ViscoPlastic Strain-Softening (VEVP-SS) rock mass.

As shown in Figure 2.18, if the VEVP-SS model is adopted to simulate the rock mass behaviour, the rock mass can be divided into two different zones: (1) viscoelastic zone and (2) viscoelastic-viscoplastic zone. In this section, an example is carried out to analyse the tunnelling excavation problems of deeply buried tunnels. The influence on the resulting longitudinal deformation profiles (LDPs) of several modelling features, such as the rock mass geotechnical quality (GSI), the post-failure behaviour model chosen, the viscosity introduced in the model, or the tunnel excavation rate, will be illustrated. Moreover, the examples show the potential applicability of the proposed VEVP-SS model.

The excavated tunnel is 5 m in diameter and buried approximately 750 m deep. The initial in situ stress is assumed to be p_0 = 18.75 MPa. The numerical model geometry, boundary conditions, and excavation process (see Figure 2.10) are the same as those described in section 2.4.2. In the following numerical simulations, Mesh_02 with 2016 quadratic triangular elements is adopted, as shown in Figure 2.11(b). Three different (high, medium and low quality) rock masses are considered, and the parameters of the rock masses, including (1) the elastic parameters, (2) the stress power, (3) the post-failure behaviour and (4) the potential, are shown in Table 2.3. To simplify the analysis, the radial displacements u_ρ are normalized by the corresponding maximum displacements of the elastic model $u_{\rho,\text{elastic}}^{\max}$, and the distance to the tunnel face x_d is normalized by the radius of the tunnel R_1. For the sake of comparison, two special cases that do not consider the time-dependent behaviour of the rock mass are presented in all of the following parametric analyses: (1) elastic behaviour and (2) elastic-plastic behaviour (EP).

2.5.1. Influence of the selection of rock mass behaviour models

The longitudinal deformation profiles (LDPs) of four different post-failure behaviour models are investigated: (1) the Mohr-Coulomb perfectly plastic (MC-PP), (2) the Mohr-Coulomb strain-softening (MC-SS), (3) the Hoek-Brown perfectly plastic (HB-PP), and (4) the Hoek-Brown strain-softening (HB-SS) models. In the example, the viscosities of the viscous and viscoplastic models are $\eta_\text{c}^\text{d} = 10^{10}$ MPa.s and $\eta_{vp} = 10^4$ MPa^{5}s, respectively. The excavation rate is 2.5 m/day.

Without considering the time-dependent behaviour of rock masses, *i.e.,* for the elastic and elastic-plastic (EP) models, Figure 2.19 shows the normalized longitudinal deformation profile along with the normalized distance to the tunnel face. For time-independent materials, the displacements first increase and then reaches a stable value when the distance to the tunnel face is large enough.

The LDP obeying the Hoek-Brown failure criterion is, from an engineering point of view, similar to the LDP obeying the Mohr-Coulomb failure criterion. Furthermore, it should be noted that the difference between the LDP calculated for perfectly plastic (PP) rock masses and for

strain-softening (SS) rock masses increases as the GSI increases (Alejano et al., 2012). For high-quality rock masses, the LDP obtained is significantly different if we consider perfectly plastic or strain-softening behaviour, while this difference can be negligible for lower-quality rock masses, as expected since PP behaviour accurately represents the behaviour of low-quality rock masses of GSI < 40 (Alejano et al., 2009).

For viscoelastic-viscoplastic (VEVP) models, the displacements are caused not only by elastic and strain-softening processes but also by the creep behaviour of the rock mass; thus, the displacements keep increasing throughout the simulation, even at high x_d/R ratios. This can be a reasonable assumption for some cases: rock salt (Tomanovic, 2006), rock masses under squeezing conditions (Sterpi and Gioda, 2009), tunnels excavated in weak or altered rock masses (Sainoki et al., 2017) or very deep excavations (Sterpi and Gioda, 2009).

Figures 2.20 and 2.21 present the longitudinal deformation profiles determined by using the elastic, elastic-plastic (EP) and viscoelastic-viscoplastic (VEVP) models, obeying the Mohr-Coulomb failure criterion and the Hoek-Brown failure criterion, respectively. The displacement results of the VEVP model are larger than the corresponding EP results, due to the additional contribution of the viscous (creep) behaviour.

At a great depth, stress redistributions due to tunnel excavation may lead to so-called squeezing conditions, both in low- and high-quality rock masses (Debernardi and Barla, 2009). In this context, large deformations may develop due to secondary and tertiary creep, while the primary creep-induced deformation may be considered negligible (Sainoki et al., 2017). Thus, the proposed ViscoElastic-ViscoPlastic Strain-Softening (VEVP-SS) model may be useful to reproduce the actual behaviour of rock masses under these conditions.

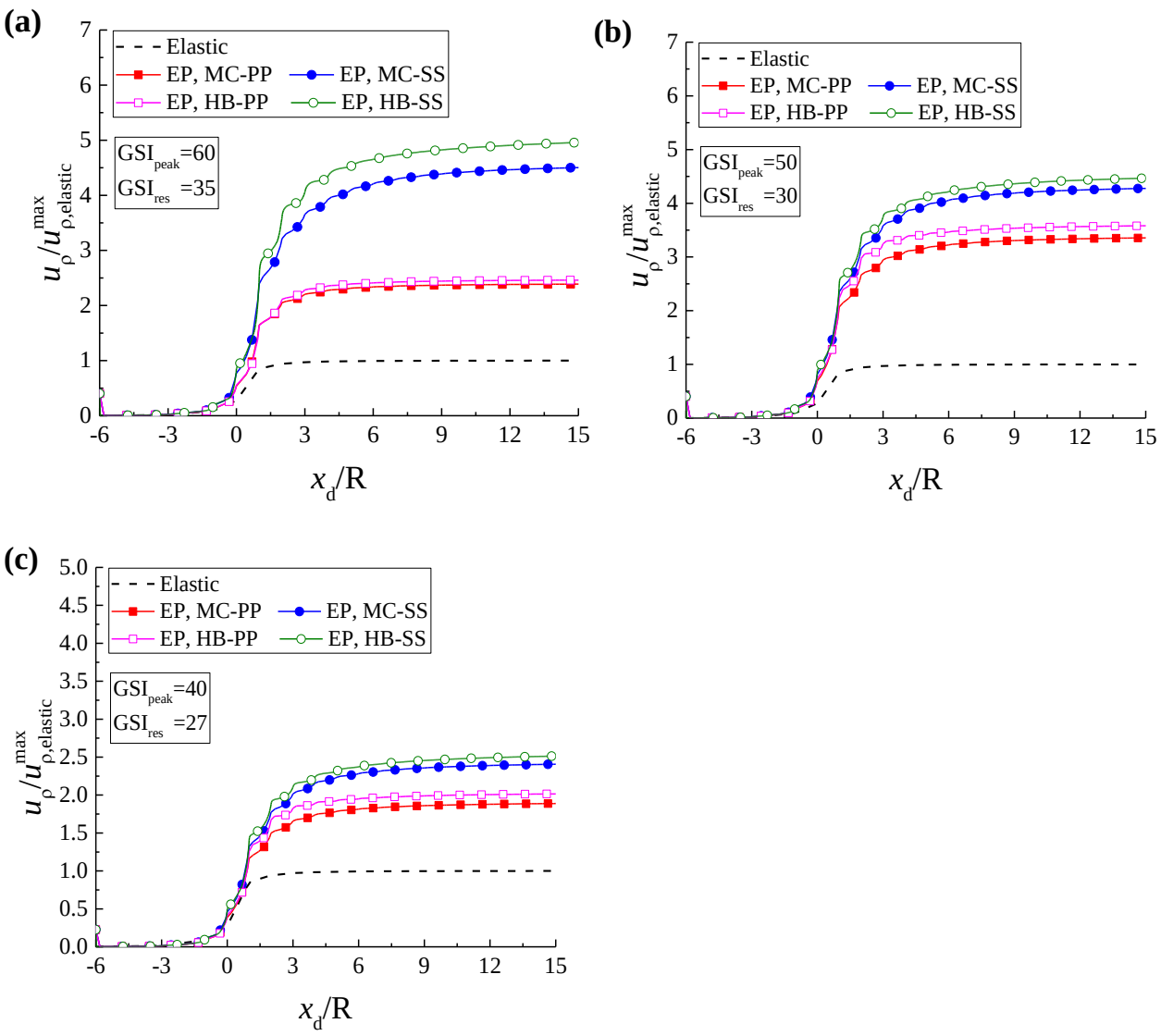

Figure 2.19. Normalized longitudinal deformation profiles along with the normalized distance to the tunnel face by using elastic and elastic-plastic (EP) mechanical models; the Mohr-Coulomb (Hoek-Brown) perfectly plastic, *i.e.*, MC-PP (HB-PP), post-failure behaviour model; and the Mohr-Coulomb (Hoek-Brown) strain-softening, *i.e.*, MC-SS (HB-SS), post-failure behaviour model. Three different rock qualities are considered: **(a)** GSI_{peak}=60, GSI_{res}=35, **(b)** GSI_{peak}=50, GSI_{res}=30, and **(c)** GSI_{peak}=40, GSI_{res}=27.

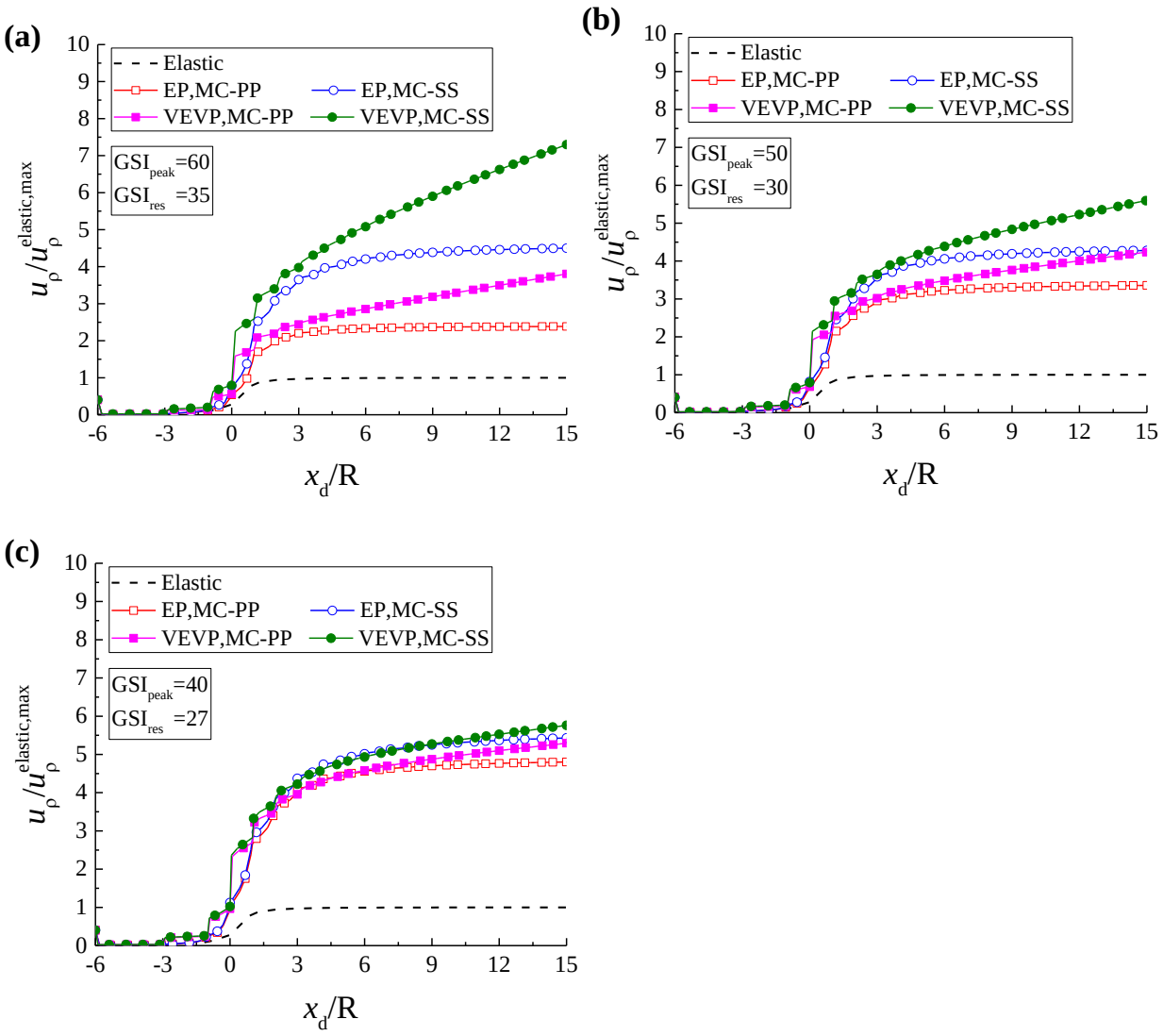

Figure 2.20. Normalized longitudinal deformation profiles along with the normalized distance to the tunnel face by using the elastic, elastic-plastic (EP), and viscoelastic-viscoplastic (VEVP) mechanical models; the Mohr-Coulomb perfectly plastic (MC-PP) post-failure behaviour model; and the Mohr-Coulomb strain-softening (MC-SS) post-failure behaviour model. Three different rock qualities are considered: **(a)** GSI_{peak}=60, GSI_{res}=35, **(b)** GSI_{peak}=50, GSI_{res}=30, **(c)** GSI_{peak}=40, and GSI_{res}=27.

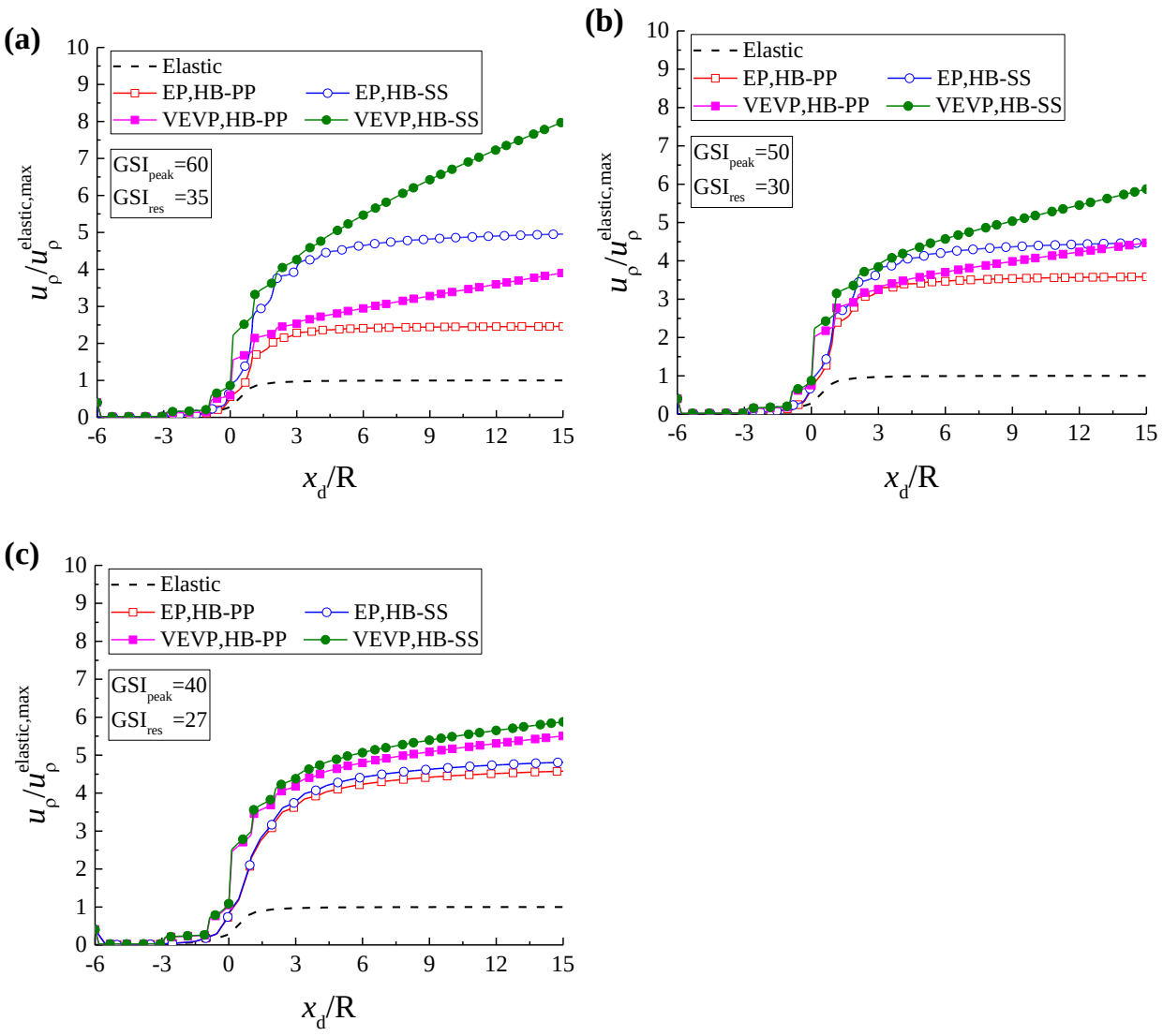

Figure 2.21. Normalized longitudinal deformation profiles along with the normalized distance to the tunnel face by using the elastic, elastic-plastic (EP), and viscoelastic-viscoplastic (VEVP) mechanical models; the Hoek-Brown perfectly plastic (HB-PP) post-failure behaviour model; and the Hoek-Brown strain-softening (HB-SS) post-failure behaviour model. Three different rock qualities are considered: **(a)** GSI_{peak}=60, GSI_{res}=35, **(b)** GSI_{peak}=50, GSI_{res}=30, **(c)** GSI_{peak}=40, and GSI_{res}=27.

2.5.2. Influence of the excavation rates

To analyse the influence of the excavation rates on the resulting longitudinal deformation profiles (LDPs), three different excavation rates were considered: V = 0.83 m/day, V = 1.25 m/day and V = 2.5 m/day. The elastic, elastic-plastic (EP), and viscoelastic-viscoplastic (VEVP) models were considered. Both Mohr-Coulomb perfectly plastic (MC-PP) and Mohr-Coulomb strain-softening (MC-SS) post-failure behaviour models were adopted in this example. In the VEVP model, the viscosities of the viscous and viscoplastic models were $\eta_c^d = 10^{10}$ MPa.s and $\eta_{vp} = 10^4$ MPa^{5}s, respectively.

Figures 2.22 and 2.23 show the LDP obeying the MC-PP and the MC-SS post-failure behaviour models, respectively. For the elastic and elastic-plastic rock masses, the LDP is identical for different excavation rates, *i.e.,* the elastic and elastic-plastic LDPs are only related to the distance to the tunnel face x_d. However, for the viscoelastic-viscoplastic rock masses, the shapes of the LDPs are very different for different excavation rates, and the displacements do not achieve a steady state in this case due to the contribution of the creep deformation. Lower excavation rates may lead to larger displacements because there is more time for creep deformation to develop. The difference between the longitudinal deformation profiles (LDPs) calculated for elastic-plastic rock masses and for viscoelastic-viscoplastic rock masses increases with the GSI.

2.5.3. Influence of the viscosity

As shown in Figure 2.5, the viscoelastic-viscoplastic model can be simplified to an elastic-viscoplastic model by assigning a sufficiently large value to η_c, while it can be simplified to a viscoelastic-plastic model when η_{vp} is close to zero. To analyse the effect of viscosity, including the viscosity of the viscous (creep) model η_c^d and the viscosity of the viscoplastic model η_{vp}, on the resulting longitudinal deformation profile (LDP), an example is presented herein. In this numerical simulation, three different excavation rates are considered: V = 0.83 m/day, V = 1.25 m/day and V = 2.5 m/day. In this sub-section, the proposed VEVP-SS model is adopted, and the

post-failure behaviour is described by the Mohr-Coulomb strain-softening (MC-SS) model. It should be noted that some of the values of η_c^d and η_{vp} in this sub-section maybe not realistic but are useful to perform a sensitivity analysis of viscosity.

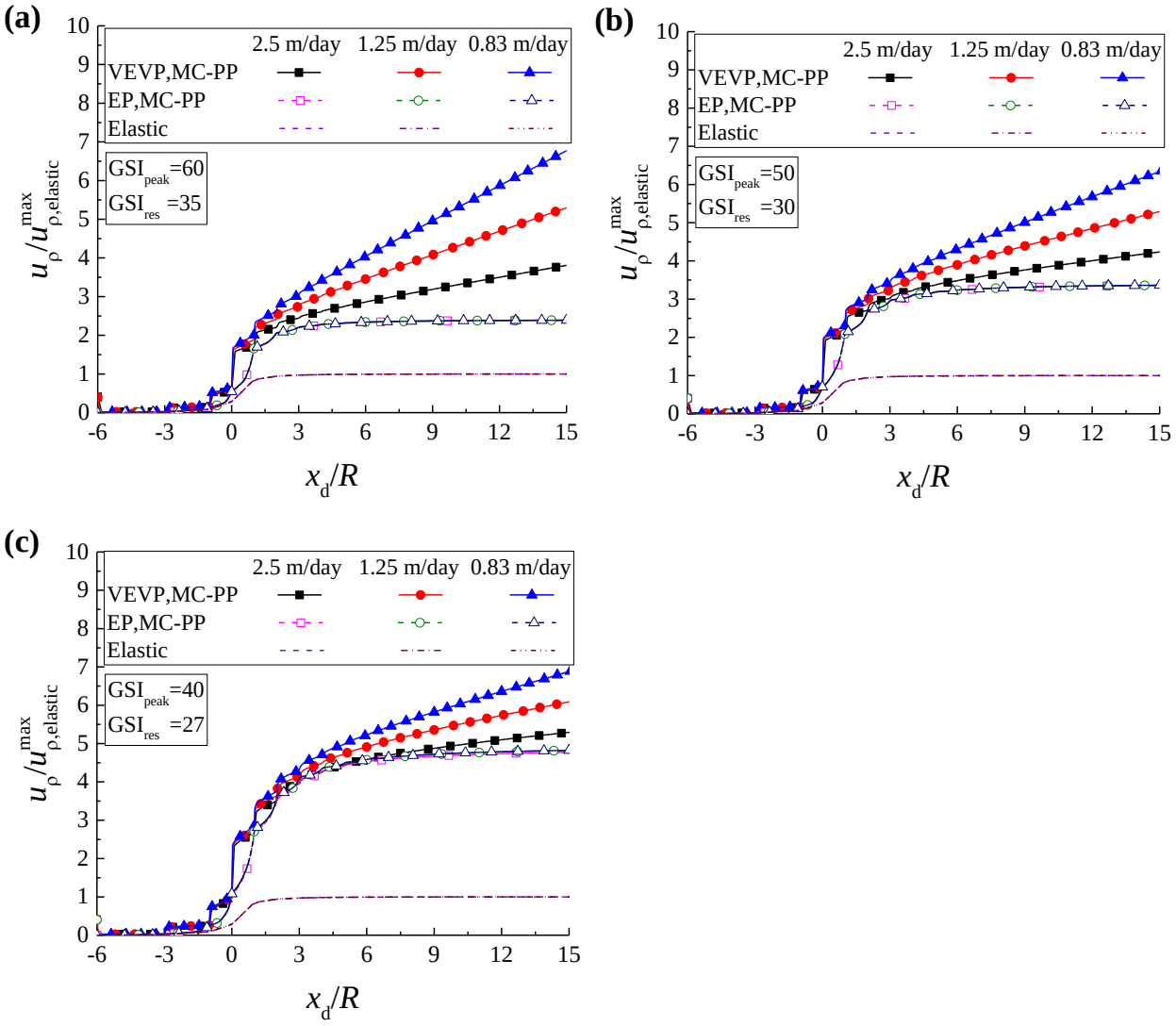

Figure 2.22. Normalized longitudinal deformation profiles along the normalized distance to the tunnel face for three different excavation rates (0.83 m/day, 1.25 m/day and 2.5 m/day) and for three different rock qualities: **(a)** GSI_{peak}=60, GSI_{res}=35, **(b)** GSI_{peak}=50, GSI_{res}=30, and **(c)** GSI_{peak}=40, GSI_{res}=27. Three different rock mass behaviour models are adopted: elastic model; the elastic-plastic and Mohr-Coulomb perfectly plastic (EP, MC-PP) model; and the viscoelastic-viscoplastic and Mohr-Coulomb perfectly plastic (VEVP, MC-PP) model.

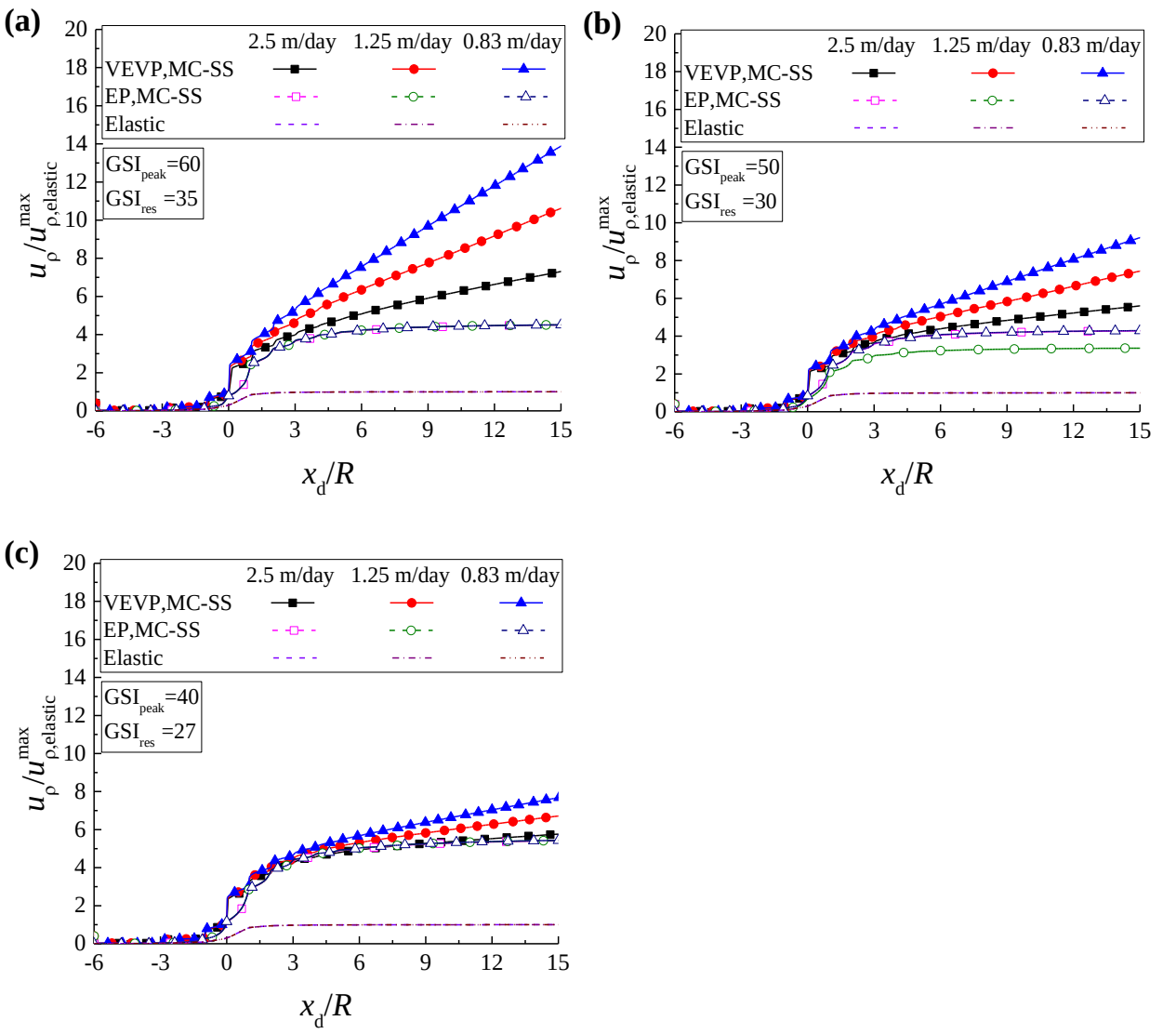

Figure 2.23. Normalized longitudinal deformation profiles along the normalized distance to the tunnel face for three different excavation rates (0.83 m/day, 1.25 m/day and 2.5 m/day) and for three different rock qualities: **(a)** GSI_{peak}=60, GSI_{res}=35, **(b)** GSI_{peak}=50, GSI_{res}=30, **(c)** GSI_{peak}=40, GSI_{res}=27. Three different rock mass behaviour models are adopted: the elastic model; the elastic-plastic and Mohr-Coulomb strain-softening (EP, MC-SS) model; and the viscoelastic-viscoplastic and Mohr-Coulomb strain-softening (VEVP, MC-SS) model.

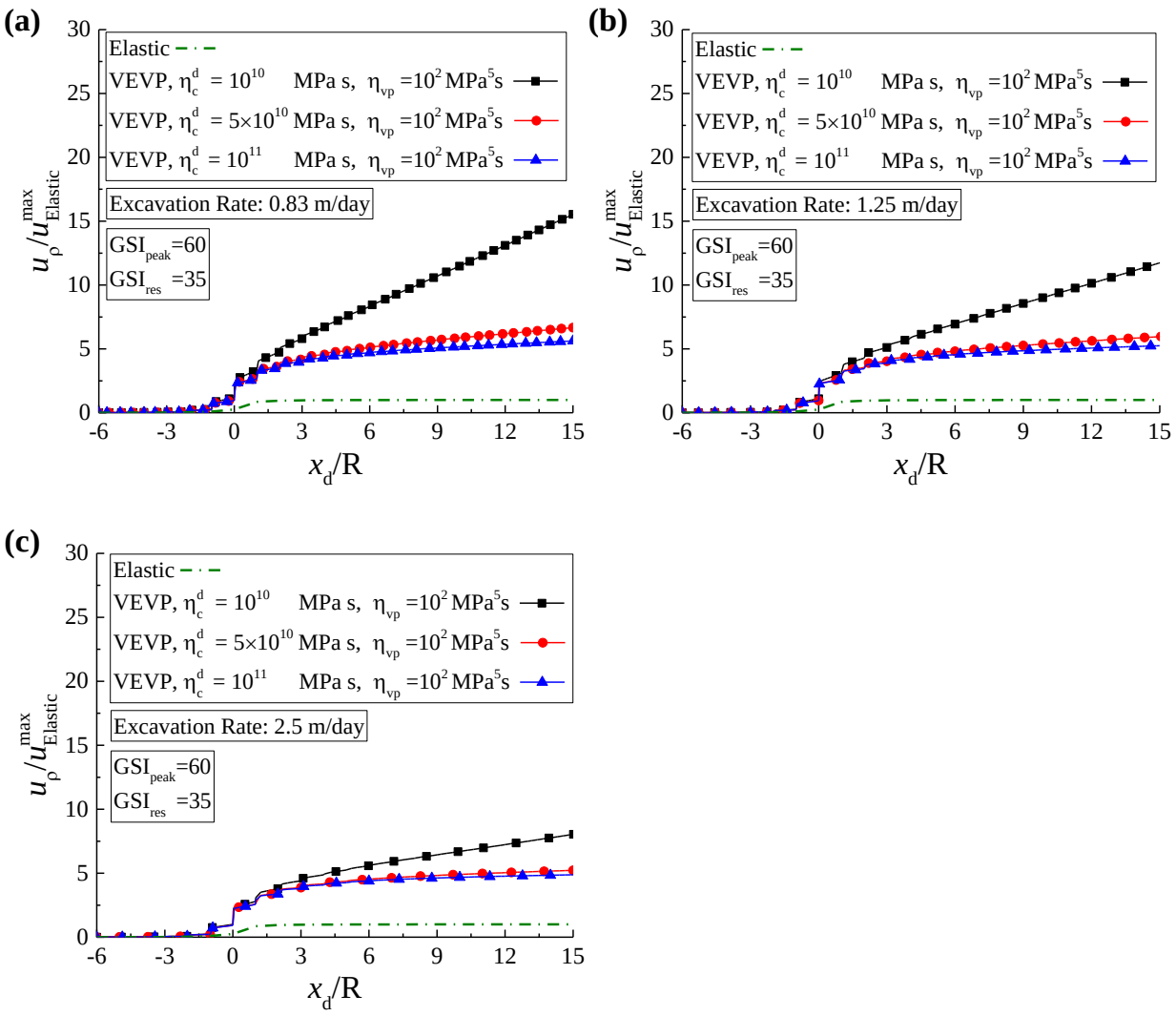

Figure 2.24. Normalized longitudinal deformation profiles along with the normalized distance to the tunnel face by using the Mohr-Coulomb strain-softening (MC-SS) rock mass behaviour model for three different viscosities of the viscous model η_c^d, for three different excavation rates: **(a)** 0.83 m/day, **(b)** 1.25 m/day, and **(c)** 2.5 m/day.

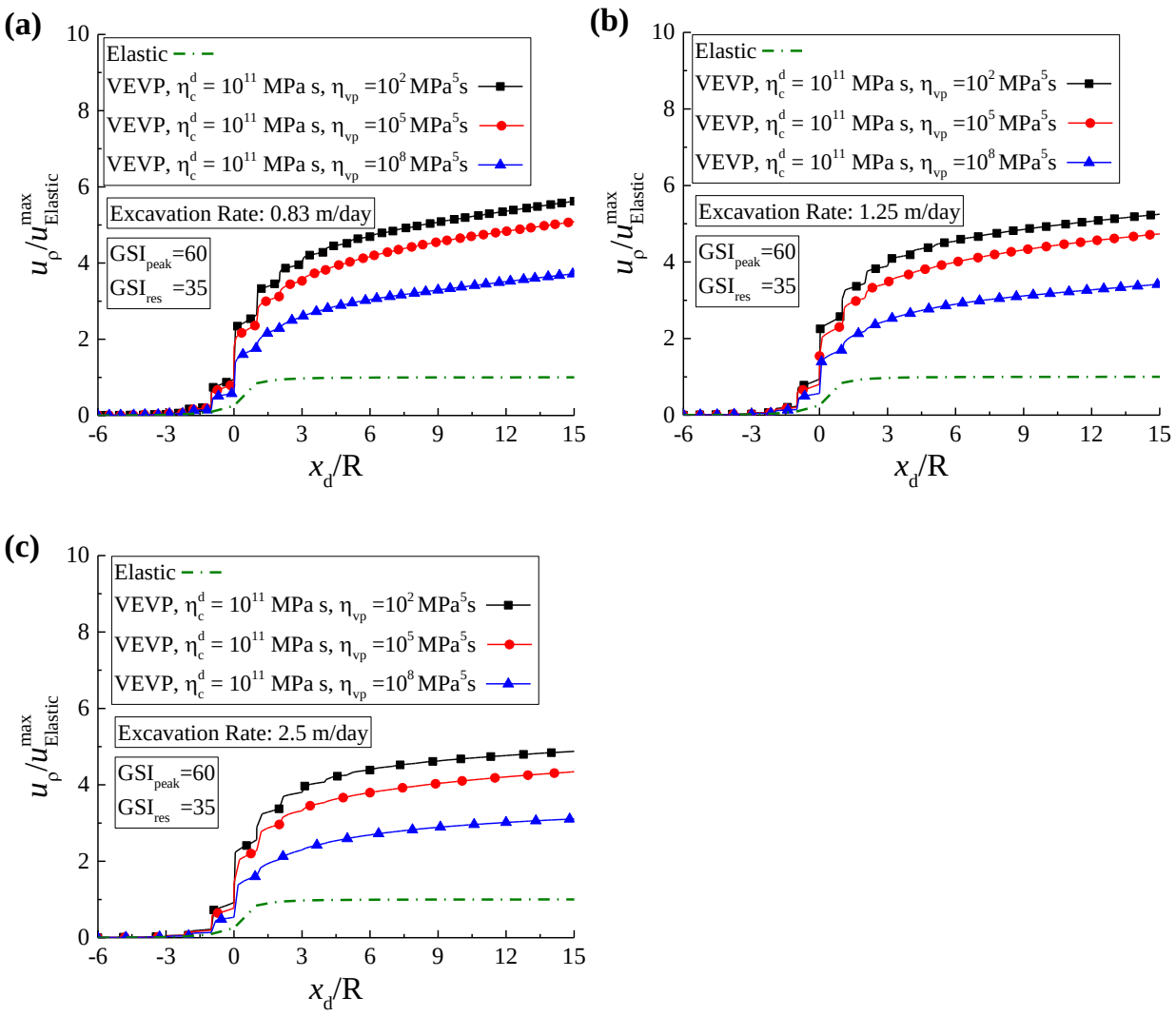

Figure 2.25. Normalized longitudinal deformation profiles along the normalized distance to the tunnel face by using the Mohr-Coulomb strain-softening (MC-SS) rock mass behaviour model for three different viscosities of the viscoplastic model η_{vp} and for three different excavation rates: **(a)** 0.83 m/day, **(b)** 1.25 m/day, and **(c)** 2.5 m/day.

Figure 2.24 shows a sensitivity analysis of the viscosity on the viscous (creep) part, η_c^d. Three different viscosities are adopted for the viscous model, η_c^d = 10^{10} MP s, 5×10^{10} MP s, and 10^{11} MP s, and the viscosity of the viscoplastic model is adopted as η_{vp} = 10^2 MPa^{5}s. The larger the value of η_c^d is, the smaller the displacement. Figure 2.25 shows a sensitivity analysis of the

viscosity on the viscoplastic part, η_{vp}. Three different viscosities are considered for the viscoplastic model, $\eta_{vp} = 10^2$ MPa^{5}s, 10^5 MPa^{5}s, and 10^8 MPa^{5}s, and the viscosity of the viscous model is adopted as $\eta_c^d = 10^{11}$ MPa s in this case. The smaller the value of η_{vp} is, the larger the displacement. In both Figures 2.24 and 2.25, lower excavation rates produce larger displacements, caused by larger creep displacements during the excavation process.

2.6. Conclusions

This study provides a general coupled ViscoElastic-ViscoPlastic Strain-Softening (VEVP-SS) model. This VEVP-SS model has been implemented into the finite element method software CODE_BRIGHT. In the VEVP-SS model, creep behaviour and strain-softening models are coupled, which can be used to simulate the creep-induced failure and subsequent damage of rock masses.

The viscous dashpot and the Perzyna models are adopted to simulate the creep and viscoplastic behaviours of rock masses, respectively. Both the Mohr-Coulomb and Hoek-Brown failure criteria, as well as the strain-softening post-failure behaviour of rock masses, are considered. By using a smoothing approximation method, the yield surfaces and the potential are smoothed in the numerical implementation. The numerical model is verified by a comparison between the CODE_BRIGHT results and other analytical or numerical results.

Finally, an example is carried out to predict the longitudinal deformation profile (LDP) used in the convergence-confinement method (CCM). The effects of the rock mass behaviour model selection, the geotechnical quality of the rock mass, the viscosity, and the excavation rates on the longitudinal deformation profile (LDP) are investigated. The proposed approach can be used in the preliminary design of tunnels excavated in time-dependent strain-softening rock masses. Some conclusions can be obtained from the parametric analysis:

1. Elastic-plastic, elastic-viscoplastic, viscoelastic, viscoelastic-plastic models can be considered special cases of the VEVP-SS model, so they can be modelled using the proposed model. In

addition, strain-softening post-failure behaviour or a simpler perfectly plastic or purely brittle post-failure behaviour can be selected for any case.

2. The LDP varies according to the selected rock mass behaviour model. For instance, the displacement results of the VEVP model are larger than the corresponding elastic-plastic results due to the contribution of the viscous (creep) behaviour. In addition, the results of the elastic and elastic-plastic models are identical for different excavation rates, while the excavation rate becomes relevant when taking into account time-dependent behaviour.

3. When using the VEVP model, the obtained LDP obeying the Hoek-Brown failure criterion is, from an engineering point of view, similar to the obtained LDP obeying the Mohr-Coulomb failure criterion. Moreover, the difference between the LDPs calculated for perfectly plastic rock masses and for strain-softening rock masses grows as the GSI increases. Furthermore, when choosing the viscoelastic-viscoplastic rock mass behaviour model, the model is more sensitive to the excavation rate in comparison to the sensitivity of the elastic-plastic behaviour model.

4. The proposed VEVP model is very sensitive to the input values of viscosity. For the VEVP model, the greater the values of η_c or η_{vp} are, the smaller the displacements.

Even if the proposed model can reproduce many different rock mass behaviours, there are still some limitations in the proposed VEVP-SS model. For instance, the strain rate is constant under a constant stress in the Maxwell viscoelastic model, which may reproduce only a limited number of practical cases. In chapter 4, the Burgers viscoelastic model has been coupled with the Perzyna model to consider the influence of primary creep and thus improve the applicability of the numerical approach to real engineering.

Chapter 3. Hydro-mechanical modelling and analysis of multi-stage tunnel excavations using a smoothed excavation method

Based on the published manuscript of the following article:

Fei Song, Alfonso Rodriguez-Dono, Sebastia Olivella. Hydro-mechanical modelling and analysis of multi-stage tunnel excavations using a smoothed excavation method. Computers and geotechnics [J]. Computers and Geotechnics, 2021, 135: 104150.

https://doi.org/10.1016/j.compgeo.2021.104150

Abstract

The main objective of this study is to provide a general numerical approach for the hydro-mechanical (HM) modelling of tunnels excavated in saturated rock masses exhibiting plastic behaviour, considering a multi-stage excavation process. First, a smoothed excavation (SE) method has been proposed and implemented in the software CODE_BRIGHT, based on the finite element method. In this method, the stresses in the excavation elements are reduced smoothly. As verification, the principle of uniqueness has been tested for multi-stage excavation. Then, numerical studies have been carried out to verify the advantages of the proposed excavation method in the numerical calculation, showing that the proposed method improves computational efficiency and mitigates convergence issues. Hence, this method can solve the usual numerical difficulties related to excavation problems and, therefore, it allows a more in-depth analysis of the HM behaviour of rock masses during tunnel excavation.

Moreover, the results obtained in CODE_BRIGHT using the proposed method are compared with existing solutions for longitudinal deformation profiles (LDP), including elastic-plastic solutions for mechanical problems and elastic solutions for HM problems. Furthermore, this study presents the HM modelling of tunnels excavated in saturated rock masses, analysing the sensitivity of the LDP to the HM conditions and to the rock mass quality. Finally, based on a large amount of data obtained from numerical simulations, empirical solutions for the LDP of tunnels excavated in saturated rock masses –in a steady-state HM framework– have been

obtained by fitting non-linear curves for the normalised radial displacements that occur ahead and behind the tunnel face. Hence, the current research attempts to provide a convenient set of alternatives for the preliminary design of tunnels excavated in saturated rock masses.

3.1. Introduction

Tunnelling in several stages is a common process in many geotechnical engineering constructions. There may be some seepage flowing towards the tunnel during excavations below the water table, affecting its behaviour (Lee and Nam, 2004; Nam and Bobet, 2007; Nogueira et al., 2011). Consequently, the effect of seepage flow cannot be ignored in tunnel design and the response of the rock mass must be analysed in a hydro-mechanical (HM) framework (Figure 3.1) (Nam and Bobet, 2007; Yuan and Harrison, 2005). Therefore, a proper simulation of the HM behaviour and the entire multi-stage excavation process is crucial to obtain a reliable tool in order to achieve an optimal tunnel design.

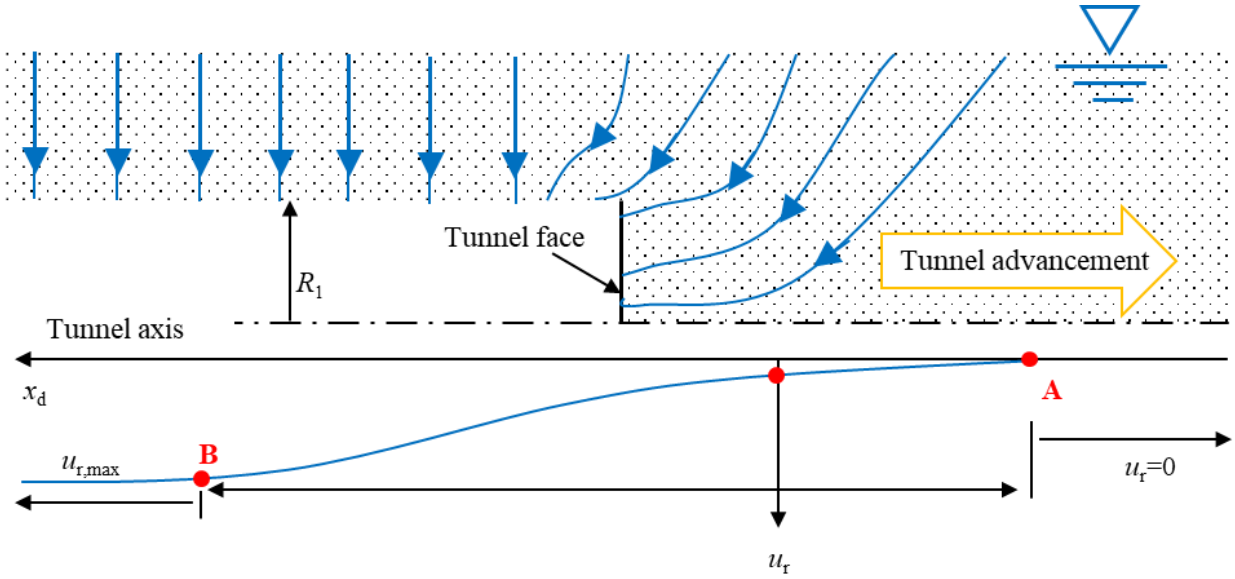

Figure 3.1. Conceptual model of a tunnel excavated in a hydro-mechanical framework. Seepage flowing towards the tunnel –above–; and its longitudinal deformation profile –below.

Tunnel design can be approached by analytical, numerical or empirical methods (Alejano et al., 2010; Alejano et al., 2009; Alejano et al., 2012; Alonso et al., 2003; Barla et al., 2011; Carranza-Torres and Fairhurst, 1999; Carranza-Torres and Fairhurst, 2000; Carranza-Torres et al., 2013; Carranza-Torres and Zhao, 2009; Cui et al., 2019; de la Fuente et al., 2019; Mánica, 2018; Paraskevopoulou, 2016; Paraskevopoulou and Diederichs, 2018; Song et al., 2018a and 2018b; Sterpi and Gioda, 2009; Vlachopoulos and Diederichs, 2009; Wang et al., 2020a; Wang et al., 2017a; Wang et al., 2019; Wang et al., 2013; Wang and Nie, 2010; Wang et al., 2020b; Wang et al., 2014; Wang et al., 2015; Wang et al., 2018d; Wang et al., 2017b; Yi et al., 2019; Zhang et al., 2012a; Zhang et al., 2019b; Zhao et al., 2015; Zhou et al., 2019; Zhu et al., 2013; Zou et al., 2017a). One such analytical method is the convergence-confinement method (CCM), developed in the 1930s (Fenner, 1938), and later refined by other researchers (Alejano et al., 2010; Alejano et al., 2012; Carranza-Torres and Fairhurst, 2000; Corbetta et al., 1991; Cui et al., 2015; Paraskevopoulou, 2016; Vlachopoulos and Diederichs, 2009). It provides an efficient way to determine support forces by considering ground-support interactions (Alejano et al., 2010; Alejano et al., 2012). The CCM consists of three graphs (Figure 3.2). The ground reaction curve (GRC) establishes the relationship between the decreasing inner pressure and the increasing radial displacements of the tunnel wall. The support characteristic curve (SCC) represents the stress-strain relationship of the support system. Furthermore, the longitudinal deformation profile (LDP) relates the radial displacements of an unsupported tunnel section with its longitudinal distance to the tunnel face (Alejano et al., 2010; Alejano et al., 2012; Cui et al., 2015).

Hence, using the CCM, an appropriate tunnel design can be achieved, taking into account the distance from the tunnel face where the support will be installed and the corresponding forces to which the support will be subjected until it reaches equilibrium with the ground (point E; Figure 3.2) (Song and Rodriguez-Dono, 2021).

This study focuses on the analysis of longitudinal deformation profiles (LDP) in a hydro-mechanical (HM) framework with plastic response. Regarding the LDP, many researchers derived solutions based on field measurements or numerical simulations. Corbeta et al. (1991) and Panet (1995) presented elastic solutions for the relationship between radial displacements and the distance to the tunnel face. Using numerical simulations, Unlu and Gercek (2003) proposed empirical equations for predicting normalised radial displacements ahead and behind the tunnel

face, considering the effect of Poisson's ratio. Additionally, based on field-measured data from a tunnel in the Mingtam Power cavern project (Chern et al., 1998), an empirical best-fit relationship was presented for the LDP of elastic-plastic problems.

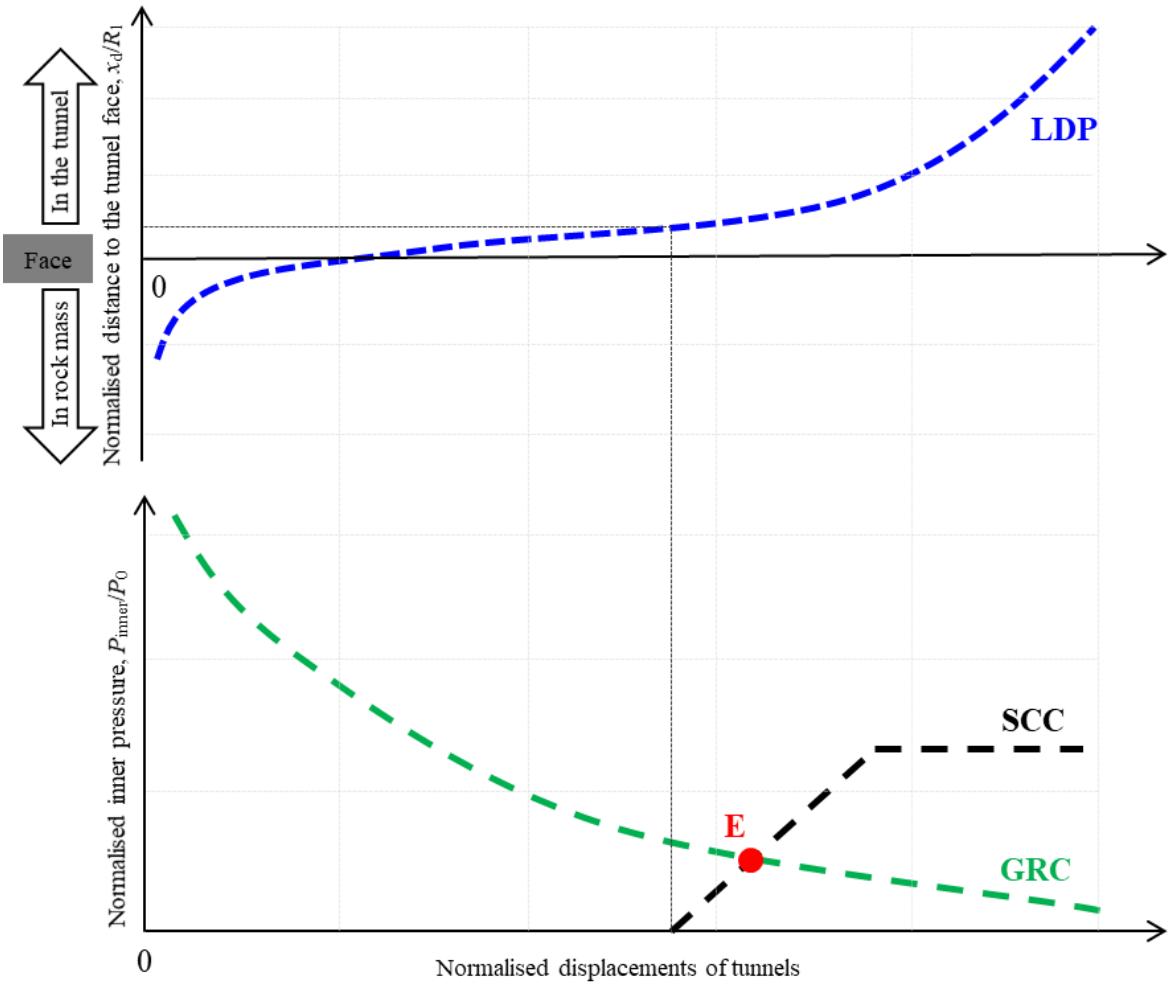

Figure 3.2. Main elements of the convergence-confinement method (CCM). Typical graphs obtained for the longitudinal deformation profile (LDP) –above–, and for the ground reaction curve (GRC) and the support characteristic curve (SCC) –below. Based on the work of Alejano et al. (2009, 2010, 2012), Song et al. (2020) and Song and Rodriguez-Dono (2021).

After that, Vlachopoulos and Diederichs (2009) presented a robust formulation for the calculation of the LDP that takes into account the significant influence of the ultimate plastic

radius. Considering post-failure behaviour, Alejano et al. (2012) extended that approach from Vlachopoulos and Diederichs (2009) to the case of strain-softening rock masses, representing a wider range of rock masses, which can be used to obtain a more realistic approach to calculate the LDP. Moreover, based on the Burgers-creep viscous (CVISC) model introduced by Itasca (2007 and 2008), Paraskevopoulou (2016) and Paraskevopoulou and Diederichs (2018) presented LDP simulations for viscoelastic rock masses. Recently, Song et al. (2020) presented analysis and modelling of LDP for tunnels excavated in strain-softening time-dependent rock masses.

Nevertheless, the studies mentioned above on LDP were conducted without considering HM conditions, yet the majority of deep tunnels are excavated below the groundwater table (Nam and Bobet, 2007). However, as explained above, when tunnelling in saturated ground, we must consider not only the purely mechanical response, but the HM response of the geomaterials in the estimation of displacements.

Furthermore, Nam and Bobet (2007) and Prassetyo and Gutierrez (2018b) proposed empirical best-fit solutions for the normalised radial displacements ahead and behind the tunnel face for saturated ground with water flow, and rock masses were assumed as linear elastic materials in their research. However, the response of rock masses will differ depending on the selected model, as have been demonstrated by other researchers considering the post-failure behaviour of rock masses in purely mechanical models (Alejano et al., 2010; Alejano et al., 2012; Alonso et al., 2003). To deepen in this analysis, HM modelling of tunnels for plastic geomaterials has been carried out in the current research.

Both the finite element method (FEM) and the multi-stage excavation method (Gharti et al., 2012; Zienkiewicz and Taylor, 2000; Zienkiewicz and Taylor, 2005) have been adopted in this research to obtain the LDP. During the multi-stage excavation process, certain parts of the model –corresponding to the tunnel excavation– are removed systematically. Hence, new boundaries are being created, which need the appropriate boundary conditions so that the stresses and pressures are properly redistributed (Gharti et al., 2012; ISHIHARA, 1970).

The typical conception in the numerical simulation of excavations has been to cancel the contributions of the nodes belonging to the excavated elements and to leave the boundary surface of the tunnel free of stress (Borja et al., 1989; Brown and Booker, 1985; Christian and Wong,

1973; Comodromos et al., 1993; Desai and Sargand, 1984; Ghaboussi and Pecknold, 1984; Gharti et al., 2012; ISHIHARA, 1970; Olivella et al., 2020). However, most of these simulations are limited to a purely mechanical (M) phase or to hydro-mechanical (HM) models for linear elastic materials. Unlike these cases, HM modelling of excavations for non-linear geomaterials may encounter numerical difficulties, being time-consuming or even suffering from non-convergence issues, due to the complex coupling between HM boundary conditions and non-linear constitutive models. To solve these numerical problems, we propose a smoothed excavation (SE) method to improve the efficiency and the convergence of the numerical calculation.

In summary, research on LDP has mainly focused on purely mechanical problems or HM problems but with linear elastic materials. To overcome these limitations, in this study we present a numerical approach for the hydro-mechanical (HM) modelling of tunnels excavated in saturated rock masses showing plastic behaviour, using the proposed SE method. The hydro-mechanical theory used in this study is described below, and the proposed SE method has been implemented in the finite element method software CODE_BRIGHT (Olivella et al., 2020). Numerical studies have been carried out to perform computational efficiency and convergence analyses for the proposed SE method. Then, the CODE_BRIGHT results have been compared to previous LDP elastic-plastic solutions for mechanical problems (Alejano et al., 2012; Vlachopoulos and Diederichs, 2009) and to previous LDP elastic solutions for HM problems (Nam and Bobet, 2007; Prassetyo and Gutierrez, 2018b), for verification purposes. Subsequently, numerical analyses related to the LDP of tunnels excavated in saturated rock masses showing plastic behaviour have been carried out. Finally, based on the large amount of data obtained by these numerical simulations, we have proposed an empirical best-fit solution of the LDP for saturated rock masses with plastic response under steady-state conditions, with the aim of facilitating its use in engineering practice.

3.2. Theoretical background

3.2.1. The coupled hydro-mechanical theoretical formulation

In this study, rock masses are composed of rocks and water –*i.e.* saturated conditions–. In CODE_BRIGHT, saturated rock masses are treated, from a modelling perspective, as an equivalent porous medium. In saturated rock masses, subjected to hydraulic and mechanical conditions, hydro-mechanical (HM) coupled phenomena takes place.

Hydraulic and mechanical aspects are considered, including the coupling between them in both directions, as shown in Figure 3.3. Changes in hydraulic conditions influence the stress/strain field through changes in pore water pressure. Moreover, changes in the volume of the pores (or joints) caused by volumetric strains influence pore (or joint) pressure distributions.

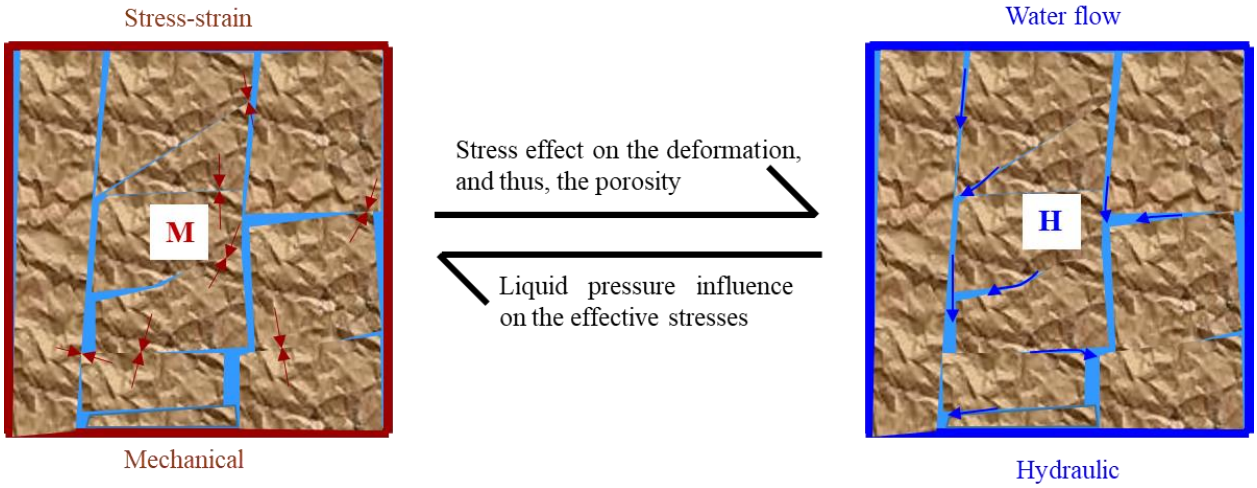

Figure 3.3. Conceptual model of the hydro-mechanical coupled behaviour.

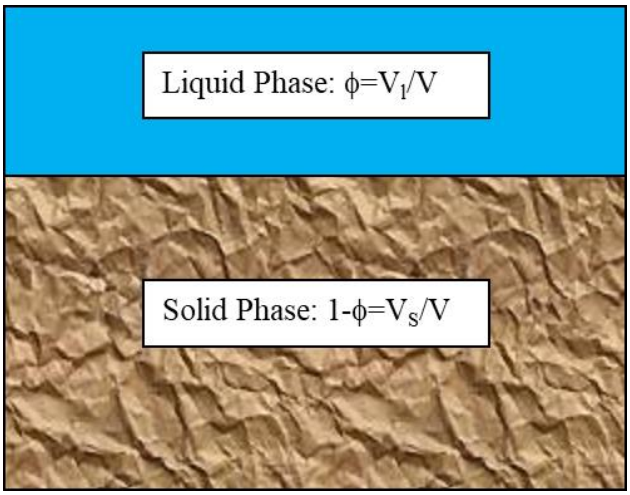

Figure 3.4. The two existing phases in saturated rock masses.

As illustrated in Figure 3.4, the problem is formulated in a multi-phases approach. In this problem, the water component is always in the liquid phase (l), and the rock component is always in the solid phase (s). Conceptually, this means that the water is considered to be in the joints of the rock mass, which are the main vector of water seepage. The theoretical HM formulation used herein is a special case of the general formulation presented in Olivella et al. (1996). However, for the sake of clarity, a brief description is presented here. More detailed finite-element formulation utilised in CODE_BRIGHT, including the weak forms of the governing equations and explicit definitions of the resulting matrices and vectors, can be found in Olivella et al. (1996).

3.2.1.1. Mass balance of the solid phase

Total solid phase per unit volume of rock mass can be expressed as in Eq. (3.1).

$$\rho_s \left(1-\phi\right) \tag{3.1}$$

where ρ_s represents the solid phase density –the density of the rock– and ϕ represents the porosity (understood as the volume of the joints per unit volume of rock mass), as shown in Figure 3.4. V_S

and V_l represent the volumes of the solid and liquid phases, respectively; $V = V_S + V_l$. The mass balance of the solid phase present in the rock mass can be expressed as in Eq. (3.2).

$$\frac{\partial}{\partial t}\left(\rho_s\left(1-\phi\right)\right)+\nabla\cdot\left(\mathbf{j}_s\right)=0 \tag{3.2}$$

$$\mathbf{j}_s=\rho_s\left(1-\phi\right)\frac{d\mathbf{u}}{dt} \tag{3.3}$$

where $\mathbf{j}_s$ represents the mass flux of the rock with respect to a fixed reference system, as shown in Eq. (3.3); and $\frac{d\mathbf{u}}{dt}$ is the velocity field due to the deformation of the rock. From Eqs. (3.2) and (3.3), an expression can be obtained for the variation of the porosity –Eq. (3.4)– using the material derivative with respect to the solid –Eq. (3.5)–. Eq. (3.4) expresses the variation of porosity caused by volumetric deformation and solid density variation (Olivella, 1995).

$$\frac{D_s\phi}{Dt}=\frac{\left(1-\phi\right)}{\rho_s}\frac{D_s\rho_s}{Dt}+\left(1-\phi\right)\nabla\cdot\frac{d\mathbf{u}}{dt} \tag{3.4}$$

$$\frac{D_s\left(\bullet\right)}{Dt}=\frac{\partial\left(\bullet\right)}{\partial t}+\frac{d\mathbf{u}}{dt}\cdot\nabla\left(\bullet\right) \tag{3.5}$$

3.2.1.2. Mass balance of the liquid phase

The total mass balance of water is expressed as shown in Eq. (3.6).

$$\frac{\partial\left(\rho_l\phi\right)}{\partial t}+\nabla\cdot\left(\rho_l\mathbf{q}_l+\rho_l\phi\frac{d\mathbf{u}}{dt}\right)=f^w \tag{3.6}$$

where $\mathbf{q}_l$, ρ_l represent liquid flux and liquid density, respectively; f^w is a source/sink term. Porosity multiplied by density gives the mass of water per unit volume of rock mass.

After using the material derivative, Eq. (3.6) can lead to Eq. (3.7).

$$\phi \frac{D_s\left(\rho_l\right)}{Dt} + \rho_l \frac{D_s \phi}{Dt} + \rho_l \phi \nabla \cdot \frac{d\mathbf{u}}{dt} + \nabla \cdot \left(\rho_l \mathbf{q}_l\right) = f^w \tag{3.7}$$

Then, combining Eq. (3.7) with Eq. (3.4), we can obtain Eq. (3.8).

$$\phi \frac{D_s\left(\rho_l\right)}{Dt} + \rho_l \frac{\left(1-\phi\right)}{\rho_s} \frac{D_s \rho_s}{Dt} + \rho_l \nabla \cdot \frac{d\mathbf{u}}{dt} + \nabla \cdot \left(\rho_l \mathbf{q}_l\right) = f^w \tag{3.8}$$

3.2.1.3. Stress equilibrium equation

The balance of momentum for the rock mass can be expressed as in Eq. (3.9).

$$\nabla \cdot \boldsymbol{\sigma} + \mathbf{b} = 0 \tag{3.9}$$

where $\boldsymbol{\sigma}$ represents the stress tensor and **b** represents the vector of body forces.

3.2.2. Constitutive theory

3.2.2.1. Phase and species fluxes

The liquid advective flux related to phase motion is governed by the generalised Darcy's law, as shown in Eq. (3.10).

$$\mathbf{q}_l = -\frac{\mathbf{k} k_{rl}}{\mu_l}\left(\nabla p_l - \rho_l \mathbf{g}\right) \tag{3.10}$$

where p_l represents the liquid pressure; **k** represents the intrinsic permeability tensor, which depends on the joint structure of the rock mass; k_{rl} and μ_l represent the relative permeability and dynamic viscosity of the fluid, respectively; **g** represents the vector of gravity forces.

3.2.2.2. Mechanical constitutive equations

Experimental results have shown that an elastic-viscoplastic approach is more adequate than an elastic-plastic approach to reproduce the yielding behaviour of geomaterials (Olivella, 1995). In addition, the viscoplastic approach facilitates the control of the size of the localised area and, therefore, avoids dependence on the mesh used (Alonso et al., 2005; Mánica, 2018; Song et al., 2020). The elastic-viscoplastic model has been frequently applied to reproduce the time-dependent effect of geomaterials (Mánica, 2018). The total strain rate $\frac{d\boldsymbol{\varepsilon}}{dt}$ can be decomposed into instantaneous elastic $\frac{d\boldsymbol{\varepsilon}_{\text{elastic}}}{dt}$ and time-dependent viscoplastic $\frac{d\boldsymbol{\varepsilon}_{\text{perzyna}}}{dt}$ components, as shown in Eq. (3.11).

$$\frac{d\boldsymbol{\varepsilon}}{dt} = \frac{d\boldsymbol{\varepsilon}_{\text{elastic}}}{dt} + \frac{d\boldsymbol{\varepsilon}_{\text{perzyna}}}{dt} \tag{3.11}$$

where $\frac{d\boldsymbol{\varepsilon}_{\text{elastic}}}{dt} = \mathbf{C}^{\text{e}} \frac{d\boldsymbol{\sigma}}{dt}$ is the generalised Hooke's law, and $\mathbf{C}^{\text{e}}$ represents the inverse of the elastic tangent stiffness matrix. Perzyna's model consists of a viscous Newtonian dashpot in parallel with a plastic slider, as shown in Figure 3.5. The strain rate of the Perzyna's model can be expressed as in Eq. (3.12).

$$\frac{d\boldsymbol{\varepsilon}_{\text{perzyna}}}{dt} = \frac{1}{\eta_{\text{perzyna}}} \langle \Phi(F) \rangle \frac{\partial G}{\partial \boldsymbol{\sigma}} \tag{3.12}$$

where F and G represent failure criterion and plastic potential, respectively; and the symbol $<\Phi(F)>$ can be expressed as in Eq. (3.13). The function $\Phi(F)$ can be chosen from experimental results (Perzyna, 1966). For the sake of simplicity, $\Phi(F) = F^{\text{m}}$ ($\text{m} \geq 1$) is adopted in the present research, where m represents the stress power.

$$< \Phi(F) > = \begin{cases} \Phi(F) & \text{if } \Phi(F) \geq 0 \\ 0 & \text{if } \Phi(F) < 0 \end{cases} \tag{3.13}$$

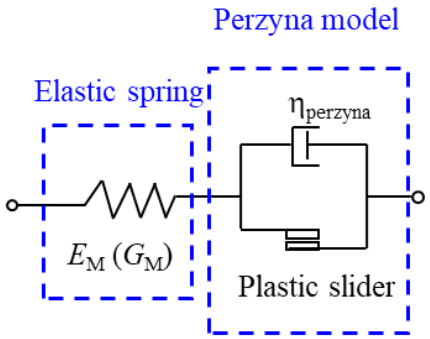

Figure 3.5. The elastic-viscoplastic model.

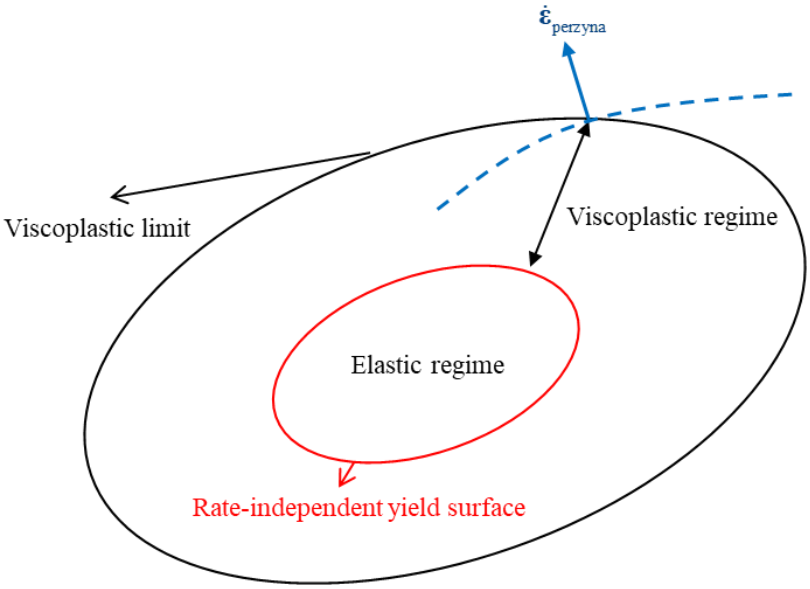

Figure 3.6. The overstress theory scheme. Based on the work of Perzyna (1966) and Manica (2018).

Moreover, the overstress theory has been considered in Perzyna's viscoplastic model (Mánica, 2018; Perzyna, 1966). Unlike the purely plastic theory, the overstress theory allows the stress points to exceed the yield surface. As shown in Figure 3.6, the yield surface establishes the limit between two different regimes in the stress space:

1. If the stress point is below the rate-independent yield surface, the geomaterial exhibits elastic behaviour;

2. If the stress point is between the rate-independent yield surface and the viscoplastic limit, the geomaterial exhibits elastic-viscoplastic properties. The viscoplastic limit is related to the viscosity of the Perzyna viscoplastic model, *i.e.* $\eta_{perzyna}$ in Eq. (3.12). As the viscosity value $\eta_{perzyna}$ approaches zero, the viscoplastic limit will be closer to the yield surface *F*. It should be noted that a viscoplastic solution as close as necessary to the 'true' purely plastic solution can always be ensured by sufficiently lowering the value of the viscosity $\eta_{perzyna}$ in the viscoplastic formulation (Alonso et al., 2005).

For the sake of numerical efficiency and convergence, a smoothed hyperbolic Mohr-Coulomb failure criterion is adopted in this study (Abbo and Sloan, 1995), as shown in Eq. (3.14).

$$F_{MC}\left(p, J_2, \theta\right) = \sqrt{J_2 K_{MC}^2 + a_{MC}^2 \sin^2\varphi} + p\sin\varphi - c\cos\varphi$$
$$a_{MC} = m_{MC} c \cot\varphi \tag{3.14}$$

where p, J_2 and θ represent the mean stress, the second invariant of the deviatoric stress tensor and the Lode angle, respectively; c and φ represent cohesion and friction angle; m_{MC} represents the hyperbolic parameter of the smoothed failure criterion, to control the hyperbolic shape; K_{MC} can be expressed as in Eq. (3.15).

$$K_{MC} = \begin{cases} A_{MC} + B_{MC}\sin 3\theta & \text{if } |\theta| > \theta_T \\ \cos\theta - \frac{1}{\sqrt{3}}\sin\varphi\sin\theta & \text{if } |\theta| \le \theta_T \end{cases} \tag{3.15}$$

where:

$$A_{MC} = \frac{1}{3}\cos\theta_T\left(3 + \tan\theta_T \tan 3\theta_T + \frac{1}{\sqrt{3}}\langle\theta\rangle\left(\tan 3\theta_T - 3\tan\theta_T\right)\sin\varphi\right)$$

$$B_{MC} = -\frac{1}{3\cos 3\theta_T}\left(\langle\theta\rangle\sin\theta_T + \frac{1}{\sqrt{3}}\sin\varphi\cos\theta_T\right)$$

$$\langle\theta\rangle = \begin{cases} +1, & \theta \ge 0 \\ -1, & \theta < 0 \end{cases}$$

where θ_T is the transition angle (usually, 25 deg). These equations have been adapted from Abbo and Sloan (1995). The reader is referred to the original source for a detailed description of the smoothed approximation to the Mohr-Coulomb failure surface.

The plastic potential G can be expressed as in Eq. (3.16).

$$G = \sqrt{J_2 K_G^2 + a_G^2 \sin^2\psi} + p\sin\psi - c\cos\psi \tag{3.16}$$

where $a_G = m_G\, c \cot\psi$; ψ represents the dilation angle; m_G represents the hyperbolic parameter of the smoothed potential surface (Song et al., 2020). The alternative form of K_G can be expressed as in Eq. (3.17).

$$K_G = \begin{cases} A_G + B_G \sin 3\theta & \text{if } |\theta| > \theta_T \\ \cos\theta - \dfrac{1}{\sqrt{3}}\sin\psi\sin\theta & \text{if } |\theta| \le \theta_T \end{cases} \tag{3.17}$$

where:

$$A_G = \frac{1}{3}\cos\theta_T\left(3 + \tan\theta_T \tan 3\theta_T + \frac{1}{\sqrt{3}}\langle\theta\rangle\left(\tan 3\theta_T - 3\tan\theta_T\right)\sin\psi\right)$$

$$B_G = -\frac{1}{3\cos 3\theta_T}\left(\langle\theta\rangle\sin\theta_T + \frac{1}{\sqrt{3}}\sin\psi\cos\theta_T\right).$$

The strain rate of the Perzyna's model can be obtained as shown in Eq. (3.18).

$$\frac{d\boldsymbol{\varepsilon}_{\text{perzyna}}}{dt} = \frac{1}{\eta_{\text{perzyna}}}\langle\Phi(F)\rangle\frac{\partial G}{\partial \boldsymbol{\sigma}} = \frac{1}{\eta_{\text{perzyna}}}\langle F^m\rangle\left(\frac{\partial G}{\partial p}\frac{\partial p}{\partial \boldsymbol{\sigma}} + \frac{\partial G}{\partial J_2}\frac{\partial J_2}{\partial \boldsymbol{\sigma}} + \frac{\partial G}{\partial \theta}\frac{\partial \theta}{\partial \boldsymbol{\sigma}}\right) \tag{3.18}$$

3.3. Numerical approach to the smoothed excavation method

A multi-stage excavation has been modelled in the finite element method (FEM) software CODE_BRIGHT (Olivella et al., 2020) to obtain longitudinal deformation profiles (LDP) of saturated rock masses that show plastic behaviour. CODE_BRIGHT has been developed by the Department of Civil and Environmental Engineering of the Technical University of Catalonia (UPC), and works in combination with the pre/post-processor GID (Coll et al., 2018), developed by the International Centre for Numerical Methods in Engineering (CIMNE).

Since the HM modelling of excavations –especially in the case of geomaterials with non-linear behaviour– usually encounters numerical difficulties, an alternative smoothed excavation (SE) method is proposed in this study to improve the efficiency of numerical calculation in excavation problems (section 3.3.1). The proposed SE method, implemented in the FEM software CODE_BRIGHT, is described in section 3.3.2. Finally, the implementation of the SE method will be verified in sections 3.3.3 and 3.3.4. Note that the same method presented in this study could be used in case of utilising other code.

The numerical approach employed in CODE_BRIGHT to solve the resulting system of partial differential equations includes a spatial and a temporal discretisation. For spatial discretisation, the finite element method is used, while for temporal discretisation the finite difference method is used. The discretisation in time is linear, and the implicit scheme uses two intermediate points, $t^{k+\varepsilon}$ and $t^{k+\theta}$ between the initial t^{k} and final t^{k+1} times. In order to solve non-linear problems, the Newton-Raphson (N-R) method has been adopted to find an iterative scheme. A more detailed description of this numerical approach can be found in the work of Olivella (1995), Olivella et al. (1996) and Olivella et al. (2020).

3.3.1. Conceptual scheme

The typical conception for numerical simulation of excavations, including the former excavation method used in CODE_BRIGHT, is to instantly remove the excavated elements from the mesh, so that the surface of the excavated tunnel is stress-free (this excavation method is named

'inactive' in this study, because excavated elements become inactive). However, when modelling the excavation of tunnels, if simply using this typical approach –deleting the elements of the excavated material–, it may result in numerical problems.

As shown in Figure 3.7, there are different possible stress unloading paths during an excavation stage (e.g. Line 1, 2 or 3). The typical excavation method used so far in CODE_BRIGHT was to remove the excavated elements from the mesh instantly, so that the surface of the excavated tunnel was stress-free (*i.e.*, line 1 in Figure 3.7). However, this sudden change in boundary conditions can lead to numerical problems that could cause not only a dramatic increase of central processing unit (CPU) time, but sometimes also non-convergences issues (probably due to divergence from the expected solution) and, as a result, the simulation stops.

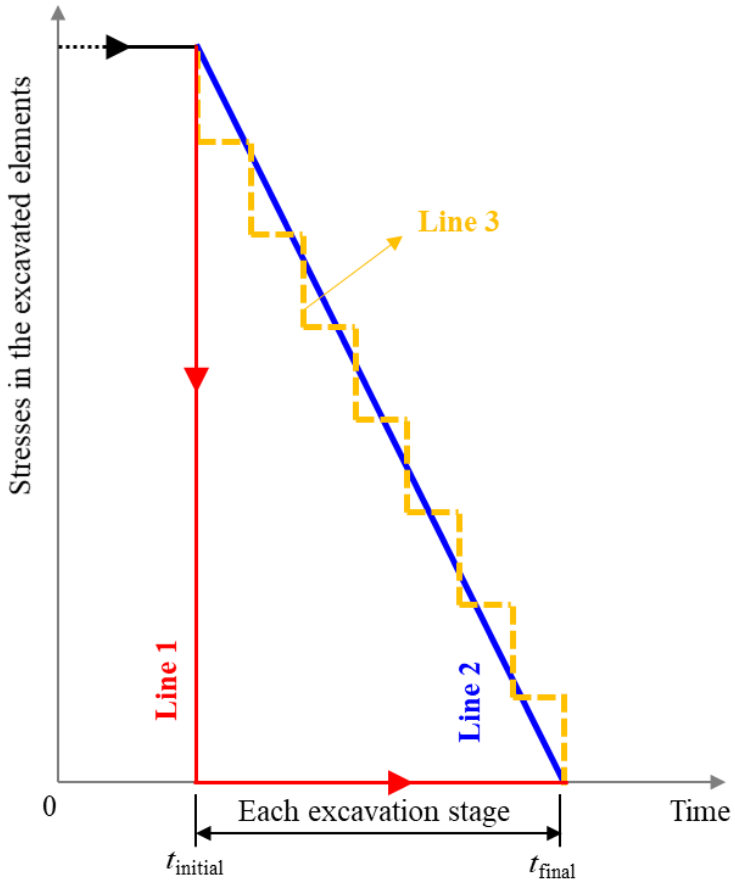

Figure 3.7. Evolution of the stresses in the elements excavated during an excavation stage.

Alternatively, using the same method, we can smooth the stress changes in the tunnel boundary by dividing each excavation stage into n phases, applying staggered boundary conditions at the successive surfaces of the excavated tunnel, as it is represented by Line 3 in Figure 3.7, which can eliminate non-convergence issues to some extent. However, to model excavations in this way, it can be a tedious process, resulting in excavations with a large number of phases, each of them with different boundary conditions to be applied. On the contrary, the SE method is a numerical approach that allows to reduce the stresses in the surfaces of the tunnel smoothly (e.g. Line 2 in Figure 3.7), so this tedious process is done automatically, hence reducing numerical difficulties.

As mentioned above, due to the sudden change in boundary conditions and the sudden removal of elements, the numerical simulation may experience numerical difficulties during excavation, especially in the initial time step of the excavation stage (time interval during which excavation is carried out on the model), as well as excessive CPU time consumption. In order to overcome these limitations, a smoothed excavation (SE) method for finite element analysis is presented here. As a first step in the proposed SE method, it is considered that the elements that are being excavated behave elastically. In addition, the stresses of the corresponding excavation elements will be reduced smoothly, according to Eq. (3.19).

$$\sigma^{t} = \sigma^{t_{initial}} \left[A - B \left(\frac{t - t_{initial}}{t_{final} - t_{initial}} \right)^{n} \right] \tag{3.19}$$

where t represents time; σ^{t} and $\sigma^{t_{initial}}$ represent the stress at time t and the stress at the initial time of the excavation stage, respectively; $t_{initial}$ and t_{final} represent the initial time and the final time of the excavation stage; A and B are user-defined parameters that take values between 0 and 1, while n is a user-defined power. The main utility of Eq. (3.19) is to smooth the process of stress unloading during excavation to mitigate numerical difficulties.

A is related to the stress at the beginning of the excavation, B is related to the stress at the end of the excavation, and n is related to the shape of the unloading function. For instance, if A = 1, then the stresses in the excavated elements are relaxed from their current stress; whereas if A < 1, then the excavated elements are relaxed from a lower stress level. On the other hand, if B = 1,

the excavated material is relaxed until it is stress-free (usual case); whereas if B < 1, then the excavated elements are relaxed to a stress level greater than zero. Finally, if n = 1, the stresses of the excavated elements are relaxed linearly; whereas if n > 1 (or n < 1), the stresses are relaxed in an accelerated (or decelerated) manner during the excavation stage. Figure 3.8 presents three examples of the stress reduction process in excavated elements, according to Eq. (3.19). After the excavation stage ends, the excavated material is completely removed from the model at the next excavation stage –if any– (using the aforementioned 'inactive' method).

In fact, to capture the correct tunnel excavation response, it is important to correctly resemble the real stress unloading path in the numerical models because a dynamic unloading condition is often created in some excavation methods (Cai, 2008). Compared with the 'inactive' method, the SE method provides an option to simulate the unloading stress path more realistic, even though it needs more research to define the most adequate unloading function.

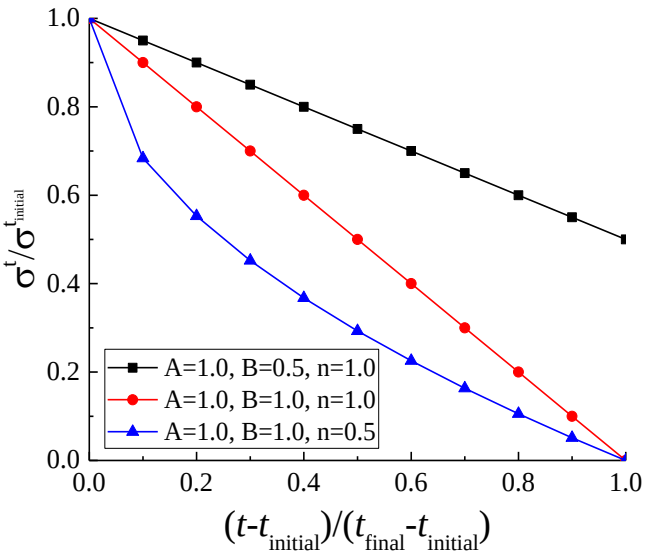

Figure 3.8. Examples of the process of stress relaxation in the elements being excavated.

Moreover, the proposed SE excavation method may be useful in modelling tunnelling problems using 2D plane-strain models. In this case, the unloading function may provide a possibility of simulating approximately the evolution of the fictitious support forces (Cui et al., 2015; Song and Rodriguez-Dono, 2021). Thus, it would be possible to set their value in the

moment when the support is installed –*i.e.* not relaxing the stresses to zero, but to a particular value of stress that would be case-dependent (we can do this changing the value of B in Eq. (3.19))–. Anyway, although it may be interesting to analyse the influence of the values of A, B and n in Eq. (3.19) for simulating more realistically the fictitious support forces, it would require much further analysis, exceeding considerably the objectives of this study.

Furthermore, a multitude of numerical tests carried out during this research have shown that volumetric deformation creates enormous pore pressures due to changes in porosity, constituting one of the main causes of the numerical issues found in HM models. Hence, if the effects of the volumetric deformation on the hydraulic behaviour were neglected, the numerical performance of the HM simulations would be improved. Thus, an option has been implemented in CODE_BRIGHT that allows ignoring the effects of volumetric deformation on the hydraulic behaviour of the excavated elements during the excavation stage. We consider that this option does not significantly affect the resulting displacements in the tunnels. However, it could provide numerical advantages.

3.3.2. Numerical implementation

As mentioned above, using the proposed SE method in those elements that are being excavated, the stresses are smoothly decreased, and the effects of volumetric deformation changes on hydraulic behaviour are avoided. To implement the proposed excavation method, it is necessary to calculate the smoothness factor f_{smooth} and the stress tensor $\boldsymbol{\sigma}$ for each element. The Newton-Raphson (N-R) iteration algorithm is used at each time step during numerical calculation. The stress tensor $\boldsymbol{\sigma}$ of the elements can be updated as described in Algorithm 3.1. The algorithm first checks whether the current element belongs to the excavated region –where ex(iel) = 2–. If true, the algorithm identifies the smoothness factor f_{smooth} and then updates the stress tensor following the method proposed in section 3.3.1. After the excavation stage ends, the smoothness factor f_{smooth} is set to zero and then, the excavated elements are completely removed from the model (‘inactive’ method).

Algorithm 3.1. Algorithm for the stress tensor (σ) update procedure in the elements

Input: numel, σ^{old} (iel), ex(iel), $t_{initial}$, t_{final}, t, A, B, n

do iel = 1, numel

if ex(iel) ≠ 2, **then**

non-excavated region. Return σ^{t} (iel) = $\sigma^{t_{initial}}$(iel)

end if

if ex(iel) = 2, **then**

if $t \geq t_{initial}$ and $t \leq t_{final}$, **then**

f_{smooth} = A-B[(t - $t_{initial}$)/(t_{final} - $t_{initial}$)]^n and an option is prepared to not consider the effects of the volumetric deformation in hydraulics.

else if $t > t_{final}$, **then**

f_{smooth} = 0 and stress-free surface

else

f_{smooth} = 1

end if

σ^{t} (iel) = f_{smooth} $\sigma^{t_{initial}}$(iel)

end if

end do

numel: the total number of elements; iel: the number of the current element;

ex(iel): excavation flag, where ex(iel) = 2 represents that the element is being excavated;

$t_{initial}$, t_{final}: the initial and final time in the excavation stage;

σ^{t}(iel), $\sigma^{t_{initial}}$(iel): the stress of an element at the current time and at the initial time, respectively;

A, B, n: the parameters in Eq. (3.19); t: the current time.

3.3.3. Preliminary numerical verification of the implementation

An example is presented here for the preliminary verification of the implementation of the SE method. In this example, the rock mass is considered to be an elastic material with an elastic modulus E = 1150 MPa and a Poisson's ratio ν = 0.25. Using CODE_BRIGHT, a 2D axisymmetric model with a discretised area of 100 m × 150 m is considered and the axisymmetry axis is the y-axis (see Figure 3.9). The tunnel is modelled as a rectangle of 100 m in length, in such a way that 40 excavation stages of 2.5 m in length can be performed. The radius of the tunnel is 2.5 m in this example.

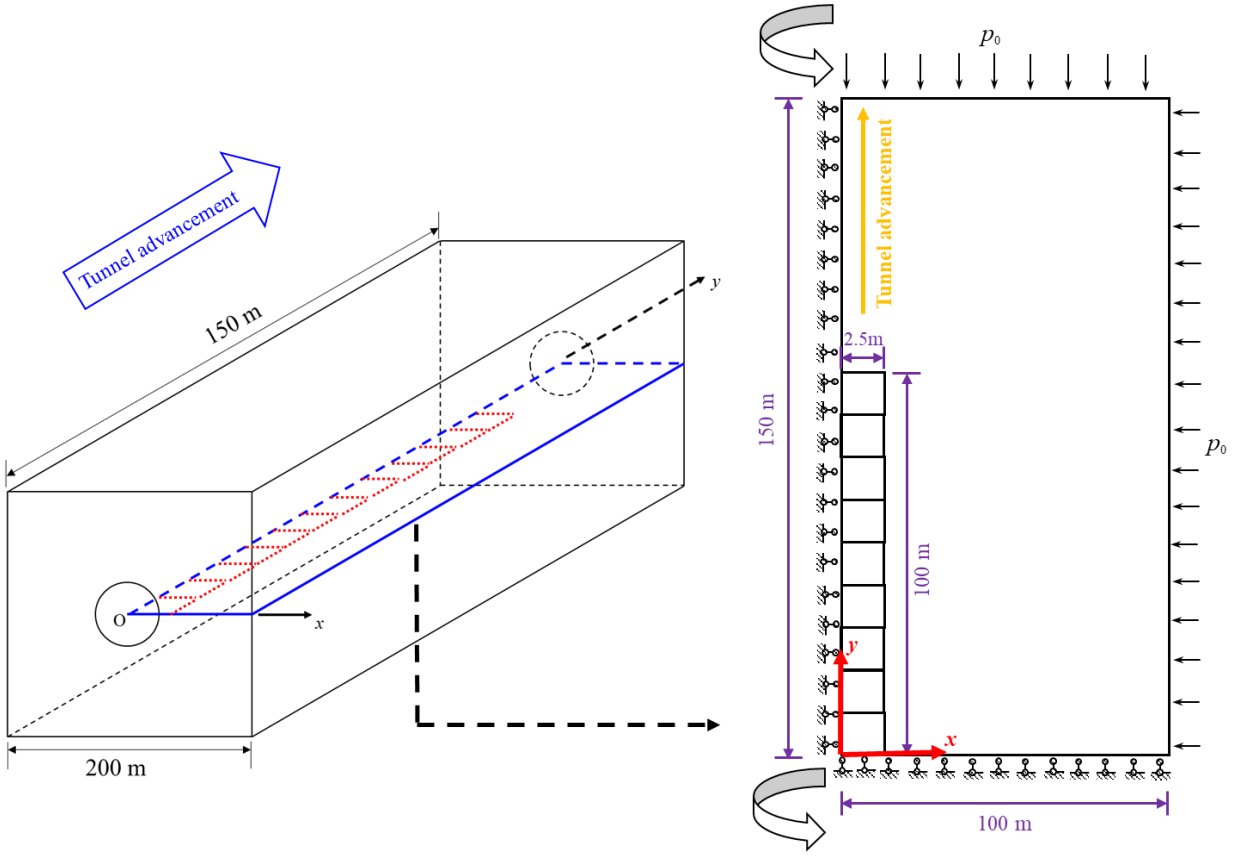

Figure 3.9. Conceptual model of the excavation problem. Basic features of the 2D axisymmetric model.

Figure 3.10 presents the mesh of the numerical model. A mesh with 5439 quadrilateral elements is adopted, *i.e.* 4 nodes quadrilateral mesh type. Note that the generalised selective

integration procedure, implemented in CODE_BRIGHT, can eliminate locking mesh and hour glassing issues of linear quadrilateral elements (Olivella et al., 1996). The mesh size is gradually reduced towards the tunnel area (see Figure 3.10). Regarding initial and boundary conditions, an isotropic initial stress of 28 MPa is considered. The normal displacements are fixed on the axis of symmetry (x = 0) and at the bottom (y = 0) of the model, and a normal pressure of 28 MPa is applied to the rest of the boundaries of the model –*i.e.* Neumann boundary conditions–.

Three different points belonging to different excavation stages have been selected, to observe their stress evolution over time (Figure 3.11). For the sake of simplicity, the values of A, B, and n in Eq. (3.19) have been taken all equal to 1.0 in this example, *i.e.* the stresses in the elements being excavated are linearly reduced from their initial values –their current stress at the moment when their excavation starts- to zero. Note that, at time t = 0 (before the first excavation stage), the stresses in all three points (points 1, 2 and 3) are equal to the value of the initial stress. As it can be observed, the radial stress –stress in the x direction– (Figure 3.11a) of point 1 (corresponding to an element being excavated in the first excavation stage) decreases linearly from the initial field stress to zero –as expected– in 1 day (the duration of each excavation stage). The radial stress evolution of points 2 and 3, corresponding to different excavation stages, is similar. Nonetheless, it can be observed that their radial stress increases slightly before excavation, due to the nearby excavation of previous stages, before being decreased to zero during their excavation. Concerning the axial stress –stress in the y direction– (Figure 3.11b), it can be observed a similar behaviour, although the axial stress decreases slightly before the corresponding excavation stage.

Furthermore, Figure 3.11(c) presents the radial displacements –displacements in the x direction- for two different points located at the tunnel crown. It can be observed that the displacements are suddenly changed at the beginning of each excavation stage when using the 'inactive' excavation method. Instead, the radial displacements increase smoothly when using the SE method, which may be more realistic in some cases. In fact, dynamic unloading conditions often exist during excavation (Cai, 2008). Note that the final displacements are equal using either method; the difference is just the displacements evolution during the excavation process. However, note that the final displacements may be different when considering time-dependent behaviour, although is not the aim of this study to analyse that effect.

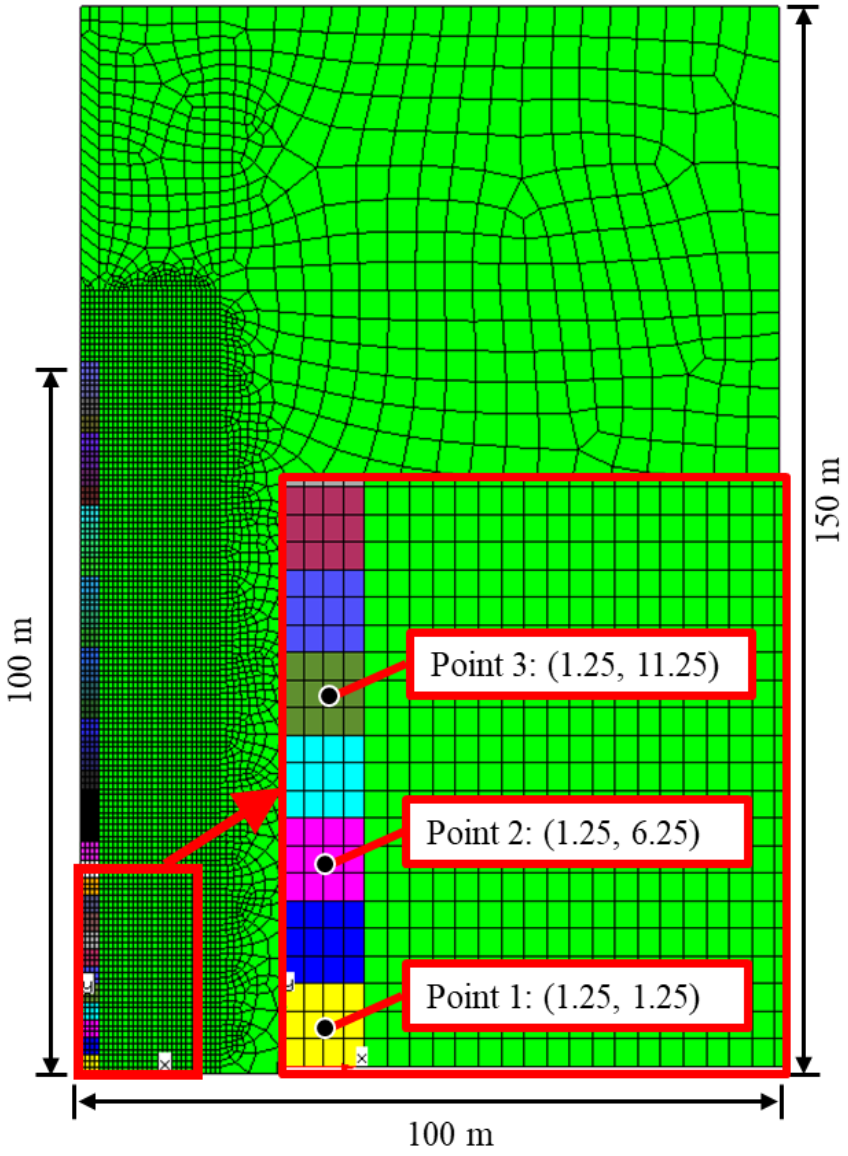

Figure 3.10. Mesh of the 2D axisymmetric numerical model (far-boundaries at distances x = 100 m and y = 150 m; quadrilateral elements –5439 elements, 4 nodes each one–; 40 excavation stages in total –one day for each one).

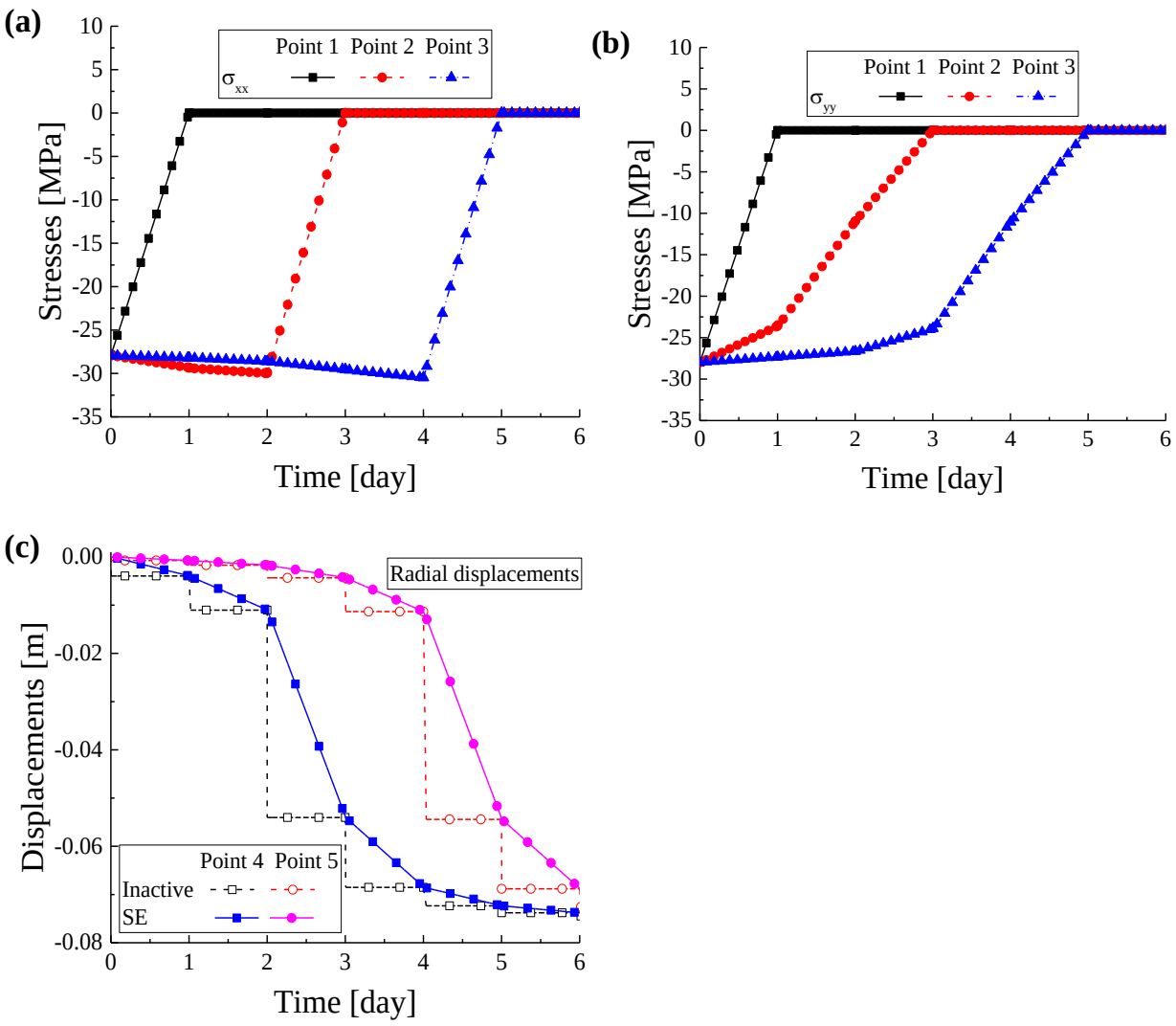

Figure 3.11. Evolution over time of **(a)** radial stresses for points 1, 2 and 3, **(b)** axial stresses for points 1, 2 and 3, and **(c)** radial displacements at the tunnel crown for points 4 and 5. SE represents the smoothed excavation method. Coordinates of the points: Point 1 (1.25, 1.25), point 2 (1.25, 6.25), point 3 (1.25, 11.25), point 4 (2.5, 6.25) and point 5 (2.5, 11.25).

3.3.4. Verification of the principle of uniqueness

The principle of uniqueness, which means that the solutions obtained by different excavation strategies (e.g. different number of excavation stages) are all equal for a time-independent linear elastic material, was proposed using the virtual work theorem (ISHIHARA, 1970). In this section, a number of numerical examples are performed to verify that the proposed SE method satisfies this principle. The numerical models chosen are the same as those already introduced in section 3.3.3, and the elastic parameters are chosen are E = 1150 MPa and v = 0.25.

Thus, seven numerical simulations have been performed with a different number of excavation stages (1, 2, 4, 8, 10, 20, 40). Information regarding geometry, boundary conditions and mesh type is the same as in section 3.3.3 (see Figures 3.9 and 3.10). Figure 3.12 shows the radial displacements (displacements in the x direction) along the section x = 2.5 m (tunnel crown), and the axial displacements (displacements in the y direction) along the section y = 100 m (tunnel face). It can be observed that the displacements are independent of the number of excavation stages for linear elastic materials. Hence, the uniqueness of the proposed SE method has been verified.

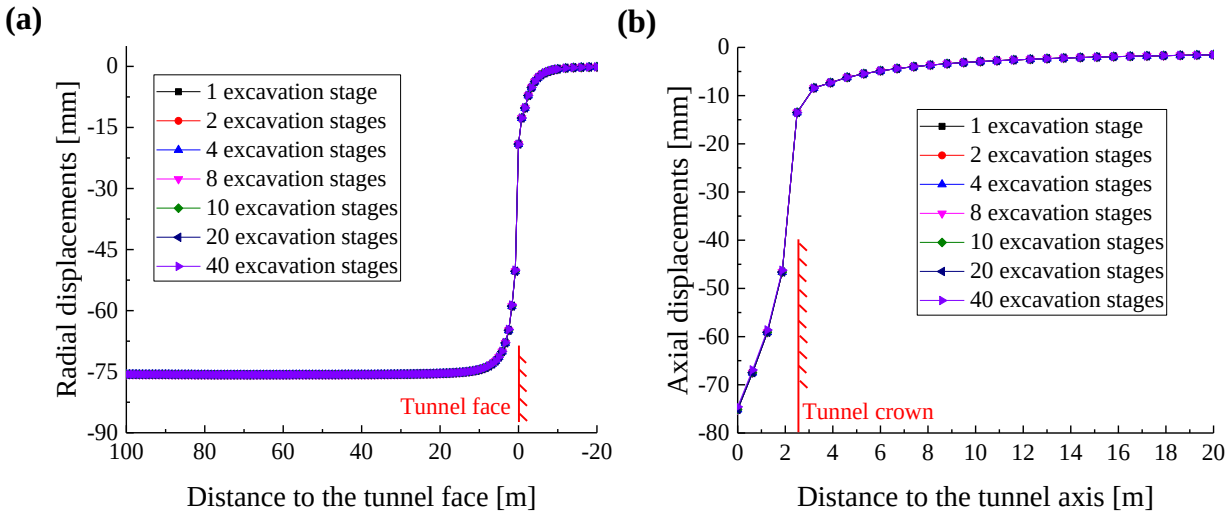

Figure 3.12. **(a)** Radial displacements along the section *x* = 2.5 m (tunnel crown); **(b)** Axial displacements along the section *y* = 100 m (tunnel face).

3.4. Convergence analysis and computational efficiency for tunnelling problems

As mentioned in section 3.3, using the inactive excavation method, simulations may experience numerical difficulties or even non-convergence problems during excavation, especially in the initial time step of the excavation stage. Excavation takes place on the model instantaneously, and the first time step receives the full effect. In addition, the central processing unit (CPU) could take excessive time in the calculation. A numerical scheme with automatic time step calculation tends to reduce the time step in order to reduce displacement variations. However, it could be unable to obtain a value that resolves the numerical issues due to the instantaneous removal of elements –*i.e.* non-convergence–.

In this section, numerical analyses of computational efficiency and convergence for excavation problems have been carried out comparing the inactive (instantaneous removal) method and the proposed smoothed excavation (SE) method. The numerical efficiency using both excavation methods has been analysed for both mechanical (M) and hydro-mechanical (HM) problems (sections 3.4.1 and 3.4.2, respectively).

In the CODE_BRIGHT simulations used for this purpose, the information regarding geometry and boundary conditions for mechanical problems is the same as in section 3.3.3 (see Figure 3.9). Concerning HM problems, in addition to that, a liquid pressure p_l is applied to the right boundary of the model (Figure 3.13a). After excavation, atmospheric pressure is prescribed on the tunnel surface (0.1 MPa in these examples).

For these analyses, three excavation stages are considered, so that the tunnel is modelled as a rectangle of 7.5 m in length, in such a way that 3 excavation stages of 2.5 m in length could be performed in the numerical model (one day for each excavation stage). As for the mesh, it is composed of 5439 quadrilateral elements –*i.e.* 4 nodes quadrilateral mesh type– and the size of the elements is gradually reduced towards the tunnel area (see Figure 3.13b). It should be noted that all input information is identical for both models in the comparison. The only difference is the excavation method used.

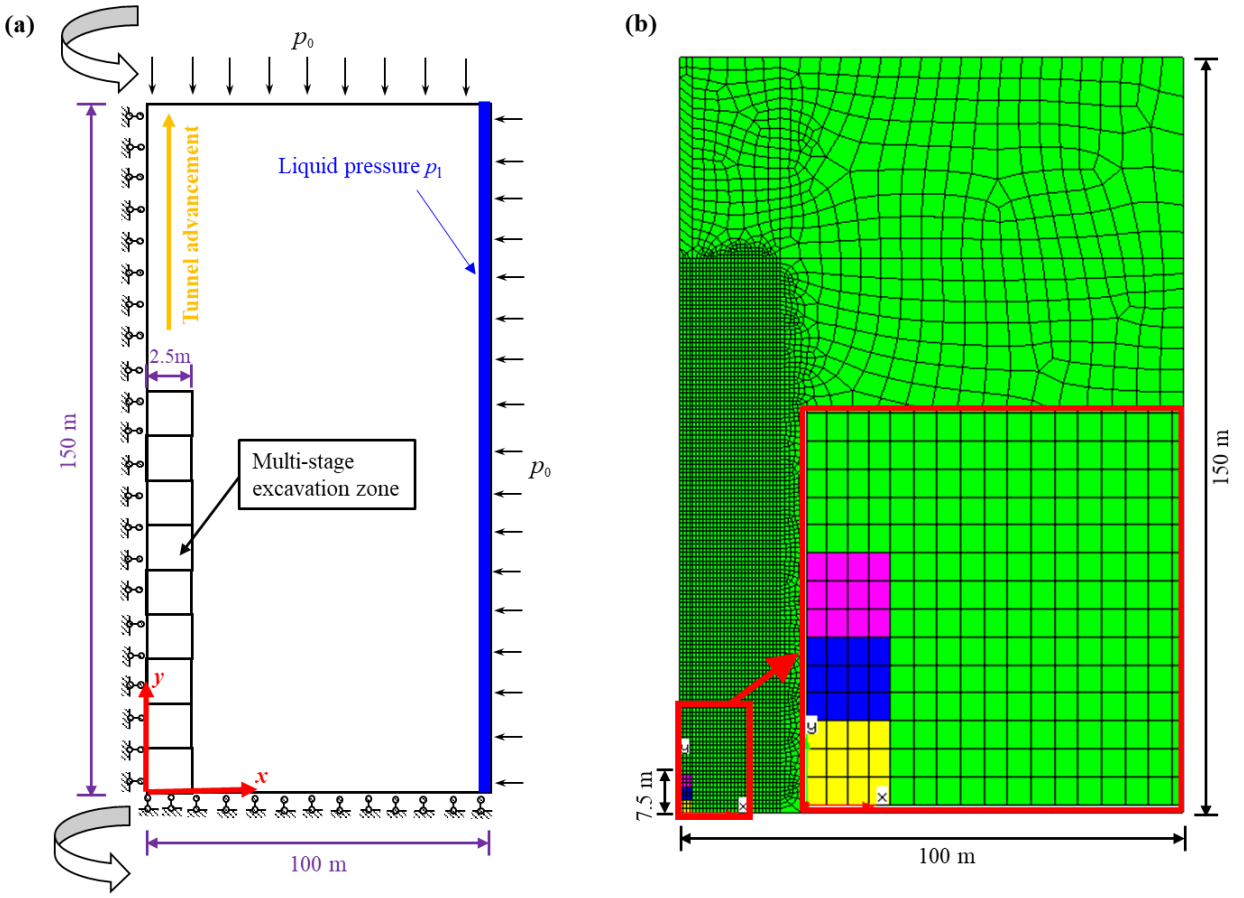

Figure 3.13. **(a)** Basic features and boundary conditions for the 2D axisymmetric excavation model under hydro-mechanical conditions; **(b)** Mesh of the mechanical and hydro-mechanical models (far-boundaries at distances x = 100 m and y = 150 m; quadrilateral element mesh –5439 elements, 4 nodes each one–; 3 excavation stages in total –one day for each one).

3.4.1. Convergence analysis and computational efficiency for mechanical models

In this section, numerical analyses of computational efficiency and convergence are carried out for the mechanical models. Six different quality rock masses (GSI = 25, 35, 45, 48, 60, 74) are considered, and Table 3.1 shows their input parameters. Two different excavation methods are

compared: the proposed SE method (with A = B = n = 1) and the so-called 'inactive' excavation method.

The numerical simulations have been executed on a desktop computer with Intel(R) Core(TM) i7-8700K CPU of 3.70 GHz and 32 GB RAM memory. The absolute and normalised CPU times of each numerical model are presented in Table 3.2. Note that the CPU time consumed using the inactive excavation method is normalised by dividing it by the CPU time consumed in the case of the rock mass with GSI = 74 and using the same method ($t_{inactive,\ GSI=74}$). As it can be observed, the CPU time depends on the GSI, being almost 18 times slower for the lowest quality rock mass (GSI = 25) compared to the highest quality rock mass (GSI = 74). Then, the CPU time using the SE method is analysed and compared to the CPU time required using the inactive excavation method, for each rock mass quality.

Additionally, Figure 3.14 shows the comparison of the computational efficiency (normalised CPU time) between the inactive method and the proposed SE method. It can be observed in both Table 3.2 and Figure 3.14 that the SE method is able to reduce CPU time in all cases. Therefore, the efficiency of the numerical calculation has improved using the SE method.

Table 3.1. Input parameters of elastic-viscoplastic behaviour models. Based on the work of Vlachopoulos and Diederichs (2009) and Alejano et al. (2012).

GSI	25	35	45	48	60	74
E (MPa)	1150	2183	4305	7500	11215	27647
c (MPa)	1.16	1.45	1.75	2.14	3.25	5.76
φ (deg)	18.52	21.12	23.71	27.08	33.43	38.98

For all cases: ψ (deg) ≈ 0; ν = 0.25; θ_T (deg) = 25; $\eta_{perzyna}$(MPa^m s) = $10^{2\,(*)}$; m = 5; R_1 (m) = 2.5

* Sufficiently small value of $\eta_{perzyna}$ so that the solution is comparable to the purely plastic case.

Table 3.2. Absolute and normalised CPU time for six different models with rock masses of different quality.

GSI	$t_{inactive}$ (s)	$t_{inactive}$ / $t_{inactive,\ GSI=74}$	t_{smooth} / $t_{inactive}$	$(t_{inactive} - t_{smooth}) / [(t_{inactive} + t_{smooth})/2]$
25	535.13	17.9	0.868	14.2 %
35	373.11	12.5	0.737	30.3 %
45	257.89	8.6	0.863	14.7 %
48	210.56	7.0	0.904	10.0 %
60	161.88	5.4	0.592	51.3 %
74	29.91	1.0	0.921	8.2 %

t_{smooth}: absolute CPU time for the smoothed excavation method.

$t_{inactive}$: absolute CPU time for the inactive excavation method.

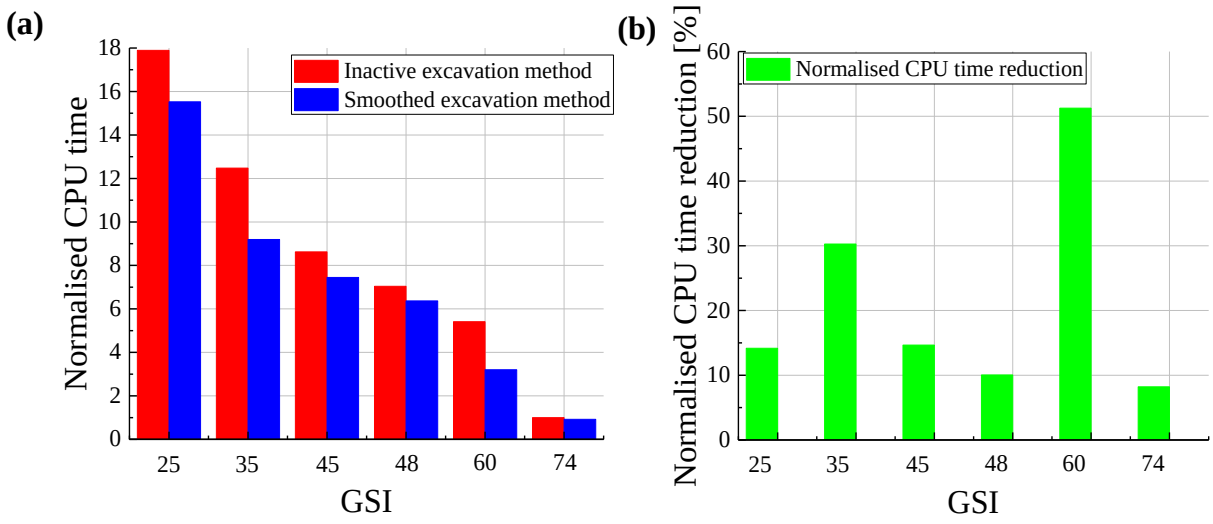

Figure 3.14. Comparison of **(a)** normalised CPU times and **(b)** normalised CPU time reduction(*), for six different quality rock masses. *Normalised CPU time reduction is defined as $(t_{inactive} - t_{smooth}) / [(t_{inactive} + t_{smooth})/2]$.

Furthermore, during the calculation process in CODE_BRIGHT, the time step (Δt) is based on the Newton-Rapson (N-R) iteration method (Olivella, 1995; Olivella et al., 1996; Olivella et al., 2020). In the case of the examples presented here, the time step is controlled based on the number of N-R iterations *iter* (Olivella, 1995; Olivella et al., 2020), according to the multiplication factor *f* shown in Eq. (3.20). Note that for different time step control protocols, absolute CPU time and time step values may be different from the current example. However, the comparative advantages of the proposed SE method would be similar.

$$\Delta t^{k+1} = f\,\Delta t^{k}; \qquad f = \left(\frac{niter}{iter}\right)^{0.25} \geq 0.5 \tag{3.20}$$

Note that $f = 1$ when *iter* = *niter*, and then the new time step Δt^{k+1} does not change. In general, *niter* is recommended to have a value between 2 and 4, and it is chosen according to the expected numerical difficulties. It is recommended to use *niter* = 4 if no numerical difficulties are expected (in that case it would be enough, due to the quadratic convergence of N-R method), but a stricter time step control can be used –*niter* = 3 or even 2– for models with strong nonlinearities, path dependency and other convergence issues. If e.g. *niter* = 4, the time step decreases when *iter* > 4 and increases when *iter* < 4. Thus, the value of Δt can be related to the numerical efficiency: very small values of Δt represent systematic numerical difficulties (*i.e.* $f < 1$) that may result in non-convergence. On the other hand, larger values of Δt represent fewer numerical difficulties (*i.e.* $f > 1$) and thus, a shorter computational time. The method tends to produce an average number of N-R iterations close to the target value *niter* defined for each calculation.

Figure 3.15 shows the values of Δt versus time for both excavation methods and for six rock masses of different quality. It can be observed that the greatest numerical difficulties –minimum values of Δt– are reached at the beginning of each excavation stage (time = 0, 1 and 2 days), for both excavation methods. However, due to the sudden removal of elements, the inactive excavation method concentrates its numerical inefficiency at the beginning of each excavation stage. On the contrary, it can be seen that the initial time step is much higher using the SE method, especially in poor quality rock masses that show plastic behaviour. Nevertheless, when using the SE method, there is still some numerical inefficiency at the end of each excavation stage (time = 1, 2 and 3 days in this case), since the excavated elements are removed from the model at that

time, although the relative change in boundary conditions caused by that removal has been smoothed.

Regarding the rest of the excavation stage –apart from the initial time step–, the time step (Δt) of the SE method is normally a little lower than that of the inactive excavation method, since by then, the inactive excavation method has solved most of its numerical inefficiencies –provided it had not experienced non-convergence issues, so that the calculation would have stopped–. Therefore, the SE method is not only numerically more efficient, but also more reliable –non-convergence issues are less likely to occur.

Note that quite simple models are performed in this analysis. Even so, the SE method has demonstrated that it can improve numerical efficiency significantly, saving computational time and –more importantly– eliminating non-convergence issues, compared with the 'inactive' method. However, when dealing with complex behaviour models and HM couplings, especially in models with complex geometries or very fine meshes containing thousands –or even millions– of elements, then the current computers can take days –or even weeks– to complete the calculation. In these cases, the SE method may save a great amount of time, compared with the inactive method.

3.4.2. Convergence analysis and computational efficiency for hydro-mechanical models

In the case of HM models, both hydraulic and mechanical boundary conditions change during the multi-stage excavation process, which may result in even greater numerical difficulties. An example is carried out herein to perform numerical analyses of computational efficiency and convergence for HM problems.

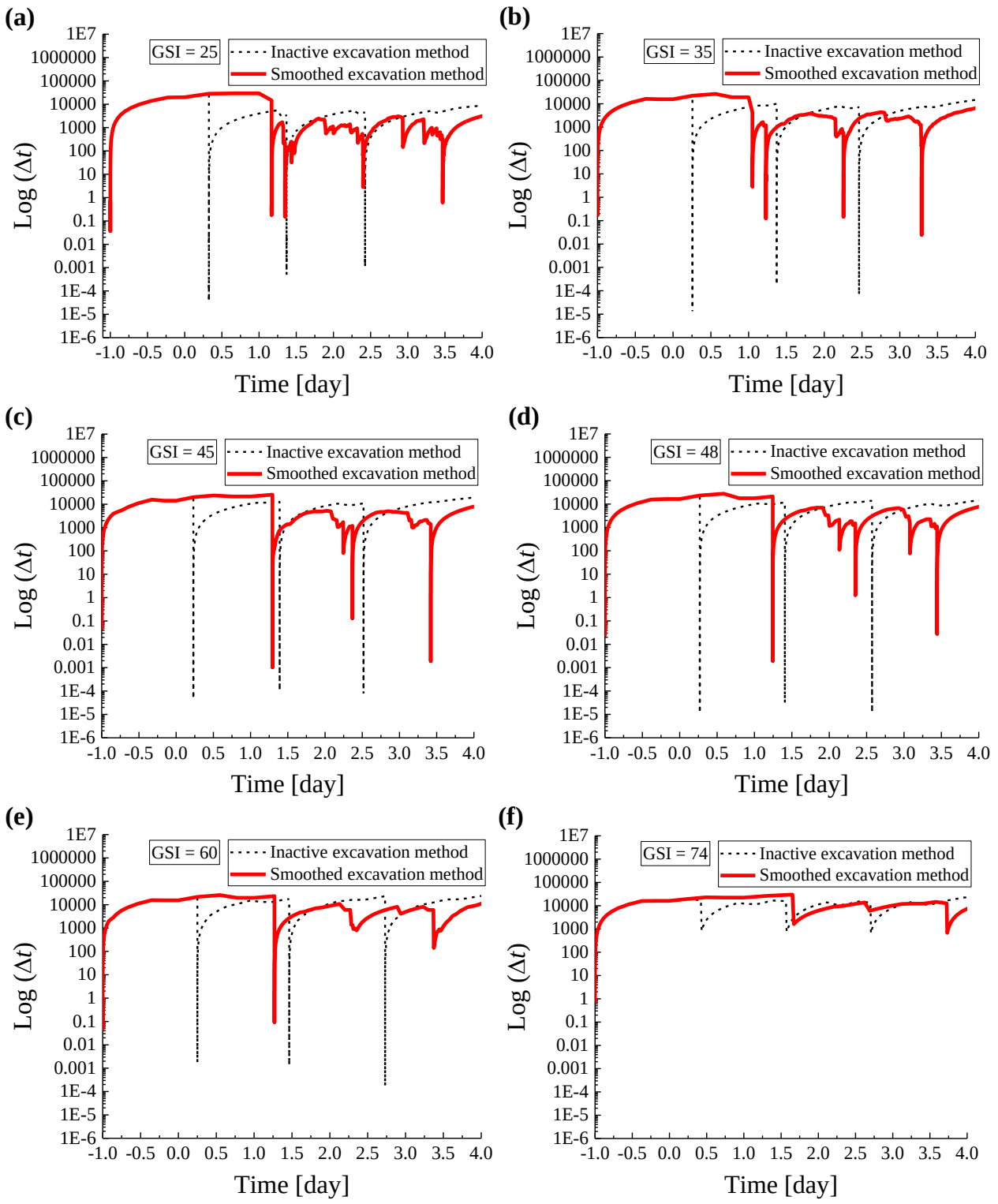

Figure 3.15. Log (Δt) versus time for six rock masses of different quality and using both inactive and SE excavation methods (with *niter* = 4): **(a)** GSI= 25, **(b)** GSI=35, **(c)** GSI=45, **(d)** GSI=48, **(e)** GSI= 60, **(f)** GSI=74.

In these analyses, both elastic and elastic-viscoplastic material models are assessed: (1) for the elastic material model: E = 7500 MPa, ν = 0.25, (2) for the elastic-viscoplastic material model: E = 7500 MPa, ν = 0.25, c = 2.14 MPa, φ = 27.08 deg, ψ = 0 deg, θ_T = 25 deg, m = 5, and $\eta_{perzyna}$ = 10^2 MPa^5s. Moreover, two different cases regarding HM boundary conditions are considered: (1) Case A: p_0 = 10 MPa, p_l = 4 MPa, and (2) Case B: p_0 = 10 MPa, p_l = 5 MPa. The intrinsic permeability is 10^{-15} m^2 for all cases. In addition, during the excavation stage, the effect of volumetric deformation on hydraulic behaviour –through changes in porosity–, is neglected on the elements being excavated, as described in section 3.3.

Table 3.3 presents the absolute CPU time using the inactive method, the normalised CPU time and the time reduction (in %) using the SE method, for all cases. Note that the normalised CPU time has been obtained dividing it by the CPU time using the inactive excavation method ($t_{inactive}$) for each case. Hence, the normalised CPU time consumed by the inactive excavation method is always 1. Note that values lower than one represent an improvement in CPU time, in comparison with the inactive method. It can be observed that there is a significant improvement in CPU time consumption in viscoplastic cases, whereas no improvement is achieved in elastic cases. Anyway, the CPU runtime for elastic cases is quite low, since no numerical difficulties have been encountered.

Table 3.3. CPU time for hydro-mechanical problems.

Cases	Model	$t_{inactive}$ (s)	$t_{smooth} / t_{inactive}$	$(t_{inactive} - t_{smooth}) / [(t_{inactive} + t_{smooth})/2]$
A	Elastic	51.06	1.156	-14.476 %
B	Elastic	53.09	1.079	-7.642 %
A	Elastic-viscoplastic	1270.03	0.600	49.998 %
B	Elastic-viscoplastic	1136.97	0.815	20.350 %

On the other hand, Figures 3.16 and 3.17 present the values of time step Δt versus time for elastic and elastic-viscoplastic models, respectively. As shown in Figure 3.16, the calculation does not have significant numerical difficulties for HM problems with elastic materials and the proposed SE method exhibits a calculation efficiency similar to the inactive excavation method in

this case. However, as shown in Figure 3.17, for rock masses with plastic response, the SE method improves numerical efficiency.

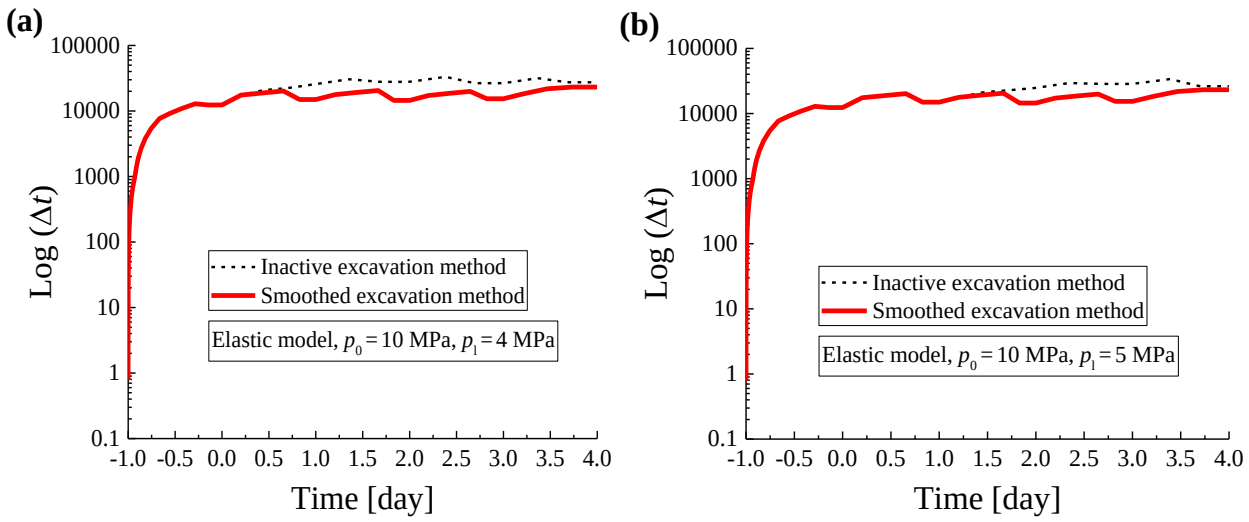

Figure 3.16. Log (Δt) versus time for two different hydro-mechanical boundary conditions and using the elastic model (with *niter* = 4): **(a)** p_0 = 10 MPa, p_1 = 4 MPa and **(b)** p_0 = 10 MPa, p_1 = 5 MPa.

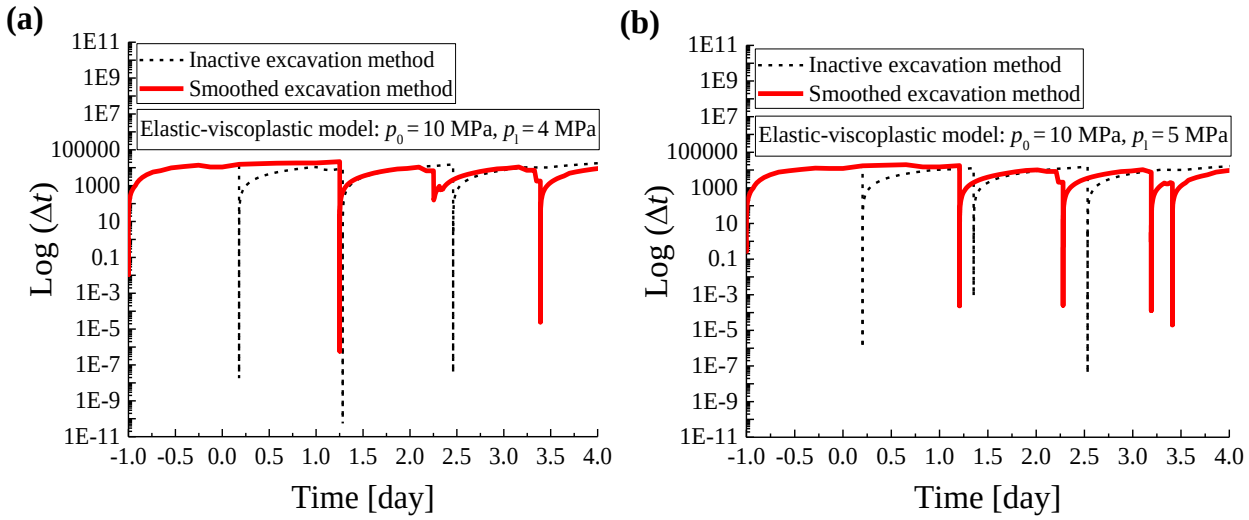

Figure 3.17. Log (Δt) versus time for two different hydro-mechanical boundary conditions and using the elastic-viscoplastic model (with *niter* = 4): **(a)** p_0 = 10 MPa, p_1 = 4 MPa, **(b)** p_0 = 10 MPa, p_1 = 5 MPa.

3.5. Comparison with the previous solutions

In this section, the obtained results using CODE_BRIGHT are compared with previous solutions. First, in section 3.5.1, CODE_BRIGHT results of the longitudinal deformation profiles (LDP) for mechanical problems with plastic response are compared with previous solutions (Alejano et al., 2012; Vlachopoulos and Diederichs, 2009). Then, steady-state hydro-mechanical (HM) problems and transient coupled HM problems with elastic materials are carried out in sections 3.5.2 and 3.5.3, respectively, and the obtained CODE_BRIGHT results are compared with the previous solutions (Nam and Bobet, 2007; Paraskevopoulou and Diederichs, 2018).

3.5.1. Elastic-plastic solutions of the LDP for mechanical problems

This section presents the LDP results for mechanical problems with elastic-plastic materials, using CODE_BRIGHT. These results have been compared with the solutions of Vlachopoulos and Diederichs (2009), and with the numerical results –using FLAC2D and FLAC3D– of Alejano et al. (2012). For the sake of consistency with the elastic-plastic model, the viscosities $\eta_{perzyna}$ in CODE_BRIGHT are considered small enough ($\eta_{perzyna}= 10^2$ MPa^{5}s in this example) to be able to assume that the model behaves like an elastic-purely-plastic model and, hence, the rock mass does not show a time-dependent behaviour (Alonso et al., 2005; Song et al., 2020).

Regarding the CODE_BRIGHT numerical models, the information regarding geometry, boundary conditions, excavation process and mesh type is the same as in section 3.3.3 (see Figures 3.9 and 3.10). The isotropic initial stress adopted is p_0 = 28 MPa. The results of six rock masses of different quality have been compared, with GSI = 25, GSI = 35, GSI = 45, GSI = 48, GSI = 60, GSI = 74, as shown in Table 3.1. It is considered that the rock masses behave in an elastic-perfectly-plastic manner, obeying the Mohr-Coulomb failure criterion.

Based on the approach of Vlachopoulos and Diederichs (2009), the LDP can be obtained from tunnel geometry and the plastic radius, as shown in Eq. (3.21).

$$\frac{u_r}{u_{r,max}} = \begin{cases} \frac{1}{3}\exp\left(-0.15\frac{R_p}{R_1}\right)\exp\left(\frac{x_d}{R_1}\right), x_d < 0 \\ 1-\left[1-\frac{1}{3}\exp\left(-0.15\frac{R_p}{R_1}\right)\right]\exp\left(-\frac{3x_d}{2R_p}\right), x_d \geq 0 \end{cases} \quad (3.21)$$

where u_r and $u_{r,max}$ represent the radial displacements and the maximum radial displacements of the tunnel wall, respectively; R_p represents the maximum plastic radius, R_1 represents tunnel radius and x_d represents the distance to the tunnel face. In these examples, R_p is determined through self-similarity solutions (Carranza-Torres, 1998).

As stated above, the results of CODE_BRIGHT have been compared with the results –using FLAC2D and FLAC3D– of Alejano et al. (2012). Neumann boundary conditions were adopted in the FLAC2D numerical models, and the discretised area was 70 m × 100 m. In the FLAC3D numerical models, Dirichlet boundary conditions were adopted, being the discretised domain 60 m × 60 m × 60 m. A more detailed description of the numerical models (FLAC2D and FLAC3D) can be found in Alejano et al. (2012).

Figure 3.18 shows a good agreement between the LDP of CODE_BRIGHT, FLAC2D (Alejano et al., 2012), FLAC3D (Alejano et al., 2012) and Vlachopoulos and Diederichs' solutions (Vlachopoulos and Diederichs, 2009) for rock masses of different qualities, which can serve as a verification of our CODE_BRIGHT models for plastic problems.

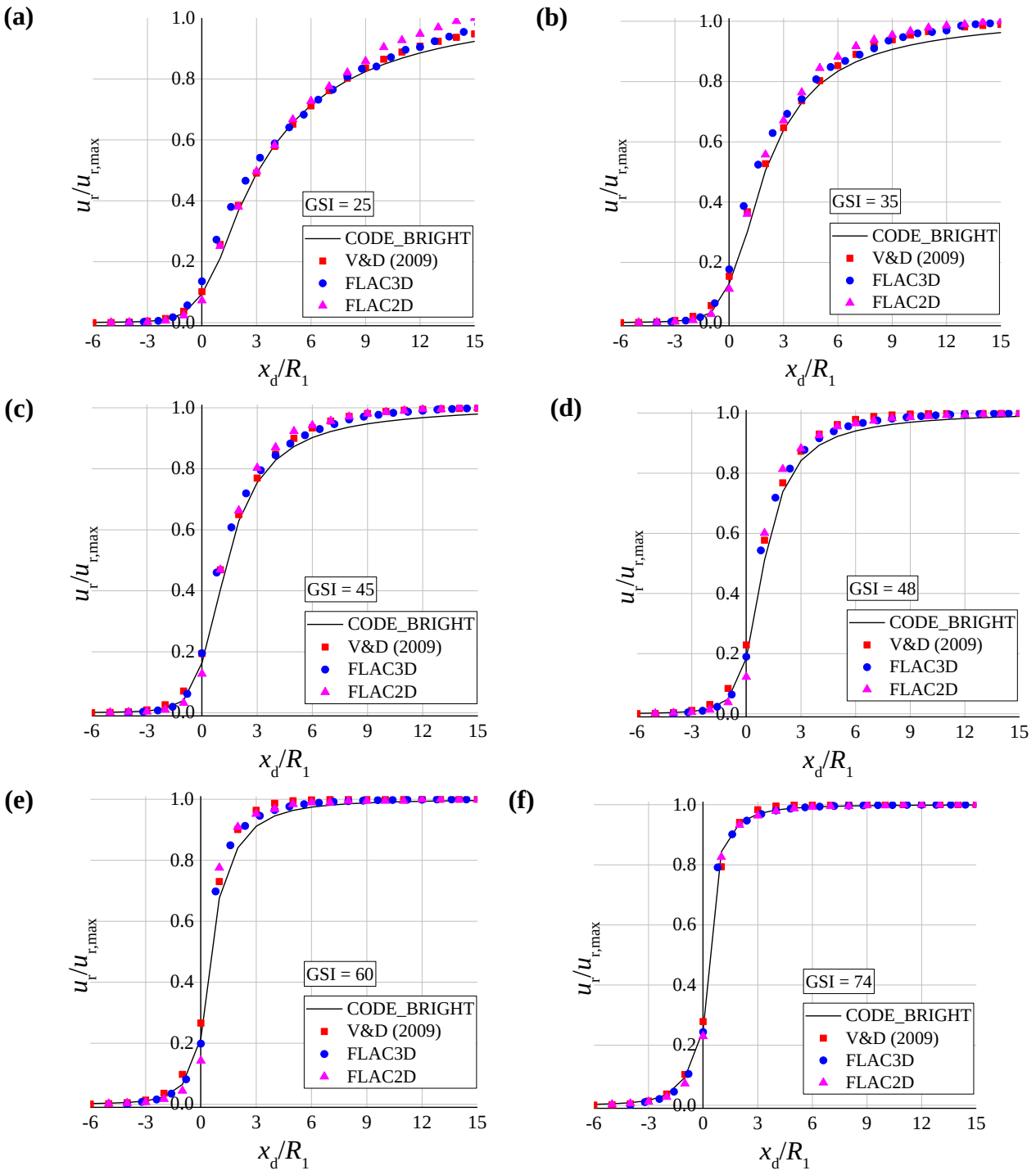

Figure 3.18. Longitudinal deformation profiles of rock masses of different quality according to different methods (CODE_BRIGHT, FLAC2D (Alejano et al., 2012), FLAC3D (Alejano et al., 2012) and the solutions of V&D (Vlachopoulos and Diederichs, 2009)): **(a)** GSI = 25, **(b)** GSI = 35, **(c)** GSI = 45, **(d)** GSI = 48, **(e)** GSI = 60, **(f)** GSI = 74. V&D represents Vlachopoulos and Diederichs' solutions.

3.5.2. Elastic solutions of the LDP for steady-state hydro-mechanical problems

In this section, numerical simulations of the LDP are performed for HM problems with elastic materials, and the CODE_BRIGHT results are compared with the solutions of Nam and Bobet (2007). The LDP expressions for deep circular tunnels excavated in saturated elastic rock masses were developed by Nam and Bobet (2007) through a series of numerical simulations under steady-state conditions, which can be expressed as in Eq. (3.22) (Nam and Bobet, 2007).

$$\frac{u_r}{u_{r,max}} = \begin{cases} 0.28\exp\left(1.05\frac{x_d}{R_1}\right) + 0.2\exp\left(\frac{x_d}{10R_1}\right)\left[1-\exp\left(-\frac{p_l}{p'}\right)\right], & x_d < 0 \\ \frac{u_{r0}}{u_{r,max}} + \left(1-\frac{u_{r0}}{u_{r,max}}\right)\left[1-\left(\frac{0.75}{0.75+x_d/R_1}\right)^2\right], & x_d \geq 0 \end{cases} \quad (3.22)$$

where $\frac{u_{r0}}{u_{r,max}} = 0.28 + 0.19\left[1-e^{-\frac{p_l}{p'}}\right]$; p_l represents the liquid pressure in the far-field, p' represents the effective stress in the centre of the tunnel; u_{r0} represents the radial displacements of the tunnel wall at the tunnel face; $u_{r,max}$ represents the maximum radial displacements of the tunnel wall. A more detailed description of the LDP for tunnels excavated in saturated elastic rock masses can be found in Nam and Bobet (2007).

The tunnel has been modelled in CODE_BRIGHT as a rectangle of 100 m in length, in such a way that 40 excavation stages of 2.5 m in length can be performed in the numerical model. Each stage of excavation takes one day and, thus, the entire multi-stage excavation process takes 40 days. The dimensions and boundary conditions of the numerical model in CODE_BRIGHT are those shown in Figure 3.13(a). A mesh with 5439 quadrilateral elements is adopted, *i.e.* 4 nodes quadrilateral mesh type. The mesh size has been gradually reduced towards the tunnel area (see Figure 3.19). Table 3.4 presents the input parameters –rock mass properties and tunnel geometry– for the steady-state saturated problems. The intrinsic permeability chosen is 10^{-10} m^2 (a value large enough to ensure steady-state drained conditions).

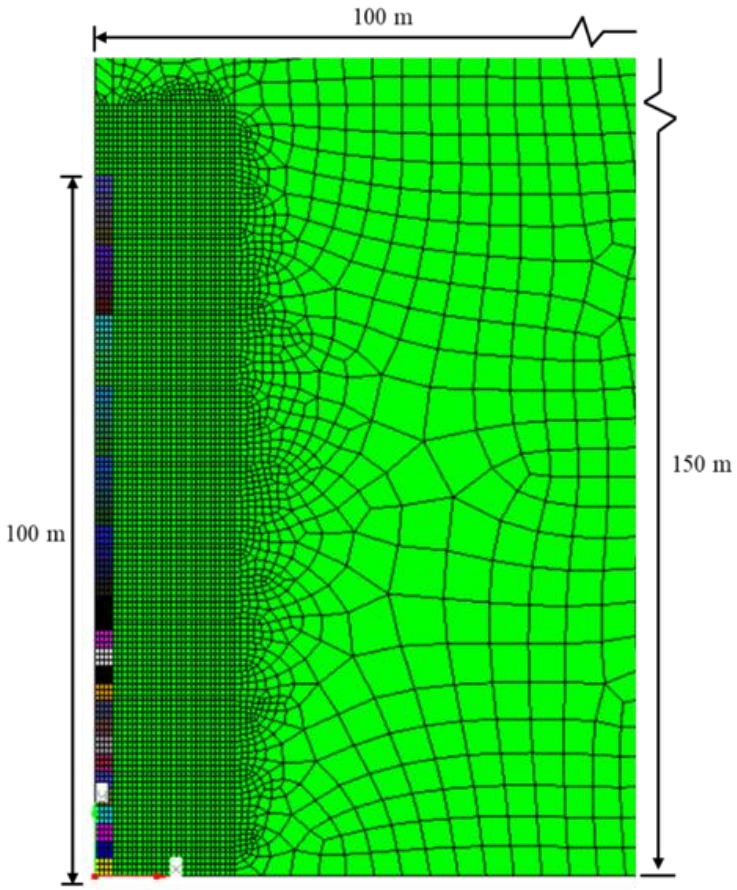

Figure 3.19. Mesh in the vicinity of the excavation area (far-boundaries at distances x = 100 m and y = 150 m; mesh of quadrilateral elements –5439 elements, 4 nodes each one–; 40 excavation stages in total –one day for each one).

Table 3.4. Rock mass properties and tunnel geometry for saturated problems with elastic response.

Cases	E (MPa)	ν	R_1 (m)	p_0 (MPa)	p_1 (MPa)	p' (MPa)	p_1 / p'
V1	1000	0.15	2.5	7.5	2.45	5.05	0.485
V2	1000	0.15	2.5	11.5	4.9	6.6	0.742
V3	1000	0.15	2.5	11.5	2.45	9.05	0.271

Figure 3.20 presents the comparison of the LDP of a saturated rock mass between the CODE_BRIGHT results and the solutions of Nam and Bobet (2007). There is a good agreement between both results, which verifies the LDP results for HM problems with elastic materials under steady-state conditions, using CODE_BRIGHT.

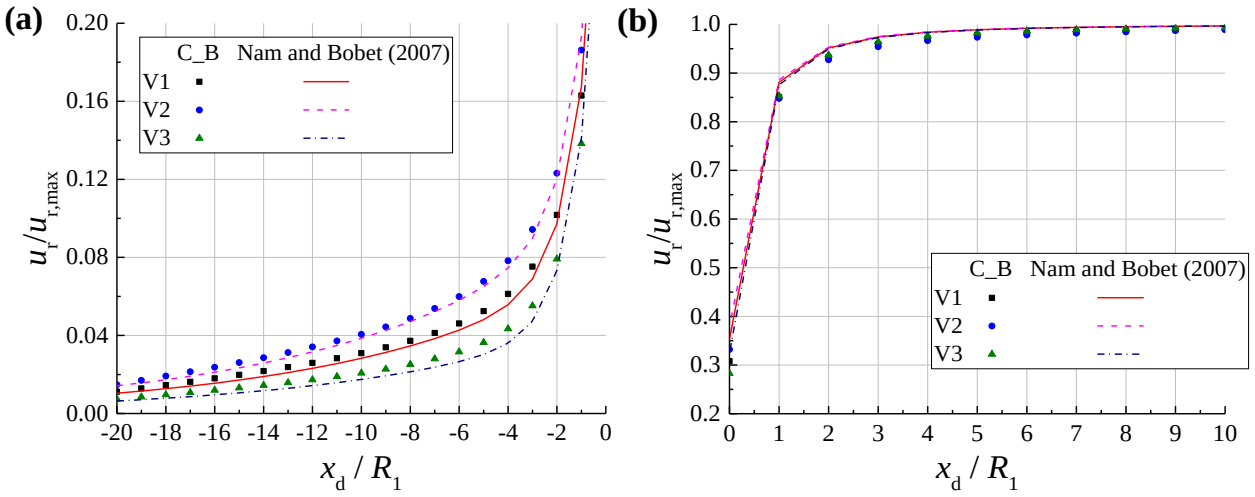

Figure 3.20. Comparison of the longitudinal deformation profiles for three different hydro-mechanical cases (p_l / p' = 0.485, 0.742, 0.271), according to CODE_BRIGHT (C_B in the figure) and Nam and Bobet's solutions (Nam and Bobet, 2007): **(a)** ahead (x_d < 0) and **(b)** behind (x_d > 0) the tunnel face.

3.5.3. Analysis of tunnelling in transient coupled hydro-mechanical conditions

In tunnelling, drained consolidation is time-dependent during the standstill period until the steady-state pore pressure distribution is reached (Prassetyo, 2017; Prassetyo and Gutierrez, 2018b; Ramoni and Anagnostou, 2011). In this section, time-dependent LDPs are compared between CODE_BRIGHT results and Prassetryo and Gutierrez's solutions (Prassetyo and Gutierrez, 2018b).

Considering the transient nature of the consolidating ground, Prassetryo and Gutierrez (2018b) proposed time-dependent LDP solutions for the saturated ground with elastic response, as shown in Eq. (3.23).

$$\frac{u_r}{u_{r,max}} = \begin{cases} \dfrac{u_{r0}}{u_{r,max}} \exp\left(2.11\dfrac{x_d}{2R_1}\right) + 0.2\exp\left(\dfrac{x_d}{10R_1}\right)\left[1-\exp(-A)\right], & x_d < 0 \\ \dfrac{u_{r0}}{u_{r,max}} + \left(1-\dfrac{u_{r0}}{u_{r,max}}\right)\left[1-\left(\dfrac{B}{B+0.5\,x_d/R_1}\right)^2\right], & x_d \geq 0 \end{cases} \tag{3.23}$$

where:

$u_{r0}/u_{r,max} = 0.28 + 0.028[1-\exp(-0.56\log t^*)]$

$A = -\ln[-(u_{r0}/u_{r,max}-0.305]/0.028]/2.4$

$B = 0.85-2.10^5\exp[-47\ u_{r0}/u_{r,max}]$

$u_{r,max}/ R_1 = 2.0 – 0.3\exp(-0.005t^*)$

t^* represents the normalized consolidation time (Giraud and Rousset, 1996; Li, 1999; Prassetyo and Gutierrez, 2018b).

In the CODE_BRIGHT numerical models performed in this analysis, the tunnel is presented as a rectangle of length 50 m, with 40 excavation steps of length 1.25 m. The radius of the tunnel is 2.5 m. The excavation rate is 5 m/day (Prassetyo and Gutierrez, 2018b) and thus, a total of 10 days for the whole excavation process. The dimensions and boundary conditions of the CODE_BRIGHT numerical model are shown in Figure 3.21(a). A mesh with 5795 four nodes-quadrilateral elements is adopted. Figure 3.21(b) presents the mesh of the numerical model. Input parameters of ground properties are: hydraulic conductivity $k_H = 5.0\times10^{-10}$ m/s, porosity $\phi = 0.39$, Young's modulus E = 292.5 MPa and Poisson's ratio $\nu = 0.125$ (Prassetyo and Gutierrez, 2018b). To be consistent with the assumptions in Prassetryo and Gutierrez's solutions (Prassetyo and Gutierrez, 2018b), no pressure is prescribed on the tunnel surface after excavation.

Figure 3.22 shows the comparison of LDP for the coupled HM problems between the CODE_BRIGHT results and the time-dependent solutions of LDP found in Prassetyo and

Gutierrez (2018b). A good agreement between both results is observed. This can serve as a verification of the CODE_BRIGHT results for transient HM coupled problems.

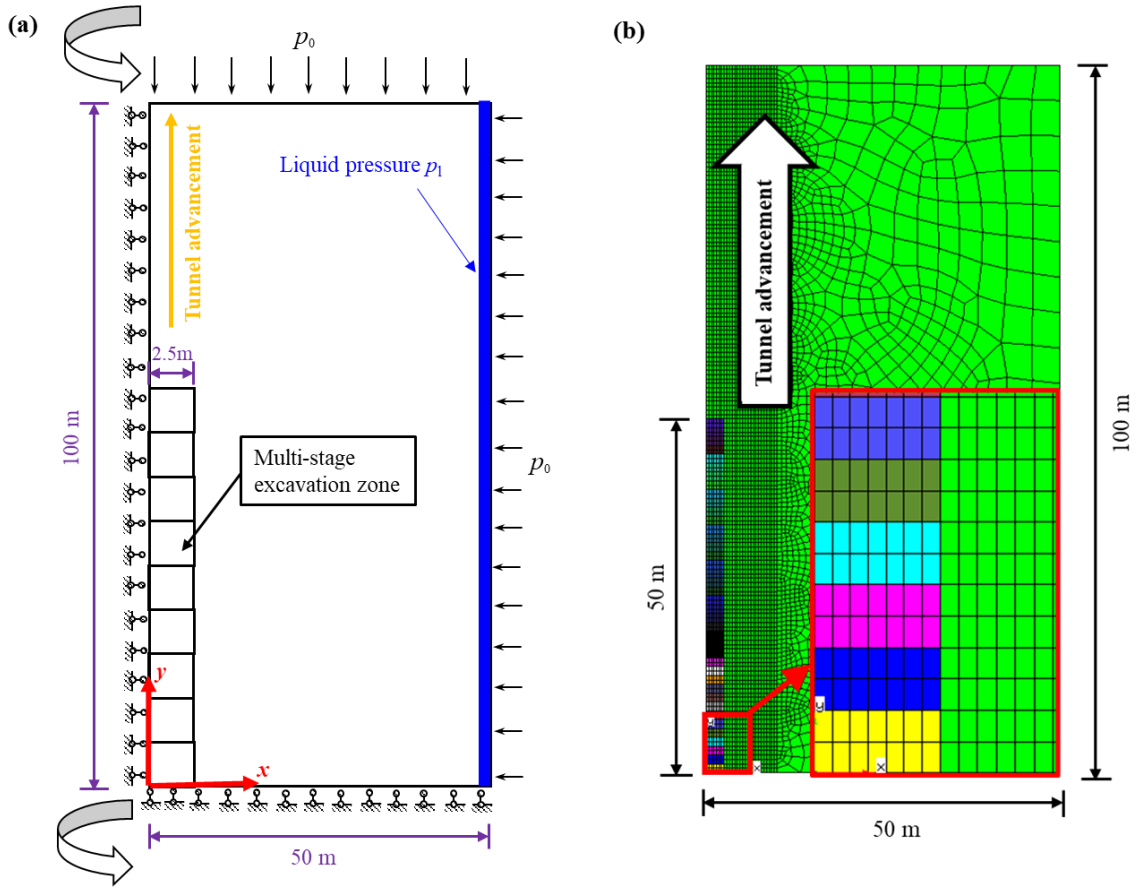

Figure 3.21. Mesh of the numerical model (far-boundaries at distances x = 50 m and y = 100 m; mesh of quadrilateral elements –5795 elements, 4 nodes each one–; 40 excavation stages in total –the excavation rate is 5 m/day).

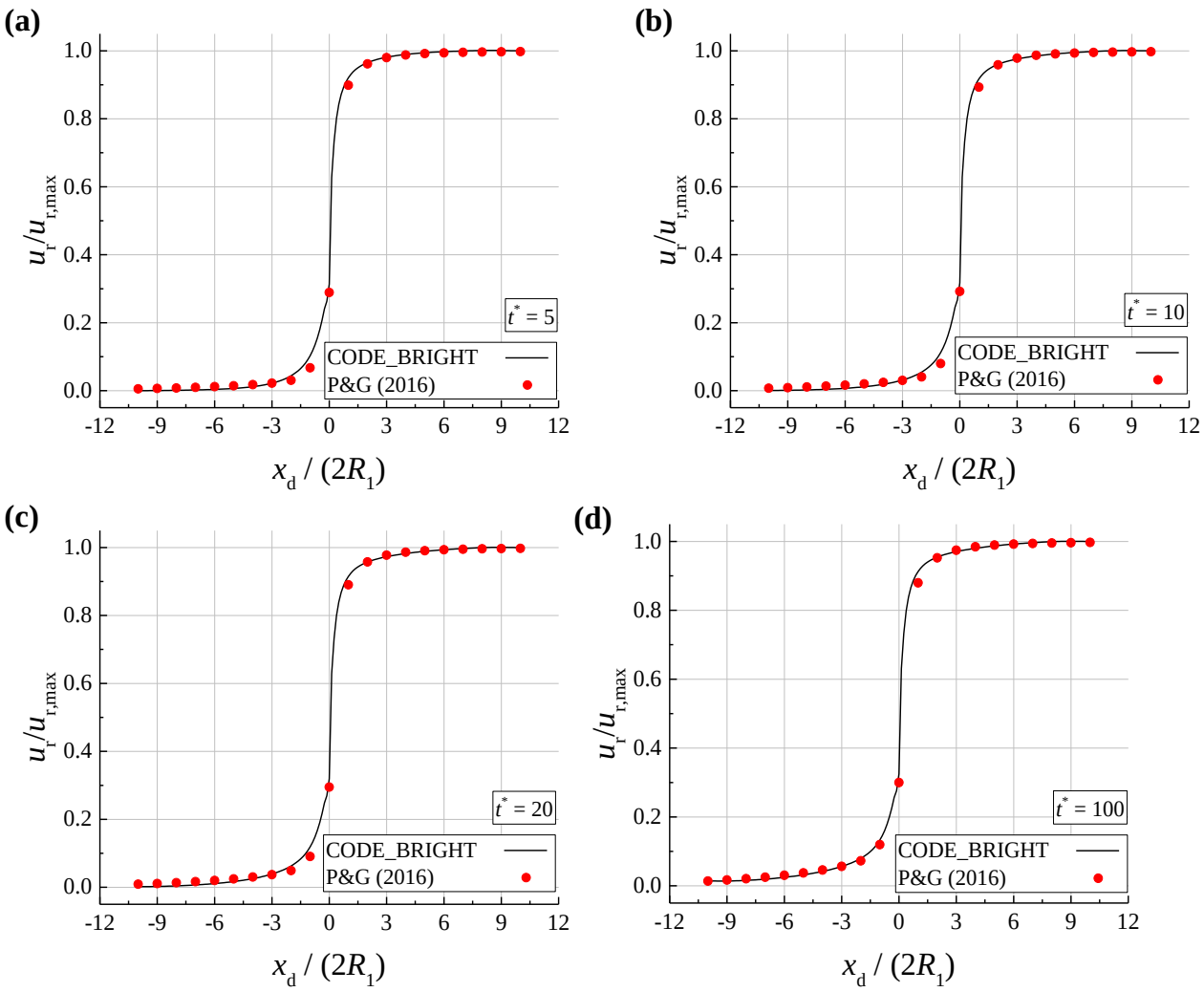

Figure 3.22. Comparison of the longitudinal deformation profiles for four different standstill times (t^* = 5, 10, 20, 100), according to CODE_BRIGHT and Prassetyo and Gutierrez's solutions (Prassetyo and Gutierrez, 2018b): **(a)** t^* = 5, **(b)** t^* = 10, **(c)** t^* = 20 and **(d)** t^* = 100. P&G represents the solutions of Prassetyo and Gutierrez (2018b).

3.6. Hydro-mechanical modelling of tunnels excavated in saturated ground with plastic response

The main objective of this section is the analysis of longitudinal deformation profiles (LDP) of tunnels excavated in saturated rock masses with plastic behaviour. When tunnelling in saturated rock masses under hydro-mechanical coupled conditions, short-term and time-dependent responses occur. The short-term response represents the HM response induced immediately after the excavation (*i.e.* the start of the standstill period) (Prassetyo, 2017; Prassetyo and Gutierrez, 2018b), which may be critical to the safety during excavation progress. The consolidation is then continued towards the total standstill period until the long-term HM response of the tunnel is in steady-state condition (Prassetyo, 2017; Prassetyo and Gutierrez, 2018b), which may be important for the long-term period safety condition.

3.6.1. Analyses of longitudinal deformation profiles for saturated problems with plastic response

In this section, parametric analyses are carried out to extend Nam and Bobet's conclusions (Nam and Bobet, 2007) to plastic problems. Thus, a series of deep tunnels are excavated in an infinite isotropic elastic-plastic medium. Six rock masses of different quality are considered (see Table 3.1) to analyse the effect of the geotechnical quality (GSI) of the rock mass on the resulting LDP. Three different cases have been considered:

(1) Mechanical (M) problem: p_0 = 15 MPa;

(2) Hydro-mechanical (HM) problem with: p_l = 4 MPa, p_0 = 15 MPa, *i.e.* p_l/p' = 0.364;

(3) Hydro-mechanical (HM) problem with: p_l = 7 MPa, p_0 = 15 MPa, *i.e.* p_l/p' = 0.875.

p' represents the effective stresses (p_0 - p_l). The results have been obtained for saturated conditions, and the intrinsic permeability adopted for the analyses is 10^{-15} m^2, which may be a realistic value for some rock masses.

The information regarding geometry, boundary conditions, excavation process and mesh type for M and HM problems, is the same as in section 3.3.3 (see Figures 3.9 and 3.10) and section 3.5.2 (see Figures 3.13a and 3.19), respectively. Figures 3.23 and 3.24 show the normalised radial displacements of tunnels excavated in saturated rock masses versus the normalised distance to the tunnel face, ahead ($x_d < 0$) and behind ($x_d > 0$) the tunnel face, respectively. As expected, the normalised radial displacements increase first and then reach a stable value when the distance to the tunnel face is large enough.

It can be observed (Figure 3.23) that there is a difference in the normalised radial displacements ahead of the tunnel face ($x_d < 0$) between the three cases –one M case and two HM cases– (in line with the previous findings of Nam and Bobet (2007) for elastic geomaterials). Extending these findings, it has been found in our analysis that this difference grows as the GSI of the excavated rock masses increases. In fact, for very low quality rock masses the difference seems to be very small, except near the tunnel face.

However, unlike in Nam and Bobet (2007), we have found a difference in normalised radial displacements behind the tunnel face ($x_d > 0$) between the three aforementioned cases. In fact, Figure 3.24 shows that this difference decreases when the GSI increases. Nevertheless, this difference appears to be relevant only for low quality rock masses, which on the other hand, develop larger plastic strains.

Hence, according to these results, it can be assumed that the resulting LDP is affected by both HM conditions and plastic behaviour. Therefore, performing HM coupled models that reproduce the plastic behaviour of rock masses may be relevant to achieve a safe design of tunnels in some cases.

Nonetheless, note that even if the normalised values are similar, the actual magnitudes of the displacements may be significantly different, since the value of the maximum radial displacements $u_{r,max}$ changes for different HM conditions. This is caused by the forces exerted by the seepage that flows into the tunnel, causing different pore pressures that will result in different deformations (Nam and Bobet, 2007) (see Figure 3.1).

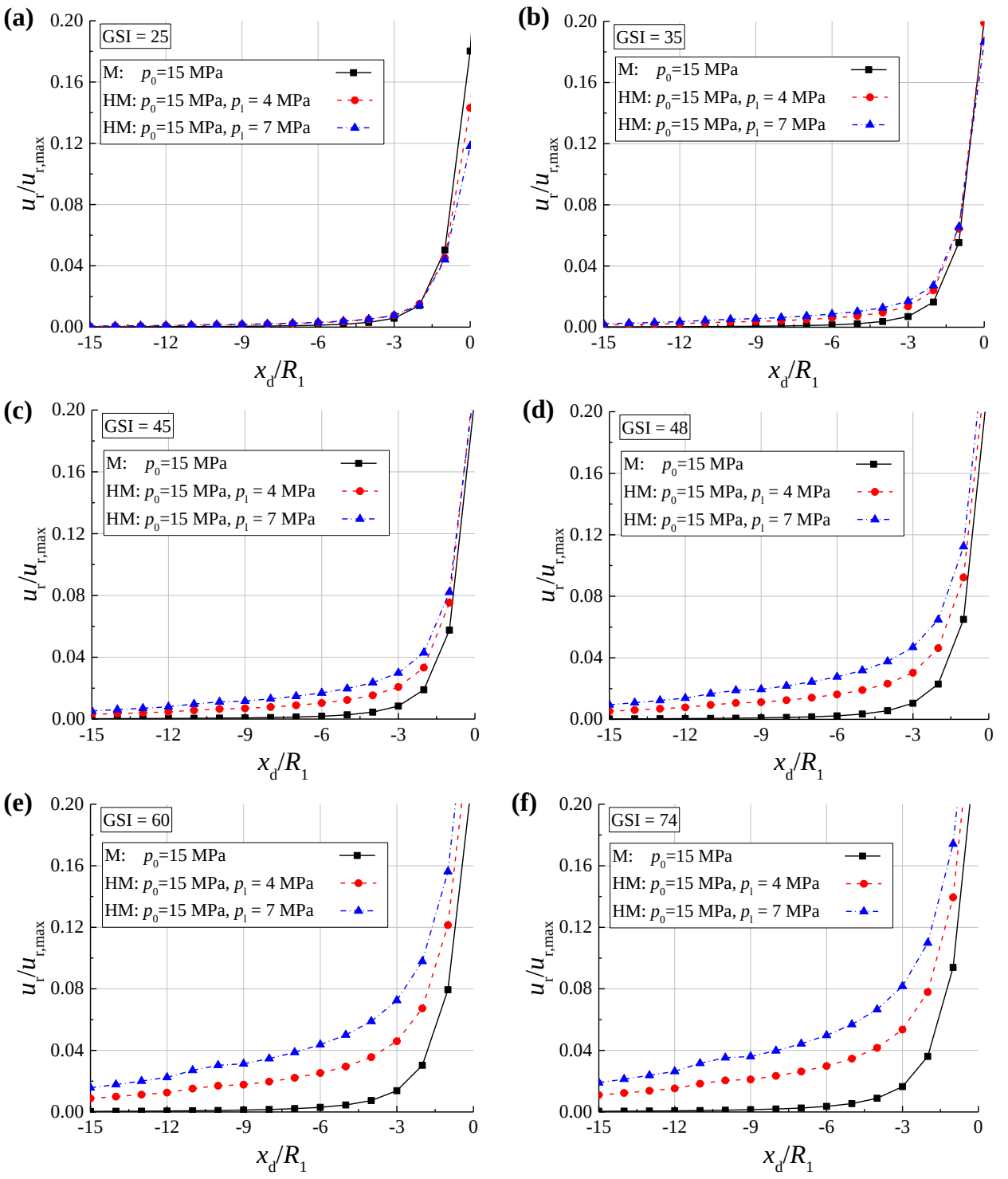

Figure 3.23. Normalized radial displacements along the tunnel wall ($r = R_1$) versus normalized distance to the tunnel face (x_d / R_1), ahead of the tunnel face ($x_d < 0$): **(a)** GSI = 25; **(b)** GSI = 35; **(c)** GSI = 45; **(d)** GSI = 48; **(e)** GSI = 60; and **(f)** GSI = 74. M and HM represent mechanical and hydro-mechanical problems, respectively.

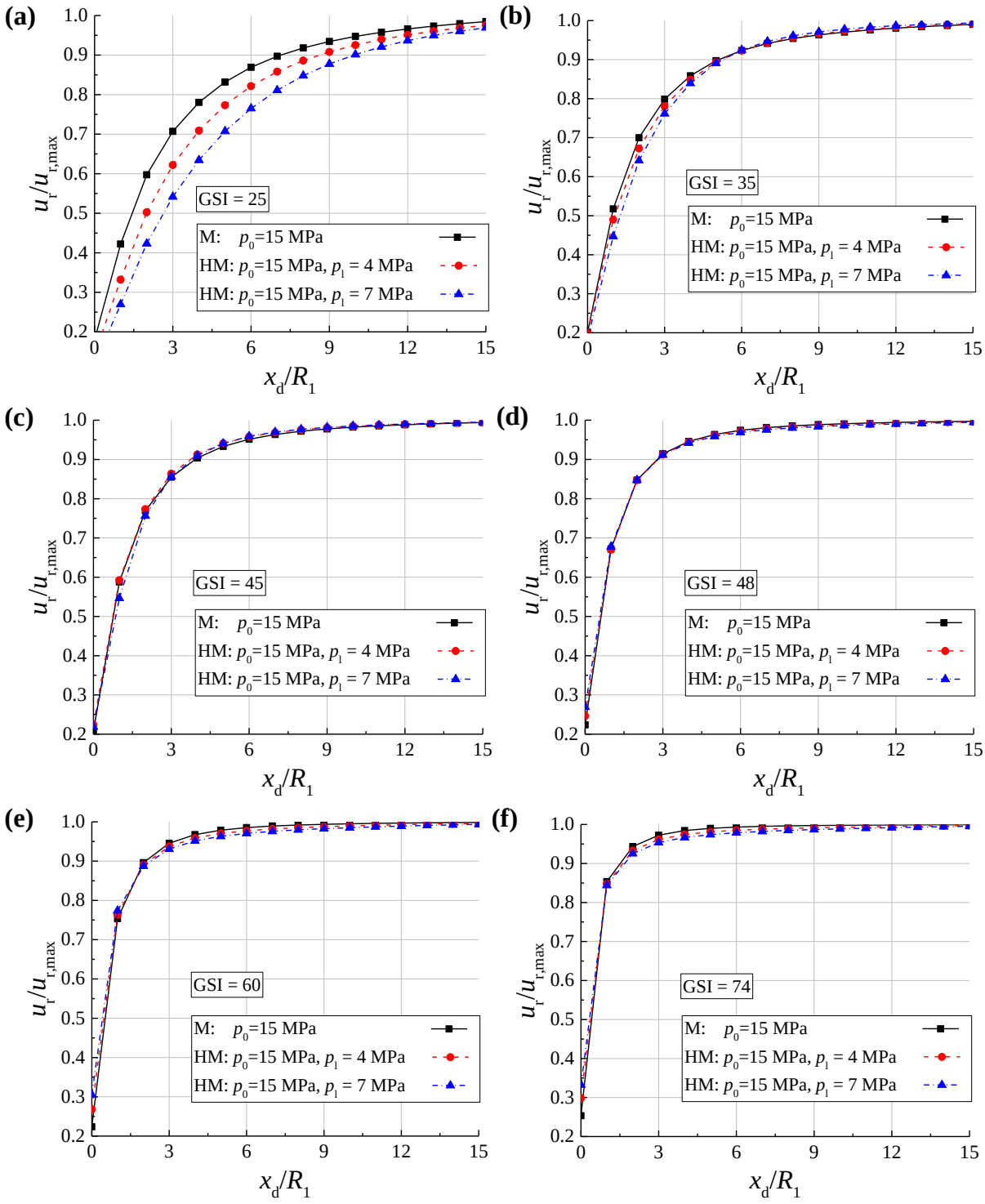

Figure 3.24. Normalized radial displacements along the tunnel wall ($r = R_1$) versus normalized distance to the tunnel face (x_d / R_1), behind the tunnel face ($x_d > 0$): **(a)** GSI = 25; **(b)** GSI = 35; **(c)** GSI = 45; **(d)** GSI = 48; **(e)** GSI = 60; and **(f)** GSI = 74. M and HM represent mechanical and hydro-mechanical problems, respectively.

In addition, for a better understanding of the deformation patterns in the surrounding rock masses, Figure 3.25 presents the contours of the radial displacements (displacements in the *x* direction) at the moment after completion of the final tunnel face excavation (*i.e.* standstill time (Prassetyo and Gutierrez, 2018b) equal to 0). Since the deformation patterns are similar for different rock mass qualities, only the results corresponding to GSI = 25 (see Table 3.1) are presented. In Figure 3.25, it can be observed that the radial displacements increase with the increase of the distance to the tunnel face (x_d), due to the decreasing fictitious support forces from the tunnel face (Cui et al., 2015; Song and Rodriguez-Dono, 2021). Moreover, the maximum radial displacements ($u_{r,max}$) are different between different HM conditions, since bigger liquid pressures (p_l) can result in bigger $u_{r,max}$, because bigger seepage forces occur.

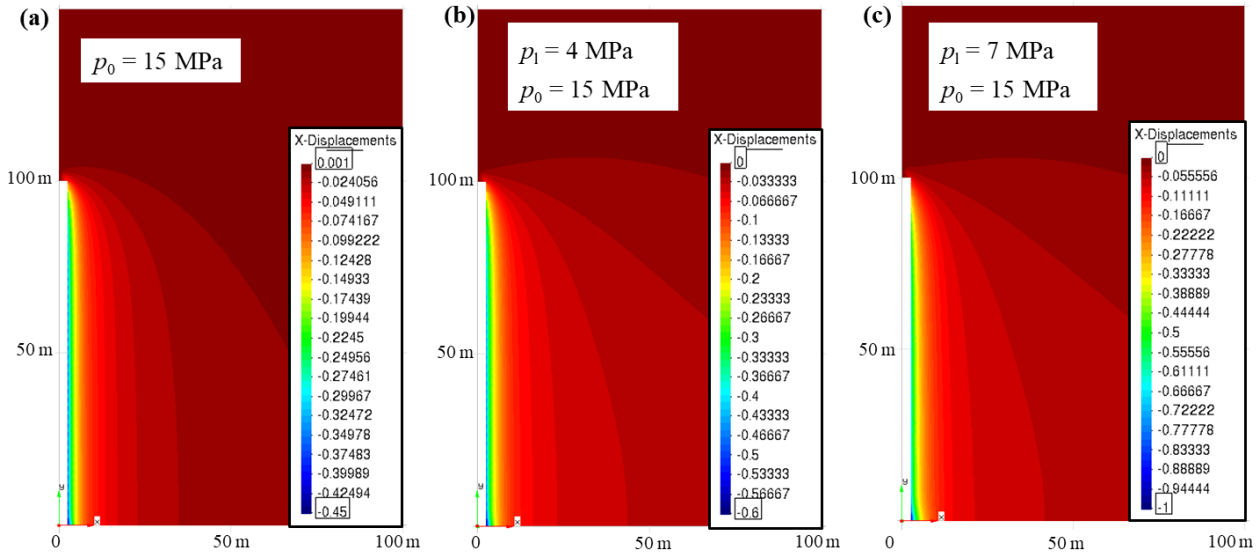

Figure 3.25. Contours of radial displacements at the end of the excavation, for **(a)** mechanical problems, **(b)** hydro-mechanical problems, p_l = 4 MPa, and, **(c)** hydro-mechanical problems, p_l = 7 MPa. Rock masses type: GSI = 25 in Table 3.1. Isotropic initial stresses: p_0 = 15 MPa.

3.6.2. Empirical solutions of the LDP for saturated problems with plastic response

This study shows a numerical approach of obtaining LDP for saturated ground with plastic response. However, it should be noted that the numerical modelling procedure may be complicated and may pose difficulties for use in tunnelling design. Therefore, by fitting the large number of data obtained from numerical simulations, this section presents empirical solutions of LDP for steady-state problems with plastic response.

In these numerical simulations, the information regarding geometry, boundary conditions, excavation process and mesh type is the same as in section 3.5.2 (see Figures 3.13 and 3.19). A wide range of material properties, initial stresses (p_0) and liquid pressures (p_l) have been adopted: in total, eight different HM cases (see Table 3.5) and six rock masses of different quality (see Table 3.1) are considered. The intrinsic permeability chosen is 10^{-10} m^2 (a big enough value and, thus, steady-state drained conditions).

Table 3.5. Hydro-mechanical conditions.

Cases	p_0 (MPa)	p_l (MPa)	p' (MPa)	p_l/p'
1	20	4	16	0.25
2	15	4	11	0.364
3	15	5	10	0.5
4	10	3.5	6.5	0.538
5	11	4	7	0.571
6	15	6	9	0.667
7	15	7	8	0.875
8	10	5	5	1

Note that the LDP expressions in this section are developed under steady-state pore pressure conditions, which means that consolidation involving dissipation of pore pressure is not considered (Nam and Bobet, 2007; Paraskevopoulou, 2016; Paraskevopoulou and Diederichs,

2018). Although the steady-state LDP solutions may oversimplify the excavation-induced coupled hydro-mechanical interaction, it may be meaningful to the preliminary design of tunnels (Nam and Bobet, 2007) and to the improvement of the CCM.

3.6.2.1. Fitting variables chosen and their normalisation

Vlachopoulos and Diederichs (2009) developed an expression of the LDP for mechanical problems with plastic response (see Eq. (3.21)) in which the normalised radial displacements ($u_r/u_{r,max}$) depend on the normalised maximum plastic radius (R_p/R_1) and the normalised distance to the tunnel face (x_d/R_1), where R_1 is the tunnel radius. On the other hand, Nam and Bobet (2007) proposed an expression of the LDP for steady-state saturated problems with elastic response (see Eq. (3.22)), in which the normalised radial displacements ($u_r/u_{r,max}$) depend on the normalised distance to the tunnel face (x_d/R_1) and the normalised liquid pressure (p_l/p'), where p' represents the effective stresses.

Instead, in this study, empirical solutions of LDP for steady-state saturated problems with plastic response have been developed. Therefore, the expressions of the normalised radial displacements ($u_r/u_{r,max}$) for this problem can be obtained through introducing p_l/p' into the LDP expressions of Vlachopoulos and Diederichs (2009), or through introducing R_p/R_1 into the LDP expressions of Nam and Bobet (2007). After that, three normalised fitting variables – p_l^*: p_l/p'; R_p^*: R_p/R_1; x_d^*: x_d/R_1– have been taken as the key variables to represent the normalised radial displacements ($u_r/u_{r,max}$) for steady-state HM problems with plastic response.

3.6.2.2. Steps taken to obtain the LDP expression

In order to obtain the LDP expressions for steady-state problems with plastic response, a theoretical analysis of the LDP expressions found in the literature (Nam and Bobet, 2007; Vlachopoulos and Diederichs, 2009) have been carried out. Meanwhile, a multitude of tests have

been performed to investigate the effect of the three independent variables ($p_l^*: p_l/p'$; $R_p^*: R_p/R_1$; $x_d^*: x_d/R_1$) to the dependent variable ($u_r/u_{r,max}$).

Ahead of the tunnel face ($x_d < 0$), the LDP for mechanical problems with plastic response can be expressed as in Eq. (3.21), while the LDP for steady-state HM problems with elastic response can be expressed as in Eq. (3.22) (Nam and Bobet, 2007).

Note that Eq. (3.21) can be expressed in the following form (M-P stands for mechanical-plastic):

$$A_1^{M\text{-}P} \exp\left(A_2^{M\text{-}P} x_d^* + A_3^{M\text{-}P} R_p^*\right)$$

While Eq. (3.22) can be expressed in the following form (HM-E stands for hydro-mechanical-elastic):

$$A_1^{HM\text{-}E} \exp\left(A_2^{HM\text{-}E} x_d^*\right) + A_3^{HM\text{-}E}\left[1-\exp\left(A_5^{HM\text{-}E} p_l^*\right)\right]\exp\left(A_4^{HM\text{-}E} x_d^*\right)$$

Combining Eqs. (3.21) and (3.22), and then introducing a new term to account for coupling effect between plastic behaviour and liquid pressures, the LDP expression for saturated problems with plastic response can result as that shown in Eq. (3.24). Note that, when working on elastic conditions, then $R_p^* = 1$ (*i.e.* $\exp\left(A_7 R_p^* - A_7\right) = 1$) and, hence, the proposed LDP can be reduced to the expression of Nam and Bobet (2007) for elastic problems.

$$\left\{A_1 \exp\left(A_2 R_p^* + A_3 x_d^*\right) + A_4\left[1-\exp\left(A_5 p_l^*\right)\right]\exp\left(A_6 x_d^*\right)\right\}\exp\left(A_7 R_p^* - A_7\right) \qquad (3.24)$$

Regarding the LDP behind the tunnel face ($x_d \geq 0$), the LDP for mechanical problems with plastic response can be expressed in the following form: $1-\left[1-B_1^{M\text{-}P}\exp\left(B_2^{M\text{-}P} R_p^*\right)\right]\exp\left(B_3^{M\text{-}P}\dfrac{x_d^*}{R_p^*}\right)$. Then, taking this expression and adding new terms to account for the effect of p_l^*, the LDP expression for saturated problems with plastic response has been proposed, as shown in Eq. (3.25). Note that, when working on dry conditions, then $p_l^* = 0$

(*i.e.* $\exp\left(\mathrm{B}_7\, p_{\mathrm{l}}^*\right)$ = 1) and, hence, the proposed LDP can be reduced to the expression of Vlachopoulos and Diederichs (2009) for mechanical problems.

$$\left\langle 1-\left\{1-\mathrm{B}_1 \exp\left[\mathrm{B}_2\left(R_{\mathrm{p}}^*\right)^{\mathrm{B}_3}+\mathrm{B}_4\, p_{\mathrm{l}}^*\right]\right\}\exp\left[\mathrm{B}_5\left(\frac{x_{\mathrm{d}}^*}{R_{\mathrm{p}}^*}\right)^{\mathrm{B}_6}\right]\right\rangle \exp\left(\mathrm{B}_7\, p_{\mathrm{l}}^*\right) \tag{3.25}$$

In summary, through theoretical analysis and tests, the LDP expression of Eq. (3.26) is proposed for steady-state saturated problems with plastic response. Moreover, the proposed expression have been verified afterwards (see Figure 3.27 in section 3.6.2.3).

$$\frac{u_r}{u_{\mathrm{r,max}}}=\begin{cases}\left\{\mathrm{A}_1 \exp\left(\mathrm{A}_2\, R_{\mathrm{p}}^*+\mathrm{A}_3\, x_{\mathrm{d}}^*\right)+\mathrm{A}_4\left[1-\exp\left(\mathrm{A}_5\, p_{\mathrm{l}}^*\right)\right]\exp\left(\mathrm{A}_6\, x_{\mathrm{d}}^*\right)\right\}\exp\left(\mathrm{A}_7\, R_{\mathrm{p}}^*-\mathrm{A}_7\right), & x_{\mathrm{d}}^*<0 \\ \left\langle 1-\left\{1-\mathrm{B}_1 \exp\left[\mathrm{B}_2\left(R_{\mathrm{p}}^*\right)^{\mathrm{B}_3}+\mathrm{B}_4\, p_{\mathrm{l}}^*\right]\right\}\exp\left[\mathrm{B}_5\left(\frac{x_{\mathrm{d}}^*}{R_{\mathrm{p}}^*}\right)^{\mathrm{B}_6}\right]\right\rangle \exp\left(\mathrm{B}_7\, p_{\mathrm{l}}^*\right), & x_{\mathrm{d}}^*\geq 0\end{cases} \tag{3.26}$$

where R_{p}^*, x_{d}^*, and p_{l}^* represent the normalised maximum plastic radius, the normalised distance to the tunnel face and the ratio between the liquid pressure and the effective stress, respectively; A_i and B_i (i=1–7) are undetermined coefficients in the empirical solutions of the LDP.

3.6.2.3. Fitting procedure and results of the empirical solutions

To get the undetermined coefficients (A_i, B_i, with i = 1–7) in Eq. (3.26), we have made a multitude of numerical models in CODE_BRIGHT with different material properties (Table 3.1) and different HM boundary conditions (Table 3.5), finally obtaining 2016 data sets (named training data hereinafter). Substituting all training data (dots in Figure 3.26) into Eq. (3.26), and doing a data regression analysis using the least squares method (data fit), 14 parameters (A_i and B_i, i =1–7) have been determined with minimum fitting errors. Table 3.6 provides the fitting results of the coefficients of Eq. (3.26). Figure 3.26 illustrates the comparison between the normalised LDP from numerical simulations and the proposed empirical formula –Eq. (3.26)–.

In the fitting procedure, the indicator $\bar{R}^2$ (the adjusted coefficient of determination), is introduced to evaluate the fitting accuracy. $\bar{R}^2$ is the statistical measure that shows the proportion of variation explained by the estimated regression line. The closer $\bar{R}^2$ is to 1.0, the closer the fitted formulas are to the training data (Song et al., 2018b). Comparing the lines obtained by empirical solutions and the dots obtained from the numerical simulations (Figure 3.26), a good agreement between them can be found ($\bar{R}^2 \cong 0.993$ for the case of $x_d^* < 0$, while $\bar{R}^2 \cong 0.997$ for the case of $x_d^* \geq 0$).

It should be noted that in the fitting procedure, the normalised liquid pressure (p_l/p') varies from 0.25 to 1.0, the normalised maximum plastic radius ($R_{p,max}/R_1$) varies from 1.0 to 6.46, and the normalised distance to the tunnel face (x_d/R_1) varies from -22.0 to 20.0, approximately. Hence, the accuracy of the proposed empirical formulas –Eq. (3.26)– would be acceptable in this range of input parameters. In summary, the calibrated parameters of Eq. (3.26) correspond to a set of different rock quality types (Table 3.1) and tunnel conditions (Case 1 to 8, Table 3.5). Note that the proposed empirical solutions in Eq. (3.26) are developed for steady-state saturated conditions.

In order to further investigate the deviation between the proposed empirical solutions of the LDP and other numerical results, we have randomly adopted some data (named test data) different from the set used in the fitting procedure, and compared the result with that of Eq. (3.26) –in the form of lines–. Figure 3.27 compares the test data obtained from the numerical simulations (dots) with the proposed empirical solutions (lines). As it can be observed, the predictions from the proposed empirical solutions compare reasonably well with the numerical results, both behind ($x_d > 0$) and ahead ($x_d < 0$) of the tunnel face. Therefore, it can be concluded that the proposed empirical solutions of the LDP exhibit almost the same accuracy as the numerical simulations for predicting the longitudinal deformation profiles of tunnels excavated in the HM framework under steady-state drained condition. Hence, for practical use in engineering, these empirical solutions provide a convenient alternative method for calculating the LDP in saturated rock masses showing plastic behaviour, given the aforementioned range of parameters.

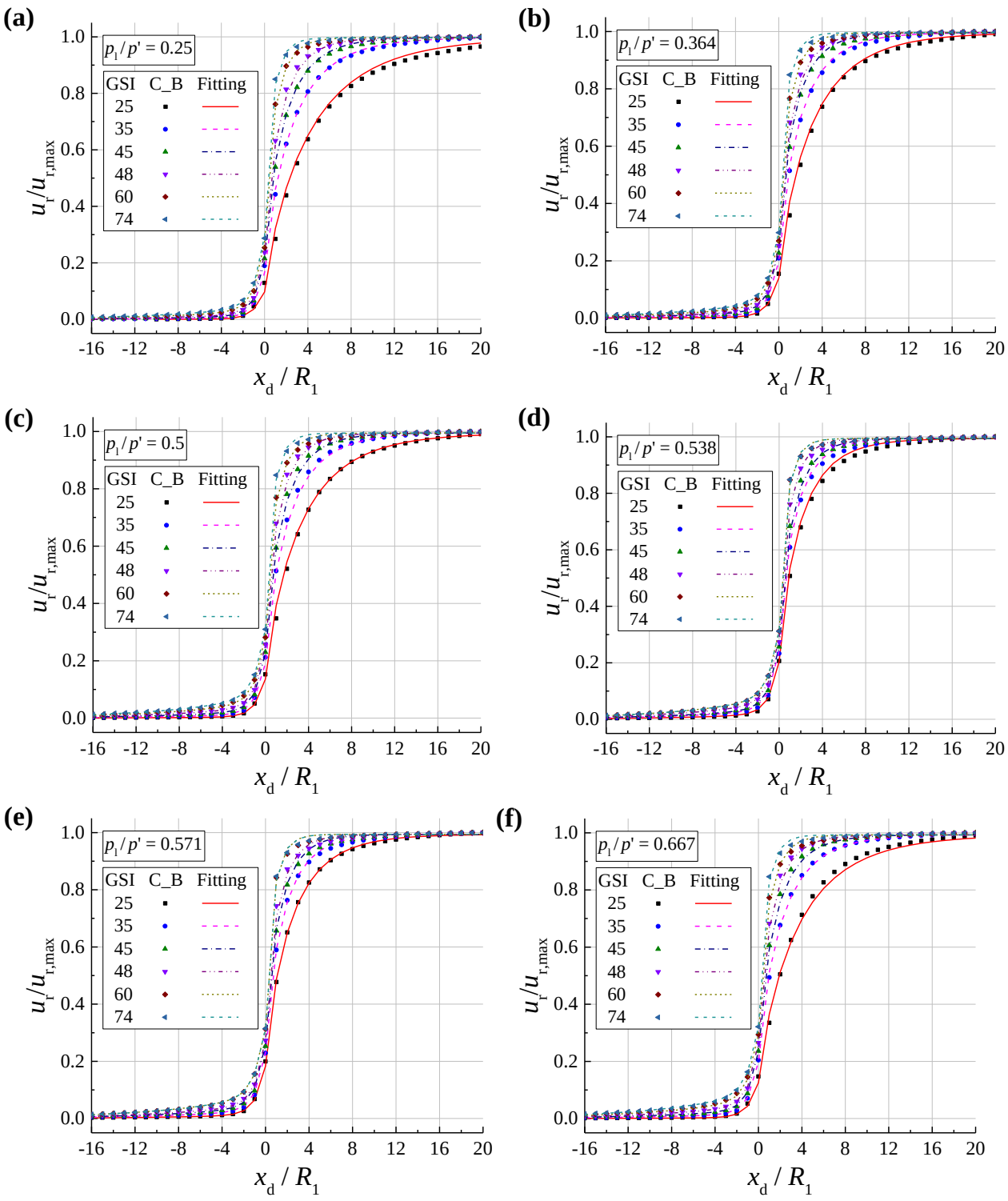
(a)
p_i/p' = 0.25
(b)
p_i/p' = 0.364
(c)
p_i/p' = 0.5
(d)
p_i/p' = 0.538
(e)
p_i/p' = 0.571
(f)
p_i/p' = 0.667
GSI C_B Fitting
25
35
45
48
60
74
$u_r/u_{r,max}$
x_d / R_1

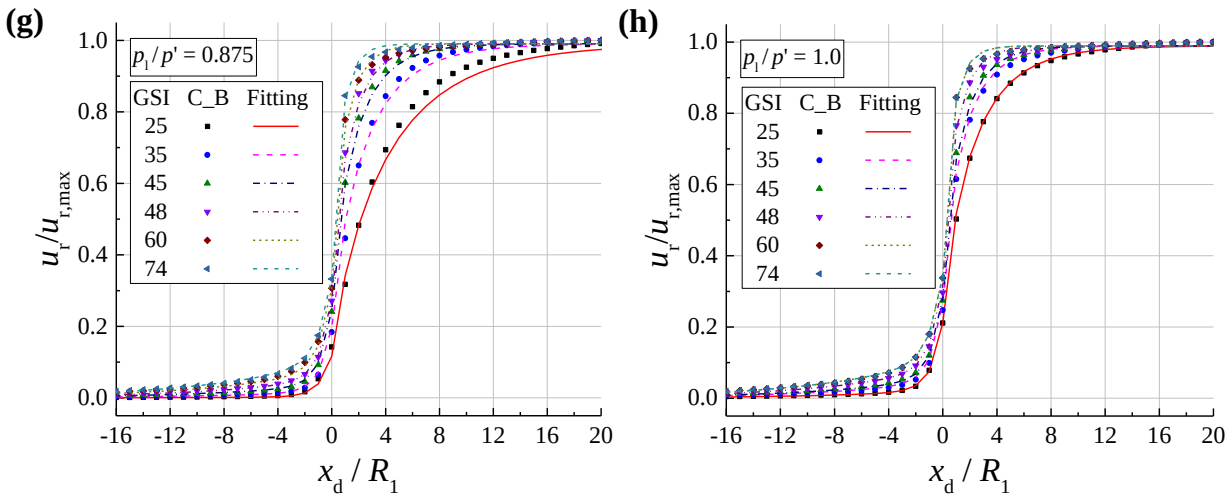

Figure 3.26. Comparison between the normalized longitudinal deformation profiles from numerical simulations (C_B: CODE_BRIGHT) and the proposed equation for cases 1 – 8 in Table 3.5: **(a)** case 1, **(b)** case 2, **(c)** case 3, **(d)** case 4, **(e)** case 5, **(f)** case 6, **(g)** case 7 and **(h)** case 8. Six different quality rock masses (shown in Table 3.1) are considered for every case. These numerical results are adopted in the function fitting.

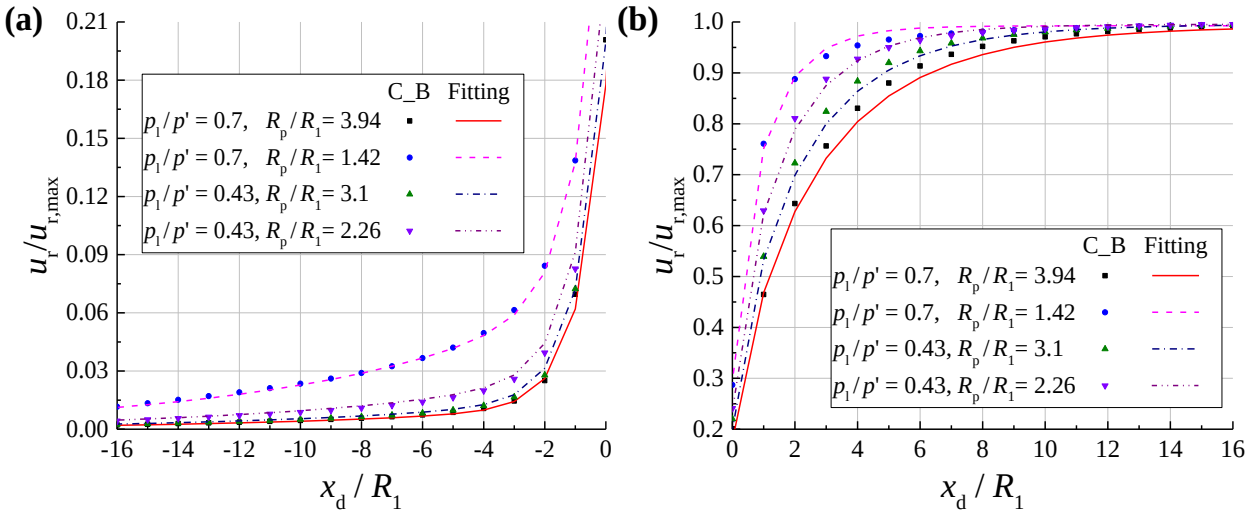

Figure 3.27. Comparison between the normalised longitudinal deformation profiles from numerical simulations (C_B: CODE_BRIGHT) and the proposed empirical equations (Eq. (3.26)): **(a)** ahead of the tunnel face (x_d < 0) and **(b)** behind the tunnel face (x_d > 0). The input parameters are randomly selected (different from the training data).

Table 3.6. Coefficients in Eq. (3.26).

A_1	A_2	A_3	A_4	A_5	A_6	A_7
0.1439	0.5344	1.1661	0.1435	-1.6493	0.1177	-0.6785
B_1	B_2	B_3	B_4	B_5	B_6	B_7
0.3422	-0.1982	1.0120	0.2071	-1.4456	0.8658	-0.0107

3.7. Summary and discussion

This study aims to provide a general and robust numerical approach to the geomechanical analysis of tunnels excavated in saturated ground with plastic behaviour. For the sake of numerical reliability and efficiency, a smoothed excavation (SE) method has been firstly introduced and implemented into the finite element method software CODE_BRIGHT. Then, hydro-mechanical (HM) modelling and analyses of the longitudinal deformation profiles (LDP) in saturated rock masses with plastic behaviour have been carried out. Finally, empirical solutions of the LDP have been proposed using data fit, which can conveniently predict the tunnel radial deformations for steady-state hydro-mechanical problems.

The generalised Darcy's law and the elastic-viscoplastic material model have been adopted to simulate the hydraulic and mechanical behaviour of rock masses, respectively. Furthermore, the Mohr-Coulomb failure criterion and a non-associated plastic flow rule have been considered. After that, the SE method is used in the excavation process, and thus, the stresses of the corresponding excavation elements are reduced smoothly. As a verification step, the uniqueness principle of the proposed excavation method for multi-stage excavation has been checked. The analysis made shows that the proposed SE method benefits the numerical convergence and improves computational efficiency, especially for problems with material models and boundary conditions that are relatively complex.

After that, the CODE_BRIGHT results for the LDP using the proposed SE method have been compared with elastic-plastic solutions for mechanical (M) problems, and with elastic solutions for HM problems. Then, HM modelling and analysis of the LDP for saturated rock masses with

plastic behaviour has been carried out. The effects of the rock mass geotechnical quality (GSI) and the HM conditions on the resulting radial tunnel deformations have been analysed. We have observed that the difference in normalised radial displacements ahead of the tunnel face ($x_d < 0$) between the three cases studied –one M case and two HM cases– grows as the GSI increases. However, behind the tunnel face ($x_d > 0$), this difference decreases when the GSI increases. Therefore, to achieve a safe tunnel design, it might be important to take into account both the plastic and the HM response.

Finally, based on a large amount of numerical data corresponding to a wide range of rock mass qualities and HM conditions, the empirical solutions of the LDP for steady-state HM problems with plastic response have been obtained by function fitting. A good agreement between the empirical prediction and the results from CODE_BRIGHT simulations has been obtained. Therefore, the proposed empirical solutions for LDP may constitute an alternative and convenient method for preliminary tunnel analysis and design.

Note that, even if the proposed method in this study can simulate different cases of tunnels excavated in hydro-mechanical saturated rock masses with plastic response, it still has some limitations. For instance, the numerical analyses are carried out through homogeneous material models and the proposed empirical solutions of LDP are only useful for steady-state conditions.

Chapter 4. Coupled solid-fluid response of tunnels excavated in saturated rock masses with a time-dependent plastic behaviour

Based on the submitted manuscript:

Fei Song, Alfonso Rodriguez-Dono, Sebastia Olivella, Antonio Gens. Hydro-mechanical analyses of longitudinal deformation profiles for tunnels excavated in saturated Burgers-viscoplastic strain-softening rock masses. Submitted to <Applied Mathematical Modelling>.

Abstract

This study provides a general numerical approach for modelling the response of tunnels excavated in saturated time-dependent plastic rock masses, considering a coupled solid-fluid interaction and time-dependent plastic behaviour. In order to do that, a Burgers-viscoplastic strain-softening model has been developed and implemented into the finite element method software CODE_BRIGHT, and a coupled solid-fluid model is used to simulate the interaction between solid deformations and fluid flow. Parametric analyses are then performed to analyse the influence on the tunnelling response of different time-dependent models, different standstill times and different excavation rates. It has been observed that the time-dependent model selection is crucial to simulate the response of underground excavations. Additionally, the coupled solid-fluid results are significantly different from the purely mechanical ones. The liquid pressure build-up in the vicinity of the tunnel face and the overpressure dissipation with time due consolidation can be accounted for. Moreover, the higher the excavation rate, the larger build-up of liquid pressures occurs.

4.1. Introduction

The multi-physics multi-phases coupling problems concerning mass transport, fluid flow and solid deformations are of significance in engineering applications, such as nuclear waste repositories, geological carbon storage, geothermal energy or underground excavation. Multi-

stage underground excavation in saturated ground is a characteristic process in many geotechnical applications. In some cases, the surrounding rock masses can deform gradually, showing large delayed deformations that may lead to creep-induced failure (Damjanac and Fairhurst, 2010; Eberhardt et al., 1999; Fabre and Pellet, 2006; Song et al., 2020). A better understanding of the time-dependency, damage evolution and creep-induced failure response is a topic of considerable interest in rock mechanics. Furthermore, the effect of the coupled solid-fluid response cannot be ignored when a underground excavation is performed below the water table (Guayacan-Carrillo et al., 2017; Nam and Bobet, 2007; Prassetyo and Gutierrez, 2018b; Yuan and Harrison, 2005). Therefore, a comprehensive analysis of the entire process of multi-stage excavation incorporating time-dependent plastic behaviour of geomaterials and the coupled solid-fluid interaction is crucial to perform a proper numerical simulation of underground excavation problems.

Empirical, analytical or numerical methods has been widely used in tunnelling design (Alejano et al., 2012; Bobet, 2009; Cai, 2008; Chen et al., 2019; Debernardi and Barla, 2009; Do et al., 2020; Galli et al., 2004; Kargar and Haghgouei, 2020; Lin et al., 2019; Lin et al., 2020; Paraskevopoulou and Diederichs, 2018; Sakurai, 2010; Shin et al., 2002; Song and Rodriguez-Dono, 2021; Song et al., 2020; Song et al., 2018a and 2018b; Unlu and Gercek, 2003; Vlachopoulos and Diederichs, 2009; Vu et al., 2013; Wang et al., 2019; Wang and Nie, 2010; Wang et al., 2018e; Zareifard, 2018). Among all these methods, the convergence-confinement method (CCM) provides an efficient way to determine support forces by considering the ground-structure interaction (Alejano et al., 2010; Alejano et al., 2012). The CCM consists of three basic components in the form of graphs: the ground reaction curve (GRC), the longitudinal deformation profile (LDP) and the support characteristic curve (SCC) (Alejano et al., 2010; Carranza-Torres and Fairhurst, 2000; Song and Rodriguez-Dono, 2021; Song et al., 2020). The main focus of this study is to analyse solid deformations (*i.e.* LDP) and fluid flows in longitudinal multi-stage excavation problems, considering the coupled solid-fluid interaction, and time-dependent plastic behaviour of geomaterials.

Some researchers have studied the LDP based on field measurements or numerical simulations, but most of them are based on elastic constitutive models (Corbetta et al., 1991; Panet, 1993; Panet, 1995; Unlu and Gercek, 2003). Based on the field measured data of a tunnel in the Mingtam Power cavern project, Chern et al. (Chern et al., 1998) presented an empirical

solution of the LDP for the elastic-plastic problems. Then, by using numerical simulations, Vlachopoulos and Diederichs (2009) proposed the elastic-plastic empirical solutions of LDP that consider the influence of the ultimate plastic radius. However, these models do not seem to model correctly the post-failure behaviour for average-quality rock masses (Alejano et al., 2012; Hoek and Brown, 1997). Subsequently, considering the post-failure behaviour, Alejano et al. (2012) extended the approach of Vlachopoulos and Diederichs (2009) to the case of strain-softening rock masses representing a wider range of rock masses.

However, in all the above references, the geomaterials exhibit time-independent properties. This condition is quite different from that in real projects in which the rock masses exhibit strong time-dependent creep properties, such as in squeezing rock masses (Paraskevopoulou, 2016; Paraskevopoulou and Diederichs, 2018; Song et al., 2020; Wang et al., 2020b). Based on the Burgers-creep viscous (CVISC) model introduced by Itasca (2007 and 2008), Paraskevopoulou (2016) and Paraskevopoulou and Diederichs (2018) presented LDP simulations for time-dependent viscoelastic rock masses, but no plastic yield was considered. Moreover, in the CVISC model, the plastic slider is not coupled with the viscous dashpot, which means that the CVISC model cannot simulate creep-induced failure behaviour (Paraskevopoulou, 2016; Song et al., 2020). Recently, Song et al. (2020) proposed a viscoelastic-viscoplastic strain-softening model and programed it in a finite element method software CODE_BRIGHT (Olivella et al., 2020); this model considers the coupled behaviour of viscous and strain-softening models, which can simulate creep-induced failure response. Then, Song et al. (2020) presented analysis and modelling of the LDP for tunnelling in time-dependent plastic rock masses, but the primary creep stage behaviour cannot be simulated by their model. Thus, the proposed viscoelastic-viscoplastic strain-softening model in Song et al. (2020) cannot represent adequately the response of geomaterials with high strength or subject to low stresses.

Furthermore, the previously mentioned research about the LDP was carried out without considering the coupled solid-fluid interaction. However, when tunnels are excavated in saturated ground, the coupled solid-fluid response of geomaterials is important for estimating the tunnelling behaviour (Guayacan-Carrillo et al., 2017; Nam and Bobet, 2007; Paraskevopoulou and Diederichs, 2018). Nam and Bobet (2007) proposed empirical best-fit solutions for the LDP for saturated ground with steady-state flow condition. Furthermore, considering coupled

interactions between solid deformations and fluid flows, Prassetyo and Gutierrez (2018) proposed a LDP for predicting time-dependent radial displacements along the tunnel axis. However, the surrounding rock masses were assumed as linear elastic materials for the coupled solid-fluid problems (Prassetyo and Gutierrez, 2018b). In chapter 3 of this thesis, we presented empirical best-fit solutions of the LDP for tunnelling in saturated ground using an elastic-perfectly-plastic constitutive model and assuming a steady-state fluid flow, but without considering time-dependent behaviour. However, the LDP heavily depends on both the behaviour model selected (Alejano et al., 2012; Paraskevopoulou, 2016; Paraskevopoulou and Diederichs, 2018; Song and Rodriguez-Dono, 2021; Song et al., 2020) and the coupled solid-fluid interaction (Nam and Bobet, 2007; Prassetyo, 2017; Prassetyo and Gutierrez, 2018b).

In summary, research on the underground excavation problems has been mostly concentrated on purely mechanical problems, or the coupled solid-fluid problems but with simpler constitutive models. Instead, in this article, we present the coupled solid-fluid modelling of multi-stage underground excavation in time-dependent plastic geomaterials, with consideration of (1) time-dependent creep properties of geomaterials, including the primary, secondary and accelerated creep responses, (2) post-failure behaviour models, which can represent elastic-perfectly, elastic-brittle and strain-softening behaviour, (3) the coupling between creep and damage evolution, thus simulating creep-induced failure behaviour, and (4) coupled interaction between solid deformations and fluid flows.

4.2. Theoretical background

4.2.1. Theoretical background for solid deformations

4.2.1.1. Rock mechanics

Experimental creep tests show that the time-dependent behaviour deformation of rocks accounts for a large amount of the total displacements (Chu et al., 2019; Paraskevopoulou, 2016; Paraskevopoulou and Diederichs, 2018; Song et al., 2020; Song et al., 2018a and 2018b; Sulem et

al., 1987). Time dependency (or creep behaviour) results in delayed deformation, which must be taken into account to design underground projects more accurately and safely (Paraskevopoulou, 2016; Paraskevopoulou and Diederichs, 2018).

Moreover, the creep-induced failure behaviour of geomaterials may be relevant, as some underground structures do not fail during the excavation process, but ultimately fail after a long-term (Fabre and Pellet, 2006; Sandrone and Labiouse, 2010; Song et al., 2020). Thus, time-dependent plastic behaviour, especially the creep-induced failure response of geomaterials, is a topic of considerable interest in rock mechanics.

As shown in Figure 4.1, the typical creep response of rocks may usually be characterised by four stages under a constant applied load (Paraskevopoulou, 2016; Paraskevopoulou and Diederichs, 2018; Song et al., 2020; Sterpi and Gioda, 2009):

1. Instantaneous elastic response: the reversible elastic strain occurs instantaneously upon loading.

2. The primary creep stage: the strain rate decreases with time.

3. The secondary creep stage: a constant strain rate with time occurs.

4. The accelerated (or named as tertiary) creep stage: the strain rate starts to accelerate once the material reaches the yield surface.

Furthermore, the post-failure behaviour of geomaterials may play a significant role in the performance of underground excavations (Alejano et al., 2010; Alejano et al., 2009; Alejano et al., 2012; Song et al., 2020). For instance, different quality rock masses may exhibit different post-failure behaviour, as shown in Figure 4.2(a) (Alejano et al., 2012; Hoek and Brown, 1997), and the response of rock masses will differ depending on the selected model (Alejano et al., 2010; Alejano et al., 2012; Alonso et al., 2003). Note that these ranges in Figure 4.2(a) are just a reference and they may vary in some cases. The strain-softening model is adopted in this study, which can be easily simplified to purely brittle behaviour or perfectly plastic behaviour (Song et al., 2020), if desired.

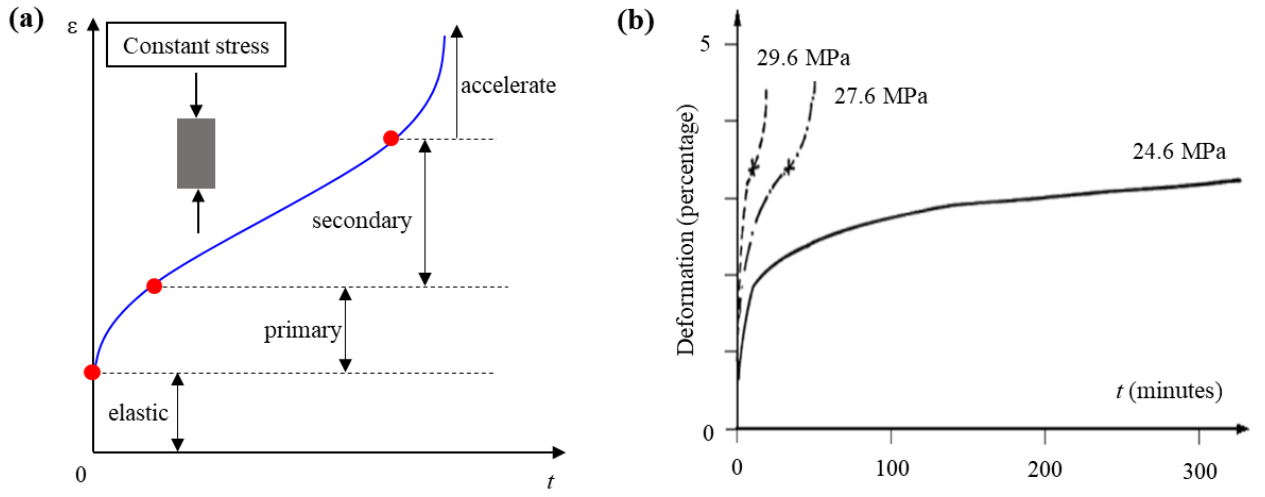

Figure 4.1. Creep response: **(a)** a conceptual model, and **(b)** experimental results specimens at different applied stresses. Based on the work of Dubey and Gairola (2008) and Ramírez Oyanguren (1966).

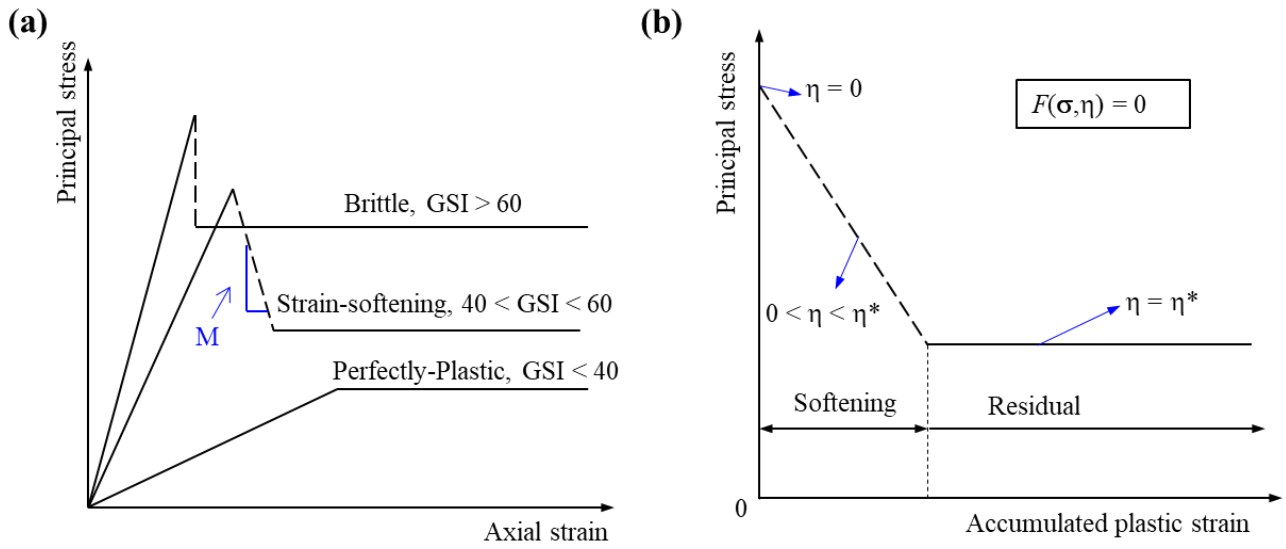

Figure 4.2. Conceptual post-failure behaviour model: **(a)** with different geological strength index (GSI), and **(b)** with a strain-softening model. Based on the work of Alejano et al. (2009, 2012), Song et al. (2020) and Song and Rodriguez-Dono (2021).

In a strain-softening model, as shown in Figure 4.2(b), the yield surfaces $F(\boldsymbol{\sigma}, \eta)$ depend on both the stress tensor $\boldsymbol{\sigma}$ and the softening parameter η. The softening parameter η describes the gradual transition from the peak yield surface to the residual failure surface, being η^* the value of the softening parameter at which the softening phase ends and the residual phase begins (Alejano et al., 2012; Song et al., 2020).

Song et al. (2020) proposed a viscoelastic-viscoplastic strain-softening model (named Maxwell-viscoplastic strain-softening or MVSS model in the following), combining the Maxwell model and the rate-dependent viscoplastic model in series. Due to the coupling between the creep deformation and the strain-softening model, the MVSS model can represent creep-induced failure (Song et al., 2020). However, the primary creep stage was neglected in the MVSS model (Song et al., 2020). However, the primary creep-induced deformations may be relevant for rock masses with high strength or subjected to low stresses (Song et al., 2018a). Hence, in the current research, by introducing the Kelvin model to the MVSS model, a new Burgers-viscoplastic strain-softening (BVSS) model has been developed. Section 4.2.1.2 shows the detailed description of the proposed BVSS model. Section 4.3 presents the numerical implementation method of the BVSS model in a finite element method (FEM) software, CODE_BRIGHT (Olivella et al., 2020).

4.2.1.2. The Burgers-viscoplastic strain-softening constitutive model

In rock mechanics, the Hookean elastic springs and the Newtonian viscous dashpot can be coupled in series or in parallel to model the time-dependent behaviour (Wang et al., 2013; Weng et al., 2010). Moreover, a plastic slider or a viscoplastic model can be used to simulate the plastic response (Paraskevopoulou, 2016; Song et al., 2020).

In the current research, a coupled Burgers-viscoplastic strain-softening (BVSS) model is proposed, consisting of a Burgers model in series with the Perzyna viscoplastic model, with the aim of representing rock behaviour more realistically. The Mohr-Coulomb strain-softening model is selected in this research. These tentative approaches are needed if, as recommended by Starfield and Cundall (1988), heuristic approaches are followed to research, analyse and understand rock mechanics problems.

Note that the BVSS model is developed to capture the critical aspects of geomaterials, which include:

1. Time-dependent properties, including the primary, secondary and accelerated creep responses.

2. Post-failure behaviour, including perfectly-plastic, strain-softening and purely-brittle models.

3. Coupled behaviour between creep response and damage evolution, so that creep-induced (or delayed) failure can be simulated.

As shown in Figure 4.3, some simpler models can be considered as particular cases of the proposed BVSS model. For example, the Burgers model can be simplified to the Maxwell model, the Kelvin model and the Generalised Kelvin model. Similarly, the rate-dependent viscoplastic model can be simplified to the purely plastic slider. Thus, the Maxwell-viscoplastic strain-softening (MVSS) model proposed in Song et al. (2020) is just a particular case of the proposed BVSS model. Figure 4.4 presents the creep response corresponding to three different mechanical models.

The total strain rate tensor of the proposed BVSS model ($\frac{d\boldsymbol{\varepsilon}}{dt}$) can be decomposed into components describing viscoelasticity ($\frac{d\boldsymbol{\varepsilon}_{\mathrm{ve}}}{dt}$) and viscoplasticity ($\frac{d\boldsymbol{\varepsilon}_{\mathrm{vp}}}{dt}$), as shown in Eq. (4.1). The viscoelasticity consists of two components: Maxwell ($\frac{d\boldsymbol{\varepsilon}_{\mathrm{M}}}{dt}$) and Kelvin ($\frac{d\boldsymbol{\varepsilon}_{\mathrm{K}}}{dt}$) parts, and the Maxwell part can be decomposed into elastic spring ($\frac{d\boldsymbol{\varepsilon}_{\mathrm{M}}^{\mathrm{e}}}{dt}$) and viscous ($\frac{d\boldsymbol{\varepsilon}_{\mathrm{M}}^{\mathrm{v}}}{dt}$) parts.

$$\begin{aligned}\frac{d\boldsymbol{\varepsilon}}{dt} &= \frac{d\boldsymbol{\varepsilon}_{\mathrm{ve}}}{dt} + \frac{d\boldsymbol{\varepsilon}_{\mathrm{vp}}}{dt} = \frac{d\boldsymbol{\varepsilon}_{\mathrm{M}}}{dt} + \frac{d\boldsymbol{\varepsilon}_{\mathrm{K}}}{dt} + \frac{d\boldsymbol{\varepsilon}_{\mathrm{VP}}}{dt} \\ &= \frac{d\boldsymbol{\varepsilon}_{\mathrm{M}}^{\mathrm{e}}}{dt} + \frac{d\boldsymbol{\varepsilon}_{\mathrm{M}}^{\mathrm{v}}}{dt} + \frac{d\boldsymbol{\varepsilon}_{\mathrm{K}}}{dt} + \frac{d\boldsymbol{\varepsilon}_{\mathrm{VP}}}{dt}\end{aligned} \tag{4.1}$$

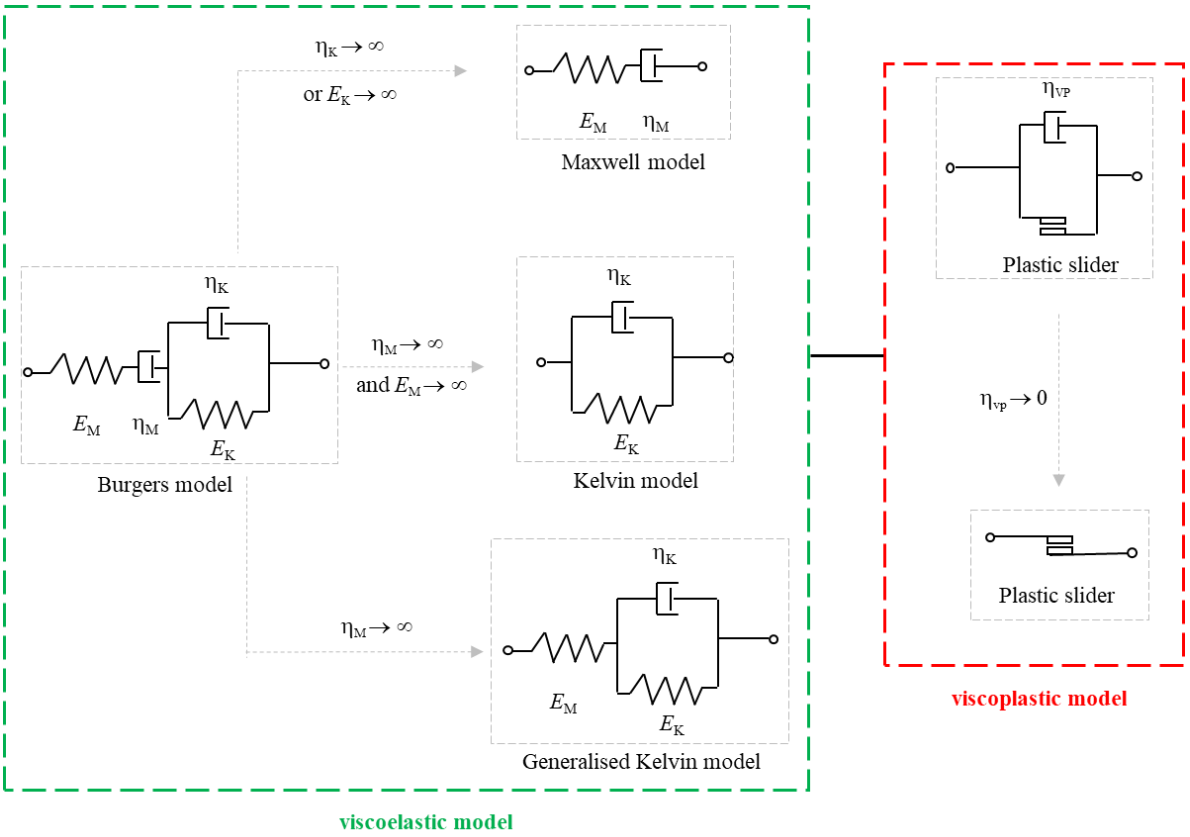

Figure 4.3. The proposed Burgers-viscoplastic strain-softening (BVSS) model for geomaterials.

The strain rates corresponding to Maxwell, Kelvin and viscoplastic models can be expressed as in Eqs. (4.2)-(4.4), respectively.

$$\frac{d\boldsymbol{\varepsilon}_M}{dt} = \frac{d\boldsymbol{\varepsilon}_M^e}{dt} + \frac{d\boldsymbol{\varepsilon}_M^v}{dt} = \mathbf{C}_M^e \frac{d\boldsymbol{\sigma}'}{dt} + \frac{\boldsymbol{\sigma}'}{\eta_M} = \left(\mathbf{D}_M^e\right)^{-1} \frac{d\boldsymbol{\sigma}'}{dt} + \frac{\boldsymbol{\sigma}'}{\eta_M} \tag{4.2}$$

$$\frac{d\boldsymbol{\varepsilon}_K}{dt} = \mathbf{C}_K^v(\boldsymbol{\sigma}' - \boldsymbol{\varepsilon}_K) = \left(\mathbf{D}_K^v\right)^{-1}(\boldsymbol{\sigma}' - \boldsymbol{\varepsilon}_K) \tag{4.3}$$

$$\frac{d\boldsymbol{\varepsilon}_{vp}}{dt} = \frac{1}{\eta_{vp}}\langle\Phi(F)\rangle\frac{\partial G}{\partial \boldsymbol{\sigma}'} \tag{4.4}$$

where $\mathbf{D}_i^e$ (or $\mathbf{C}_i^e$) and $\mathbf{D}_i^v$ (or $\mathbf{C}_i^v$) represent the tangent stiffness matrices (or the compliance matrices) of the elastic spring and of the viscous dashpot in the i model (i = M or K represents the

Maxwell model or the Kelvin model); η_M (or η_K) is the viscosity of the viscous dashpot in the Maxwell (or the Kelvin) model; η_{vp} is the viscosity of the viscoplastic model; F and G represent the overstress function and the viscoplastic potential, respectively, of the viscoplastic model. The symbol $<\Phi(F)>$ can be expressed as in Eq. (4.5) and $\Phi(F) = F^m$ ($m \geq 1$) (Mánica, 2018; Perzyna, 1966; Song et al., 2020) is adopted in this research.

$$<\Phi(F)> = \begin{cases} \Phi(F) & \text{if } \Phi(F) \geq 0 \\ 0 & \text{if } \Phi(F) < 0 \end{cases} \tag{4.5}$$

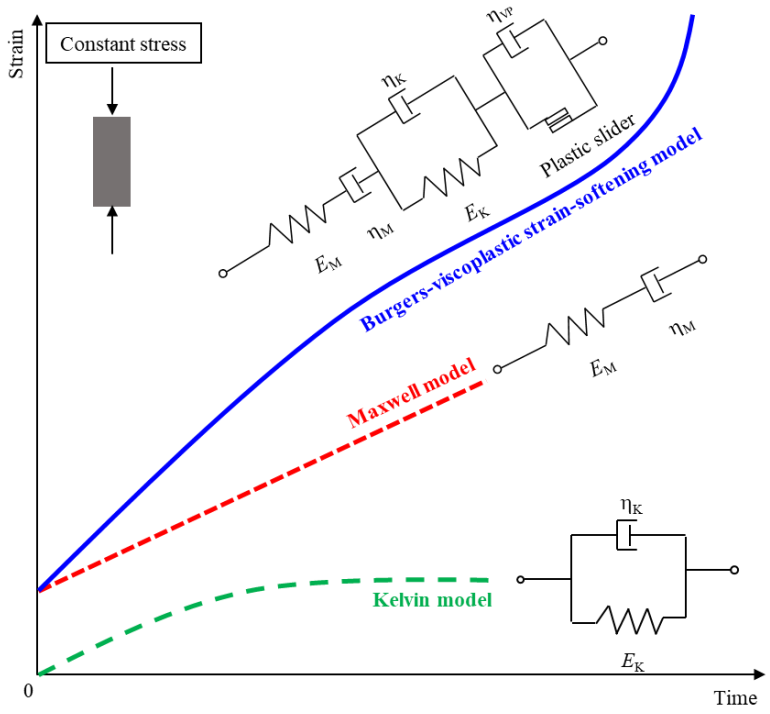

Figure 4.4. Creep response considering three different mechanical models. Based on the work of Wang et al. (2014).

The expression of the Mohr-Coulomb strain-softening model is shown in Eq. (4.6), where $c(\eta)$ and $\varphi(\eta)$ are cohesion and friction angle, respectively. p', J_2 and θ represent the mean

effective stress, the second invariant of the deviatoric stress tensor, and the Lode angle, respectively.

$$F = p^{'} \sin\varphi(\eta) + \sqrt{J_2}\left[\cos\theta - \frac{1}{\sqrt{3}} \cdot \sin\varphi(\eta)\sin\theta\right] - c(\eta)\cos\varphi(\eta) \tag{4.6}$$

The viscoplastic potential G is expressed as in Eq. (4.7), where α is a parameter for the viscoplastic potential ($0 \le \alpha \le 1$) and $\psi(\eta)$ is the dilatancy angle.

$$G = \alpha p^{'} \sin\psi(\eta) + \sqrt{J_2}\left[\cos\theta - \frac{1}{\sqrt{3}}\sin\psi(\eta)\sin\theta\right] \tag{4.7}$$

A piecewise linear plastic parameter functions of the plastic parameters $k(\eta)$ is adopted (Alejano et al., 2009; Alonso et al., 2003; Song et al., 2020), as shown in Eq. (4.8), where k can represent the cohesion c, the friction angle φ and the dilatancy angle ψ. k_{peak} and k_{res} are the peak and residual values of k, respectively. The softening parameter η is defined in Eq. (4.9), where $\boldsymbol{\varepsilon}^{\mathbf{p}}$ (or $\boldsymbol{\gamma}^{\mathbf{p}}$) represents the accumulated plastic strain and $\varepsilon_m^p = \frac{1}{3}\left(\varepsilon_x^p + \varepsilon_y^p + \varepsilon_z^p\right)$ (Mánica, 2018; Song et al., 2020).

$$\mathrm{k}(\eta) = \begin{cases} \mathrm{k}_{peak}, & \text{for } \eta < 0 \\ \mathrm{k}_{peak} + \left(\dfrac{\mathrm{k}_{res} - \mathrm{k}_{peak}}{\eta^*}\right)\eta, & \text{for } 0 \le \eta < \eta^* \\ \mathrm{k}_{res}, & \text{for } \eta \ge \eta^* \end{cases} \tag{4.8}$$

$$\eta = \sqrt{\frac{3}{2}\left[\left(\varepsilon_x^p - \varepsilon_m^p\right)^2 + \left(\varepsilon_y^p - \varepsilon_m^p\right)^2 + \left(\varepsilon_z^p - \varepsilon_m^p\right)^2 + \left(\frac{1}{2}\gamma_{xy}^p\right)^2 + \left(\frac{1}{2}\gamma_{yz}^p\right)^2 + \left(\frac{1}{2}\gamma_{zx}^p\right)^2\right]} \tag{4.9}$$

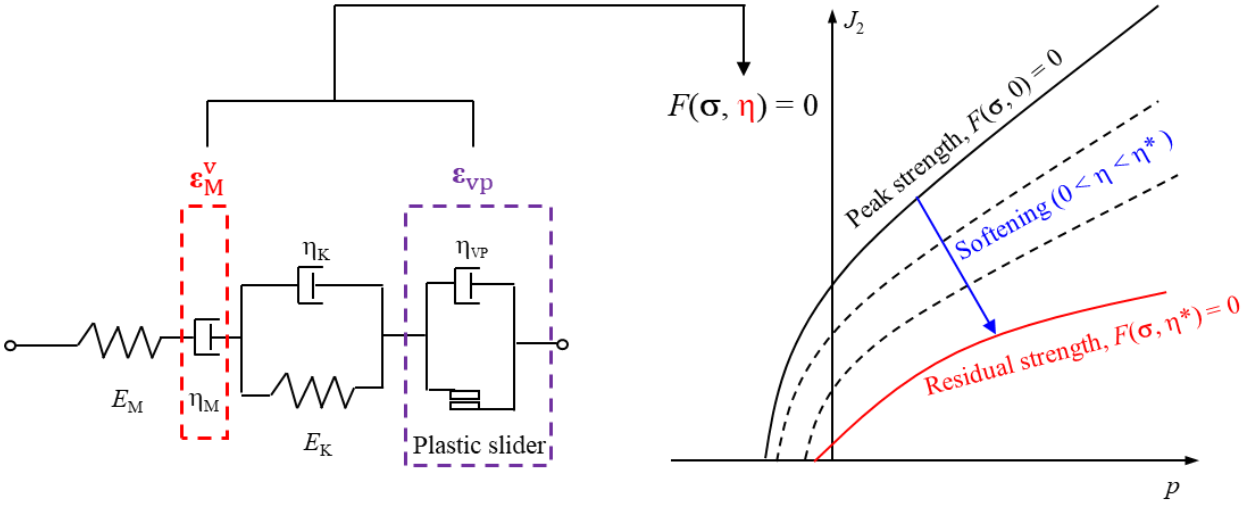

Figure 4.5. Coupling between the creep behaviour and the strain-softening behaviour in the BVSS model.

The strains developed in the viscous dashpot of the Maxwell model ($\boldsymbol{\varepsilon}_M^v$) and in the viscoplastic model ($\boldsymbol{\varepsilon}_{vp}$) are accumulated to account for the softening evolution, as shown in Figure 4.5. In that way, although the rock mass behaviour may be inside the yield surface initially, eventually it may reach failure. This is due to the yield surface shrinkage caused by the increase of the accumulated plastic strain ($\boldsymbol{\varepsilon}_M^v$) (Song et al., 2020). Thus, creep-induced failure behaviour can be simulated using the proposed BVSS model.

Moreover, regarding the creep-induced failure behaviour, some experimental results show that the creep response differ according to the applied load level (Figure 4.1b). In addition, for stress values below the so-called 'limited stress level', *i.e.* stress points inside the residual failure surface domain (see Figure 4.5 and line 1 in Figure 4.6b), no failure occurs even in the long term (Barla and Borgna, 2000; Paraskevopoulou, 2016; Song et al., 2020), because the yield surface would never be reached.

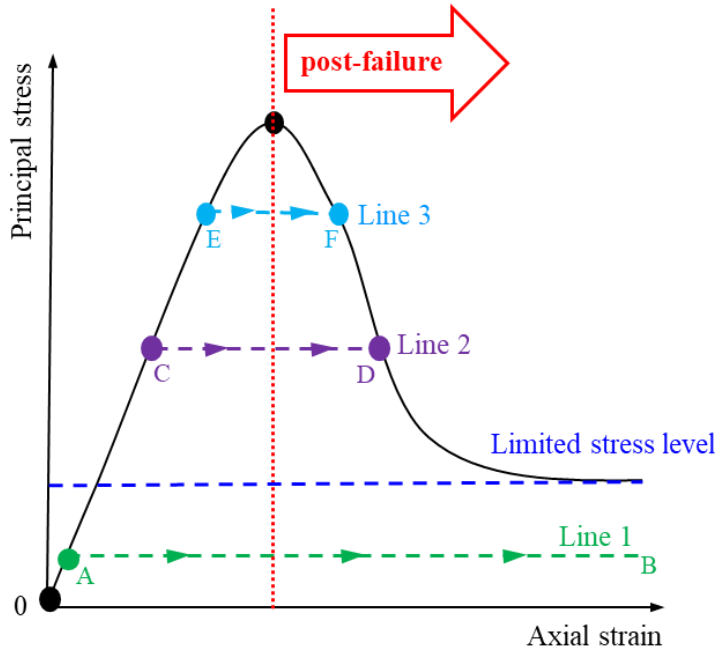

Figure 4.6. Conceptual representation of the long-term stress-strain response (lines 1, 2 and 3) at different constant stress levels, based on the work of Paraskevopoulou (2016) and Song et al. (2020).

As shown in Figure 4.6(b), after some stress increment $\Delta\sigma$ is applied up to points A, C and E, the applied stress is kept constant for a long period of time. It shows that the stress state will result in failure response for stress states above the so-called 'limited stress level' (lines 2 and 3). This failure will happen at different accumulated plastic strain values: for lines 2 and 3, failure initiates at points D and F, respectively. Based on Eq. (4.2), higher applied stresses would result in bigger values of $\frac{d\boldsymbol{\varepsilon}_{\mathrm{M}}^{\mathrm{v}}}{dt}$ and thus, earlier failure times will occur due to the faster softening evolution. Hence, different stress levels will result in a different creep response in the proposed BVSS model.

4.2.2. The multi-physics multi-phases theory

4.2.2.1. The coupled solid-fluid interaction

In this study, the problem is formulated in a multi-physics (hydro-mechanical) multi-phases (solid-fluid) approach. From a modelling perspective, saturated rock masses are treated as an equivalent porous medium (Olivella et al., 1996 and 2020). The adopted generalised effective stress expression is that in Eq. (4.10).

$$\boldsymbol{\sigma}' = \boldsymbol{\sigma} - p_l \, \mathrm{B}\,\mathbf{I} \tag{4.10}$$

where $\boldsymbol{\sigma}$ is the total stress tensor, $\boldsymbol{\sigma}'$ is the effective stress tensor, p_l is the liquid pressure, B is Biot's coefficient and $\mathbf{I}$ is the identity tensor.

As shown in Figure 4.7, two aspects (hydraulic and mechanical) and two phases (solid and fluid), are considered, including the coupling between them in both directions. Changes in hydraulic conditions influence the stress/strain field through changes in pore water pressure. Moreover, changes in the volume of the pores (or joints) caused by volumetric strains influence pore (or joint) liquid pressure distributions.

In this case, saturated rock masses are composed of two phases -rocks and water–. The water component is always in the liquid phase (l), and the rock component is always in the solid phase (s). Conceptually, this means that the water is considered to be in the joints of the rock mass, which are the main vector of water seepage.

The mass balance of the solid phase is expressed in Eq. (4.11). ρ_s represents the solid phase density, *i.e.* the density of the rock; ϕ represents the porosity, which can be understood as the volume of the joints per unit volume of rock mass; $\mathbf{j}_s$ represents the mass flux of the rock concerning a fixed reference system.

$$\frac{\partial}{\partial t}\left(\rho_s\left(1-\phi\right)\right)+\nabla\cdot\left(\mathbf{j}_s\right)=0 \tag{4.11}$$

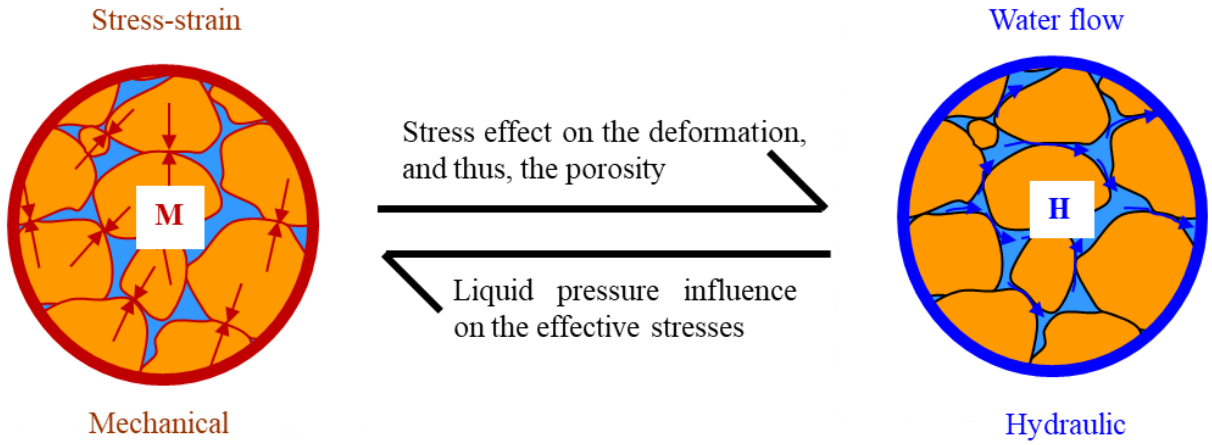

Figure 4.7. Conceptual model of the hydro-mechanical coupled behaviour. Based on the work of Olivella et al. (2020).

The mass balance of the liquid phase is expressed in Eq. (4.12). $\mathbf{q}_l$, ρ_l represent the liquid flux and liquid density, respectively; f^w is a source/sink term.

$$\frac{\partial\left(\rho_l \phi\right)}{\partial t}+\nabla\cdot\left(\rho_l \mathbf{q}_l+\rho_l \phi \frac{d\mathbf{u}}{dt}\right)=f^w \tag{4.12}$$

The stress equilibrium equation is expressed in Eq. (4.13). $\boldsymbol{\sigma}$ represents the stress tensor and $\mathbf{b}$ represents the vector of body forces.

$$\nabla\cdot\boldsymbol{\sigma}+\mathbf{b}=0 \tag{4.13}$$

Using the material derivative with respect to the solid –Eq. (4.14)–, the mass balance of solid phase becomes that in Eq. (4.15).

$$\frac{D_s\left(\bullet\right)}{Dt}=\frac{\partial\left(\bullet\right)}{\partial t}+\frac{d\mathbf{u}}{dt}\cdot\nabla\left(\bullet\right) \tag{4.14}$$

$$\frac{D_s \phi}{Dt}=\frac{\left(1-\phi\right)}{\rho_s}\frac{D_s \rho_s}{Dt}+\left(1-\phi\right)\nabla\cdot\frac{d\mathbf{u}}{dt} \tag{4.15}$$

Combining Eq. (4.15) with the mass balance of the liquid phase and then making use of the material derivative –Eq. (4.14)– again, Eq. (4.16) can be obtained.

$$\phi \frac{D_s\left(\rho_l\right)}{Dt} + \rho_l \frac{\left(1-\phi\right)}{\rho_s} \frac{D_s \rho_s}{Dt} + \rho_l \nabla \cdot \frac{d\mathbf{u}}{dt} + \nabla \cdot \left(\rho_l \mathbf{q}_l\right) = f^w \tag{4.16}$$

The theory of the coupled multi-physics multi-phases formulation used herein is a particular case of the general formulation presented in Olivella (1995) and Olivella et al. (1996). More details on the finite-element formulation employed in CODE_BRIGHT, including the weak forms of the governing equations and explicit definitions of the resulting matrices and vectors, can be found in (Olivella, 1995; Olivella et al., 1996).

4.2.2.2. Fluid flow

The liquid advective flux related to phase motion is governed by the generalised Darcy's law, as shown in Eq. (3.10).

$$\mathbf{q}_l = -\frac{\mathbf{k} k_{rl}}{\mu_l}\left(\nabla p_l - \rho_l \mathbf{g}\right) \tag{4.17}$$

where p_l represents the liquid pressure; **k** represents the intrinsic permeability tensor, which depends on the joint structure of the rock mass; k_{rl} and μ_l represent the relative permeability and dynamic viscosity of the fluid, respectively; **g** represents the gravity forces vector.

4.3. Numerical implementation of the Burgers-viscoplastic strain-softening model

The Burgers-viscoplastic strain-softening (BVSS) model is programmed in a finite element method software CODE_BRIGHT (Olivella et al., 2020). If another code is adopted, the same constitutive model presented in this study can be used. The programming of the proposed BVSS model should consider the following aspects:

1. The existence of corners in the yield and potential surfaces at which the gradients are not uniquely defined.

2. The strain localisation and the development of strain-softening behaviour.

3. The coupled behaviour between creep response and softening evolution.

4. The fact that the development of the Kelvin model depend not only on the current state of stress and strain, but also on the full history of their variation.

The first three aspects are already addressed in Song et al. (2020), from which the same approaches of the smoothing method for the yield and potential surfaces, strength parameters update for the strain-softening model and the viscoplastic model for strain localisation have been assumed for this study. Thus, this section concentrates on the fourth aspect, presenting the implementation of the proposed BVSS model. The numerical calculation and implementation of the Kelvin model involve theoretical difficulties, because this model depends on the full history of its development (Zienkiewicz and Taylor, 2000) and thus, history variables (Olivella et al., 2020) are required in the numerical implementation.

The strain rate of the Maxwell model only depends on the current stress state and the material properties, as shown in Eq. (4.18) .

$$\left.\frac{d\boldsymbol{\varepsilon}_{\mathrm{M}}}{dt}\right|_{t=t^{k}} = \mathbf{C}_{\mathrm{M}}^{\mathrm{e}} \left.\frac{d\boldsymbol{\sigma}^{'}}{dt}\right|_{t=t^{k}} + \mathbf{C}_{\mathrm{M}}^{\mathrm{v}} \left.\boldsymbol{\sigma}^{'k}\right|_{t=t^{k}} \tag{4.18}$$

$\mathbf{C}_{\mathrm{M}}^{\mathrm{e}}$ and $\mathbf{C}_{\mathrm{M}}^{\mathrm{v}}$ are shown in Eq. (4.19).

$$\mathbf{C}_{\mathrm{M}}^{\mathrm{e}} = \begin{bmatrix} \mathrm{M}_{3\times3}^{\mathrm{Me}} & 0_{3\times3} \\ 0_{3\times3} & \mathrm{N}_{3\times3}^{\mathrm{Me}} \end{bmatrix}, \quad \mathbf{C}_{\mathrm{M}}^{\mathrm{v}} = \begin{bmatrix} \mathrm{M}_{3\times3}^{\mathrm{Mv}} & 0_{3\times3} \\ 0_{3\times3} & \mathrm{N}_{3\times3}^{\mathrm{Mv}} \end{bmatrix} \tag{4.19}$$

where $\mathrm{M}^{\mathrm{Me}} = \begin{bmatrix} \frac{1}{3\mathrm{G_M}}+\frac{1}{9\mathrm{K_M}}, -\frac{1}{6\mathrm{G_M}}+\frac{1}{9\mathrm{K_M}}, -\frac{1}{6\mathrm{G_M}}+\frac{1}{9\mathrm{K_M}} \\ -\frac{1}{6\mathrm{G_M}}+\frac{1}{9\mathrm{K_M}}, \frac{1}{3\mathrm{G_M}}+\frac{1}{9\mathrm{K_M}}, -\frac{1}{6\mathrm{G_M}}+\frac{1}{9\mathrm{K_M}} \\ -\frac{1}{6\mathrm{G_M}}+\frac{1}{9\mathrm{K_M}}, -\frac{1}{6\mathrm{G_M}}+\frac{1}{9\mathrm{K_M}}, \frac{1}{3\mathrm{G_M}}+\frac{1}{9\mathrm{K_M}} \end{bmatrix}$, $\mathrm{N}^{\mathrm{Me}} = \begin{bmatrix} \frac{1}{\mathrm{G_M}}, 0, 0 \\ 0, \frac{1}{\mathrm{G_M}}, 0 \\ 0, 0, \frac{1}{\mathrm{G_M}} \end{bmatrix}$;

$$\mathrm{M}^{\mathrm{Mv}} = \begin{bmatrix} \frac{1}{3\eta_{\mathrm{M}}^{\mathrm{d}}} + \frac{1}{9\eta_{\mathrm{M}}^{\mathrm{v}}}, -\frac{1}{6\eta_{\mathrm{M}}^{\mathrm{d}}} + \frac{1}{9\eta_{\mathrm{M}}^{\mathrm{v}}}, -\frac{1}{6\eta_{\mathrm{M}}^{\mathrm{d}}} + \frac{1}{9\eta_{\mathrm{M}}^{\mathrm{v}}} \\ -\frac{1}{6\eta_{\mathrm{M}}^{\mathrm{d}}} + \frac{1}{9\eta_{\mathrm{M}}^{\mathrm{v}}}, \frac{1}{3\eta_{\mathrm{M}}^{\mathrm{d}}} + \frac{1}{9\eta_{\mathrm{M}}^{\mathrm{v}}}, -\frac{1}{6\eta_{\mathrm{M}}^{\mathrm{d}}} + \frac{1}{9\eta_{\mathrm{M}}^{\mathrm{v}}} \\ -\frac{1}{6\eta_{\mathrm{M}}^{\mathrm{d}}} + \frac{1}{9\eta_{\mathrm{M}}^{\mathrm{v}}}, -\frac{1}{6\eta_{\mathrm{M}}^{\mathrm{d}}} + \frac{1}{9\eta_{\mathrm{M}}^{\mathrm{v}}}, \frac{1}{3\eta_{\mathrm{M}}^{\mathrm{d}}} + \frac{1}{9\eta_{\mathrm{M}}^{\mathrm{v}}} \end{bmatrix}, \mathrm{N}^{\mathrm{Mv}} = \begin{bmatrix} \frac{1}{\eta_{\mathrm{M}}^{\mathrm{d}}}, 0, 0 \\ 0, \frac{1}{\eta_{\mathrm{M}}^{\mathrm{d}}}, 0 \\ 0, 0, \frac{1}{\eta_{\mathrm{M}}^{\mathrm{d}}} \end{bmatrix}.$$

Moreover, the elastic spring in the Maxwell model is characterised by an elastic modulus E_M, a Poisson's ratio ν_M^e, a shear modulus $G_M = \frac{E_M}{2\left(1+\nu_M^e\right)}$ and a volumetric modulus $K_M = \frac{E_M}{3\left(1-2\nu_M^e\right)}$. η_M^v (or η_M^d) represents the volumetric (or deviatoric) viscosity of the viscous dashpot in the Maxwell model.

The strain rate of the Kelvin model depends on the current stress state and the material properties and the full history of their development (Olivella et al., 2020; Zienkiewicz and Taylor, 2000), as shown in Eq. (4.20).

$$\left.\frac{d\boldsymbol{\varepsilon}_K}{dt}\right|_{t=t^k} = \mathbf{C}_K^v(\boldsymbol{\sigma}'|_{t=t^k} - \boldsymbol{\varepsilon}_K|_{t=t^k}) \tag{4.20}$$

$$\boldsymbol{\varepsilon}_K|_{t=t^{k+1}} = \left[\boldsymbol{\varepsilon}_K + \frac{d\boldsymbol{\varepsilon}_K}{dt}dt\right]_{t=t^k} \tag{4.21}$$

where $\boldsymbol{\varepsilon}_K|_{t=t^k}$ and $\boldsymbol{\varepsilon}_K|_{t=t^{k+1}}$ are the accumulated strains of the Kelvin model at time $t = t^k$ and $t = t^{k+1}$, respectively. $\mathbf{C}_K^v$ is shown in Eq. (4.22). History variables (Olivella et al., 2020) are applied to store the accumulated strain of the Kelvin model.

$$\mathbf{C}_K^v = \begin{bmatrix} \mathrm{M}_{3\times3}^{\mathrm{Kv}} & 0_{3\times3} \\ 0_{3\times3} & \mathrm{N}_{3\times3}^{\mathrm{Kv}} \end{bmatrix} \tag{4.22}$$

where $\mathrm{M}^{\mathrm{Kv}} = \begin{bmatrix} \frac{1}{3\eta_{\mathrm{K}}^{\mathrm{d}}}+\frac{1}{9\eta_{\mathrm{K}}^{\mathrm{v}}}, -\frac{1}{6\eta_{\mathrm{K}}^{\mathrm{d}}}+\frac{1}{9\eta_{\mathrm{K}}^{\mathrm{v}}}, -\frac{1}{6\eta_{\mathrm{K}}^{\mathrm{d}}}+\frac{1}{9\eta_{\mathrm{K}}^{\mathrm{v}}} \\ -\frac{1}{6\eta_{\mathrm{K}}^{\mathrm{d}}}+\frac{1}{9\eta_{\mathrm{K}}^{\mathrm{v}}}, \frac{1}{3\eta_{\mathrm{K}}^{\mathrm{d}}}+\frac{1}{9\eta_{\mathrm{K}}^{\mathrm{v}}}, -\frac{1}{6\eta_{\mathrm{K}}^{\mathrm{d}}}+\frac{1}{9\eta_{\mathrm{K}}^{\mathrm{v}}} \\ -\frac{1}{6\eta_{\mathrm{K}}^{\mathrm{d}}}+\frac{1}{9\eta_{\mathrm{K}}^{\mathrm{v}}}, -\frac{1}{6\eta_{\mathrm{K}}^{\mathrm{d}}}+\frac{1}{9\eta_{\mathrm{K}}^{\mathrm{v}}}, \frac{1}{3\eta_{\mathrm{K}}^{\mathrm{d}}}+\frac{1}{9\eta_{\mathrm{K}}^{\mathrm{v}}} \end{bmatrix}$, $\mathrm{N}^{\mathrm{Kv}} = \begin{bmatrix} \frac{1}{\eta_{\mathrm{K}}^{\mathrm{d}}}, 0, 0 \\ 0, \frac{1}{\eta_{\mathrm{K}}^{\mathrm{d}}}, 0 \\ 0, 0, \frac{1}{\eta_{\mathrm{K}}^{\mathrm{d}}} \end{bmatrix}$.

The strain rate of the viscoplastic model is Eq. (4.4). The derivative of Eq. (4.4) with respect to the stress tensor can be expressed in Eq. (4.23).

$$\frac{d}{d\boldsymbol{\sigma}'}\left(\frac{d\boldsymbol{\varepsilon}_{\mathrm{vp}}}{dt}\right) = \frac{1}{\eta_{\mathrm{vp}}}\frac{d}{d\boldsymbol{\sigma}'}\left(F^{\mathrm{m}}\frac{\partial G}{\partial \boldsymbol{\sigma}'}\right) = \frac{1}{\eta_{\mathrm{vp}}}\left[\mathrm{m}\,F^{\mathrm{m-1}}\frac{\partial F}{\partial \boldsymbol{\sigma}'}\frac{\partial G}{\partial \boldsymbol{\sigma}'} + F^{\mathrm{m}}\frac{\partial^2 G}{\partial \boldsymbol{\sigma}'^2}\right] \tag{4.23}$$

where:

$$\frac{\partial F}{\partial \boldsymbol{\sigma}'} = \frac{\partial F}{\partial p'}\frac{\partial p'}{\partial \boldsymbol{\sigma}'} + \frac{\partial F}{\partial \sqrt{J_2}}\frac{\partial \sqrt{J_2}}{\partial \boldsymbol{\sigma}'} + \frac{\partial F}{\partial \theta}\frac{\partial \theta}{\partial \boldsymbol{\sigma}'},$$

$$\frac{\partial G}{\partial \boldsymbol{\sigma}'} = \frac{\partial G}{\partial p'}\frac{\partial p'}{\partial \boldsymbol{\sigma}'} + \frac{\partial G}{\partial \sqrt{J_2}}\frac{\partial \sqrt{J_2}}{\partial \boldsymbol{\sigma}'} + \frac{\partial G}{\partial \theta}\frac{\partial \theta}{\partial \boldsymbol{\sigma}'},$$

$$\frac{\partial^2 G}{\partial \boldsymbol{\sigma}'^2} = \left(\frac{\partial^2 G}{\partial \sqrt{J_2}^2}\frac{\partial \sqrt{J_2}}{\partial \boldsymbol{\sigma}'} + \frac{\partial^2 G}{\partial \sqrt{J_2}\partial\theta}\frac{\partial \theta}{\partial \boldsymbol{\sigma}'}\right)\frac{\partial \sqrt{J_2}}{\partial \boldsymbol{\sigma}'} + \frac{\partial G}{\partial \sqrt{J_2}}\frac{\partial^2 \sqrt{J_2}}{\partial \boldsymbol{\sigma}'^2} + \left(\frac{\partial^2 G}{\partial\theta\partial\sqrt{J_2}}\frac{\partial \sqrt{J_2}}{\partial \boldsymbol{\sigma}'} + \frac{\partial^2 G}{\partial\theta^2}\frac{\partial\theta}{\partial\boldsymbol{\sigma}'}\right)\frac{\partial\theta}{\partial\boldsymbol{\sigma}'} + \frac{\partial G}{\partial\theta}\frac{\partial^2\theta}{\partial\boldsymbol{\sigma}'^2}$$

4.4. Numerical verification and comparison with other solutions

4.4.1. Creep tests

Uniaxial creep numerical tests are carried out to analyse the response of different mechanical models. Firstly, CODE_BRIGHT viscoelastic results are compared with analytical solutions.

After that, creep tests are carried out to analyse the creep-induced failure behaviour of the proposed Burgers-viscoplastic strain-softening (BVSS) model. Five different models are adopted in the comparison: three different viscoelastic models, including Maxwell, Kelvin and Generalized Kelvin models; two different Burgers-viscoplastic models, including Burgers-viscoplastic perfectly-plastic (BVPP) model and Burgers-viscoplastic strain-softening (BVSS) model.

The numerical model used here is 2D axisymmetric with dimensions of 0.01 m × 0.05 m. The normal displacements along the bottom and left boundaries have been restrained, as shown in Figure 4.8(a). A mesh with 2250 quadratic triangle elements has been considered for the analysis, as shown in Figure 4.8(b). In the numerical simulations, a constant stress p_y is applied along the top boundary at time $t = 0$. The calculation is stopped at 150 days.

The analytical solutions of creep strains are shown in Eq. (4.24) for three different viscoelastic models. The rock mass is considered incompressible and the input material parameters are shown in Table 4.1. No dilatancy is considered in the perfectly-plastic behaviour model. Note that the analyses do not represent any particular experiment.

$$\varepsilon(t)=\begin{cases}\dfrac{p_y}{E_{\mathrm{M}}}+\dfrac{p_y}{\eta_{\mathrm{M}}}t & \text{for the Maxwell model}\\[2ex] \dfrac{p_y}{E_{\mathrm{M}}}+\dfrac{p_y}{E_{\mathrm{K}}}\left(1-e^{-\frac{t}{\eta_{\mathrm{K}}/E_{\mathrm{K}}}}\right) & \text{for the Generalized Kelvin model}\\[2ex] \dfrac{p_y}{E_{\mathrm{M}}}+\dfrac{p_y}{\eta_{\mathrm{M}}}t+\dfrac{p_y}{E_{\mathrm{K}}}\left(1-e^{-\frac{t}{\eta_{\mathrm{K}}/E_{\mathrm{K}}}}\right) & \text{for the Burgers model}\end{cases} \tag{4.24}$$

Figure 4.9(a) shows that the responses of different viscoelastic models (at Point A; see Figure 4.8a) differ and, hence, the selection of time-dependent models might be relevant. Moreover, a good agreement is observed between analytical solutions and CODE_BRIGHT results, which verifies the correctness of the implementation of the CODE_BRIGHT viscoelastic models.

Table 4.1. Input parameters for the uniaxial creep tests.

Viscoelastic model	Maxwell model	E_M	6000 MPa	η_M	7.776×10^9 MPa.s
	Kelvin model	E_K	3000 MPa	η_K	1.296×10^9 MPa.s
Viscoplastic model	Cohesion	c_{peak}	10 MPa	c_{res}	5 MPa
	Friction angle	φ_{peak}	50 deg	φ_{res}	20 deg
	Dilatancy	α	1	$\psi_{peak} = \psi_{res}$	5 deg
	Perzyna model	m	5	η_{vp}	10^{10} MPa^{m}s

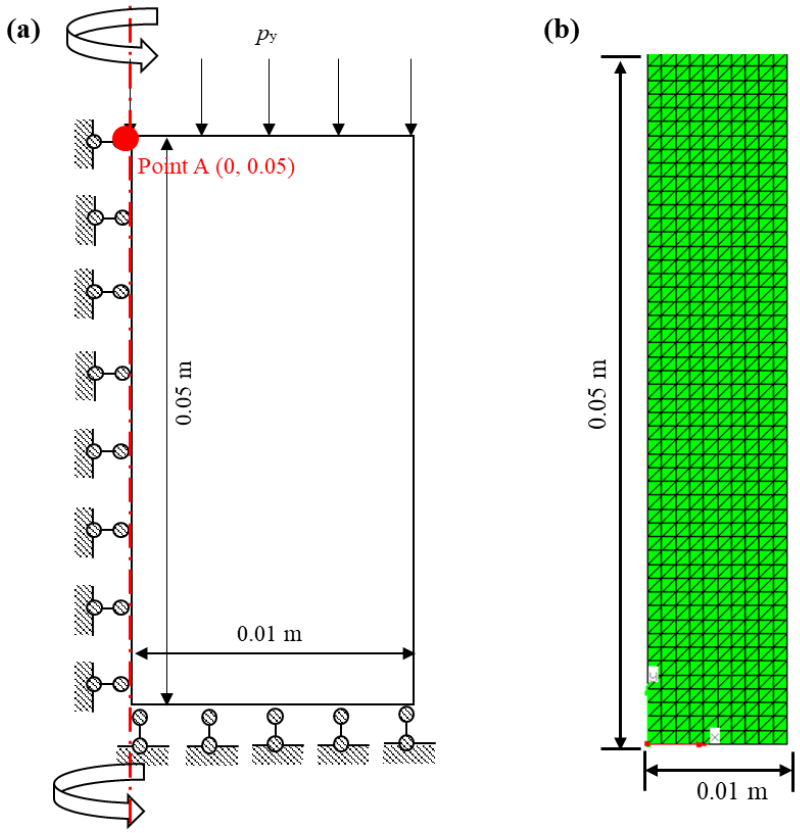

Figure 4.8. Creep numerical test: **(a)** basic features and boundary conditions; **(b)** mesh (2250 quadratic triangle elements).

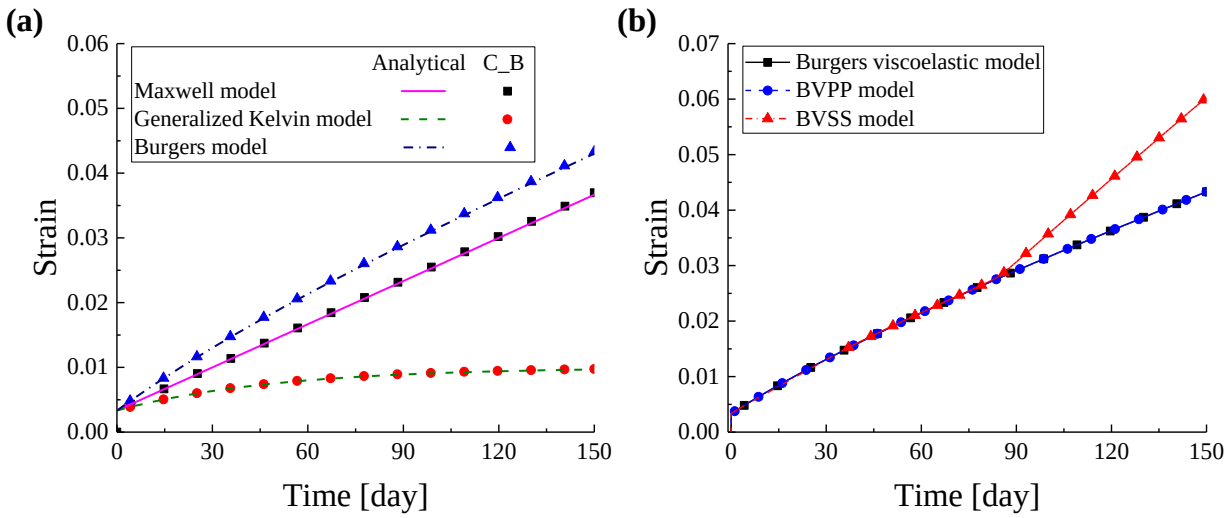

Figure 4.9. Axial strains of point A versus time: **(a)** comparison between analytical solutions and CODE_BRIGHT results for three different viscoelastic models; **(b)** comparison between Burgers, BVPP and BVSS models. Note that C_B represents the CODE_BRIGHT results.

For further verification, another group of creep tests is performed to analyse creep-induced failure behaviour. The numerical geometry, mesh and input parameters are the same as in the former example (see Figure 4.8). In Figure 4.9(b), the resulting strains of the Burgers model are the same as those of the BVPP model, which means that the viscoplastic part of the BVPP model is not engaged in this case.

In the case of the BVSS model, the resulting strain is the same as that of Burgers at the start of the simulation –*i.e.* when there is only viscoelastic response–. However, when the stress reaches the yield surface at point A, the geomaterial starts to fail, given that the yield surface shrinks due to creep-induced softening (see Figure 4.5), and hence the strain rate accelerates (Song et al., 2020). Therefore, the proposed BVSS model can simulate creep-induced failure behaviour.

4.4.2. Comparison with tunnelling results based on the viscoelastic model

The proposed BVSS model can be simplified to a viscoelastic model (see Figure 4.3). In order to verify the BVSS model for tunnelling in viscoelastic rock masses, examples of circular tunnels excavated in rock masses using the Generalised Kelvin model and the Burgers model are carried out using CODE_BRIGHT. The numerical results are compared with the analytical solutions of Wang et al. (2013). The expressions for tunnels excavated in the Generalised Kelvin and Burgers viscoelastic geomaterials under isotropic initial stresses are shown in Eqs. (4.25) and (4.26), respectively.

$$u_{\mathrm{r}}(t) = -\frac{p_0}{2r}\int_0^t \left[\frac{1}{\eta_{\mathrm{K}}}\exp\left(-\frac{\mathrm{G}_K}{\eta_{\mathrm{K}}}(t-\tau)\right)+\frac{1}{\mathrm{G}_{\mathrm{M}}}\delta(t-\tau)\right]R^2(\tau)\,d\tau \tag{4.25}$$

$$u_{\mathrm{r}}(t) = -\frac{p_0}{2r}\int_0^t \left[\frac{1}{\eta_{\mathrm{M}}}+\frac{1}{\eta_{\mathrm{K}}}\exp\left(-\frac{\mathrm{G}_K}{\eta_{\mathrm{K}}}(t-\tau)\right)+\frac{1}{\mathrm{G}_{\mathrm{M}}}\delta(t-\tau)\right]R^2(\tau)\,d\tau \tag{4.26}$$

where $R(t)$ represents the time-dependent radius of the tunnel cross-section; t represents time; p_0 represents the isotropic initial stress; u_{r} represents the incremental radial displacements occurring during the excavation; r represents the radial location in polar coordinates (r, θ), where $r = 0$ represents the location of the tunnel centre.

The numerical model developed using CODE_BRIGHT is consistent with the hypothesis made in the analytical solutions, and both of them are calculated under plane-strain conditions with small deformations. Only a quarter of the domain is analysed in the numerical model (see Figure 4.10) because of the double symmetry of the geometry and the boundary conditions on both the x and y axes. In addition, the normal displacements along the bottom (y = 0) and the left (x = 0) boundaries are restrained. Figure 4.10(b) shows the mesh of the numerical model. A mesh of 1560 quadratic triangular elements is adopted, with smaller elements near the excavation. The isotropic initial stress in the model is $p_0 = 20$ MPa.

First, the model is run for a sufficiently long time (100 days in this example) before excavation, to reach the equilibrium stress-strain conditions before starting the excavation, ensuring that we only consider the incremental deformations induced by excavation.

Subsequently, the first section of the tunnel is instantaneously excavated. That time will be considered zero (t = 0 day) in this study. The following sections of the tunnel are excavated step by step, and the radii of the tunnel cross-section can be expressed by Eq. (4.27). After the completion of all excavation steps, the calculation is stopped at t = 60 days.

$$R(t)=\begin{cases}2\,\text{m}, & \text{for } 0\le t<5 \text{ days}\\ 4\,\text{m}, & \text{for } 5 \text{ days}\le t<10 \text{ days}\\ 6\,\text{m}, & \text{for } 10 \text{ days}\le t<15 \text{ days}\\ 8\,\text{m}, & \text{for } t\ge 15 \text{ days}\end{cases} \tag{4.27}$$

In the comparison, for both the Generalised Kelvin and Burgers models, three different groups of material properties are considered for each model, as shown in Table 4.2. The rock masses are assumed as incompressible, *i.e.* Poisson's ratio is close to 0.5. A comparison of the time-dependent incremental radial displacements that occurred during the excavation along the tunnel wall (r = 8 m, θ = 0 deg) predicted by the analytical solutions and the numerical simulations is shown in Figure 4.11. A good agreement between the numerical and analytical results is observed, hence verifying the viscoelastic models implemented in CODE_BRIGHT.

Table 4.2. Input parameters of the viscoelastic models.

		E_{M} (MPa)	E_{K} (MPa)	$\eta^{\text{d}}_{\text{M}}$ (MPa.day)	$\eta^{\text{d}}_{\text{K}}$ (MPa.day)
Generalised Kelvin model	Case 1	2000	2000	-	10000
	Case 2	2000	5000	-	20000
	Case 3	5000	100	-	5000
Burgers model	Case 1	5000	2000	50000	10000
	Case 2	2000	500	10000	20000
	Case 3	2000	1000	20000	30000

$\eta^{\text{v}}_{\text{M}} \to \infty$ and $\eta^{\text{v}}_{\text{K}} \to \infty$.

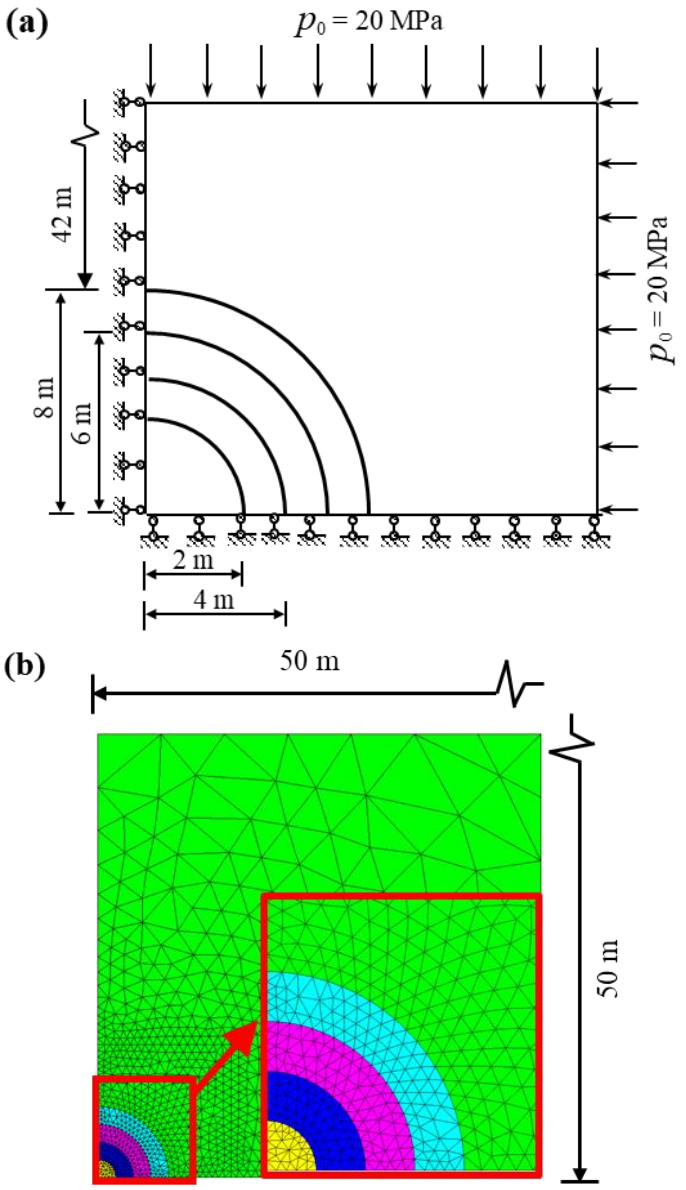

Figure 4.10. 2D plane-strain excavation model: **(a)** Basic features and boundary conditions (conceptual model). **(b)** Mesh in the vicinity of the excavation zone (far-boundaries at distances x = 50 m and y = 50 m; quadratic triangular mesh –1560 elements, 6 nodes each one–; 4 excavation steps in total).

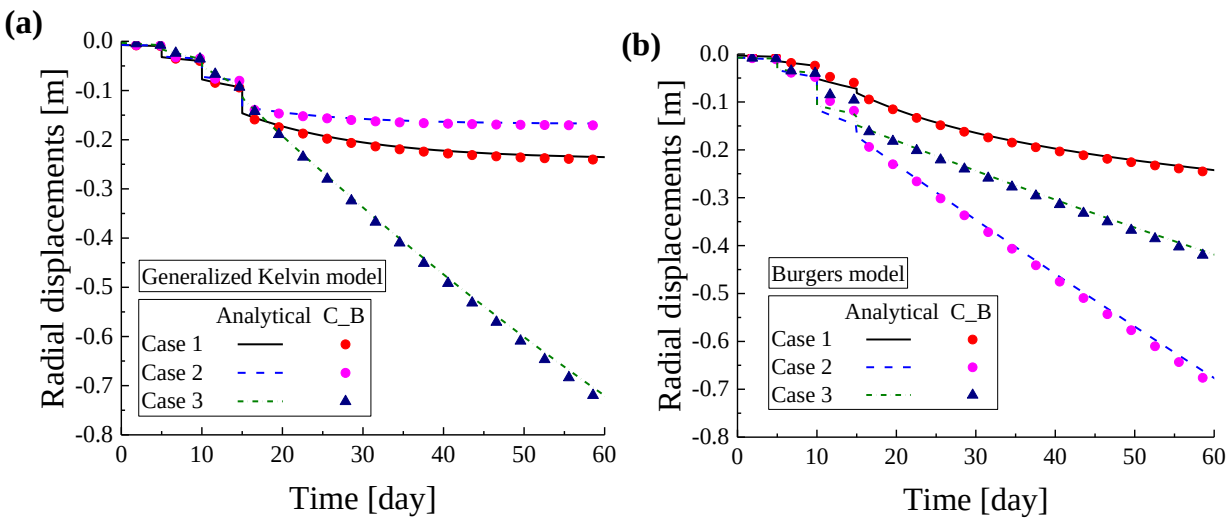

Figure 4.11. Comparison between analytical solutions (Wang et al., 2013) and CODE_BRIGHT results for the incremental radial displacements u_r along the tunnel wall (r = 8 m, θ = 0 deg): **(a)** Generalized Kelvin model, and **(b)** Burgers model. Note that C_B represents CODE_BRIGHT results.

4.4.3. Comparison with the elastic solutions of the LDP for hydro-mechanical problems

Numerical simulations of the LDP for the coupled solid-fluid problems with elastic materials are carried out in this section. The CODE_BRIGHT results are compared with the solutions for steady-state problems found in Nam and Bobet (2007) and the solutions for coupled solid-fluid problems found in Prassetyo and Gutierrez (2018b). A more detailed description of the steady-state and the time-dependent coupled solutions of the LDP for tunnels excavated in saturated rock masses can be found in the aforementioned references (Nam and Bobet, 2007; Prassetyo and Gutierrez, 2018b).

Considering tunnels below the water table with drainage towards the tunnel under steady-state conditions, Nam and Bobet (2007) proposed the steady-state empirical solutions for normalised radial displacements ahead ($x_d < 0$) and behind ($x_d \geq 0$) the tunnel face, as shown in Eqs. (4.28) and (4.29).

$$\frac{u_{\mathrm{r}}}{u_{\mathrm{r,max}}}=\begin{cases}0.28\exp\left(1.05\dfrac{x_{\mathrm{d}}}{R_{1}}\right)+0.2\exp\left(\dfrac{x_{\mathrm{d}}}{10R_{1}}\right)\left[1-\exp\left(-\dfrac{p_{\mathrm{l}}}{p^{'}}\right)\right], & x_{\mathrm{d}}<0\\ \dfrac{u_{\mathrm{r0}}}{u_{\mathrm{r,max}}}+\left(1-\dfrac{u_{\mathrm{r0}}}{u_{\mathrm{r,max}}}\right)\left[1-\left(\dfrac{0.75}{0.75+x_{\mathrm{d}}/R_{1}}\right)^{2}\right], & x_{\mathrm{d}}\geq 0\end{cases} \tag{4.28}$$

$$\frac{u_{\mathrm{r0}}}{u_{\mathrm{r,max}}}=0.28+0.19\left[1-\exp\left(-\frac{p_{\mathrm{l}}}{p^{'}}\right)\right] \tag{4.29}$$

where p_{l}, p' represent the far-field liquid pressure and effective stress at the centre of the tunnel, respectively; u_{r0} represents the radial displacement of the tunnel wall at the tunnel face; and $u_{\mathrm{r,max}}$ represents the maximum radial displacement of the tunnel wall.

Considering the effect of the coupled solid-fluid interaction, Prassetyo and Gutierrez (2018) proposed the transient coupled solutions of LDP shown in Eqs. (4.30)- (4.34).

$$\frac{u_{\mathrm{r}}}{u_{\mathrm{r,max}}}=\begin{cases}\dfrac{u_{\mathrm{r0}}}{u_{\mathrm{r,max}}}\exp\left(2.11\dfrac{x_{\mathrm{d}}}{2R_{1}}\right)+0.2\exp\left(\dfrac{x_{\mathrm{d}}}{10R_{1}}\right)\left[1-\exp\left(-\mathrm{A}\right)\right], & x_{\mathrm{d}}<0\\ \dfrac{u_{\mathrm{r0}}}{u_{\mathrm{r,max}}}+\left(1-\dfrac{u_{\mathrm{r0}}}{u_{\mathrm{r,max}}}\right)\left[1-\left(\dfrac{\mathrm{B}}{\mathrm{B}+0.5\,x_{\mathrm{d}}/R_{1}}\right)^{2}\right], & x_{\mathrm{d}}\geq 0\end{cases} \tag{4.30}$$

$$\frac{u_{\mathrm{r0}}}{u_{\mathrm{r,max}}}=0.28+0.028\left[1-\exp\left(-0.56\log t^{*}\right)\right] \tag{4.31}$$

$$A=-\frac{1}{2.4}\ln\left[-\left(\frac{u_{\mathrm{r0}}}{u_{\mathrm{r,max}}}-0.305\right)\Big/0.028\right] \tag{4.32}$$

$$B=0.85-2.10^{5}\exp\left(-47\frac{u_{\mathrm{r0}}}{u_{\mathrm{r,max}}}\right) \tag{4.33}$$

$$\frac{u_{\mathrm{r,max}}}{R_{1}}=2.0-0.3\exp\left[-0.005t^{*}\right] \tag{4.34}$$

where t^* represents the normalised consolidation time (Giraud and Rousset, 1996; Li, 1999; Prassetyo and Gutierrez, 2018b).

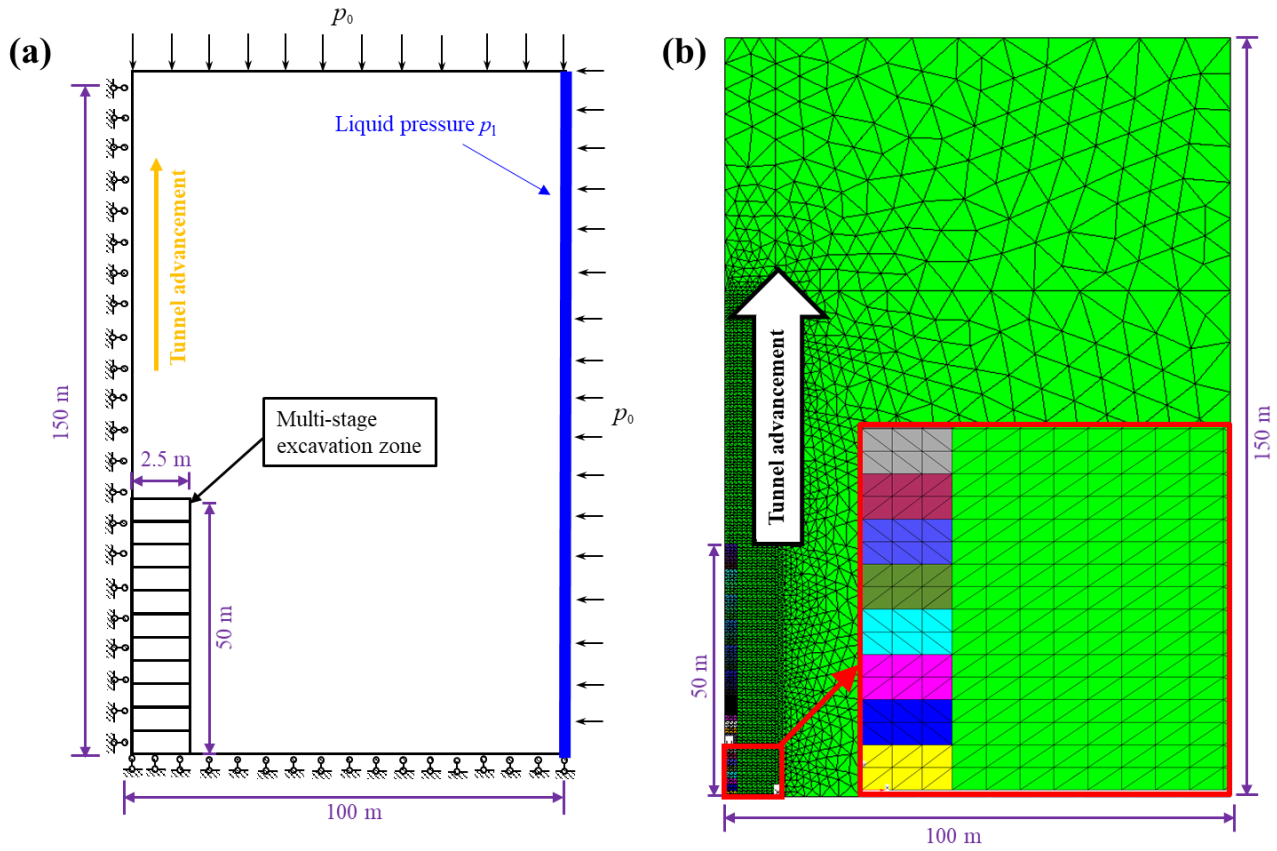

Figure 4.12. 2D axisymmetric excavation model: **(a)** Basic features and boundary conditions; **(b)** mesh (5640 quadratic triangular elements).

Table 4.3. Rock mass properties and tunnel geometry for the hydro-mechanical problems. Based on the work of Prassetyo and Gutierrez (2018).

Cases	E (MPa)	v	R_1 (m)	p_0 (MPa)	p_l (MPa)	Porosity	$\mathbf{K}$ (m^2)
Steady-state	292.5	0.125	2.5	4.5	2.25	0.39	10^{-10}
Coupled interaction	292.5	0.125	2.5	4.5	2.25	0.39	5.12×10^{-17}

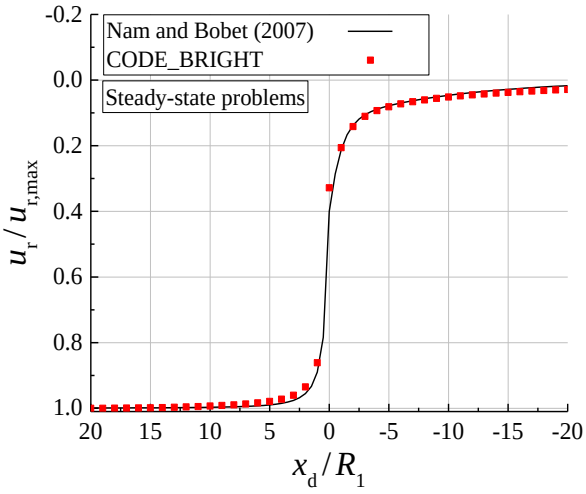

Figure 4.13. Comparison of the longitudinal deformation profiles for steady-state saturated problems, according to CODE_BRIGHT results and Nam and Bobet's analytical solutions (Nam and Bobet, 2007).

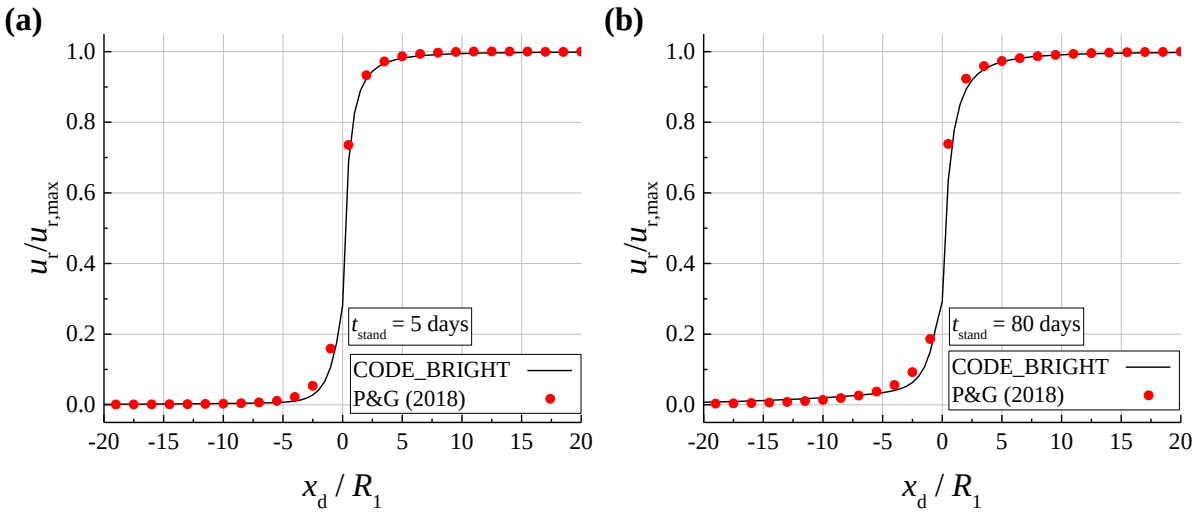

Figure 4.14. Comparison of the longitudinal deformation profiles for two different standstill times (t_{stand} = 5 days, 80 days), according to CODE_BRIGHT and Prassetyo and Gutierrez's solutions (P&G in the figure) (Paraskevopoulou and Diederichs, 2018): **(a)** t_{stand} = 5 days, **(b)** t_{stand} = 80 days.

In the CODE_BRIGHT numerical model, the tunnel is represented as a rectangle of length 50 m, excavated in 40 excavation steps 1.25 m long. The excavation rate selected is 5 m/day, as recommended by Prassetyo and Gutierrez (2018) and therefore, the whole excavation process takes 10 days. The dimensions and boundary conditions of the CODE_BRIGHT numerical model are shown in Figure 4.12(a). A mesh with 5894 quadratic triangle (six nodes) elements is adopted. Figure 4.12(b) presents the mesh of the numerical model. Table 4.3 contains the input parameters –rock mass properties and tunnel geometry. For the steady-state case, the intrinsic permeability chosen is 10^{-10} m^2, which is a big enough value to ensure drained conditions; while for the coupled solid-fluid case the intrinsic permeability adopted is 5.12×10^{-17} m^2, the same used by Prassetyo and Gutierrez (2018). No pressure is prescribed on the tunnel surface after excavation to be consistent with the numerical models found in Prassetyo and Gutierrez (2018).

Figure 4.13 presents the comparison between the CODE_BRIGHT results and the solutions of Nam and Bobet (2007) of the LDP for tunnels excavated in saturated elastic rock masses under steady-state conditions. Similarly, Figure 4.14 shows the comparison of time-dependent LDP considering the coupled solid-fluid interaction between the CODE_BRIGHT results and the solutions of Prassetyo and Gutierrez (2018). A good agreement between is observed for all the cases analysed. Therefore, the use of CODE_BRIGHT for representing the LDP considering the solid-fluid interaction and elastic materials has been verified.

4.5. Application in the design of tunnels

In this section, several analyses are carried out to examine the coupled solid-fluid response of tunnels excavated in time-dependent plastic rock masses (Figure 4.15). The time-dependent deformation of a tunnel depends on the creep response of the geomaterial and on the tunnel advancement rate (Paraskevopoulou, 2016; Paraskevopoulou and Diederichs, 2018; Song et al., 2018a and 2018b). In addition, the coupled solid-fluid interaction also affects the deformation of the tunnel (Prassetyo, 2017; Prassetyo and Gutierrez, 2018b and 2020). In this respect, the effects of selecting different time-dependent models is analysed in section 4.5.1 and the influence of the

standstill time and of the excavation rate on the tunnelling response is analysed in sections 4.5.2 and 4.5.3.

The tunnels analysed in this section have a radius 2.5 m. The selected initial stress (p_0 = 4.5 MPa), initial liquid pressure (p_l = 2.25 MPa), intrinsic permeability (**K** = 5.12 × 10^{-17} m^2) and initial porosity (0.39) values are taken from the work of Prassetyo (2017 and 2020) and Prassetyo and Gutierrez (2018). The numerical model geometry, boundary conditions, excavation process and mesh, are the same as those described in section 4.4.3 (see Figure 4.12). After excavation, atmospheric pressure (0.1 MPa) is prescribed on the tunnel surface. Note that no hydraulic boundary conditions were applied for the purely mechanical problems. If not specified, the implied excavation rate is 5 m/day (Prassetyo, 2017; Prassetyo and Gutierrez, 2018b). Two rock masses (set#1 and set#2) with different input parameters are considered (Table 4.4). Set#1 mainly consists of sandstones and schists under extreme squeezing conditions (Barla et al., 2010), while Set#2 is mostly composed of gray to black shale, Marl and calcareous Shale (Sharifzadeh et al., 2013).

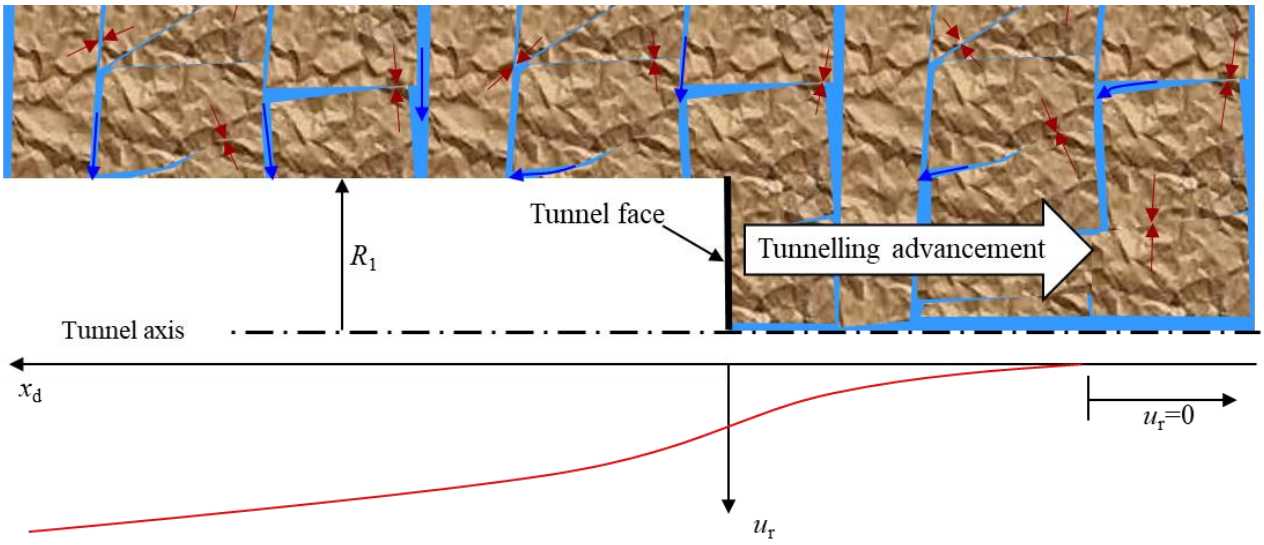

Figure 4.15. Conceptual solid-fluid coupled model for longitudinal deformation profiles (LDP).

Table 4.4. Sets of input parameters for the modelled rock masses. Based on previous work (Alejano et al., 2010; Barla et al., 2010; Barla and Borgna, 2000; Barla et al., 2011; Bonini and Barla, 2012; Paraskevopoulou, 2016; Sharifzadeh et al., 2013).

	Set #1	**Set #2**
E_M	1415	1870
ν_M	0.25	0.26
E_K	1494	1800
η^d_M (MPa.s)	8.82×10^8	5.05×10^{14}
η^d_K (MPa.s)	1.34×10^8	9.46×10^9
c_{peak} (MPa)	0.61	0.3
φ_{peak} (deg)	28	29.7
c_{res} (MPa)	0.5	0.29
φ_{res} (deg)	25.8	29.3
$\psi_{peak}=\psi_{res}$ (deg)	1.0	0.1
η^*	0.0177	0.0043
T_K (s)	2.69×10^5	1.58×10^7
$\eta^v_M \rightarrow \infty$; $\eta^v_K \rightarrow \infty$; $_K = 0.5$; m = 5; $\eta_{vp} = 1.25 \times 10^4$ MPa^{m}s; $\alpha = 1$; $G_K = E_K/3$; for both sets.		

4.5.1. Influence of the rock mass behaviour model selection

This sub-section focuses on analysing the effect of rock mass behaviour model selection on the resulting radial displacements of tunnels. Three different cases are investigated:

1. MVSS-M: a mechanical problem (M) using the Maxwell-viscoplastic strain-softening (MVSS) model.

2. BVSS-M: a mechanical problem (M) using the Burgers-viscoplastic strain-softening (BVSS) model.

3. BVSS-HM: a hydro-mechanical (HM) coupled problem using the BVSS model.

Note that the MVSS model is the same as the proposed model by Song et al. (2020), which is a particular case of the BVSS model. Moreover, to investigate the long-term response of tunnelling, two different standstill times (t_{stand} = 0 and 1 year) are considered. The reader can find more information about the concept of standstill time in previous work (Prassetyo, 2017; Prassetyo and Gutierrez, 2018b and 2020).

Unlike the MVSS-M model, the BVSS-M model incorporates the Kelvin model, which can simulate the primary creep behaviour of geomaterials. Furthermore, the BVSS-HM model considers the coupled solid-fluid interaction. However, the MVSS-M and BVSS-M models can only analyse mechanical problems. Regarding the Kelvin model, the displacements increase over time under a constant applied stress, while the strain rate progressively decreases to zero. Therefore, after a long enough standstill period, the Kelvin model will have no contribution to the induced deformations. Note that $T_K = \eta^d_M / G_K$ denotes the retardation time, which is the delayed response to an applied stress and can be described as 'delay of the elasticity'. As the value of T_K decreases, the less time is needed for the Kelvin model to achieve a very low strain rate *i.e.* the response of the rock mass to an applied stress will be faster.

The first rock mass (set#1 in Table 4.4) is expected to exhibit a stronger primary and secondary creep response, because the Maxwell (η^d_M) and Kelvin (η^d_K) viscosities are lower. At time t_{stand} = 0, the resulting deformations using the BVSS-M model are significantly higher than those using the MVSS-M (Figure 4.16), due to the additional contribution of the Kelvin model. However, with increasing standstill time, the response of the Kelvin model may achieve a stable condition. Hence, after that, the difference between MVSS-M and BVSS-M results may be caused only by the creep response of the Maxwell model. This may be the reason why the difference between MVSS-M and BVSS-M results is smaller, although still significant, at t_{stand} = 1 year. On the other hand, at both t_{stand} = 0 and t_{stand} = 1 year, the BVSS-HM and the BVSS-M results are significantly different. This is caused by the additional contribution of the coupled solid-fluid response.

Regarding the second rock mass (set#2 in Table 4.4), its secondary creep response is expected to be residual, given the large value of η^d_M considered. Moreover, the retardation time of

set#2 has a higher value ($T_K = 1.58 \times 10^7$ s), which means that the primary creep develops during a longer time than in the case of set#1. In the short-term ($t_{stand} = 0$), both MVSS-M and BVSS-M results are similar (Figure 4.16), probably because there is not enough time to develop a significant primary creep (or creep of the Kelvin model), given the aforementioned high value of T_K. On the contrary, at $t_{stand} = 1$ year, there is a considerable difference between MVSS-M and BVSS-M results, probably due to the additional contribution of the Kelvin model, which now has had enough time to induce deformations. Furthermore, it can be observed that BVSS-HM and BVSS-M results are significantly different, due to the coupled solid-fluid effect, both for short-term ($t_{stand} = 0$) and long-term ($t_{stand} = 1$ year) cases.

Hence, the MVSS model may represent the response of some tunnels in which large deformations occur due to secondary and accelerated creep and in which the primary creep-induced deformation is marginal. For example, this may be the case of tunnels excavated in weak or altered rock masses, or the case of hard rock masses excavated very deep, or the case of rock masses with significant values of η_K^d (Olivella and Gens, 2002; Sainoki et al., 2017; Song et al., 2020; Sterpi and Gioda, 2009).

However, in some other cases, where the primary creep-induced deformations should be relevant, the proposed BVSS model may be able to represent more accurately the time-dependent behaviour and hence, it may contribute to a safer and more efficient tunnel design than the MVSS model. This is the case of tunnels excavated in rock masses exhibiting high strength or subjected to low stresses (Song et al., 2018a). In addition, note that the MVSS model is actually a particular case of the BVSS model (as described in section 4.2).

Additionally, hydro-mechanical (HM) results are significantly different from the purely mechanical results. Therefore, both the selected rock mass behaviour model and the coupled solid-fluid interaction may be relevant in the preliminary design of tunnels.

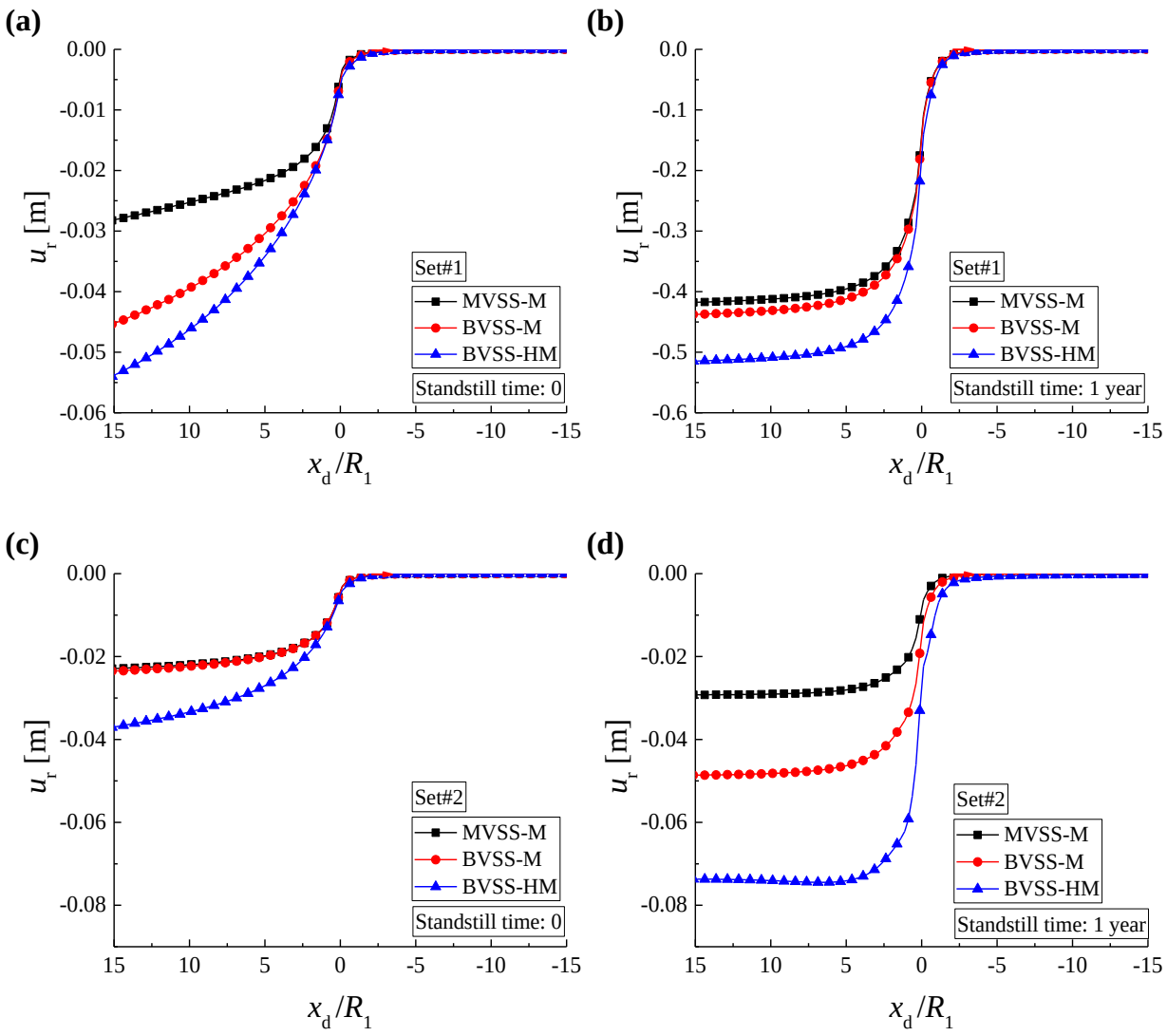

Figure 4.16. Radial displacements of the tunnel wall along the normalized distance to the tunnel face for three (MVSS-M, BVSS-M and BVSS-HM) models and two different standstill times (0 and 1 years): **(a)** set #1 and t_{stand} = 0, **(b)** set #1 and t_{stand} = 1 year, **(c)** set #2 and t_{stand} = 0, **(d)** set #2 and t_{stand} = 1 year.

4.5.2. Time-dependent responses of tunnels during the standstill period

Some tunnels do not fail during excavation but ultimately fail after a long period of operation (Fabre and Pellet, 2006; Sandrone and Labiouse, 2010). This phenomenon might be caused by the creep-induced failure behaviour and/or by the pore pressure time-dependent dissipation process due to the coupled solid-fluid interaction. In this section, the tunnelling response for four different standstill times (t_{stand} = 0, 0.1, 1 year and 2 years) is presented. Two different rock masses (set#1 and set#2) are considered. The BVSS-HM model has been used for this analysis.

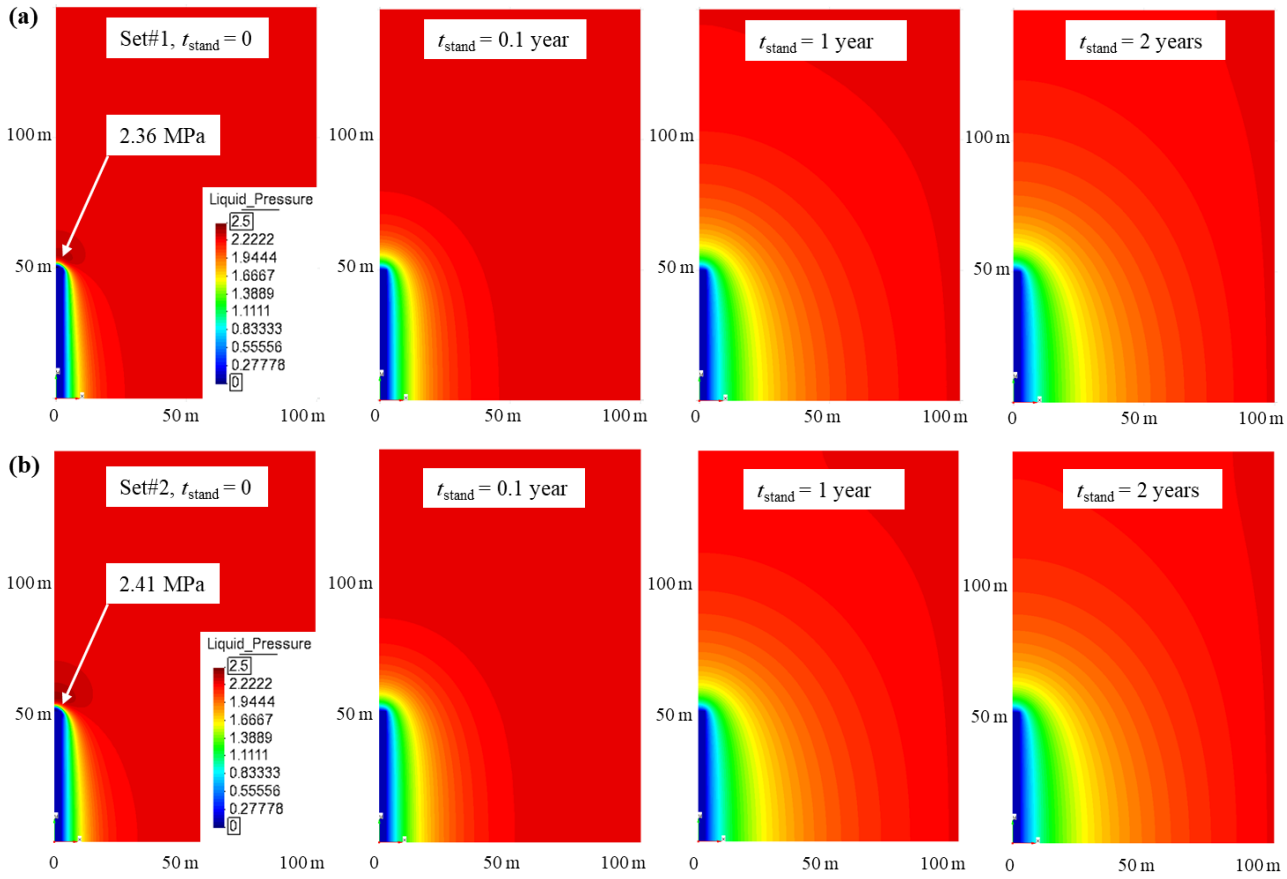

Figure 4.17. Contours of liquid pressure for two different rock masses (set#1 and set#2) and four different standstill times (t_{stand} = 0, 0.1, 1 year and 2 years) for: **(a)** set#1, and **(b)** set#2.

Concerning the pore pressure evolution, it can be observed that the liquid pressure builds up just ahead of the tunnel face (Figure 4.17) in the short term after the excavation (t_{stand} = 0), increasing around 5% and 7% for set#1 and set#2, respectively. This phenomenon may be due to the fact that the liquid pressure dissipation rate is lower than the excavation rate (Prassetyo, 2017; Prassetyo and Gutierrez, 2018b and 2020). Then, with the increase of the standstill time, this overpressure dissipates and, eventually, the liquid pressure achieves a steady-state condition, after a long enough period (Prassetyo, 2017; Prassetyo and Gutierrez, 2018b and 2020), as it can be observed in Figure 4.17.

Moreover, although the hydro-mechanical boundary conditions are the same for both cases, it can be observed that the fluid responses are different for set#1 and set#2 (Figure 4.17). This difference is due to the coupled solid-fluid interaction (see Figure 4.7), that may cause different solid deformations for different geomaterials, in turn affecting fluid flow differently.

Figures 4.18 and 4.19 show the liquid pressure profile along the normalised distance to the tunnel face (x_d/R_1). Note for reference that the liquid pressure is taken at a radius of 4.5 m. For both sets #1 and #2, it can be observed that the liquid pressure profile is initially higher all along the tunnel, and then it experiences a certain dissipation as the standstill time increases. In addition, Figures 4.18 and 4.19 show that there is some overpressure just ahead of the tunnel face, as it has been commented above. This overpressure seems to dissipate relatively fast. Certainly, the liquid pressure profiles are similar after a standstill time of 1 year, which means that most of this dissipation process has been completed. Moreover, note that the dissipation rate decreases with the standstill time, according to the results. Finally, it can be observed that this dissipation is much slower as we move away from the tunnel face in the tunnel advance direction (e.g. x_d/R_1 = -15). These effects may be caused by the coupled solid-fluid interaction.

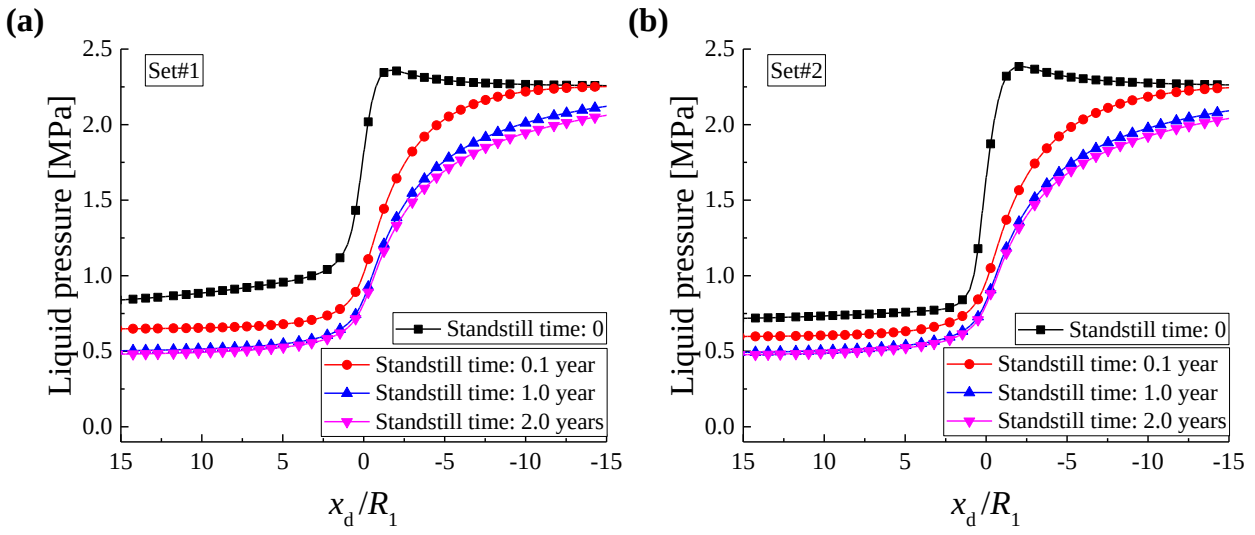

Figure 4.18. 2D liquid pressure profile evolution over four different standstill times (t_{stand} = 0, 0.1, 1, 2 years) for two different rock masses: **(a)** set#1 and **(b)** set#2.

Finally, Figures 4.20 and 4.21 show the longitudinal deformation profile evolution. For set#1, the induced displacements increase linearly even after a long standstill time, which indicates that the displacements may be fundamentally induced by secondary creep (Maxwell part of the Burgers model). This phenomenon may be consistent with some reported engineering cases (Olivella and Gens, 2002; Sainoki et al., 2017; Song et al., 2020; Sterpi and Gioda, 2009).

In contrast, for set#2, it can be observed that the incremental rates of induced displacements decrease along the standstill time (Figures 4.20 and 4.21), which indicates that the induced displacements by secondary creep may not be significant. Furthermore, the results show that the primary creep induced displacements (Kelvin part of the Burgers model) are more relevant at a shorter term and less significant afterwards, as could be expected. This response may represent the behaviour of rock masses exhibiting high strength or subjected to low stresses (Song et al., 2018a).

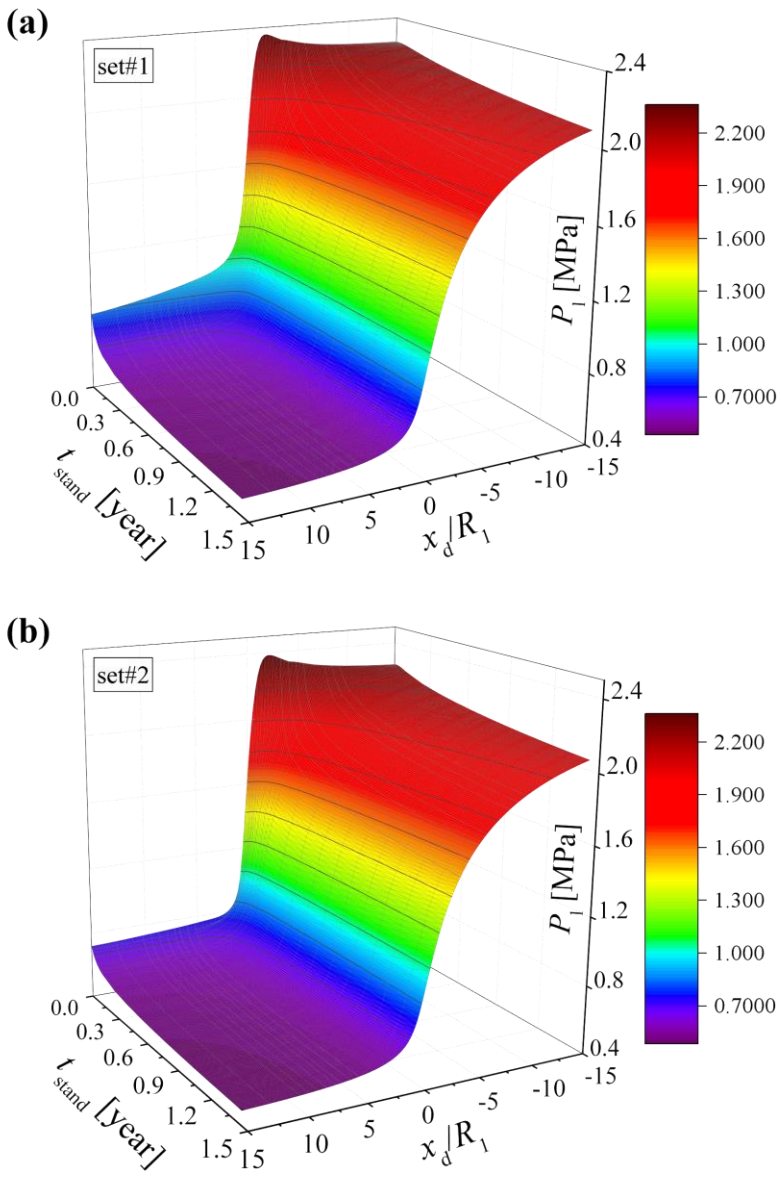

Figure 4.19. 3D liquid pressure profile evolution for two different rock masses: **(a)** set#1 and **(b)** set#2.

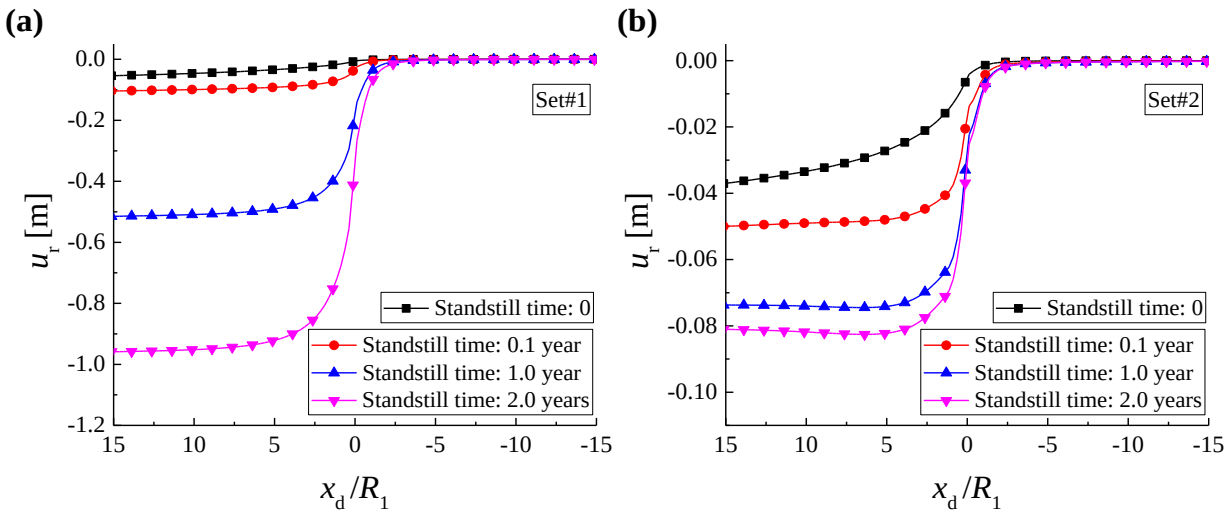

Figure 4.20. 2D longitudinal deformation profile evolution over four different standstill times (t_{stand} = 0, 0.1, 1, 2 years) for two different rock masses: **(a)** set#1 and **(b)** set#2.

4.5.3. Influence of the excavation rate

During the excavation process, solid deformations and liquid flows are coupled, and thus, tunnelling responses become more complex and difficult to anticipate. The excavation rate may heavily affect the creep response of tunnels (Song et al., 2020) and the pressure dissipation of the fluid phase. In this section, three different excavation rates (5 m/day, 10 m/day and 20 m/day) are adopted to analyse the influence of the excavation rate on the tunnelling response. The liquid pressure is taken at a radius of 4.5 m in these examples. All presented results in this section assume a standstill time t_{stand} = 0, *i.e.* just after the excavation of the tunnel face.

During excavation, the high undrained loads experienced by the rock mass near the tunnel face, causes the liquid pressure to increase from its initial value (2.25 MPa). This phenomenon can be called overpressure. Figure 4.22 shows contours of liquid pressure for two different rock masses (set #1 and #2) and three different excavation rates (5 m/day, 10 m/day and 20 m/day). It can be observed that different excavation rates result in different overpressure values. Table 4.5 presents the maximum overpressure reached during the different simulations, both in absolute

value and in percentage increment from the initial liquid pressure value. It can be observed that overpressure increases with the excavation rate, being slightly higher for set#2.

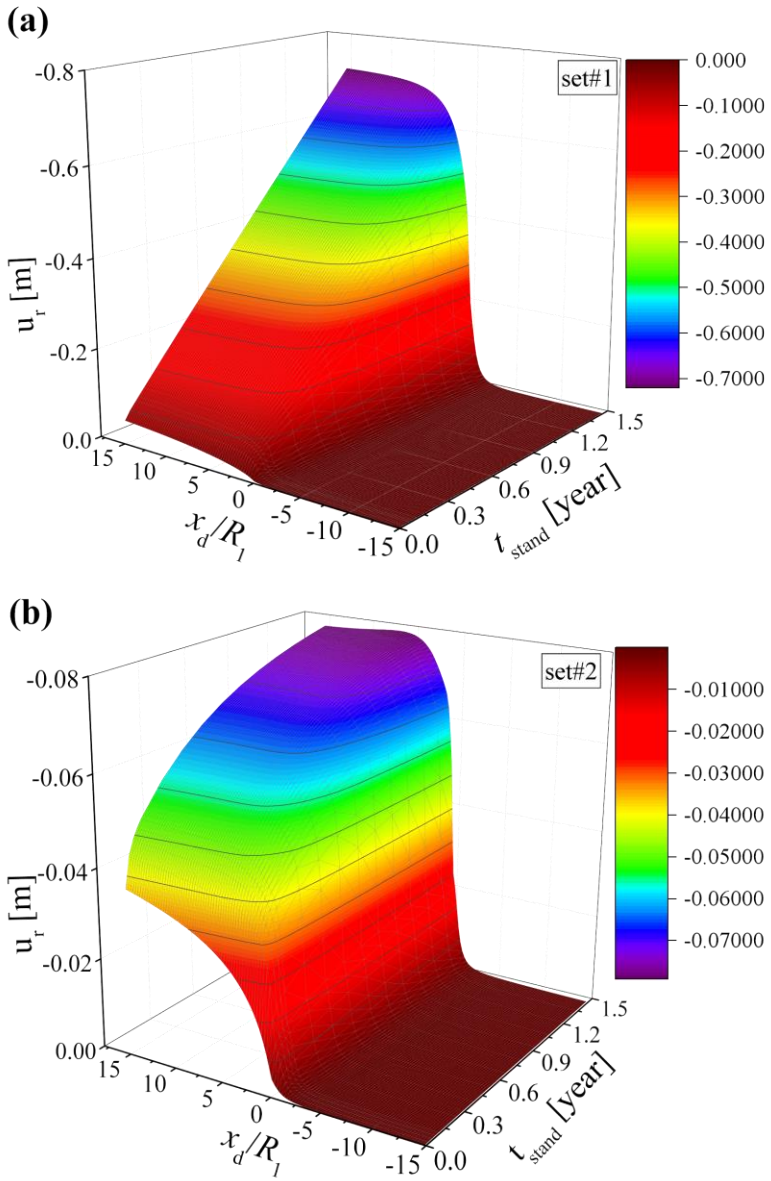

Figure 4.21. 3D longitudinal deformation profile evolution for two different rock masses: **(a)** set#1 and **(b)** set#2.

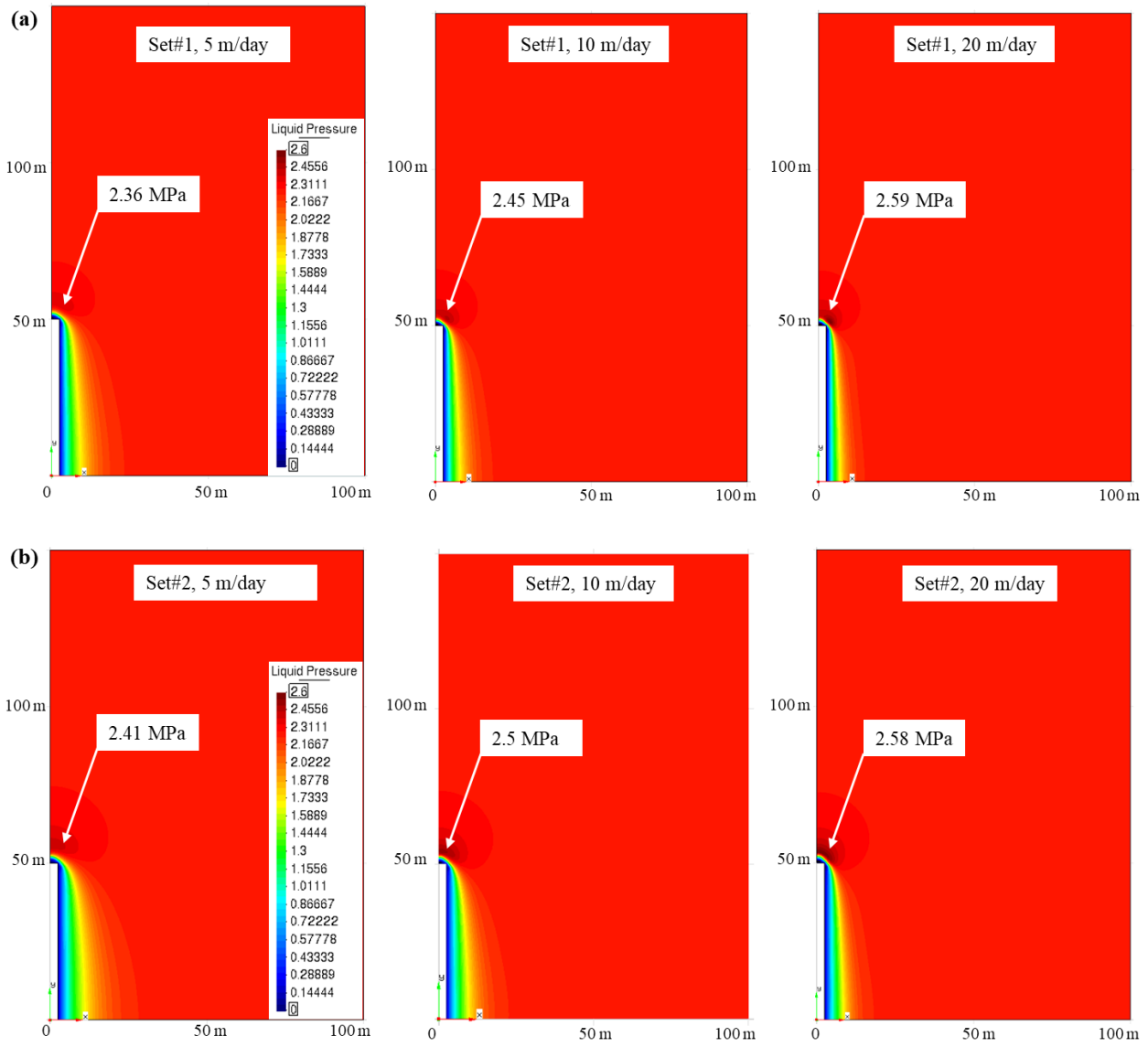

Figure 4.22. Contours of liquid pressure for three different excavation rates (5 m/day, 10 m/day, 20 m/day) and two different rock masses: **(a)** set#1, and **(b)** set#2. A standstill time t_{stand} = 0 is assumed.

Furthermore, Figure 4.23 plots the profiles of liquid pressure along the normalised distance to the tunnel face (x_d/R_1). Behind the tunnel face ($x_d > 0$), faster excavation rates results in larger liquid pressures. Moreover, ahead of the tunnel face ($x_d < 0$), the faster the excavation rate, the more significant build-up values of liquid pressures occur in the vicinity of the tunnel face, due to

the shorter time available for dissipation. In addition, note that the maximum values of liquid pressure are attained at points closer to the tunnel face, as the excavation rate increases. However, there is no significant effect of the excavation rate on the liquid pressure as we move away from the tunnel face in the tunnel advance direction.

Similarly, Figure 4.24 presents the radial displacements of the tunnel wall ($r = R_1$) along the normalised distance to the tunnel face (x_d/R_1), *i.e.* the longitudinal deformation profiles, for three different excavation rates and two different rock masses. It can be observed that lower excavation rates may lead to larger deformations, since there is more time for creep deformations to develop (Song et al., 2020) and for pore pressures to dissipate (Prassetyo, 2017; Prassetyo and Gutierrez, 2018b). Moreover, the radial displacements ahead of the tunnel face do not seem to be affected by the excavation rate. However, behind the tunnel face, the radial displacement difference corresponding to different excavation rates grow as we move away from the tunnel face.

In summary, the different excavation rates can result in different fluid flows for two reasons: (1) the faster the excavation rate, the slower dissipation of liquid pressure ahead of the tunnel face and thus, the higher liquid pressure build-up; (2) different excavation rates result in different periods of time for the development of creep deformations, in turn affecting the fluid flow.

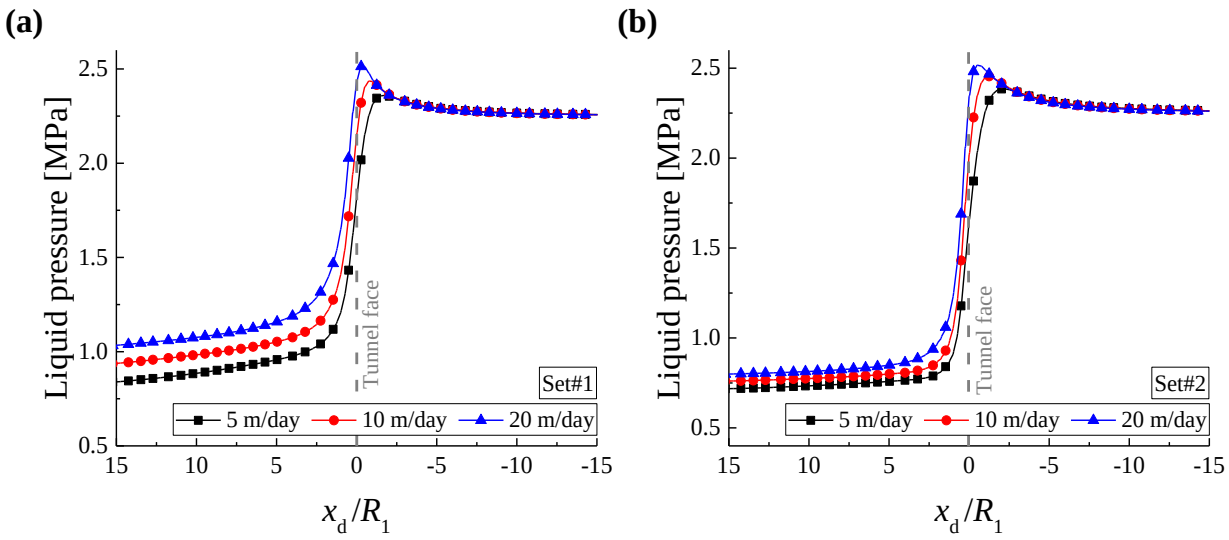

Figure 4.23. Profiles of liquid pressure for two different rock masses: **(a)** set#1 and **(b)** set#2. Three different excavation rates (5 m/day, 10 m/day, 20 m/day) are considered.

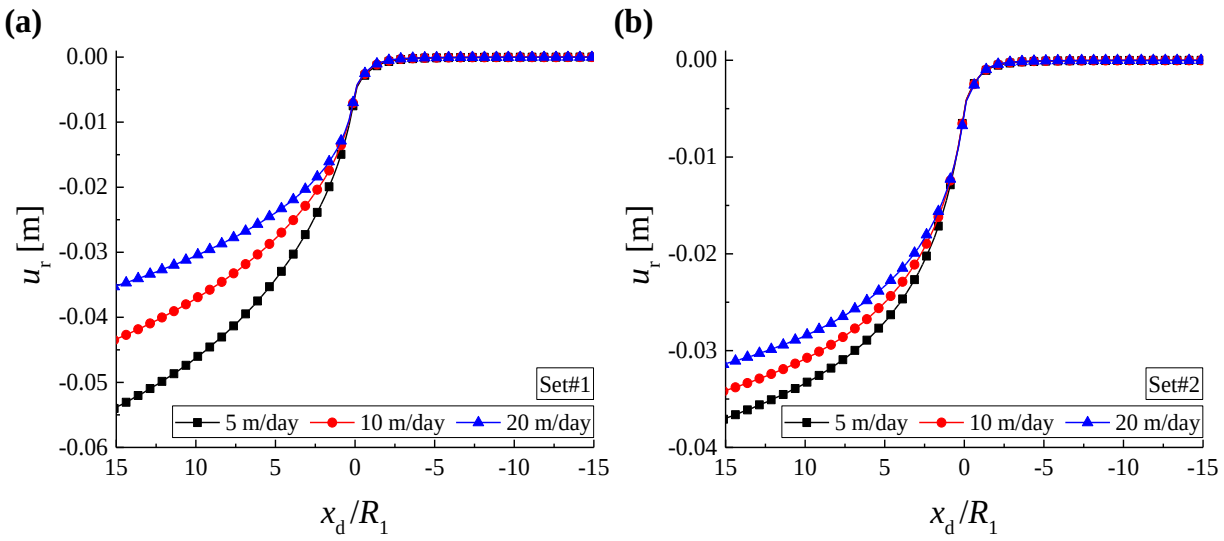

Figure 4.24. Profiles of radial displacements for two different rock masses: **(a)** set#1 and **(b)** set#2. Three different excavation rates (5 m/day, 10 m/day, 20 m/day) are considered.

Table 4.5. Maximum overpressure reached for two different rock masses (set #1 and #2) and three different excavation rates (5 m/day, 10 m/day and 20 m/day).

Excavation rate [m/day]	Maximum liquid pressure [MPa]		Percentage increment of P_l [%]	
	Set#1	Set#2	Set#1	Set#2
5	2.36	2.41	5	7
10	2.45	2.5	9	11
20	2.59	2.58	15	15

4.6. Conclusions

This study provides an alternative approach for modelling multi-stage excavation in saturated time-dependent plastic rock masses, considering a coupled solid-fluid interaction and a time-dependent plastic behaviour. To do that, a Burgers-viscoplastic strain-softening (BVSS) model has been proposed and implemented into the finite element method software CODE_BRIGHT to be able to simulate the time-dependent behaviour and the plastic behaviour (stress-induced or/and creep-induced) of geomaterials. In addition, a coupled solid-fluid model is used to simulate the interaction between solid deformations and fluid flows.

Firstly, the Burgers viscoelastic model and the viscoplastic model are combined in series, to simulate the mechanical response of geomateirals. The Mohr-Coulomb strain-softening model and a non-associated plastic flow rule have been used. The creep deformations are coupled with the strain-softening model to simulate the damage evolution, and hence, the creep-induced failure behaviour can be simulated. The generalised Darcy's law has been adopted in the simulation of fluid flow.

The numerical results are verified by comparing the CODE_BRIGHT results with other analytical or numerical results. Finally, parametric analyses are performed to analyse the effects of the selection of different constitutive model, the standstill time and the excavation rate on tunnelling response. Some conclusions can be drawn from this study:

1. The proposed Burgers-viscoplastic strain-softening (BVSS) model provides the possibility of modelling rock masses in which both plastic and time-dependent responses take place.
2. The results obtained considering the coupled solid-fluid interaction are significantly different from the purely mechanical results. Liquid pressure builds up just ahead of the tunnel face in the short term after the excavation. Afterwards, this overpressure dissipates with the increase of the standstill time, and the dissipation rate decreases with the standstill time. Moreover, over pressure dissipation is much slower as we move away from the tunnel face in the tunnel advance direction.
3. Excavation rate is relevant to tunnelling response. Behind the tunnel face, a higher excavation rate results in a higher liquid pressure. Also, ahead of the tunnel face, the higher

the excavation rate, the more significant build-up values of liquid pressure occur in the vicinity of the tunnel face, due to the shorter time available for dissipation. In addition, as the excavation rate increase, the maximum values of liquid pressure are attained at points closer to the tunnel face.

Note that, even if the proposed method in this study can simulate different cases of coupled solid-fluid response for tunnelling in saturated rock masses with time-dependent plastic behaviour, it still has some limitations. For instance, the numerical analyses are carried out through homogeneous material models. In future research, three-dimensional numerical models will be utilised to model tunnels excavated in non-homogeneous geomaterials, thus improving the applicability of the numerical approach to real engineering.

Chapter 5. Numerical solutions for tunnels excavated in strain-softening rock masses considering a combined support system

Based on the published manuscript of the following article:

Fei Song, Alfonso Rodriguez-Dono. Numerical solutions for tunnels excavated in strain-softening rock masses considering a combined support system [J]. Applied Mathematical Modelling, 2021, 92: 905-930. https://doi.org/10.1016/j.apm.2020.11.042

Abstract

In this study, an alternative numerical procedure to calculate displacements and stresses of supported circular tunnels is proposed, considering the whole process of tunnel advancement, and sequential installation of the primary and secondary support systems. In the derivation, the plastic area of the rock mass is divided into a large number of annuli around the tunnel, and then the Finite Difference Method (FDM) is employed. First, the strain-softening behaviour model is taken to simulate the post-failure behaviour of the rock mass. Furthermore, the Mohr-Coulomb or the Hoek-Brown failure criteria can be chosen, a non-associated plastic flow rule is assumed and the dilatancy of the rock mass is considered. After that, the fictitious support forces concept is used to simulate the process of tunnel advancement, and thus, the three-dimensional effect of the tunnel face is considered. Finally, the solutions of displacements and stresses for the rock mass and the supports can be obtained, by using the compatibility conditions of stresses and displacements at both rock-support and support-support interfaces. The results obtained from these solutions agree well with those of the self-similar solutions for circular openings, and the compatibility conditions of supported tunnels were verified. The proposed method has been compared with the convergence-confinement method. Parametric analyses are then carried out to investigate the sensitivity of support forces and displacements to the rock mass behaviour model selection. Then, the application of the proposed solutions in the design of tunnels is presented. The proposed method provides a convenient alternative method for the preliminary design of tunnels.

5.1. Introduction

The tunnels supported with a system comprising several supports are in high demand due to the increasing demands of transportation, geological disposal, hydraulic and mining engineering. The primary support system is usually put in place to seal the rock and withstand the loads that may arise during the excavation, while the secondary support system is installed to ensure the long-term stability of tunnels (Leca and Clough, 1992; Oreste, 2003; Song et al., 2018b). Thus, a reliable analysis of the secondary support system constitutes a critical topic to the long-term stability of tunnels. At the same time, the acting support forces at the support-support interface directly affect the stability of the secondary support system.

In addition, many accidents are related to fractures when dealing with mining or civil engineering underground projects. Therefore, the complexity of the behaviour of the different geomaterials is a critical topic in the mitigation of the accidents that may occur in works such as tunnel excavation (Song et al., 2020; Zhao et al., 2015). Thus, both rock mass behaviour model selection and the design method of the support system are crucial topics in the design of tunnels. A proper simulation of the whole process of tunnelling and support installation is critical to achieving an optimal design of tunnels.

The design of tunnels can be tackled by various different methods, such as analytical solutions, numerical simulations or the convergence-confinement method (CCM) (Alejano et al., 2010; Alejano et al., 2009; Alejano et al., 2012; Alonso et al., 2008; Alonso et al., 2003; Carranza-Torres and Fairhurst, 1999; Carranza-Torres and Fairhurst, 2000; Carranza-Torres et al., 2013; Carranza-Torres and Zhao, 2009; Chu et al., 2019; Cui et al., 2020; Cui et al., 2019; Cui et al., 2015; Do et al., 2020; Fahimifar and Ranjbarnia, 2009; Fahimifar et al., 2010; Kabwe et al., 2020b and 2020c; Kargar, 2019; Lu et al., 2011; Maghous et al., 2012; Nomikos et al., 2011; Oreste, 2003; Paraskevopoulou and Diederichs, 2018; Prassetyo and Gutierrez, 2018a and 2018b; Song et al., 2020; Song et al., 2018a and 2018b; Wang et al., 2018a; Wang et al., 2020a; Wang et al., 2019; Wang et al., 2013; Wang and Nie, 2010; Wang et al., 2020b; Wang et al., 2014; Wang et al., 2015; Wang et al., 2018b; Wang et al., 2018c; Wang et al., 2018e; Wang et al., 2017b; Wang and Li, 2009; Wang et al., 2010; Zeng et al., 2019; Zhang et al., 2015; Zhang et al., 2016; Zhang et al., 2012a; Zhang et al., 2019b; Zou et al., 2017a). Numerical simulations have been

widely used in the analysis of underground projects, considering more complex geological conditions. Although numerical simulations can provide some useful results, usually they require long runtimes and sometimes meet numerical difficulties, especially when complete parametric analyses need to be performed (Song et al., 2018b). On the other hand, analytical solutions provide an efficient and quick approach to gain insights into the nature of the problem (Carranza-Torres and Fairhurst, 1999). However, solutions for plastic problems are not easy to develop. The CCM provides an efficient way of determining support forces by considering the ground-support interactions (Alejano et al., 2010; Alejano et al., 2012). Although the CCM has been widely used in the design of tunnels, the application of the CCM including two different support systems is limited (Song et al., 2018b). In addition, it is not possible to use the CCM in the design of a tunnel support system if ground reaction curves, support characteristic curves or longitudinal deformation profiles are not available (Prassetyo and Gutierrez, 2018a). As an alternative, a simple stepwise approach has been adopted to obtain solutions for tunnels excavated in strain-softening rock masses in this study, considering the sequential installation of two different support systems, as explained below.

Moreover, revising the literature so far on existing solutions for supported tunnels, some researchers presented elastic solutions for their stresses and displacements (Carranza-Torres et al., 2013; Li and Wang, 2008; Wang and Li, 2009). Some other researchers presented solutions for supported tunnels constructed in time-dependent viscoelastic rock masses (Song et al., 2018a and 2018b; Wang et al., 2013; Wang et al., 2014). However, no plastic behaviour is considered in these references, ergo the solutions obtained may lead to an unsafe design of tunnels, since plastic behaviour is common in many real engineering projects. On the other hand, many researchers developed so far various approaches for the plastic problems of tunnelling in rock masses, but mostly for elastic-perfectly-plastic (EPP) or elastic-brittle (EB) behaviour of rock masses (Shen et al., 2019; Vrakas and Anagnostou, 2014; Yu, 1992; Zhang et al., 2016; Zhang et al., 2012a). Nonetheless, the average quality rock masses behave in a strain-softening (SS) manner and thus, it is important to study the response of tunnels in rock masses exhibiting SS behaviour (Alejano et al., 2010; Alejano et al., 2009; Alejano et al., 2012; Alonso et al., 2003). Note that both EPP and EB models are special cases of the SS model.

Regarding rock masses exhibiting strain-softening behaviour, through defining a fictitious 'time' variable and re-scaling some variables, Carranza-Torres (1998a) and Alonso et al. (2003) presented self-similarity numerical solutions of circular openings excavated in strain-softening geomaterials. Later, based on those solutions in Alonso et al. (2003), Alejano et al. (2009) presented ground reaction curves considering EPP, EB and SS behaviour models and increasingly realistic parameters.

Furthermore, by using a simple stepwise procedure that successively determines the stresses and strains on the boundaries of a number of annuli into which the plastic zone is divided, some researchers (Brown et al., 1983; Lee and Pietruszczak, 2008; Park et al., 2008b; Wang et al., 2012b; Wang et al., 2010; Zhang et al., 2012a; Zhang et al., 2018; Zou et al., 2017a) presented numerical solutions for tunnelling in rock masses that exhibit strain-softening behaviour. Combining them with the CCM, the above plastic solutions can be used for designing supported tunnels. However, the application of the CCM is limited to tunnels with a single support (Song et al., 2018b).

On the other hand, Oreste (2003) proposed support characteristic curves for a combined support system, which extended the CCM in the application of tunnels with several different supports (Alejano et al., 2009; Alonso et al., 2008; Oreste, 2015; Oreste, 2003). However, in order to make a correct design of the secondary support system, the modified ground reaction curve due to the influence of the primary support system is needed; research that was missing until now. To do that, the compatibility conditions at the interface between supports should be considered. Therefore, at this point, the CCM meets one of its limitations.

In summary, the solutions of supported tunnels were mostly concerned with elastic or viscoelastic problems, and rarely geomaterial-support/support-support coupled interaction is considered in the plastic solutions. Instead, in this research, we have proposed solutions for tunnels with two different support systems constructed in rock masses showing strain-softening behaviour. In these solutions, we consider: (1) the tunnel advancement, (2) the sequential installation of primary and secondary support systems, (3) different rock mass post-failure behaviour models: elastic-perfectly-plastic (EPP), strain-softening (SS) and elastic-brittle (EB), and (4) both displacements and stress compatibility conditions on the rock-support and support-support interfaces.

In our approach for unsupported circular tunnels, the numerical solutions for the stresses and displacements are first derived for the strain-softening rock masses. Then, based on the coupled model at both rock-support and support-support interfaces, the solutions for the supported circular tunnels are presented, considering the tunnel advancement and different installation time of the primary and secondary support systems. Finally, the sensitivity of support forces and deformation of tunnels to the rock mass behaviour model selection are analysed, and an application example is presented to illustrate the application of the proposed method in the design of tunnels.

5.2. State of the problem

5.2.1. Assumptions and description of the problem

This study considers the design of tunnels with two different support systems constructed in rock masses showing strain-softening (SS) post-failure behaviour. The process of tunnel advancement and the sequential installation of primary and secondary support systems have been considered. Throughout the analyses, the following assumptions have been made:

1. The surrounding rock is homogeneous and isotropic, and exhibits an elastic-plastic mechanical behaviour. The strain-softening (SS), the elastic-perfectly-plastic (EPP) as well as the elastic-brittle (EB) models are adopted to simulate the post-failure behaviour of rock masses.

2. The initial isotropic stress field around the tunnel is idealized as an axisymmetric condition, and the stresses in the far field can be assumed as P_0.

3. Both the primary and secondary support systems are assumed to behave linearly elastic. The primary and secondary supports are instantaneously installed at a distance from the tunnel face $x_d = x_1$ and $x_d = x_2$, respectively. The outer and inner radii of the primary (secondary) support system are R_1 (R_2) and R_2 (R_3), respectively, and thus, the thickness of the primary (secondary) support is $d_1 = R_1 - R_2$, $d_2 = R_2 - R_3$, as shown in Figures 5.1 and 5.2.

4. The excavation rate is slow enough that it may be assumed that it does not induce any dynamic stress. Small strain theory is considered.

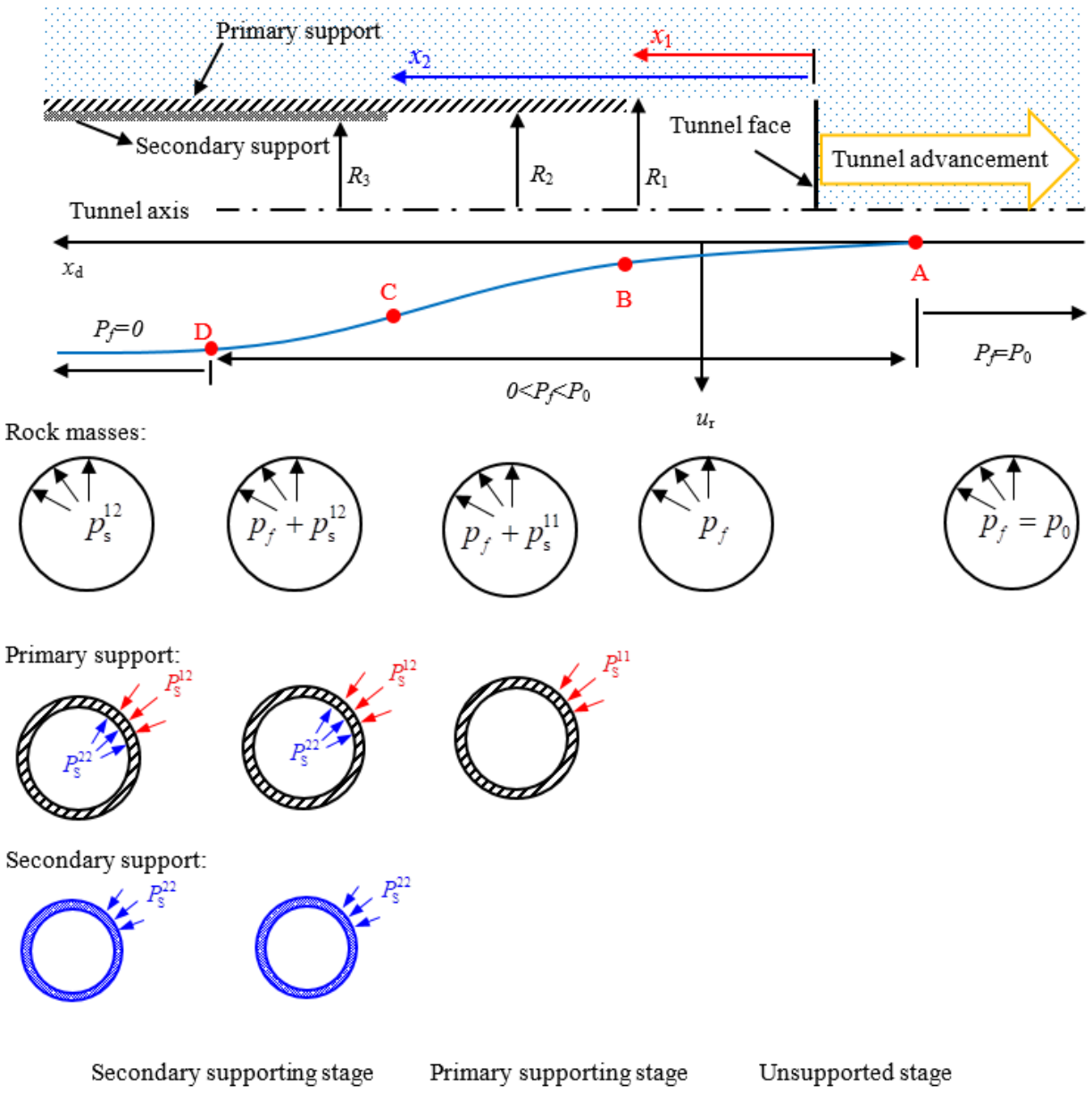

Figure 5.1. The three-dimensional effect of the tunnel advancement, including the boundary conditions in the rock mass and in the primary and secondary support systems.

Considering the tunnel advancement, the analysis of the distribution of the stresses and displacements near the periphery of the tunnel is a three-dimensional (3D) problem. As shown in Figure 5.1, the support forces from the tunnel face (named fictitious support forces in this study), P_f, progressively decrease along with the increased distance to the tunnel face, from the initial stress P_0 (ahead of point A), to zero (behind point D) when the tunnel face is at a distance where it has no influence on the considered section.

Moreover, after the installation of the primary support system (behind point B in Figure 5.1), both the fictitious support forces P_f and the interaction support forces between the rock mass and the primary support system P_S^{1j} (j = 1, 2 represents the primary or secondary support stage, respectively) act on the periphery of the tunnel. At last, with the advancement of the tunnel face, P_f will eventually decrease to zero while P_S^{1j} will increase from zero to a constant value. Before the installation of the secondary support (between point B and C), only the support forces P_S^{11} act on the outer boundary of the primary support; after the installation of the secondary support (behind point C), P_S^{12} and P_S^{22} act on the outer and inner boundaries of the primary support, while P_S^{22} acts on the outer boundary of the secondary support (Figures 5.1 and 5.2).

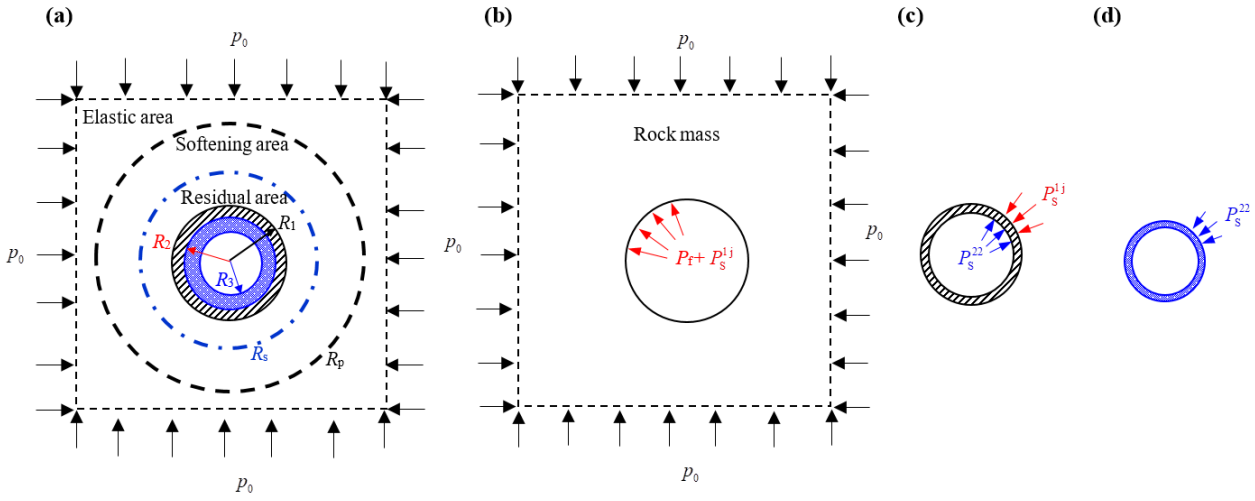

Figure 5.2. Geometry and boundary conditions for: **(a)** rock mass and support systems; **(b)** rock mass; **(c)** the primary support system; **(d)** the secondary support system.

By introducing the fictitious support forces P_f, to account for the effect of the tunnel face, the 3D problem can be treated as an equivalent plane-strain one (Carranza-Torres et al., 2013; Sulem et al., 1987), as shown in Figure 5.2. This infinite plane, subjected to uniform isotropic far field stresses and made of an elastic-plastic medium, contains a circular tunnel with primary and secondary support systems sequentially installed. Figure 5.2 presents the mechanical models of the tunnel and the support system. R_p and R_s represent the peak and residual plastic radii of the rock mass, respectively. Polar coordinates (r, θ) will be employed in the derivation of the solutions. The sign convention is defined as positive for compression and negative for tension.

5.2.2. Rock mass behaviour models

Some researchers (Alejano et al., 2009; Hoek and Brown, 1997) provided post-peak strength guidelines. These guidelines are based on the geotechnical quality of the rock by means of the geotechnical strength index (GSI). According to these guidelines, (1) for high quality rock masses (GSI > 60), the rock mass behaves in an elastic-brittle (EB) manner; (2) for average quality rock masses (40 < GSI < 60), the rock mass presents a strain-softening (SS) behaviour, which can also be referred to as strength-weakening behaviour; (3) for weak rock masses (GSI < 40), elastic-perfectly-plastic (EPP) behaviour is assumed (Figure 5.3). Note that these ranges are just a reference and they may vary in some cases.

SS behaviour can accommodate EB behaviour (the SS model with a drop modulus, M, equal to infinite) and EPP behaviour (the SS model with a drop modulus, M, equal to zero). Thus, EPP and EB behaviours are just two particular cases of SS behaviour. In the current research, the SS model will be adopted to simulate the post-failure behaviour of rock masses.

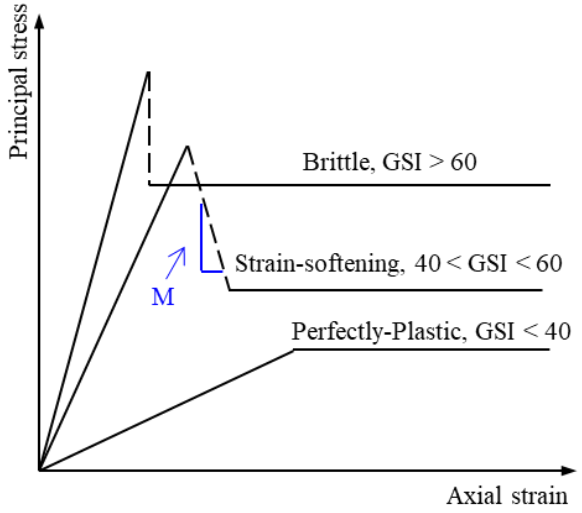

Figure 5.3. Different post-failure behaviour of rock masses with different geological strength indexes (GSI). Based on the work of Alejano et al. (2009 and 2010).

One of the main features of the SS behaviour model is that the yield surfaces depend not only on the stress tensor $\boldsymbol{\sigma}$, but also on the plastic or softening parameter η (Alejano et al., 2010; Alejano et al., 2009), as shown in Figure 5.4. The failure criterion is defined as shown in Eq. (5.1).

$$F(\boldsymbol{\sigma},\eta)=0 \tag{5.1}$$

The SS behaviour model is characterized by a gradual transition from the peak failure surface to the residual failure surface, which is governed by the plastic or softening parameter η. In a SS model, a softening regime occurs whenever $0 < \eta < \eta^*$, and the residual regime takes place when $\eta \geq \eta^*$, as shown in Figure 5.4. η^* is the value of the softening parameter whereon the softening phase ends, beginning the residual phase. The softening parameter η is defined as shown in Eq. (5.2), where ε^p (γ^p) represents the accumulated plastic strain (Alejano et al., 2009; Alonso et al., 2003).

$$\eta = \varepsilon_{\theta}^{p} - \varepsilon_{r}^{p} \tag{5.2}$$

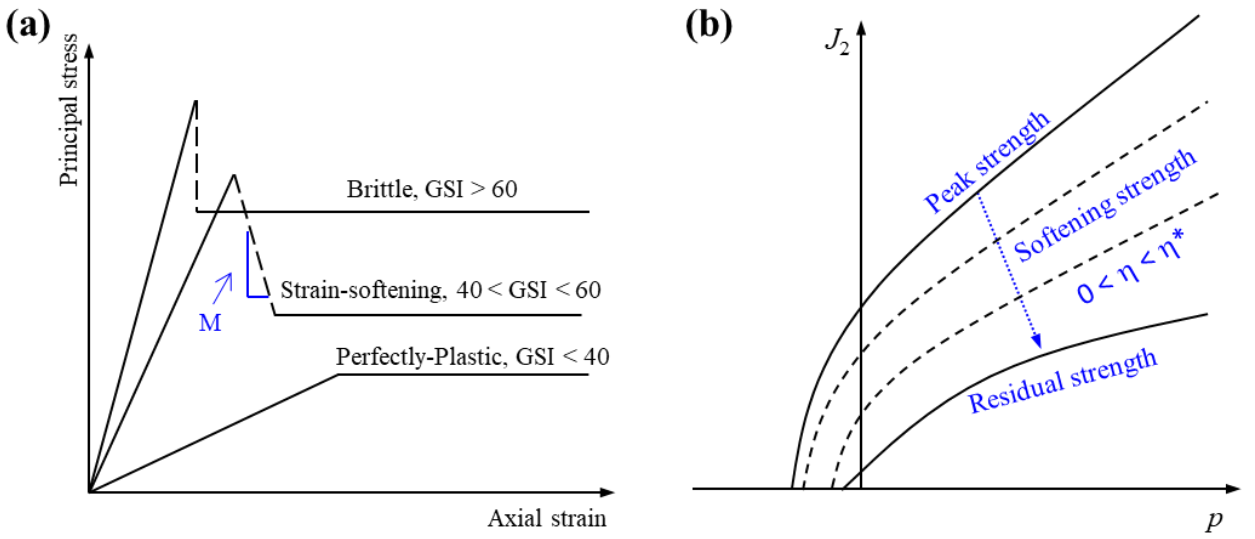

Figure 5.4. **(a)** Theoretical strain-softening model for a triaxial test performed on a rock sample. **(b)** Yield surface evolution for a rock mass with strain-softening behaviour. Based on the work of Alejano et al. (2009 and 2010) and Song et al. (2020).

In this study, a linear decrease function of the plastic parameters $k(\eta)$ is adopted to represent the strain-softening behaviour (Alejano et al., 2009; Alonso et al., 2003), as shown in Eq. (5.3), where k_p and k_s are the peak and residual values of k, respectively. If a Mohr-Coulomb strain-softening model is adopted, k represents cohesion c, friction angle φ and dilatancy angle ψ, while k represents the m_{HB}, s_{HB}, a_{HB} and ψ when considering the Hoek-Brown strain-softening model.

$$k(\eta)=\begin{cases} k_p, & \text{for } \eta \le 0 \\ k_p+\left(\dfrac{k_s-k_p}{\eta^*}\right)\eta, & \text{for } 0 \le \eta \le \eta^* \\ k_s, & \text{for } \eta \ge \eta^* \end{cases} \tag{5.3}$$

The Mohr-Coulomb strain-softening model can be shown in Eq. (5.4) (Alonso et al., 2003).

$$F_{MC}=\sigma_\theta - N(\eta)\sigma_r - S(\eta) \tag{5.4}$$

where $N(\eta)=\left[1+\sin\varphi(\eta)\right]/\left[1-\sin\varphi(\eta)\right]$, $S(\eta)=2c(\eta)\sqrt{N(\eta)}$. The peak and residual Mohr-Coulomb failure criteria can be expressed as in Eqs. (5.5) and (5.6), respectively.

$$F_{\mathrm{MC,p}}=\sigma_\theta-N_{\mathrm{p}}\sigma_r-S_{\mathrm{p}} \tag{5.5}$$

$$F_{\mathrm{MC,s}}=\sigma_\theta-N_{\mathrm{s}}\sigma_{\mathrm{r}}-S_{\mathrm{s}} \tag{5.6}$$

where $N_{\mathrm{i}}=\left[1+\sin\varphi_{\mathrm{i}}\right]/\left[1-\sin\varphi_{\mathrm{i}}\right]$, $S_{\mathrm{i}}=2c_{\mathrm{i}}\sqrt{N_{\mathrm{i}}}$, and i = p (or s) represent the peak (or residual) parameters in the Mohr-Coulomb strain-softening model.

The Hoek-Brown strain-softening model is represented by Eq. (5.7), where $m_{HB}(\eta)$, $s_{HB}(\eta)$ and $a_{HB}(\eta)$ are the plastic strain-dependent parameters in the Hoek-Brown strain-softening model (Hoek et al., 2002).

$$F_{\mathrm{HB}}=\sigma_\theta-\sigma_r-\sigma_{\mathrm{ci}}\left[m_{\mathrm{HB}}(\eta)\frac{\sigma_{\mathrm{r}}}{\sigma_{\mathrm{ci}}}+s_{\mathrm{HB}}(\eta)\right]^{a_{\mathrm{HB}}(\eta)} \tag{5.7}$$

where $m_{\mathrm{HB}}=m_{\mathrm{i}}e^{\frac{\mathrm{GSI-100}}{\mathrm{28-14D}}}$, $s_{\mathrm{HB}}=e^{\frac{\mathrm{GSI-100}}{\mathrm{9-3D}}}$ and $a_{\mathrm{HB}}=\frac{1}{2}+\frac{1}{6}\left(e^{-\frac{\mathrm{GSI}}{15}}-e^{-\frac{20}{3}}\right)$; D is a disturbance factor for rock masses. From an engineering point of view, the tunnel deformations obtained using the Hoek-Brown model and the Mohr-Coulomb model are similar (Alejano et al., 2012; Song et al., 2020) and thus, we think it is reasonable to use the equivalent Mohr-coulomb model to represent the tunnel deformation of the Hoek-Brown model. Hence, in this study, if a Hoek-Brown strain-softening model is chosen, the equivalent cohesion and friction angle for each rock mass and stress range will be determined through the fitting process. Then, the equivalent Mohr-Coulomb parameters will be used in the process of derivation. Based on the work of Hoek et al. (2002) the equivalent cohesion and friction angle can be obtained from Eqs. (5.8) and (5.9).

$$\phi=\sin^{-1}\left[\frac{6a_{\mathrm{HB}}m_{\mathrm{HB}}\left(s_{\mathrm{HB}}+m_{\mathrm{HB}}\frac{\sigma'_{3\max}}{\sigma_{\mathrm{ci}}}\right)}{2\left(1+a_{\mathrm{HB}}\right)\left(2+a_{\mathrm{HB}}\right)+6a_{\mathrm{HB}}m_{\mathrm{HB}}\left(s_{\mathrm{HB}}+m_{\mathrm{HB}}\frac{\sigma'_{3\max}}{\sigma_{\mathrm{ci}}}\right)^{a_{\mathrm{HB}}-1}}\right] \tag{5.8}$$

$$c = \frac{\sigma_{ci}\left[\left(1+2a_{HB}\right)s_{HB} + \left(1-a_{HB}\right)m_{HB}\dfrac{\sigma'_{3max}}{\sigma_{ci}}\right]\left(s_{HB} + m_{HB}\dfrac{\sigma'_{3max}}{\sigma_{ci}}\right)^{a_{HB}-1}}{\left(1+a_{HB}\right)\left(2+a_{HB}\right)\sqrt{1+\left[6a_{HB}m_{HB}\left(s_{HB} + m_{HB}\dfrac{\sigma'_{3max}}{\sigma_{ci}}\right)^{a_{HB}-1}\right]\Big/\left[\left(1+a_{HB}\right)\left(2+a_{HB}\right)\right]}} \quad (5.9)$$

where σ'_{3max} is the upper limit of the confining stress over which the relationship between the Hoek-Brown and the Mohr-Coulomb criteria is considered. The equivalent method has been adapted from Hoek et al. (2002). The reader is referred to the original source for a detailed description of the equivalent method between the Hoek-Brown and Mohr-Coulomb failure criteria.

The plastic potential in the form of Eq. (5.10) has been adopted, and ψ(η) is the plastic strain-dependent dilatancy angle.

$$G = \sigma_\theta - K_\psi(\eta)\sigma_r \quad (5.10)$$

where $K_\psi(\eta) = \left[1+\sin\psi(\eta)\right]/\left[1-\sin\psi(\eta)\right]$.

5.3. Numerical solutions for supported tunnels

In this work, the process of construction of the supported circular tunnel is divided into 3 stages:

1. *The unsupported circular tunnel stage*: which extends from $x_d = 0$ to $x_d = x_1$, with x_1 being the distance to the tunnel face where the primary support system is installed;

2. *The primary support stage*: which extends from $x_d = x_1$ to $x_d = x_2$, where x_2 represents the distance to the tunnel face where the secondary support system is installed;

3. *The secondary support stage*: which extends from $x_d = x_2$ onwards, where the tunnel is supported by the primary and secondary support systems.

Both displacements and stress compatibility conditions on the interface between the rock mass and the primary support system (rock-support interface), and the interface between the primary and secondary support systems (support-support interface) should be satisfied. Section 5.3.1 introduces the basic theory of the Finite Difference Method (FDM) used in the current research for solving the strain-softening problems. Section 5.3.2 presents the method of determination of the fictitious support forces P_f. Sections 5.3.3 and 5.3.4 present the derivation of the solutions for *the unsupported circular tunnel stage* and *the primary/secondary support stage*, respectively.

5.3.1. The Finite Difference Method (FDM) for strain-softening problems

The Finite Difference Method (FDM) (Lee and Pietruszczak, 2008) has been used for deriving the solutions of strain-softening problems. In the FDM, the plastic zone of the rock mass (including softening and residual area) has been divided into a set of annuli, and the total number of annuli is assumed as n, as shown in Figure 5.5. The outer radius of the first annulus is the radius of plastic zone, *i.e.* $r_{(0)} = R_p$, where R_p represents the radius of the plastic zone; the inner radius of the n-th annulus is the radius of the tunnel wall, *i.e.* $r_{(n)} = R_1$, where R_1 represents the radius of tunnels. The outer and inner radii of the i-th annulus are $r_{(i-1)}$ and $r_{(i)}$, respectively. In each annulus, the material properties are assumed as isotropic, uniform and unchangeable: the material parameters in the i-th annulus are equal to the one at the outer boundary of the i-th annulus, *i.e.* $k_i = k_{(i-1)}$, where k represents the material parameters.

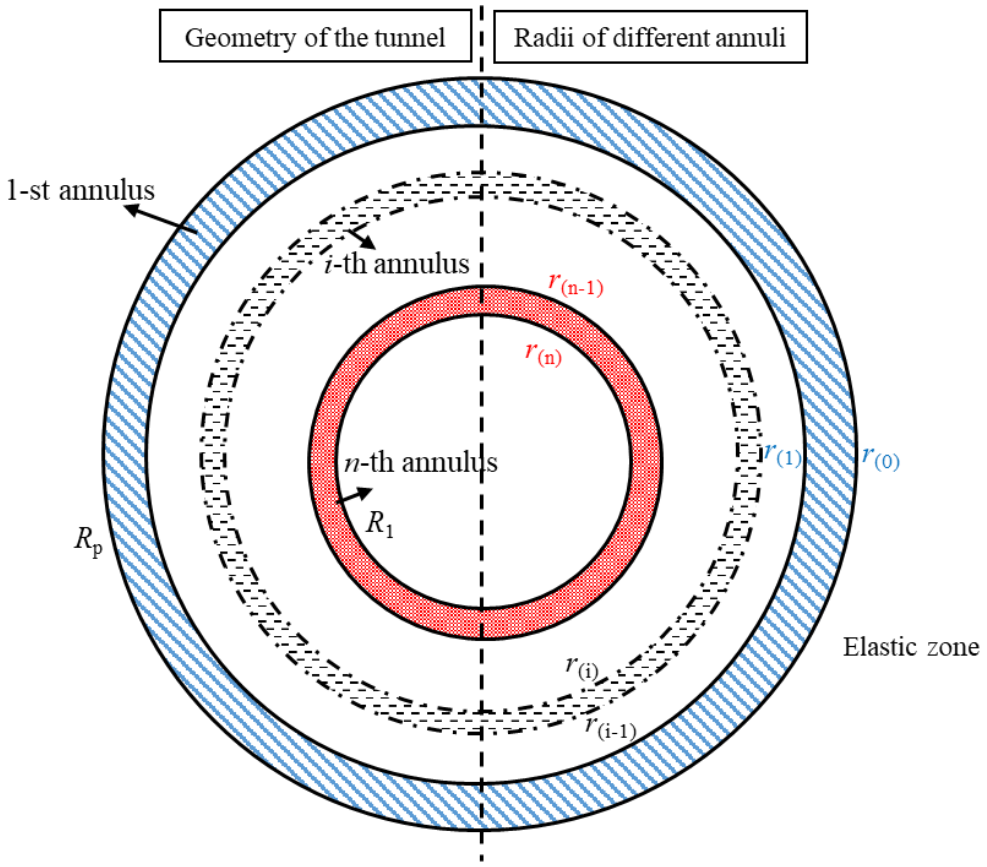

Figure 5.5. The radii of the different *n* annuli used in the numerical procedure.

5.3.2. The determination of the fictitious support forces P_f

In this study, the fictitious support forces P_f are adopted to simulate the effect of the tunnel face. The expression of P_f can be determined by combining the ground reaction curve (GRC) and the longitudinal deformation profile (LDP), and the method to determine P_f has been introduced in detail in Cui et al. (2015). For unsupported tunnels, no interaction support forces act on the tunnels (P_S^{1j} equal to 0), so only the fictitious support forces P_f act on the tunnel wall ($r = R_1$). As e.g. shown in Figure 5.6, at a specific distance to the tunnel face, $x_d = x_k^{(i)}$ (i = 1, 2), the radial displacements $u_r = u_r^{(i)}$ (i = 1, 2) for unsupported tunnels can be determined by using the LDP;

then, combining it with the GRC, the corresponding fictitious support forces $P_f^{(i)}$ (i = 1, 2) can be determined.

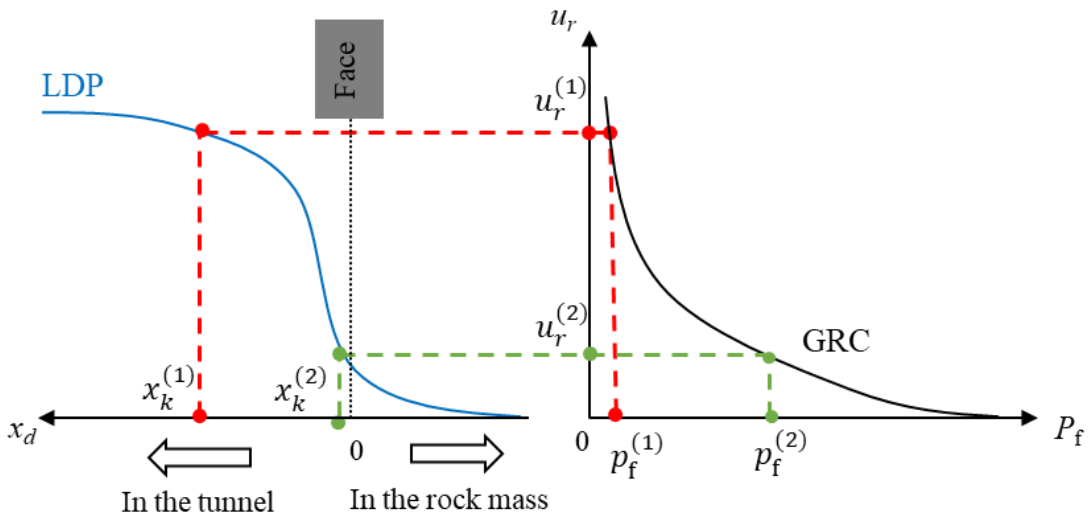

Figure 5.6. Determining of the support forces from tunnel face P_f, by combining the ground reaction curves (GRC) and the longitudinal deformation profiles (LDP). Based on the work of Cui et al. (2015).

To determine the fictitious support forces P_f, the LDP and the GRC should be presented first. A numerical procedure to calculate the GRC, considering the strain-softening behaviour model of rock masses, is presented in the sub-section 5.3.3 (solutions for unsupported tunnels). The solutions for LDP found in Vlachopoulos and Diederichs (2009) have been adopted in this study. Vlachopoulos and Diederichs (2009) presented the LDP for elastic-plastic rock mass shown in Eq. (5.11), with respect to the tunnel geometry, the distance to the tunnel face x_d and the maximum plastic radius R_p^{max}. Initially, the empirical formula by Vlachopoulos and Diederichs (2009) has been developed for rock masses exhibiting EPP behaviour. Furthermore, by comparison with numerical simulations in FLAC (Itasca, 2007 and 2008), Alejano et al. (2012) and Rodriguez-Dono (2011) have proved that the empirical formula of Eq. (5.11) by Vlachopoulos and Diederichs (2009) can be also used for strain-softening rock masses, although

the plastic radius used would be the strain-softening one. Therefore, it is reasonable to choose the empirical formula of Eq. (5.11) by Vlachopoulos and Diederichs (2009) in this research.

$$\frac{u_{\mathrm{r}}^{\mathrm{Rock}}\left(R_1, x_{\mathrm{d}}\right)}{u_{\mathrm{r,max}}^{\mathrm{Rock}}\Big|_{r=R_1}} = \begin{cases} \dfrac{1}{3} e^{\frac{x_{\mathrm{d}}-0.15R_{\mathrm{p}}^{\max}}{R_1}}, \text{for } x_{\mathrm{d}} < 0 \\ 1-\left(1-\dfrac{1}{3} e^{-\frac{0.15R_{\mathrm{p}}^{\max}}{R_1}}\right) e^{-\frac{3x_{\mathrm{d}}}{2R_{\mathrm{p}}^{\max}}}, \text{for } x_{\mathrm{d}} \geq 0 \end{cases} \tag{5.11}$$

where $u_{\mathrm{r,max}}^{\mathrm{Rock}}$ represents the maximum radial displacements and $u_{\mathrm{r}}^{\mathrm{Rock}}$ represents the radial displacements of unsupported tunnels at a distance of x_{d}. Figure 5.7 presents the flow chart for determining the fictitious support forces.

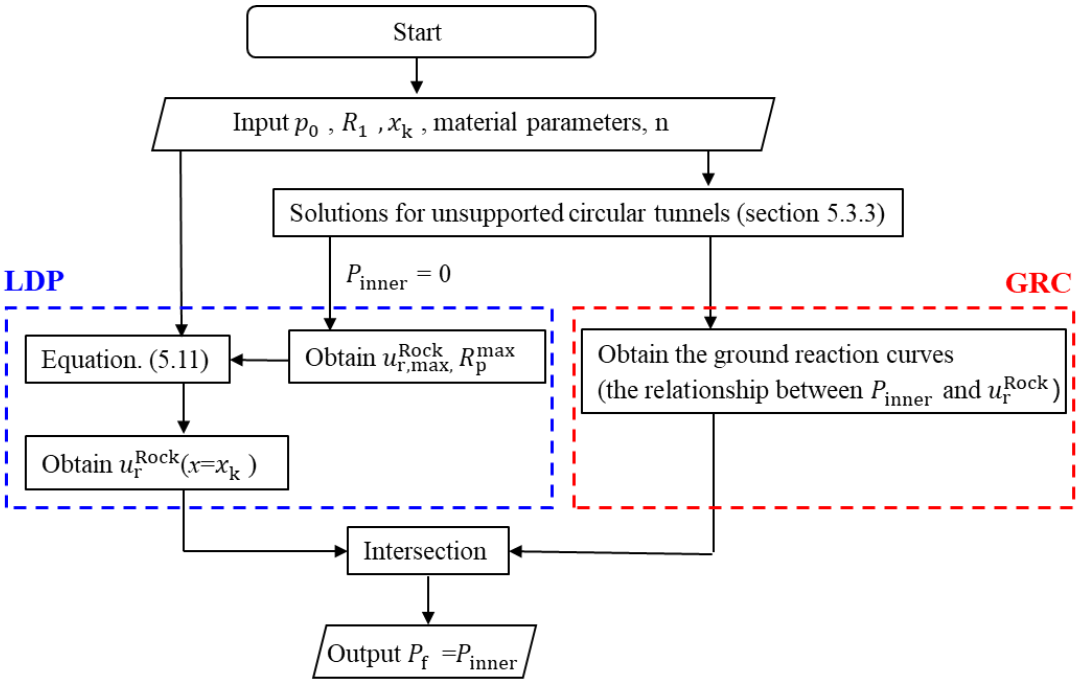

Figure 5.7. The flow chart in determining of the support forces P_{f}, by combining the ground reaction curves (GRC) and the longitudinal deformation profiles (LDP).

5.3.3. Solutions for the unsupported circular tunnels

5.3.3.1. Elastic solutions

Based on the theory of elasticity, the stresses and strains in the elastic area can be expressed as in Eqs. (5.12) and (5.13), respectively.

$$\begin{Bmatrix} \sigma_r^e \\ \sigma_\theta^e \end{Bmatrix} = \begin{Bmatrix} p_0 + \left(\sigma_{R_p} - p_0\right)\dfrac{R_p^2}{r^2} \\ p_0 + \left(p_0 - \sigma_{R_p}\right)\dfrac{R_p^2}{r^2} \end{Bmatrix} \tag{5.12}$$

$$\begin{Bmatrix} \varepsilon_r^e \\ \varepsilon_\theta^e \end{Bmatrix} = \frac{(1+\nu)}{E}\left(\frac{R_p^2}{r^2}\right)\begin{Bmatrix} \sigma_{R_p} - p_0 \\ p_0 - \sigma_{R_p} \end{Bmatrix} \tag{5.13}$$

where σ_r^e (or σ_θ^e) and ε_r^e (or ε_θ^e) represent elastic radial (or hoop) stresses, and incremental radial (or circumferential) strains, respectively; σ_{R_p} represents radial stresses at the elastic-plastic boundary ($r = R_p$). Note that the strains are the incremental strains occurred after the excavation of the tunnel and the stresses are the total stresses.

It should be noted that if the acting force P_{inner} along the tunnel wall is bigger than the critical support force P_{critical}, the whole region of the circular opening will exhibit elastic behaviour, *i.e.* no plastic zone is formed. For the Mohr-Coulomb model, P_{critical} can be expressed in Eq. (5.14) (Lee and Pietruszczak, 2008).

$$p_{\text{critical}} = \frac{2P_0 - S_{\text{p}}}{1 + N_{\text{p}}} \tag{5.14}$$

5.3.3.2. Plastic solutions for circular openings

The outer boundary of the 1-st annulus is the elastic-plastic interface (see Figure 5.5). By substituting $r = R_p$ into Eqs. (5.12) and (5.13), the stresses, strains at the outer boundary of the 1-st annulus can be expressed as in Eqs. (5.15) and (5.16).

$$\begin{Bmatrix} \sigma_{r(0)} \\ \sigma_{\theta(0)} \end{Bmatrix} = \begin{Bmatrix} \sigma_{R_p} \\ 2p_0 - \sigma_{R_p} \end{Bmatrix} \tag{5.15}$$

$$\begin{Bmatrix} \varepsilon_{r(0)} \\ \varepsilon_{\theta(0)} \end{Bmatrix} = \begin{Bmatrix} \dfrac{(1+\nu)\left(\sigma_{R_p} - p_0\right)}{E} \\ \dfrac{(1+\nu)\left(p_0 - \sigma_{R_p}\right)}{E} \end{Bmatrix} \tag{5.16}$$

where σ_{R_p} represents the radial stresses along with the elastic-plastic interface ($r = R_p$).

Based on the FDM described in the section 5.3.1, in the 1-st annulus, the material parameters should be equal to the material parameters at the outer boundary of the 1-st annulus (plastic zone), *i.e.* the peak values of plastic parameters. And thus, the properties of the 1-st annulus should satisfy the peak failure criterion, which can be expressed as in Eq. (5.17).

$$F_1^{\mathrm{MC}} = \sigma_\theta - N_{(0)}(\eta)\sigma_r - S_{(0)}(\eta) \tag{5.17}$$

where $N_{(0)}(\eta) = N_p = \left[1+\sin\varphi_p\right] / \left[1-\sin\varphi_p\right]$, $S_{(0)}(\eta) = 2c_p\sqrt{N_p}$.

Combining the expressions of stresses (5.15) and the peak failure criterion (5.17), the radial stresses in the elastic-plastic interface σ_{R_p} can be expressed as in Eq. (5.18).

$$\sigma_{R_p} = \frac{2P_0 - S_{(0)}(\eta)}{1 + N_{(0)}(\eta)} \tag{5.18}$$

No plastic strain occurs in the outer boundary of the 1-st annulus, *i.e.* $\varepsilon_{r(0)}^p = \varepsilon_{\theta(0)}^p = 0$. The failure criterion in the *i*-th annulus, can be expressed as in Eq. (5.19).

$$F_{\mathrm{i}}^{\mathrm{MC}} = \sigma_{\theta i} - N_{(i-1)}\sigma_{ri} - S_{(i-1)} \tag{5.19}$$

where $N_{(i-1)}(\eta) = \left[1+\sin\varphi_{(i-1)}(\eta)\right] \Big/ \left[1-\sin\varphi_{(i-1)}(\eta)\right]$, $S_{(i-1)}(\eta) = 2c_{(i-1)}(\eta)\sqrt{N_{(i-1)}(\eta)}$; $c_{(i-1)}(\eta)$ and $\varphi_{(i-1)}(\eta)$ represents the cohesion and friction angle at the outer boundary of the *i*-th annulus.

A constant radial stress increment, $\Delta\sigma_r$, is assumed for each annulus, and thus, the radial stress increment can be expressed as in Eq. (5.20).

$$\Delta\sigma_r = \frac{P_{\mathrm{inner}} - \sigma_{R_p}}{n} \tag{5.20}$$

On the other hand, the radial stresses at the inner boundary of the *i*-th annulus $\sigma_{r(i)}$, can be expressed by the radial stresses at the outer boundary $\sigma_{r(i-1)}$, as shown in Eq. (5.21).

$$\sigma_{r(i)} = \sigma_{r(i-1)} + \Delta\sigma_r \tag{5.21}$$

And thus, the hoop stresses are expressed as in Eq. (5.22).

$$\sigma_{\theta(i)} = N_{(i-1)}\sigma_{r(i)} + S_{(i-1)} \tag{5.22}$$

In the derivation, both the radius r and displacements u_{r} are normalized by dividing by the peak plastic radius R_{p}, *i.e.*, $\tilde{r} = r \big/ R_{\mathrm{p}}$ and $\tilde{u} = u \big/ R_{\mathrm{p}}$, where $\tilde{x}$ represent the normalized variable of x. And thus, the normalized peak plastic radius is equal to 1, *i.e.*, $\tilde{r}_{\mathrm{p}} = \tilde{r}_{(0)} = 1$. For the axisymmetric problem, the equilibrium equation in the *i*-th annulus can be expressed as in Eq. (5.23).

$$\frac{d\sigma_{\mathrm{ri}}}{d\tilde{r}} + \frac{\sigma_{\mathrm{ri}} - \sigma_{\theta\mathrm{i}}}{\tilde{r}} = 0 \tag{5.23}$$

The strain in the *i*-th annulus can be obtained by geometric relations, as shown in Eq. (5.24).

$$\begin{cases} \varepsilon_{\mathrm{ri}} = \dfrac{d\tilde{u}_{\mathrm{i}}}{d\tilde{r}} \\ \varepsilon_{\theta \mathrm{i}} = \dfrac{\tilde{u}_{\mathrm{i}}}{\tilde{r}} \end{cases} \tag{5.24}$$

The strain can be decomposed into an elastic and a plastic parts, as shown in Eq. (5.25).

$$\begin{Bmatrix} \varepsilon_{\mathrm{ri}} \\ \varepsilon_{\theta \mathrm{i}} \end{Bmatrix} = \begin{Bmatrix} \varepsilon_{\mathrm{ri}}^{\mathrm{e}} \\ \varepsilon_{\theta \mathrm{i}}^{\mathrm{e}} \end{Bmatrix} + \begin{Bmatrix} \varepsilon_{\mathrm{ri}}^{\mathrm{p}} \\ \varepsilon_{\theta \mathrm{i}}^{\mathrm{p}} \end{Bmatrix} \tag{5.25}$$

where the elastic strain can be expressed as in Eq. (5.26), and the plastic strains satisfy the flow rule as shown in Eq. (5.27).

$$\begin{cases} \varepsilon_{\mathrm{ri}}^{\mathrm{e}} = \dfrac{1-\nu^2}{E}\left[\left(\sigma_{\mathrm{ri}} - P_0\right) - \dfrac{\nu}{1-\nu}\left(\sigma_{\theta \mathrm{i}} - P_0\right)\right] \\ \varepsilon_{\mathrm{ri}}^{\mathrm{e}} = \dfrac{1-\nu^2}{E}\left[\left(\sigma_{\theta \mathrm{i}} - P_0\right) - \dfrac{\nu}{1-\nu}\left(\sigma_{\mathrm{ri}} - P_0\right)\right] \end{cases} \tag{5.26}$$

$$\varepsilon_{\mathrm{ri}}^{\mathrm{p}} + K_{\psi(\mathrm{i}\text{-}1)}\varepsilon_{\theta \mathrm{i}}^{\mathrm{p}} = 0 \tag{5.27}$$

where $K_{\psi(\mathrm{i}\text{-}1)}(\eta) = \left[1 + \sin\psi_{(\mathrm{i}\text{-}1)}(\eta)\right] \Big/ \left[1 - \sin\psi_{(\mathrm{i}\text{-}1)}(\eta)\right]$.

The boundary conditions can be expressed as in Eq. (5.28).

$$\begin{cases} \sigma_{\mathrm{ri}} = \sigma_{\mathrm{r}(\mathrm{i}\text{-}1)}, \ \text{for } \tilde{r} = \tilde{r}_{(\mathrm{i}\text{-}1)} \\ \tilde{u}_{\mathrm{ri}} = \tilde{u}_{\mathrm{r}(\mathrm{i}\text{-}1)}, \quad \text{for } \tilde{r} = \tilde{r}_{(\mathrm{i}\text{-}1)} \end{cases} \tag{5.28}$$

In the *i*-th annulus, combining the failure criterion equation (5.19), the equilibrium equation (5.23), and the stress boundary conditions equations (5.28), the stresses can be expressed as in Eq. (5.29).

$$\begin{cases} \sigma_{\mathrm{ri}} = \dfrac{S_{(\mathrm{i}-1)}}{1 - N_{(\mathrm{i}-1)}} + \left(\dfrac{\tilde{r}_{\mathrm{i}}}{\tilde{r}_{(\mathrm{i}-1)}}\right)^{N_{(\mathrm{i}-1)}-1}\left[\sigma_{\mathrm{r}(\mathrm{i}-1)} - \dfrac{S_{(\mathrm{i}-1)}}{1 - N_{(\mathrm{i}-1)}}\right] \\ \sigma_{\theta \mathrm{i}} = N_{(\mathrm{i}-1)}\sigma_{\mathrm{ri}} + S_{(\mathrm{i}-1)} \end{cases} \tag{5.29}$$

Thus, the corresponding elastic strain in the *i*-th annuli can be obtained by substituting Eq. (5.29) into Eq. (5.26). Combining Eqs. (5.21) and (5.29), the inner radius of the *i*-th annuli can be expressed as in Eq. (5.30).

$$\tilde{r}_{(\mathrm{i})} = \tilde{r}_{(\mathrm{i}-1)} \left[\frac{\sigma_{\mathrm{r}(\mathrm{i}-1)} + \Delta\sigma_{\mathrm{r}} - \dfrac{S_{(\mathrm{i}-1)}}{1-N_{(\mathrm{i}-1)}}}{\sigma_{\mathrm{r}(\mathrm{i}-1)} - \dfrac{S_{(i-1)}}{1-N_{(i-1)}}} \right]^{\frac{1}{N_{(\mathrm{i}-1)}-1}} \tag{5.30}$$

By combining Eqs. (5.24), (5.25) and (5.27), the differential equation of the normalized radial displacements $\tilde{u}_{\mathrm{i}}$ can be expressed as in Eq. (5.31).

$$\frac{d\tilde{u}_{\mathrm{i}}}{d\tilde{r}} + K_{\psi(\mathrm{i}-1)} \frac{\tilde{u}_{\mathrm{i}}}{\tilde{r}} = f_{(\mathrm{i}-1)} \tag{5.31}$$

where $f_{(\mathrm{i}-1)} = \varepsilon_{\mathrm{ri}}^{\mathrm{e}} + K_{\psi(\mathrm{i}-1)}\varepsilon_{\theta\mathrm{i}}^{\mathrm{e}}$. Combining it with Eq. (5.31) and the compatibility condition of displacements (5.28), the displacements in the *i*-th annuli can be expressed as shown in Eq. (5.32).

$$\tilde{u}_{\mathrm{i}} = \tilde{u}_{(\mathrm{i}-1)} \left(\frac{\tilde{r}_{(\mathrm{i}-1)}}{\tilde{r}} \right)^{K_{\psi(\mathrm{i}-1)}} + \tilde{r}^{-K_{\psi(\mathrm{i}-1)}} \int_{\tilde{r}_{(\mathrm{i}-1)}}^{\tilde{r}} f_{(\mathrm{i}-1)} \tilde{r}^{K_{\psi(\mathrm{i}-1)}} d\tilde{r} \tag{5.32}$$

Substituting Eq. (5.32) into Eq. (5.24), and combining it with Eqs. (5.25) and (5.26), the plastic strain in the *i*-th annulus can be expressed as in Eq. (5.33).

$$\begin{cases} \varepsilon_{\theta\mathrm{i}}^{\mathrm{p}} = \dfrac{\tilde{u}_{\mathrm{i}}}{\tilde{r}_{\mathrm{i}}} - \varepsilon_{\theta\mathrm{i}}^{\mathrm{e}} \\ \varepsilon_{\mathrm{ri}}^{\mathrm{p}} = -K_{\psi(\mathrm{i}-1)}\varepsilon_{\theta\mathrm{i}}^{\mathrm{p}} \end{cases} \tag{5.33}$$

And thus, the softening parameter at $r = r_{\mathrm{i}}$ can be expressed as in Eq. (5.34).

$$\eta_{\mathrm{i}} = \varepsilon_{\theta\mathrm{i}}^{\mathrm{p}} - \varepsilon_{\mathrm{ri}}^{\mathrm{p}} \tag{5.34}$$

Consequently, the material parameters of the rock mass can be updated by substituting Eq. (5.34) into Eq. (5.3). For the case of $\eta_i = \eta^*$, the corresponding radius $\tilde{r}_i$ represents the normalized residual plastic radius $\tilde{r}_s$.

Repeating the numerical calculation procedure for *n* times, the stress on the last annulus $\sigma_{r(n)}$ reach the value of the inner pressure acting on the surface of the circular opening with $r = R_1$ ($P_{inner}=P_f + P_s^{1j}$). Then, the peak plastic radius can be expressed as in Eq. (5.35).

$$R_p = \frac{R_1}{\tilde{r}_{(n)}} \tag{5.35}$$

The radial displacements and the residual plastic radius can be expressed as in Eqs. (5.36) and (5.37), respectively.

$$u_i = \tilde{u}_i R_p \tag{5.36}$$

$$R_s = \tilde{r}_s R_p \tag{5.37}$$

where the normalized displacements $\tilde{u}_i$ can be obtained from Eq. (5.32). Algorithm 5.1 presents the calculation procedure for the elastic-plastic solutions for circular openings in rock masses.

Algorithm 5.1. Calculation procedure to obtain the elastic-plastic solutions for circular openings in rock masses

Input: R_1, P_0, n, P_{inner}, material parameters, x_d
Calculate the fictitious support forces $P_f(x_d)$, following section 5.3.2 and Figures 5.6 and 5.7
For unsupported tunnels, $P_{inner} = P_f(x_d)$; for supported tunnels $P_{inner} = P_f(x_d) + P_s^{1j}(x_d)$
Calculate $P_{critical}$ using Eq. (5.14)

if Hoek-brown model, **then**
Calculate the equivalent Mohr-Coulomb parameters, based on Eqs. (5.8) and (5.9)
end if

if $P_{inner} > P_{critical}$, **then**

typical elastic solutions

else

$\omega_{(0)} = \omega_p$ (ω represents plastic parameters)

$\sigma_{R_p} = (2P_0 - S_{(0)})/(1+N_{(0)})$, $\Delta\sigma_r = (P_{inner} - \sigma_{R_p})/n$

$\sigma_{r(0)} = \sigma_{R_p}$, $\sigma_{\theta(0)} = 2P_0 - \sigma_{R_p}$

$\varepsilon_{r(0)} = (\sigma_{R_p} - P_0)/(2G)$, $\varepsilon_{\theta(0)} = (P_0 - \sigma_{R_p})/(2G)$

$\varepsilon^p_{r(0)} = 0$, $\varepsilon^p_{\theta(0)} = 0$, $\eta^p_{(0)} = 0$

$\rho_0 = 1$, $\tilde{u}_{r(0)} = u_{r(0)} \big/ R_p = \varepsilon_{\theta(0)} \rho_{(0)}$

do i=1, n

$\tilde{r}_{(i)} = \{[\sigma_{r(i-1)} + \Delta\sigma_r - S_{(i-1)}/(1-N_{(i-1)})]/[\sigma_{r(i-1)} - S_{(i-1)}/(1-N_{(i-1)})]\}^{[1/(N_{(i-1)}-1)]}$

$\sigma_{r(i)} = \sigma_{r(i-1)} + \Delta\sigma_r$, $\sigma_{\theta(i)} = N_{(i-1)}\sigma_{r(i)} + S_{(i-1)}$

$$\varepsilon^e_{r(i)} = \frac{1-\nu^2}{E}\left[\left(\sigma_{r(i)} - p_0\right) - \frac{\nu}{1-\nu}\left(\sigma_{\theta(i)} - p_0\right)\right], \varepsilon^e_{\theta(i)} = \frac{1-\nu^2}{E}\left[\left(\sigma_{\theta(i)} - p_0\right) - \frac{\nu}{1-\nu}\left(\sigma_{r(i)} - p_0\right)\right]$$

$$\tilde{u}_{(i)} = \tilde{u}_{(i-1)}\left(\frac{\tilde{r}_{(i-1)}}{\tilde{r}}\right)^{K_{\psi(i-1)}} + \tilde{r}^{-K_{\psi(i-1)}} \int_{r_{(i-1)}}^{r} f_{(i)}(\tilde{r})\, \tilde{r}^{K_{\psi(i-1)}} d\tilde{r};\ f_{(i)}(r) = \varepsilon^e_{r(i)} + K_{\psi(i-1)}\varepsilon^e_{\theta(i)} \text{ for } \tilde{r} = \tilde{r}_{(i)}$$

$$\varepsilon^p_{\theta(i)} = \frac{\tilde{u}_{(i)}}{\rho_{(i)}} - \varepsilon^e_{\theta(i)},\ \varepsilon^p_{r(i)} = -K_{\psi(i-1)}\varepsilon^p_{\theta(i)}$$

$$\eta^p_{(i)} = \varepsilon^p_{\theta(i)} - \varepsilon^p_{r(i)}$$

if $0 < \eta^p_{(i)} < \eta^*$, **then**

$$\omega_{(i)} = \omega_p - \frac{\omega_p - \omega_s}{\eta^*}\eta^p_{(i)},\ \tilde{r}_s = \tilde{r}_{(i)}$$

else

$$\omega_{(i)} = \omega_s$$

end if

end do

end if

Output: $R_p = R_1/\tilde{r}_{(i)}, R_s = \tilde{r}_s \cdot R_1/\tilde{r}_{(i)}$, $u_r^{rock}(r=R_1) = \tilde{u}_{(i)} \cdot R_1/\tilde{r}_{(i)}$

5.3.4. Solutions for the tunnel with supports

5.3.4.1. Mechanical analysis of the supports

For supports of the type of shotcrete or concrete rings, the parameters of the supports are: shear moduli G_{L1} and G_{L2}, and Poisson's ratios ν_{L1} and ν_{L2}. According to the theory of elasticity, the radial displacements and the stresses of the primary support under the boundary conditions (see Figure 5.2) can be expressed as in Eqs. (5.38) and (5.39), respectively (Wang et al., 2013).

$$u_{rL1}\left(r, x_d\right) = \begin{cases} p_S^{11}\left(x_d\right)\left(\dfrac{1}{2G_{L1}r}\dfrac{R_1^2R_2^2}{R_1^2-R_2^2}\right) + \dfrac{1-2\nu_{L1}}{2G_{L1}}\dfrac{R_1^2 p_S^{11}\left(x_d\right)}{R_1^2-R_2^2}r, x_1 \le x_d < x_2 \\ \left[p_S^{12}\left(x_d\right) - p_S^{22}\left(x_d\right)\right]\left(\dfrac{1}{2G_{L1}r}\dfrac{R_1^2R_2^2}{R_1^2-R_2^2}\right) + \dfrac{1-2\nu_{L1}}{2G_{L1}}\dfrac{R_1^2 p_S^{12}\left(x_d\right) - R_2^2 p_S^{22}\left(x_d\right)}{R_1^2-R_2^2}r, x_d \ge x_2 \end{cases} \tag{5.38}$$

$$\begin{cases} \sigma_{rL1}\left(r, x_d\right) = \begin{cases} \left(1-\dfrac{R_2^2}{r^2}\right)\dfrac{R_1^2}{R_1^2-R_2^2}p_S^{11}\left(x_d\right), x_1 \le x_d < x_2 \\ \left(1-\dfrac{R_2^2}{r^2}\right)\dfrac{R_1^2}{R_1^2-R_2^2}p_S^{11}\left(x_d\right) - \left(1-\dfrac{R_1^2}{r^2}\right)\dfrac{R_2^2}{R_1^2-R_2^2}p_S^{22}\left(x_d\right), x_d \ge x_2 \end{cases} \\ \sigma_{\theta L1}\left(r, x_d\right) = \begin{cases} \left(1+\dfrac{R_2^2}{r^2}\right)\dfrac{R_1^2}{R_1^2-R_2^2}p_S^{11}\left(x_d\right), x_1 \le x_d < x_2 \\ \left(1+\dfrac{R_2^2}{r^2}\right)\dfrac{R_1^2}{R_1^2-R_2^2}p_S^{11}\left(x_d\right) - \left(1+\dfrac{R_1^2}{r^2}\right)\dfrac{R_2^2}{R_1^2-R_2^2}p_S^{22}\left(x_d\right), x_d \ge x_2 \end{cases} \end{cases} \tag{5.39}$$

where p_S^{1j} represents the support forces acting on the outer boundary of the primary support in the j support stage, and j = 1, 2 represent the primary and secondary support stage, respectively;

P_S^{22} represents the support forces acting on the outer boundary of the secondary support (r = R_2) in *the secondary support stage*. The radial displacements and stresses of the secondary support system under the boundary conditions in Figure 5.2 can be expressed as in Eqs. (5.40) and (5.41) (Wang et al., 2013).

$$u_{rL2}\left(r,x_d\right)=P_S^{22}\left(x_d\right)\left(\frac{1}{2G_{L2}r}\frac{R_2^2R_3^2}{R_2^2-R_3^2}\right)+\frac{1-2\nu_{L2}}{2G_{L2}}\frac{R_2^2P_S^{22}\left(x_d\right)}{R_2^2-R_3^2}r, x_d\geq x_2 \tag{5.40}$$

$$\begin{cases}\sigma_{rL2}\left(r,x_d\right)=\left(1-\dfrac{R_3^2}{r^2}\right)\dfrac{R_2^2}{R_2^2-R_3^2}P_S^{22}\left(x_d\right), x_d\geq x_2\\ \sigma_{\theta L2}\left(r,x_d\right)=\left(1+\dfrac{R_3^2}{r^2}\right)\dfrac{R_2^2}{R_2^2-R_3^2}P_S^{22}\left(x_d\right), x_d\geq x_2\end{cases} \tag{5.41}$$

5.3.4.2. Determination of the solutions in the primary support stage, $x_1 \leq x_d < x_2$

The primary support was installed at the distance of $x_d = x_1$. Only the fictitious support forces P_f (x_d) act on the tunnels before the installation of the primary support system, and the support force acting on the rock mass along the tunnel face is equal to P_f (x_1) at the moment of installation. After the installation of the primary support system, both P_f (x_d) and the interaction support forces P_S^{11} (x_d) act on the tunnel wall. Then, with tunnel advancement, the fictitious support forces P_f (x_d) decrease, while the interaction support forces P_S^{11} (x_d) increase. Thus, the compatibility conditions of stresses at the rock-support interface ($r = R_1$) are satisfied. In the derivation, the additional compatibility conditions of displacements should also be satisfied, as shown in Eq. (5.42).

$$u_r^{Rock}\left(R_1,x_d\right)-u_r^{Rock}\left(R_1,x_1\right)=u_{rL1}\left(R_1,x_d\right), \text{ for } x_1\leq x_d\leq x_2 \tag{5.42}$$

where $u_r^{Rock}\left(R_1,x_d\right)=R_1\varepsilon_{\theta(n)}^{Rock}$, $p_s^{11}\left(x_d\right)=\sigma_{r(n)}^{Rock}-p_f\left(x_d\right)$. Then, Eq. (5.42) can be simplified to Eq. (5.43).

$$R_1\varepsilon_{\theta(n)}^{Rock}-u_r^{Rock}\left(R_1,x_1\right)-\left[\frac{1}{2G_Lr}\frac{R_1^2R_2^2}{R_1^2-R_2^2}+\frac{1-2\nu_L}{2G_L}\frac{R_1^3}{R_1^2-R_2^2}\right]\left[\sigma_{r(n)}^{Rock}-p_f\left(x_d\right)\right]=0 \tag{5.43}$$

Below is shown the procedure to obtain the support forces $p_S^{11}(x_d)$:

1. Assume that both P_S^{11} and P_f are 0, to obtain the maximum displacements of the tunnel $u_{r,max}^{Rock}$ and the maximum peak plastic radius R_p^{max} of the unsupported tunnels;
2. Substitute $x_d = x_1$, $u_{r,max}^{Rock}$ and R_p^{max} into Eq. (5.11), to obtain the displacements at the moment of installation of the primary support $u_r^{Rock}\left(R_1, x_1\right)$;
3. Follow the method presented in section 5.3.2, to obtain the fictitious support forces $P_f(x_d)$;
4. Find the specific stress and strain at $x = x_d$, $\sigma_{r(n)}^{Rock}$ and $\varepsilon_{r(n)}^{Rock}$, that can satisfy Eq. (5.43).

The fictitious support forces $P_f(x_d)$, and the interaction support forces $P_S^{11}\left(x_d\right) = \sigma_{r(n)}^{Rock} - P_f(x_d)$, can be obtained through the above steps (1)-(4). In *the primary support stage*, the forces acting on the rock masses are $P_f(x_d) + P_S^{11}\left(x_d\right)$, while the forces acting on the outer and inner boundaries of the primary support are $P_S^{11}(x_d)$ and 0, respectively. Then, the stresses and displacements of the rock mass can be obtained through the method in section 5.3.3; the stress and displacements of the primary support can be obtained by substituting $P_S^{11}(x_d)$ into Eqs. (5.38) and (5.39). It should be noted that the Eq. (5.43) cannot be solved directly, but it can be easily determined by using a numerical calculation method such as the dichotomy method (Atkinson, 2008; Sastry, 2012). Algorithm 5.2 presents the calculation procedure for the elastic-plastic solutions of supported tunnels in *the primary support stage*.

Algorithm 5.2. Calculation procedure to obtain the solutions for tunnels in the primary support stage

Input: R_1, R_2, P_0, n, P_{inner}, material parameters, x_1, x_d, Δf (error limit of f)
Obtain $u_r^{Rock}\left(R_1, x_1\right)$, from Algorithm 5.1
Calculate the fictitious support forces $P_f(x_d)$, following section 5.3.2 and Figures 5.6 and 5.7
$f(\sigma_{r(n)}^{Rock}) = R_1 \varepsilon_{\theta(n)}^{Rock} - u_r^{Rock}\left(R_1, x_1\right) - \left[\frac{1}{2G_L r}\frac{R_1^2 R_2^2}{R_1^2 - R_2^2} + \frac{1-2\nu_L}{2G_L}\frac{R_1^3}{R_1^2 - R_2^2}\right]\left[\sigma_{r(n)}^{Rock} - p_f\left(x_d\right)\right]$

$P_{\text{inner}}\_\text{a}=0$, $P_{\text{inner}}\_\text{b}=P_0$

$P_{\text{inner}} = P_{\text{inner}}\_\text{a}$, $\sigma_{\text{r(n)}}^{\text{Rock}} = P_{\text{inner}}$

Obtain $f\text{a}=f(\text{a})$, from Algorithm 5.1

$P_{\text{inner}} = P_{\text{inner}}\_\text{b}$, $\sigma_{\text{r(n)}}^{\text{Rock}} = P_{\text{inner}}$

Obtain $f\text{b}=f(\text{b})$, from Algorithm 5.1

do while ($f\text{a} - f\text{b} > \Delta f$)

$P_{\text{inner}}\_\text{c}=(P_{\text{inner}}\_\text{a} + P_{\text{inner}}\_\text{b})/2$

$P_{\text{inner}} = P_{\text{inner}}\_\text{c}$, $\sigma_{\text{r(n)}}^{\text{Rock}} = P_{\text{inner}}$

Obtain $f\text{c}=f(\text{c})$, from Algorithm 5.1

if $f\text{a}\cdot f\text{c} \geq 0$ **then**

$f\text{a} = f\text{c}$, a=c

else

$f\text{b} = f\text{c}$, b=c

end if

end do

Output: $P_{\text{s}}^{11}(x_{\text{d}})= P_{\text{inner}}(x_{\text{d}}) - P_{\text{f}}(x_{\text{d}})$, $u_{\text{r}}^{\text{Rock}}\left(R_1, x_{\text{d}}\right)=R_1\,\varepsilon_{\theta(\text{n})}^{\text{Rock}}$

5.3.4.3. Determination of the solutions in the secondary support stage, $x_{\text{d}} \geq x_2$

The secondary support system is installed at the distance of $x_{\text{d}} = x_2$. At the moment of installation of the secondary support ($x_{\text{d}} = x_2$), the support forces acting on the tunnel wall ($r = R_1$) are assumed to be $P_{\text{f}}(x_2)$ and $P_{\text{S}}^{11}\left(x_2\right)$, while the support forces acting on the outer and inner boundary of the primary support system are $P_{\text{S}}^{11}\left(x_2\right)$ and 0, respectively. After the installation of the secondary support ($x_{\text{d}} \geq x_2$), both the fictitious support forces $P_{\text{f}}(x_{\text{d}})$ and the interaction support forces $P_{\text{S}}^{12}(x_{\text{d}})$ act on the tunnel wall, while $P_{\text{S}}^{12}(x_{\text{d}})$ and $P_{\text{S}}^{22}(x_{\text{d}})$ act on the outer and inner boundaries of the primary support system, respectively. Moreover, $P_{\text{S}}^{22}(x_{\text{d}})$ acts on the outer

boundary of the secondary support, meanwhile, at its inner boundary, the acting force is equal to 0.

With tunnel advancement, the fictitious support forces $P_{\mathrm{f}}\ (x_{\mathrm{d}})$ decrease to 0, and the interaction support forces $P_{\mathrm{S}}^{12}\ (x_{\mathrm{d}})$ and $P_{\mathrm{S}}^{22}\ (x_{\mathrm{d}})$ increase to the constant values. The compatibility conditions of stresses at both the rock-support interface ($r = R_1$), and the support-support interface ($r = R_2$), are satisfied. In the derivation, the additional compatibility conditions of displacements should be satisfied, as shown in Eqs. (5.44) and (5.45).

$$u_{\mathrm{r}}^{\mathrm{Rock}}\left(R_1, x_{\mathrm{d}}\right) - u_{\mathrm{r}}^{\mathrm{Rock}}\left(R_1, x_1\right) = u_{\mathrm{rL1}}\left(R_1, x_{\mathrm{d}}\right), x_{\mathrm{d}} \geq x_2 \tag{5.44}$$

$$u_{\mathrm{rL1}}\left(R_2, x_{\mathrm{d}}\right) - u_{\mathrm{rL1}}\left(R_2, x_2\right) = u_{\mathrm{rL2}}\left(R_2, x_{\mathrm{d}}\right), x_{\mathrm{d}} \geq x_2 \tag{5.45}$$

where $u_{\mathrm{r}}^{\mathrm{Rock}}\left(R_1, x_{\mathrm{d}}\right) = R_1 \varepsilon_{\theta(\mathrm{n})}^{\mathrm{Rock}}$, $p_{\mathrm{s}}^{12}\left(x_{\mathrm{d}}\right) = \sigma_{\mathrm{r(n)}}^{\mathrm{Rock}} - p_{\mathrm{f}}\left(x_{\mathrm{d}}\right)$. Moreover, $u_{\mathrm{rL1}}\left(R_1, x_{\mathrm{d}}\right)$, $u_{\mathrm{rL1}}\left(R_2, x_{\mathrm{d}}\right)$ and $u_{\mathrm{rL2}}\left(R_2, x_{\mathrm{d}}\right)$ can be expressed as in Eqs. (5.46), (5.47) and (5.48), respectively.

$$u_{\mathrm{rL1}}\left(R_1, x_{\mathrm{d}}\right) = \mathrm{A} \cdot p_{\mathrm{S}}^{12}\left(x_{\mathrm{d}}\right) - \mathrm{B} \cdot p_{\mathrm{S}}^{22}\left(x_{\mathrm{d}}\right) \tag{5.46}$$

$$u_{\mathrm{rL1}}\left(R_2, x_{\mathrm{d}}\right) = \mathrm{C} \cdot p_{\mathrm{S}}^{12}\left(x_{\mathrm{d}}\right) - \mathrm{D} \cdot p_{\mathrm{S}}^{22}\left(x_{\mathrm{d}}\right) \tag{5.47}$$

$$u_{\mathrm{rL2}}\left(R_2, x_{\mathrm{d}}\right) = \mathrm{E} \cdot p_{\mathrm{S}}^{22}\left(x_{\mathrm{d}}\right) \tag{5.48}$$

where $\mathrm{A} = \left(\frac{1}{2G_{L1}} \frac{R_1 R_2^2}{R_1^2 - R_2^2} + \frac{1-2\nu_{L1}}{2G_{L1}} \frac{R_1^3}{R_1^2 - R_2^2} \right)$,

$\mathrm{B} = \left(\frac{1}{2G_{L1}} \frac{R_1 R_2^2}{R_1^2 - R_2^2} + \frac{1-2\nu_{L1}}{2G_{L1}} \frac{R_1 R_2^2}{R_1^2 - R_2^2} \right)$,

$\mathrm{C} = \left(\frac{1}{2G_{L1}} \frac{R_1^2 R_2}{R_1^2 - R_2^2} + \frac{1-2\nu_{L1}}{2G_{L1}} \frac{R_1^2 R_2}{R_1^2 - R_2^2} \right)$,

$\mathrm{D} = \left(\frac{1}{2G_{L1}} \frac{R_1^2 R_2}{R_1^2 - R_2^2} + \frac{1-2\nu_{L1}}{2G_{L1}} \frac{R_2^3}{R_1^2 - R_2^2} \right)$,

$$\mathrm{E}=\left[\left(\frac{1}{2G_{L2}}\frac{R_2R_3^2}{R_2^2-R_3^2}\right)+\frac{1-2\nu_{L2}}{2G_{L2}}\frac{R_2^3}{R_2^2-R_3^2}\right].$$

Substituting Eqs. (5.46)-(5.48) into Eqs. (5.44) and (5.45), then Eqs. (5.44) and (5.45) can be simplified into Eqs. (5.49) and (5.50).

$$R_1\varepsilon_{\theta(\mathrm{n})}^{\mathrm{Rock}}-u_{\mathrm{r}}^{\mathrm{Rock}}\left(R_1,x_1\right)=\mathrm{A}\cdot\left[\sigma_{\mathrm{r(n)}}^{\mathrm{Rock}}-p_{\mathrm{f}}\left(x_{\mathrm{d}}\right)\right]-\frac{\mathrm{B}\cdot\mathrm{C}}{\mathrm{D}+\mathrm{E}}\left[\sigma_{\mathrm{r(n)}}^{\mathrm{Rock}}-p_{\mathrm{f}}\left(x_{\mathrm{d}}\right)\right]+\frac{\mathrm{B}\cdot\mathrm{C}\cdot P_{\mathrm{S}}^{11}\left(x_2\right)}{\mathrm{D}+\mathrm{E}} \quad (5.49)$$

$$p_{\mathrm{S}}^{22}\left(x_{\mathrm{d}}\right)=\frac{\mathrm{C}\cdot\left[P_{\mathrm{S}}^{12}\left(x_{\mathrm{d}}\right)-P_{\mathrm{S}}^{11}\left(x_2\right)\right]}{\mathrm{D}+\mathrm{E}} \quad (5.50)$$

Here is the procedure to obtain the support forces $P_{\mathrm{S}}^{12}(x_{\mathrm{d}})$ and $P_{\mathrm{S}}^{22}(x_{\mathrm{d}})$:

1. $P_{\mathrm{S}}^{11}\left(x_2\right)$ and $u_{\mathrm{r}}^{\mathrm{Rock}}\left(R_1,x_1\right)$ can be obtained from sub-section 5.3.4.2;
2. Follow the method presented in section 5.3.2, to obtain the fictitious support forces $P_{\mathrm{f}}(x_{\mathrm{d}})$;
3. Obtain the specific stress and strain at $x = x_{\mathrm{d}}$ ($x_{\mathrm{d}} \geq x_2$), finding $\sigma_{\mathrm{r(n)}}^{\mathrm{Rock}}$ and $\varepsilon_{\mathrm{r(n)}}^{\mathrm{Rock}}$, that can satisfy Eq. (5.49). Then, the support forces acting on the outer boundary of the primary support $P_{\mathrm{S}}^{12}\left(x_{\mathrm{d}}\right)$ can be obtained through $P_{\mathrm{S}}^{12}(x_{\mathrm{d}})=\sigma_{\mathrm{r(n)}}^{\mathrm{Rock}}-P_{\mathrm{f}}\ (x_{\mathrm{d}})$;
4. Obtain $P_{\mathrm{S}}^{22}\ (x_{\mathrm{d}})$ by using Eq. (5.50).

For a specific value of x_{d}, $P_{\mathrm{f}}(x_{\mathrm{d}})$, $P_{\mathrm{S}}^{12}\ (x_{\mathrm{d}})$ and $P_{\mathrm{S}}^{22}\ (x_{\mathrm{d}})$ can be obtained through the above steps (1)-(4), and thus, we can determine the forces acting on the rock mass and on the boundaries of the supports. Then, the stresses and displacements for the rock mass can be obtained through the method shown in section 5.3.3. Moreover, the stresses and displacements of the primary and secondary support systems can be calculated by substituting $P_{\mathrm{S}}^{12}\ (x_{\mathrm{d}})$ and $P_{\mathrm{S}}^{22}\ (x_{\mathrm{d}})$ into Eqs. (5.38) -(5.41). It should be noted that Eq. (5.49) cannot be solved directly, but it can be easily determined by using a numerical calculation method such as the dichotomy method (Atkinson, 2008; Sastry, 2012). Algorithm 5.3 presents the calculation procedure for the elastic-plastic solutions of supported tunnels in *the secondary support stage*.

Algorithm 5.3. Calculation procedure to obtain the solutions for tunnels in the secondary support stage

Input: R_1, R_2, R_3, P_0, n, P_{inner}, material parameters, x_1, x_2, x_d, Δf (error limit of f), Δg (error limit of g)

From algorithms 5.1 and 5.2, obtain $P_S^{11}\left(x_2\right)$ and $u_r^{\text{Rock}}\left(R_1, x_1\right)$

Calculate the fictitious support forces $P_f(x_d)$, following section 5.3.2 and Figures 5.6 and 5.7

$$\text{A}=\left(\frac{1}{2G_{L1}}\frac{R_1R_2^2}{R_1^2-R_2^2}+\frac{1-2\nu_{L1}}{2G_{L1}}\frac{R_1^3}{R_1^2-R_2^2}\right)$$

$$\text{B}=\left(\frac{1}{2G_{L1}}\frac{R_1R_2^2}{R_1^2-R_2^2}+\frac{1-2\nu_{L1}}{2G_{L1}}\frac{R_1R_2^2}{R_1^2-R_2^2}\right)$$

$$\text{C}=\left(\frac{1}{2G_{L1}}\frac{R_1^2R_2}{R_1^2-R_2^2}+\frac{1-2\nu_{L1}}{2G_{L1}}\frac{R_1^2R_2}{R_1^2-R_2^2}\right)$$

$$\text{D}=\left(\frac{1}{2G_{L1}}\frac{R_1^2R_2}{R_1^2-R_2^2}+\frac{1-2\nu_{L1}}{2G_{L1}}\frac{R_2^3}{R_1^2-R_2^2}\right)$$

$$\text{E}=\left[\left(\frac{1}{2G_{L2}}\frac{R_2R_3^2}{R_2^2-R_3^2}\right)+\frac{1-2\nu_{L2}}{2G_{L2}}\frac{R_2^3}{R_2^2-R_3^2}\right]$$

$$\text{g}(\sigma_{r(n)}^{\text{Rock}})=R_1\varepsilon_{\theta(n)}^{\text{Rock}}-u_r^{\text{Rock}}\left(R_1,x_1\right)-\text{A}\cdot\left[\sigma_{r(n)}^{\text{Rock}}-p_f\left(x_d\right)\right]+\frac{\text{B}\cdot\text{C}}{\text{D}+\text{E}}\left[\sigma_{r(n)}^{\text{Rock}}-p_f\left(x_d\right)\right]-\frac{\text{B}\cdot\text{C}\cdot P_S^{11}\left(x_2\right)}{\text{D}+\text{E}}$$

P_{inner}_d=0, P_{inner}_e=P_0

$P_{\text{inner}} = P_{\text{inner}}$_d, $\sigma_{r(n)}^{\text{Rock}} = P_{\text{inner}}$

Obtain gd=g(d), from Algorithm 5.1

$P_{\text{inner}} = P_{\text{inner}}$_e, $\sigma_{r(n)}^{\text{Rock}} = P_{\text{inner}}$

Obtain ge=g(e), from Algorithm 5.1

do while (gd – ge > Δg)

P_{inner}_m=(P_{inner}_d + P_{inner}_e)/2

$P_{\text{inner}} = P_{\text{inner}}$_m, $\sigma_{r(n)}^{\text{Rock}} = P_{\text{inner}}$

Obtain gm=g(m), from Algorithm 5.1

if gd·gm ≥ 0

*g*d = *g*m, d=m

else

*g*e = *g*m, e=m

end if

end do

Output: $u_{\mathrm{r}}^{\mathrm{Rock}}\left(R_1, x_{\mathrm{d}}\right)=R_1 \varepsilon_{\theta(\mathrm{n})}^{\mathrm{Rock}}$, $P_{\mathrm{S}}^{12}\left(x_d\right)=\sigma_{\mathrm{r(n)}}^{\mathrm{Rock}} \square P_{\mathrm{f}}\left(x_{\mathrm{d}}\right)$, $p_{\mathrm{S}}^{22}\left(x_{\mathrm{d}}\right)=\dfrac{\mathrm{C}\cdot\left[P_{\mathrm{S}}^{12}\left(x_{\mathrm{d}}\right)-P_{\mathrm{S}}^{11}\left(x_2\right)\right]}{\mathrm{D}+\mathrm{E}}$

5.3.4.4. Reliability analysis of the supported tunnels

Concerning the support systems, the failure happens when the equivalent stress exceeds the allowable stress of the constitutive material (Do et al., 2020; Song et al., 2018a). The equivalent stress F^{L} of the primary (L1) and secondary (L2) support systems are defined as shown in Eqs. (5.51) and (5.52), respectively (Do et al., 2020). We assume that the support system will fail in case $F^{\mathrm{L}} \leq 0$.

$$F^{\mathrm{L1}}=\sigma_{\mathrm{cL1}}-\left|\sigma_{\theta \mathrm{L1}}-\sigma_{\mathrm{rL1}}\right| \tag{5.51}$$

$$F^{\mathrm{L2}}=\sigma_{\mathrm{cL2}}-\left|\sigma_{\theta \mathrm{L2}}-\sigma_{\mathrm{rL2}}\right| \tag{5.52}$$

where σ_{cL1} and σ_{cL2} represent the compressive strength of the primary and secondary support system, respectively. Following the conclusions in Song et al. (2018a), the points at the inner boundary of the concrete liners are the most critical points of the supports, *i.e.* the first points that would start to fail. In this research, the safety factor of the primary and secondary support systems are defined as shown in Eqs. (5.53) and (5.54), respectively.

$$F_{\mathrm{safety}}^{\mathrm{L1}}=\frac{\sigma_{\mathrm{cL1}}}{\left|\sigma_{\theta \mathrm{L1}}-\sigma_{\mathrm{rL1}}\right|}, \qquad r=R_2 \tag{5.53}$$

$$F_{\mathrm{safety}}^{\mathrm{L2}}=\frac{\sigma_{\mathrm{cL2}}}{\left|\sigma_{\theta \mathrm{L2}}-\sigma_{\mathrm{rL2}}\right|}, \qquad r=R_3 \tag{5.54}$$

Consequently, the safety factor of the combined support system can be defined as shown in Eq. (5.55).

$$F_{\text{safety}} = \min\left[F_{\text{safety}}^{\text{L1}}, F_{\text{safety}}^{\text{L2}} \right] \tag{5.55}$$

where min [$x1$, $x2$] represents the minimum value of $x1$ and $x2$.

For a simplified case on which the support forces (P_{S}) only act on the outer boundary of the liner (R_{outer}) and no support forces act on the inner boundary of the liner (R_{inner}), *e.g.* the case of the secondary support system, combining the Eqs. (5.39), (5.41) and (5.51), (5.52), the equivalent stress F^{L} can be simplified to Eq. (5.56).

$$F^{\text{L}} = \sigma_{\text{cL}} - 2P_{\text{S}} \frac{R_{\text{outer}}^2}{R_{\text{outer}}^2 - R_{\text{inner}}^2} \tag{5.56}$$

Thus, by assigning F^{L} equal to 0 in Eq. (5.56), the maximum support forces that the support system can accept ($P_{\text{S}}^{\max}$) can be expressed as in Eq. (5.57) and its safety factor ($F_{\text{safety}}^{\text{L}}$) can be expressed as in Eq. (5.58).

$$P_{\text{S}}^{\max} = \frac{1}{2}\sigma_{\text{cL}}\left(1 - \frac{R_{\text{inner}}^2}{R_{\text{outer}}^2}\right) \tag{5.57}$$

$$F_{\text{safety}}^{\text{L}} = \frac{\sigma_{\text{cL}}}{2P_{\text{S}}}\left(1 - \frac{R_{\text{inner}}^2}{R_{\text{outer}}^2}\right) \tag{5.58}$$

It should be noted that the expressions of the maximum support forces $P_{\text{S}}^{\max}$ and the safety factor $F_{\text{safety}}^{\text{L}}$ are consistent with those used in the CCM for the above simplified case (Oreste, 2003).

However, for tunnels with a combined support system, the support forces not only act on the outer boundary but also on the inner boundary of the primary support system, and thus, the support forces and the safety factor should be determined by the compatibility conditions of the tunnels. Therefore, at this point, the CCM meets one of its limitations: the design of tunnels with a combined support system.

5.3.5. Application in the design of non-circular tunnels

Although the obtained solutions are rigorously applicable only for the supported circular tunnels, the solutions are meaningful for a much wider range of non-circular tunnels (Bonini et al., 2009; Kabwe et al., 2020b and 2020c; Zhang et al., 2019a). By using the equivalent radius (R_{eq}), the proposed solutions may be used to approximate estimate the mechanical response of non-circular tunnels. The equivalent radius (R_{eq}) function can be determined based on the equal area method (Kabwe et al., 2020b and 2020c; Zhang et al., 2019a), as shown in Eq. (5.59).

$$R_{eq} = \sqrt{\frac{A}{\pi}} \tag{5.59}$$

where A represents the cross-section area. The reader is referred to the original source for a detailed description of the equivalent method and its application in the design of non-circular tunnels.

5.4. Verification of the proposed method

5.4.1. Verification of the solutions for unsupported circular tunnels

Alonso et al. (2003) proposed self-similar solutions for the ground reaction curves (GRC) of unsupported circular tunnels. In this sub-section, the results obtained with our proposed numerical solution are compared with those obtained with self-similar solutions (Alejano et al., 2009; Alonso et al., 2003). In the calculation process, the number of annuli *n* adopted is 500. To be consistent with the assumptions of Alonso et al. (2003), no supports and no tunnel advancement have been considered. The Mohr-Coulomb strain-softening behaviour model has been adopted for the rock mass, and the input data is shown in Figure 5.8. In this figure, we can observe a good match between the proposed numerical solutions and the self-similar solutions for the ground reaction curves and the peak and residual plastic radii, which can serve as a verification of the proposed strain-softening solutions for unsupported tunnels.

5.4.2. Verification of the solutions for supported tunnels

The support forces acting on the rock mass are assumed to be the fictitious support forces P_f and the interaction support forces $P_S^{1j}\left(R_1, x_d\right)$. The support forces acting on the outer and inner boundaries of the primary support system are $P_S^{1j}\left(R_1, x_d\right)$ and $P_S^{22}\left(R_2, x_d\right)$, while those acting on the outer and inner boundaries of the secondary support system are $P_S^{22}\left(R_2, x_d\right)$ and 0. The strain-softening solutions of the ground reaction curves have been verified in the section 5.4.1, and thus, as long as the expressions of P_f, P_S^{1j} and P_S^{22} are correct, the solutions for supported tunnels will be acceptable. The adopted method for determining the fictitious support forces P_f has been verified in Cui et al. (2015). Thus, in this sub-section, only the interaction support forces P_S^{1j} and P_S^{22}, as well as the compatibility conditions at the rock-support interface ($r = R_1$) and the support-support ($r = R_2$) are checked to verify the correctness of the derivation.

In this sub-section, an example is carried out to verify the compatibility conditions. A tunnel with radius R_1 = 7 m is excavated in a strain-softening rock mass. Table 5.1 presents the input parameters of the rock mass (Alejano et al., 2009). The primary and secondary support systems present elastic moduli of E_{L1} = 29400 MPa and E_{L2} = 33300 MPa, respectively, and the same Poisson's ratio ($\nu_{L1} = \nu_{L2} = 0.25$) (Carranza-Torres and Fairhurst, 2000). The thickness of the primary and secondary supports is considered: d_1 = 0.20 m and d_2 = 0.25 m. The installation distance of the supports from the tunnel face is considered as x_1 = 2.0 m, x_2 = 7.0 m. In the calculation process, the number of annuli *n* adopted is 500.

Figure 5.9 shows a good agreement between the incremental displacements occurring on the rock mass after the installation of the primary support system ($x_d \geq x_1$; $u_r^{rock}(R_1, x_d) - u_r^{rock}(R_1, x_1)$) and the absolute displacements of the primary support at the rock-support interface ($r = R_1$; $u_{rL1}(R_1, x_d)$). In addition, it can be observed a good agreement between the incremental displacements of the primary support system –occurring after the installation of the secondary support system ($x_d \geq x_{2;}\ u_r^{rock}(R_2, x_d) - u_r^{rock}(R_2, x_2)$)– and the absolute displacements of the

secondary support system at the support-support interface ($r = R_2$; $u_{rL2}(R_2, x_d)$). It can be noted that the solutions perfectly satisfy the compatibility conditions of both rock-support interface ($r = R_1$) and support-support interface ($r = R_2$). Therefore, we can confirm that the solutions for the supported circular tunnels are correct.

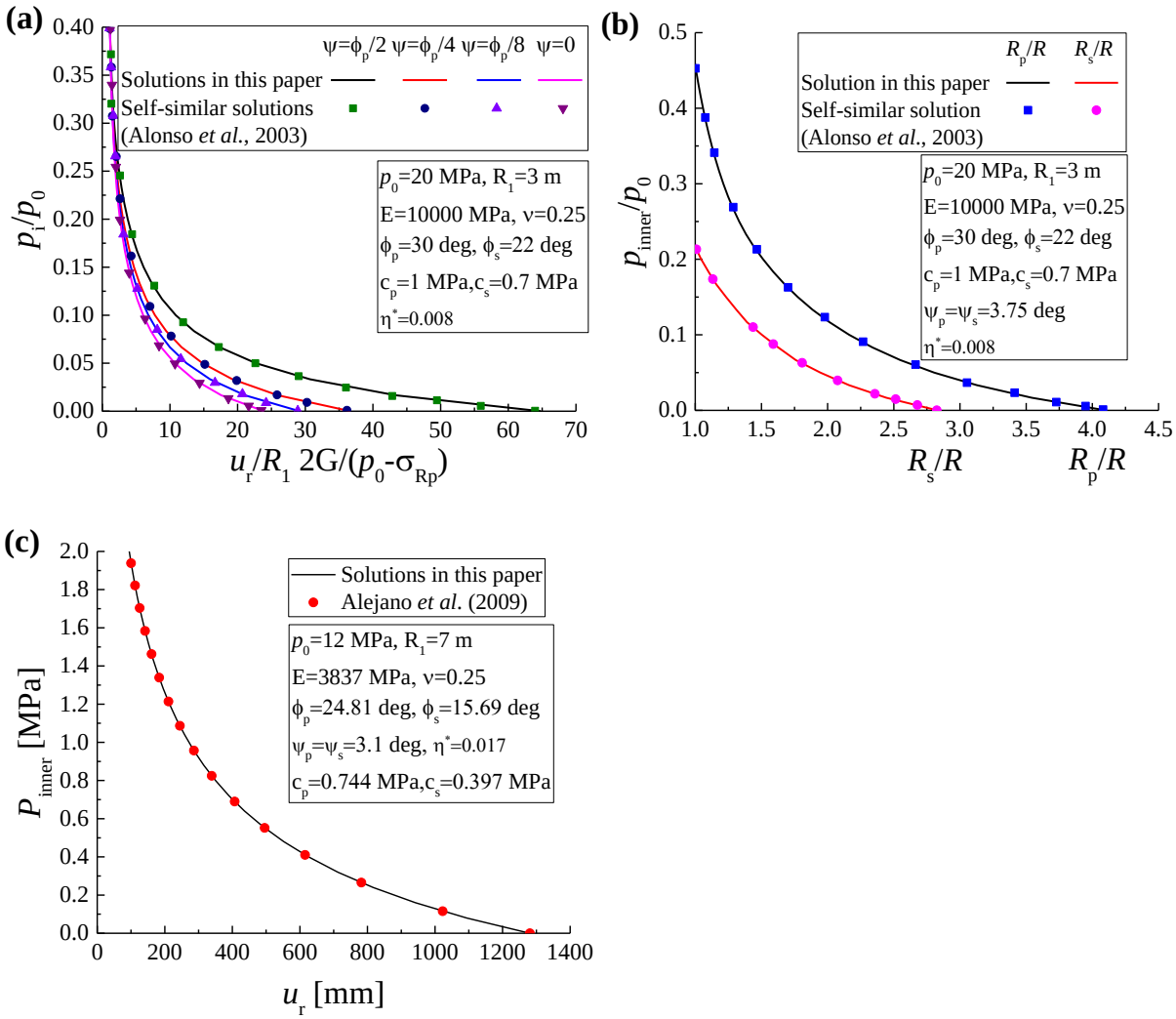

Figure 5.8. Comparison of **(a)** normalized displacements, **(b)** normalized peak and residual plastic radii, and **(c)** absolute displacements, for the circular openings between the proposed solutions and the self-similar solutions.

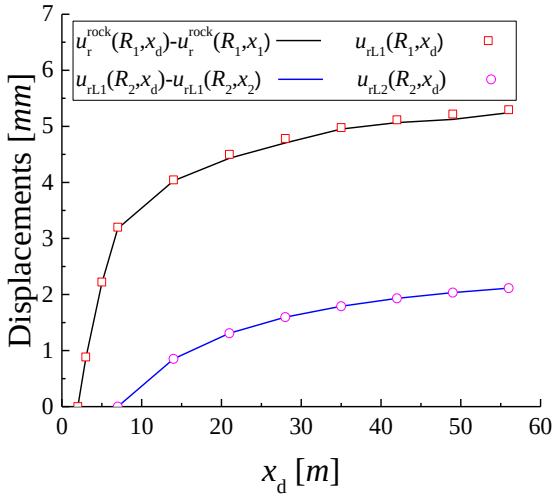

Figure 5.9. Comparison of incremental displacements on the surrounding rock mass occurring after the installation of supports, and the displacements of supports.

Table 5.1. Input parameters of the rock mass.

Input parameters of the rock mass					
GSI	peak	55	Dilatancy	ψ_p [deg]	3.1
	residual	33		ψ_s [deg]	3.1
Cohesion	c_p [MPa]	0.744	Softening parameters	η^*	0.017
	c_s [MPa]	0.397	Initial stress	P_0 [MPa]	12
Friction angle	φ_p [deg]	24.81	Elastic modulus	E [MPa]	3837
	φ_s [deg]	15.69	Poisson's ratio	ν	0.25

5.5. Comparison between the proposed method and the convergence-confinement method

In this section, the results obtained from between the proposed method and the convergence-confinement method (CCM) for designing of tunnels with the primary and two support systems are compared in sections 5.5.1 and 5.5.2, respectively. The CCM consists of three basic graphs:

1. The longitudinal deformation profile (LDP), which relates the radial displacements of an unsupported tunnel section with its longitudinal distance to the tunnel face;

2. The ground reaction curve (GRC), which establishes the relationship between the decreasing inner pressure and the increasing radial displacements of the tunnel wall in plane-strain problems;

3. The support characteristic curve (SCC), which represents the stress-strain relationship of the support system.

At the distance $x_d = x_1$ to the tunnel face, *i.e.* point A in Figure 5.10, the radial displacements of the tunnel $u_r^{rock}\left(R_1, x_1\right)$, can be determined by the LDP. Thus, we could obtain the inner pressure at that distance from the GRC (point C). Moreover, the support system is installed at point B, when some convergence has already occurred and, thus, a part of fictitious support forces from the tunnel face P_f has been dissipated and will not be loaded by the support. Point D represents the failure point of the support system. The intersection between the GRC and the SCC in Figure 5.10 represents the equilibrium of the rock-support system, when the load on the support matches the inner pressure in the tunnel (*i.e.* support forces from the tunnel face P_f equal to 0). The detailed description of the CCM can be found in the scientific literature (Alejano et al., 2010; Carranza-Torres and Fairhurst, 2000; Oreste, 2003).

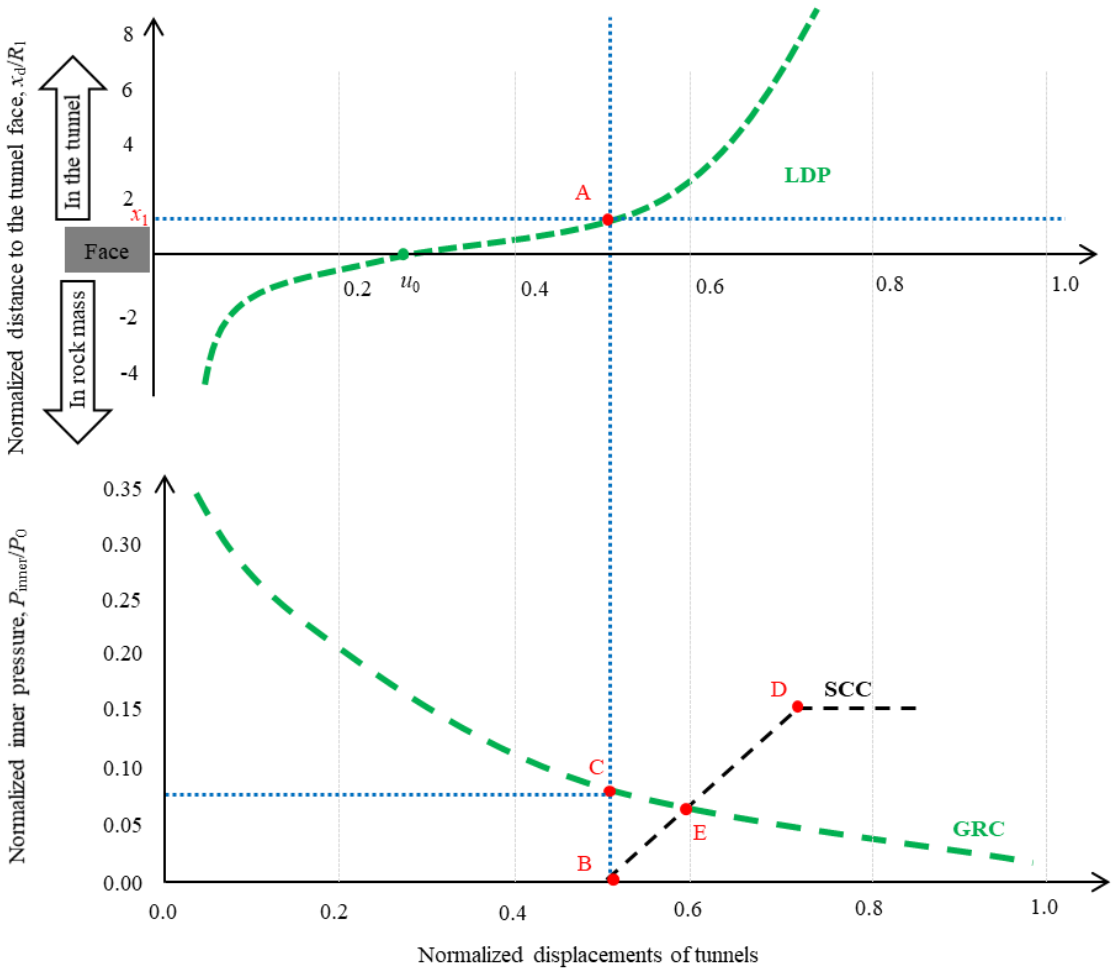

Figure 5.10. Main elements of the convergence-confinement method (CCM). Typical graphs obtained for the longitudinal deformation profile (LDP) –above–, and for the ground reaction curve (GRC) and the support characteristic curve (SCC) –below. Based on the work of Alejano et al. (2009, 2010 and 2012).

In tunnel engineering projects, the primary and secondary support systems are put in place at different times to ensure the temporary and long-term stability of the tunnel, respectively. Oreste (2003) proposed support characteristic curves for a compound support system, extending the application of the CCM for the design of tunnels with a combined support system. Nonetheless, for tunnels with two different support systems, the support forces not only act on the outer boundary but also on the inner boundary of the primary support system, and thus, the support forces and the safety factor should be determined by the compatibility conditions of the tunnels.

However, no compatibility conditions at the interface between supports are considered in the CCM. Therefore, at this point, the CCM meets one of its limitations in the design of secondary support systems. The reason is that the ground reaction curve is modified by the primary support system, and thus, we should use this modified GRC for the correct application of the CCM in the design of the secondary support system. In our proposed method, the real compatibility conditions at both the rock-support interface and the support-support interface are considered, and, hence, the safety factors obtained using our method are probably closer to reality than those obtained using the CCM.

5.5.1. Design of the primary support system

In this sub-section, the results for the design of the primary support system obtained with our proposed method are compared with those from the CCM. In our method, the support forces acting on the rock mass are the sum of the fictitious support forces $P_{\mathrm{f}}(x_{\mathrm{d}})$, and the support forces caused by the interaction between the support and the tunnel $P_{\mathrm{S}}^{1\mathrm{j}}\left(R_{1}, x_{\mathrm{d}}\right)$ (hereinafter referred to as interaction support forces), while only interaction support forces $P_{\mathrm{S}}^{1\mathrm{j}}\left(R_{1}, x_{\mathrm{d}}\right)$ act on the primary support system.

However, in the CCM, as shown in Figure 5.10, at the equilibrium point E, the support forces acting on the rock mass are equal to the support forces acting on the primary support system. In fact, when the distance to the tunnel face x_{d} tends to a big enough value, the fictitious support force from the tunnel face $P_{\mathrm{f}}(x_{\mathrm{d}})$ is zero and, in that case, our solutions are consistent with the solutions of the CCM. Thus, the solutions of the CCM constitute a particular case of the solutions of this study.

To explain it better, an example is carried out herein. The geometry and the material properties are the same as those used in section 5.4.2. The primary support system is installed at a distance x_1 = 10 m from the tunnel face. Based on the CCM, as shown in Figure 5.11, the equilibrium solutions (Point E in Figure 6.10) between the support forces and the displacements on the surrounding rock mass are $P_{\mathrm{inner}} = P_{\mathrm{S}}^{11}\left(R_{1}, \infty\right) = 0.638$ MPa, and $u_{\mathrm{r}}^{\mathrm{rock}} = 0.434$ m, respectively.

In this study, however, we present the equilibrium solutions for the whole process of tunnel advancement, as shown in Figure 5.12. In the calculation process of the proposed solutions, the number of annuli n adopted is 500. With the advancement of the tunnel, the fictitious support force $P_f(x_d)$ decreases from the initial stress to zero, while the support force acting on the primary support system $P_s^{11}(R_1, x_d)$ increases from zero to a constant value at a big enough distance to the tunnel face. In CCM, only the solution for $P_f(x_d)=0$ –*i.e.* big enough distance from tunnel face– is presented. However, the equilibrium solutions of displacements and support forces during the whole process of excavation and advancement are significantly important, especially for the design of the secondary support system.

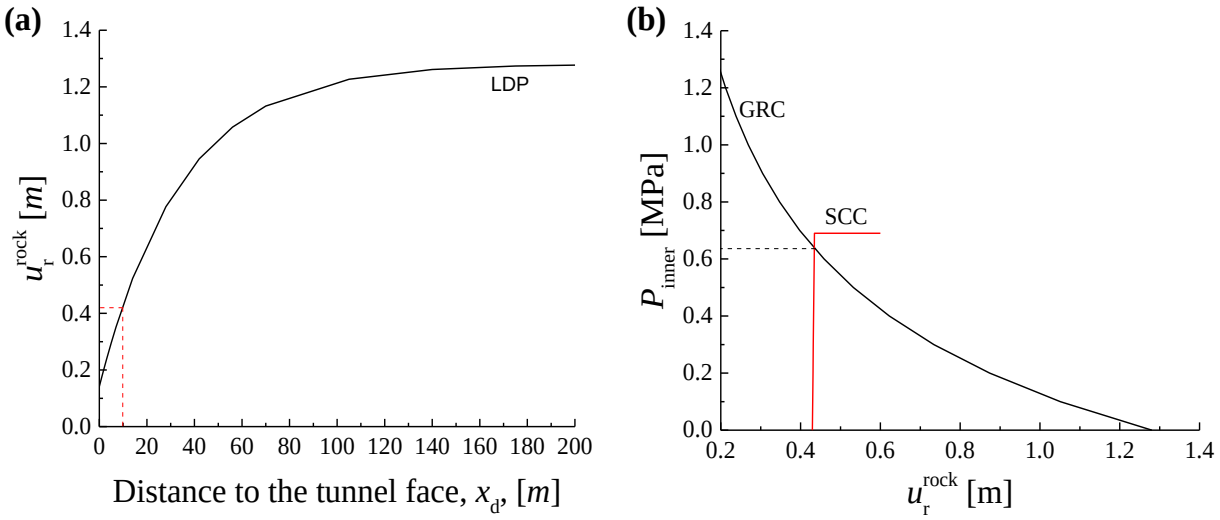

Figure 5.11. **(a)** The longitudinal deformation profile (LDP), **(b)** the ground reaction curve (GRC) and the support characteristic curve (SCC), for a medium quality rock mass using the strain-softening model.

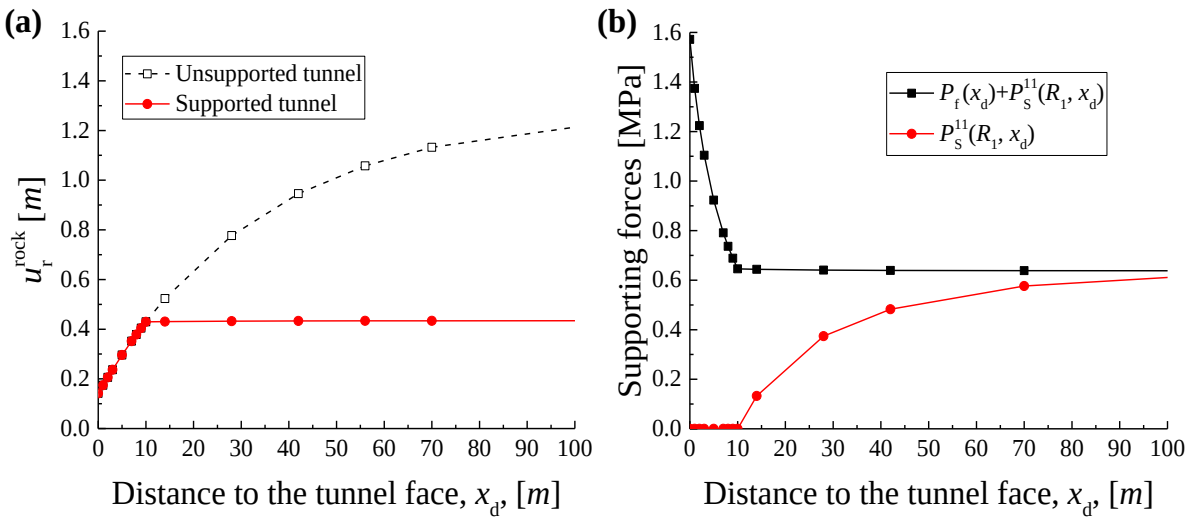

Figure 5.12. **(a)** The displacements of tunnels along with $r = R_1$ for supported and unsupported tunnels, **(b)** support forces act on the rock mass ($P_f(x_d)+P_S^{11}(R_1, x_d)$) and support forces acting on the primary support system ($P_S^{11}(R_1, x_d)$), versus the distance to the tunnel face x_d.

5.5.2. Design for tunnels with two support systems

Regarding the design of tunnels with a combined support system, in this sub-section, we show a comparison between the results obtained with our proposed method and those from the CCM. Thus, an example is carried out herein, where the geometry and the properties of the rock mass are the same as those used in section 5.4.2 (Table 5.1). In the calculation process of the proposed solutions, the number of annuli n adopted is 500. Concerning the thickness d of the support systems, we have selected $d_1 = 0.15$ m for the primary support and $d_2 = 0.20$ m for the secondary support. In addition, two different cases have been considered:

- Case (1): In this case, we consider steel fibre reinforced shotcrete as the primary support system (L1) and a concrete liner as the secondary support (L2). Moreover, their corresponding parameters are: $E_{L1} = 37$ GPa, $E_{L2} = 8$ GPa, $\nu_{L1} = \nu_{L2} = 0.2$, $\sigma_{cL1} = 45$ MPa, $\sigma_{cL2} = 16$ MPa. The primary and secondary support systems are installed at a distance $x_1 = 1$ m and $x_2 = 1.2$ m from the tunnel face, respectively.

- **Case (2)**: In this case, unreinforced shotcrete have been considered for the primary (L1) support system and a concrete liner for the secondary (L2). Their parameters are E_{L1} = 8000 MPa, E_{L2} = 10000 MPa, $\nu_{L1} = \nu_{L2} = 0.2$, σ_{cL1} = 16 MPa, σ_{cL2} = 20 MPa. The primary and secondary support systems are installed at a distance x_1 = 10 m and x_2 = 10.5 m from the tunnel face, respectively.

Hence, following our method, and through a number of calculations, we can obtain the maximum value of the support forces acting on the support systems –when the fictitious support forces P_f are equal to 0 at a certain distance from the tunnel face–, as well as the safety factor.

In this example, according to the proposed method in this study, the maximum values of the support forces ($P^{12}_{S,max}$ and $P^{22}_{S,max}$) and the minimum safety factors of the primary (F^{L1}_{safety}) and secondary (F^{L2}_{safety}) support systems can be obtained for **case (1)** and **case (2)**, as shown in Table 5.2. According to Eqs. (5.53)-(5.55), the safety factor of the combined support system ($F^{L1\text{-}L2}_{safety}$) for **case (1)** and **case (2)** are 0.9 and 1.4, respectively. Regarding the maximum displacements for the tunnel wall $u^{rock}_{r,max}$, for **case (1)** and **case (2)** we obtain 0.18 m and 0.44 m, respectively (Table 5.3). In any case, it must be kept in mind that the maximum displacements obtained –especially in **case (2)**– might not be tolerable, depending of the project.

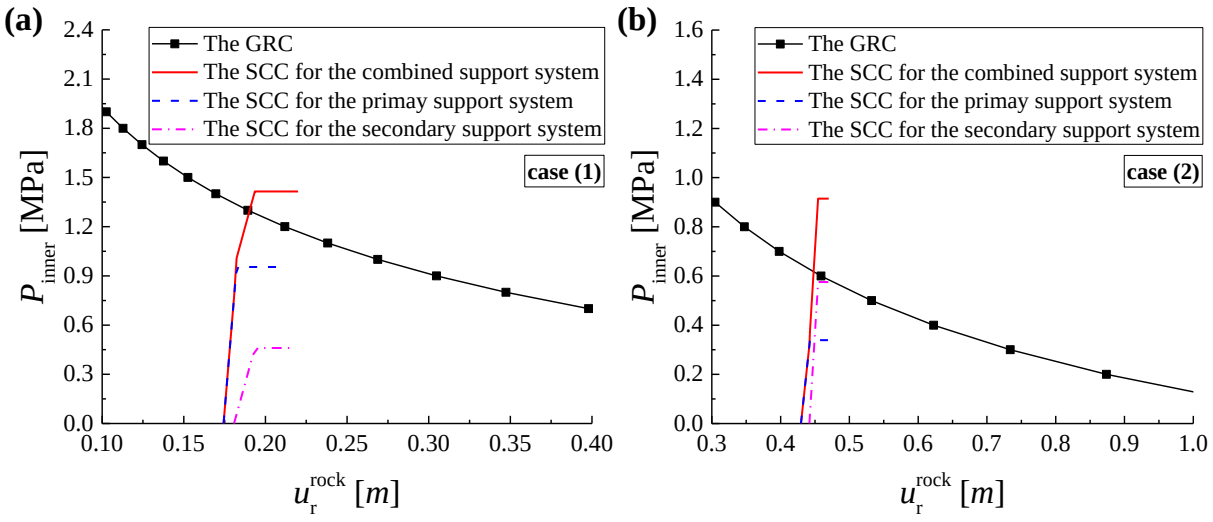

Figure 5.13. Ground reaction curves (GRC) and support characteristic curves (SCC), in the convergence-confinement method (CCM); **(a)** for **case (1)**, and **(b)** for **case (2)**.

Furthermore, following Oreste (Alejano et al., 2009; Oreste, 2015; Oreste, 2003), Figure 5.13 presents the results obtained by the CCM for tunnels with a combined support system. In Figure 5.13, the final support forces that act on the tunnel wall reach a value of around 1.30 MPa for **case (1)**, and around 0.62 MPa for **case (2)**. On the other hand, the maximum tunnel deformations are around 0.19 m for **case (1)** and around 0.45 m for **case (2)**. Based on the CCM, the safety factors for **case (1)** and **case (2)** would be 1.1 and 1.5, respectively, which are different from the safety factors obtained by the method proposed in this study: safety factor: 0.9 for **case (1)**, and 1.4 for **case (2)**.

Table 5.3 shows a comparison between the results obtained with our proposed method and the CCM in terms of maximum displacements on the tunnel wall ($u_{r,max}^{rock}$) and safety factors of the combined support system ($F_{safety}^{L1\text{-}L2}$). We can observe that the maximum displacements obtained with our method are similar, but slightly lower than those obtained with the CCM. However, the safety factors obtained with our method are significantly lower than those obtained using the CCM. The difference in the results between both methods is due to the fact that, unlike the CCM, our method considers the real compatibility conditions at both the rock-support interface ($r = R_1$) and the support-support interface ($r = R_2$). Instead, no compatibility conditions between the primary and secondary support system are considered in the CCM. In consequence, because of an overestimation of the safety factor, the use of the CCM can lead to an unsafe design of tunnels with combined support systems.

Table 5.2. Safety factors ($F_{safety}^{L1\text{-}L2}$) obtained using our proposed method.

	The maximum support forces		The minimum safety factors of the	
Cases	$P_{S,max}^{12}$ [MPa]	$P_{S,max}^{22}$ [MPa]	F_{safety}^{L1}	F_{safety}^{L2}
Case (1)	1.33	0.30	0.9 (failure)	1.5
Case (2)	0.63	0.39	1.4	1.4

Table 5.3. Safety factors ($F_{\text{safety}}^{\text{L1-L2}}$) obtained using our proposed method and the convergence-confinement method (CCM).

	The maximum displacements, $u_{\text{r,max}}^{\text{rock}}$ $[m]$		The safety factor, $F_{\text{safety}}^{\text{L1-L2}}$	
Cases	Our method	CCM	Our method	CCM
Case (1)	0.18	0.19	0.9 (failure)	1.1
Case (2)	0.44	0.45	1.4	1.5

5.6. Analysis and discussion

5.6.1. Discussion on the selection of rock mass behaviour models

In this section, the results of our proposed numerical solutions are analysed using an example. In this example, three different models have been used, including the elastic-perfectly-plastic (EPP), strain-softening (SS) and elastic-brittle (EB) behaviour models. Nonetheless, note that the SS model can be simplified to the EPP model by assigning a big enough value of η^* (in this example, $\eta^* = 1.0$), or to the EB model by assigning a small value of η^* (in this example, $\eta^* = 0$). In addition, four different quality rock masses have been considered in the analysis. Table 5.4 presents the parameters of the different rock masses considered. In the calculation process, the number of annuli n adopted is 500.

On the other hand, the primary and secondary support systems are installed at the distance x_1 = 2.5 m, and x_2 = 10 m, respectively. The primary and secondary support systems are assumed to behave as elastic materials. The elastic properties (elastic modulus and Poisson's ratio) of the primary (L1) and secondary (L2) supports systems are: E_{L1} = 8000 MPa, E_{L2} = 12000 MPa, and $\nu_{\text{L1}} = \nu_{\text{L2}} = 0.15$. The tunnel has a diameter of 5 m and its depth of 1500 m implies a field stress of 37.5 MPa (Alejano et al., 2012). Rock mass specific weight is 25 KN/m^3 and the Poisson's ratio is 0.25 (Alejano et al., 2012). The radii related to the primary and secondary support systems (see Figures 5.1 and 5.2) are: R_1 = 2.5 m, R_2 = 2.4 m and R_3 = 2.25 m.

Table 5.4. Input parameters of four different quality rock masses.

Input parameters of four different quality rock masses						
Different quality rock masses			A2	B2	C2	D2
GSI	Peak value	GSI_{peak}	75	60	50	40
	Residual value	GSI_{res}	40	35	30	27
Elastic parameters	Elastic modulus	E (MPa)	36500	15400	8660	4870
	Passion's Ratio	v	0.25	0.25	0.25	0.25
Post-failure behaviour	Peak values	Cohesion (MPa)	3.637	2.67	2.24	1.88
		Friction angle (deg)	29.52	25.7	23.1	20.6
	Residual values	Cohesion (MPa)	1.878	1.71	1.54	1.43
		Friction angle (deg)	20.64	19.4	18.2	17.5
	Dilatancy angle	$\psi_{peak}=\psi_{res}$ (deg)	7.38	4.49	2.89	1.55
	Critical softening parameter	η^*	0.0011	0.0062	0.0288	0.119

Figure 5.14 shows the displacements (u_r^{rock}) along the tunnel wall ($r = R_1$) versus the distance to the tunnel face (x_d) for a variety of cases, *i.e.* the longitudinal deformation profiles. These results meet the same conclusion of Alejano et al. (2012): there are significant differences in the displacements of unsupported tunnels when using different behaviour models (EPP, SS or EB), and the difference between the displacements of tunnels calculated for EB rock masses and for SS rock masses grows as the GSI decreases.

In addition, in this study, it can be found that the behaviour model selection also makes a significant effect on the behaviour of supported tunnels. It is therefore important to note that SS behaviour plays a role in the behaviour of tunnels, and hence, in the design and installation of supports. In Figure 5.14, it can be observed that, initially, the displacements gradually increase with the tunnel advancement, as expected (e.g. Alejano et al., 2012 (Alejano et al., 2012)).

However, after the installation of the support system, the displacement rate decelerates suddenly and the maximum displacement achieved is significantly lower.

The support forces acting on the tunnel wall are the sum of the fictitious support forces P_f and the interaction support forces at the rock-support interface P_S^{1j} (j = 1, 2 represent the primary and secondary support stages, respectively). Moreover, the support forces acting on the outer boundary of the primary support system (r = R_1) are P_S^{1j} and the support forces at the support-support interface (r = R_2) are P_S^{22}.

Figure 5.15 and 5.16 respectively present the acting forces on the tunnel wall and on the support systems versus the distance to the tunnel face. In Figure 5.15, we can observe that the support forces acting on the tunnel wall ($P_f + P_S^{1j}$) decrease with the increasing distance to the tunnel face, and eventually reach a constant value. P_f represents the fictitious support forces from the tunnel face for unsupported tunnels. Figure 5.16 presents the variety of support forces P_S^{1j} and P_S^{22} versus the distance to the tunnel face x_d: the support forces (P_S^{1j}, P_S^{22}) firstly increased and then achieve a constant value when the distance to the tunnel face is large enough.

Moreover, in Figures 5.15 and 5.16, there are significant differences in the fictitious support forces (P_f) as well as the support forces calculated by different behaviour models (EPP, SS or EB), and the difference between the displacements of tunnels calculated for EPP rock masses and for SS rock masses grows as the GSI increases. The differences of stresses and displacements calculated by SS and EPP models can be negligible for lower quality rock masses, as expected, since the EPP behaviour represents well the behaviour of low quality rock masses (Alejano et al., 2012). Furthermore, there is a significant difference between displacements and support forces for unsupported and supported tunnels.

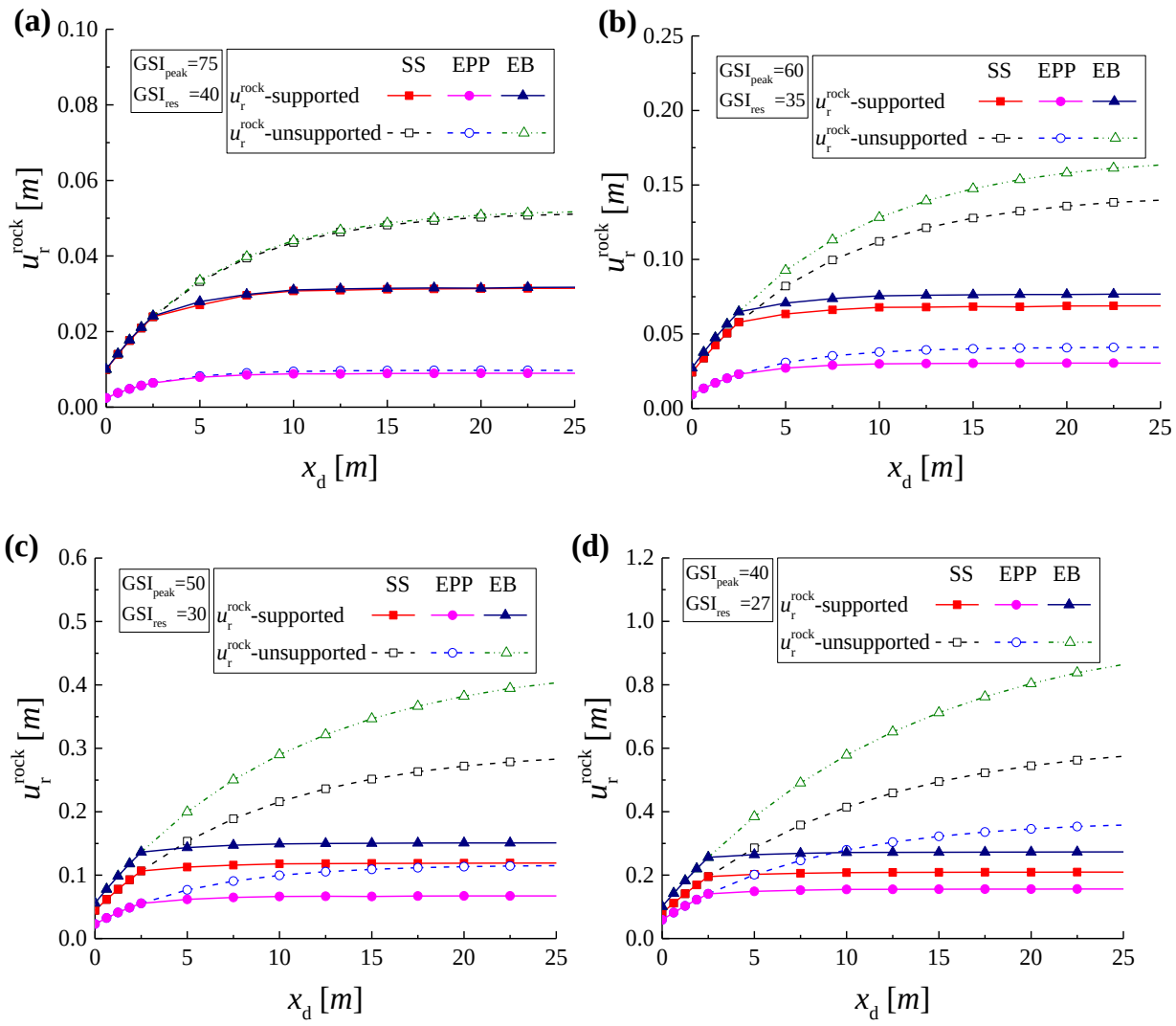

Figure 5.14. Tunnel displacements along the cross-section $r = R_1$, versus the distance to the tunnel face, for four different quality rock masses: **(a)** A2 (GSI_{peak} = 75, GSI_{res} = 40), **(b)** B2 (GSI_{peak} = 60, GSI_{res} = 35), **(c)** C2 (GSI_{peak} = 50, GSI_{res} = 30), and **(d)** D2 (GSI_{peak} = 40, GSI_{res} = 27).

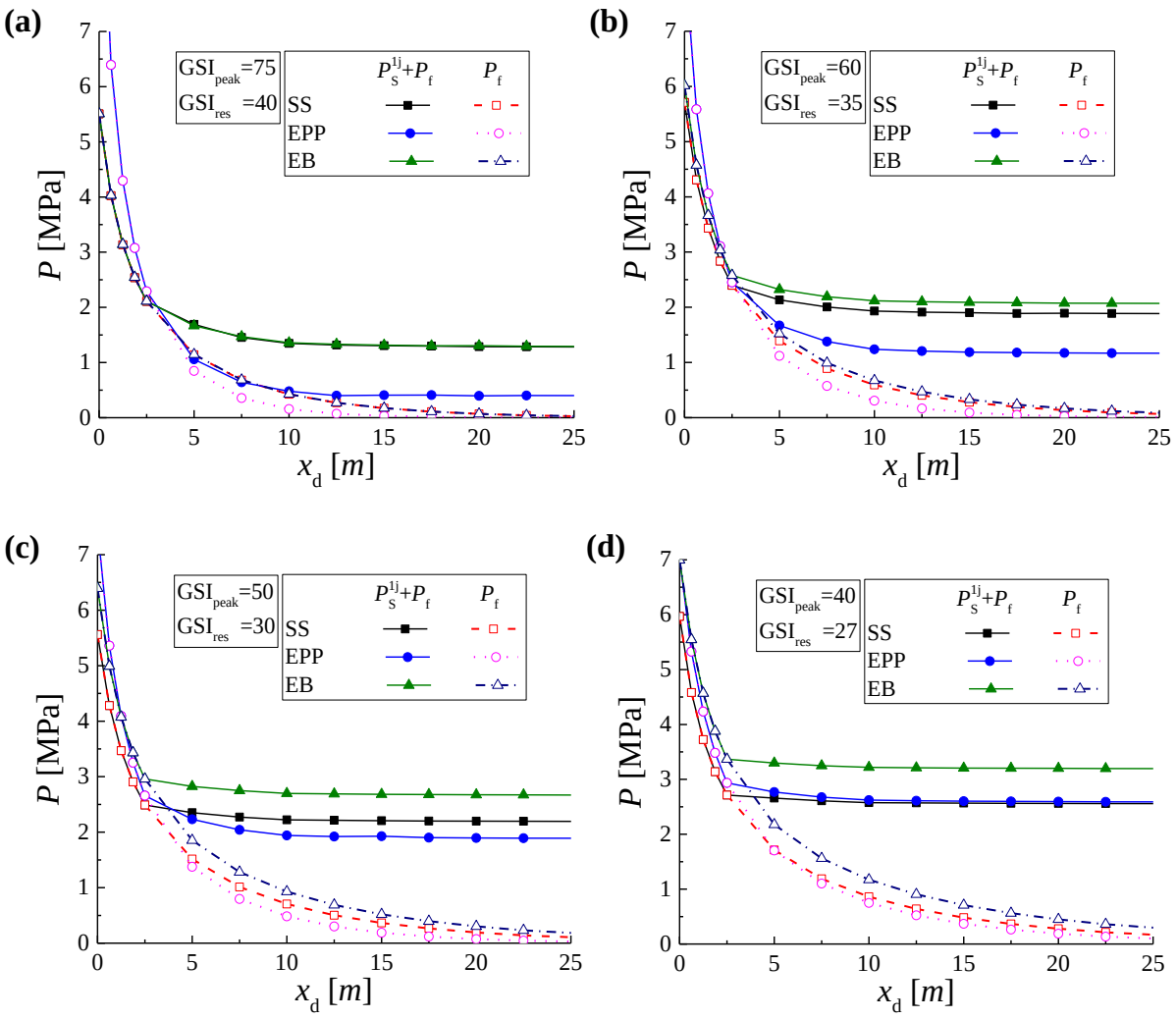

Figure 5.15. Support forces acting on the tunnel wall, $P_f + P_S^{1j}$, and fictitious support forces from the tunnel face P_f (see Figures 5.1 and 5.2), versus the distance to the tunnel face x_d, for four different quality rock masses: **(a)** A2 (GSI_{peak} = 75, GSI_{res} = 40); **(b)** B2 (GSI_{peak} = 60, GSI_{res} = 35); **(c)** C2 (GSI_{peak} = 50, GSI_{res} = 30); and **(d)** D2 (GSI_{peak} = 40, GSI_{res} = 27).

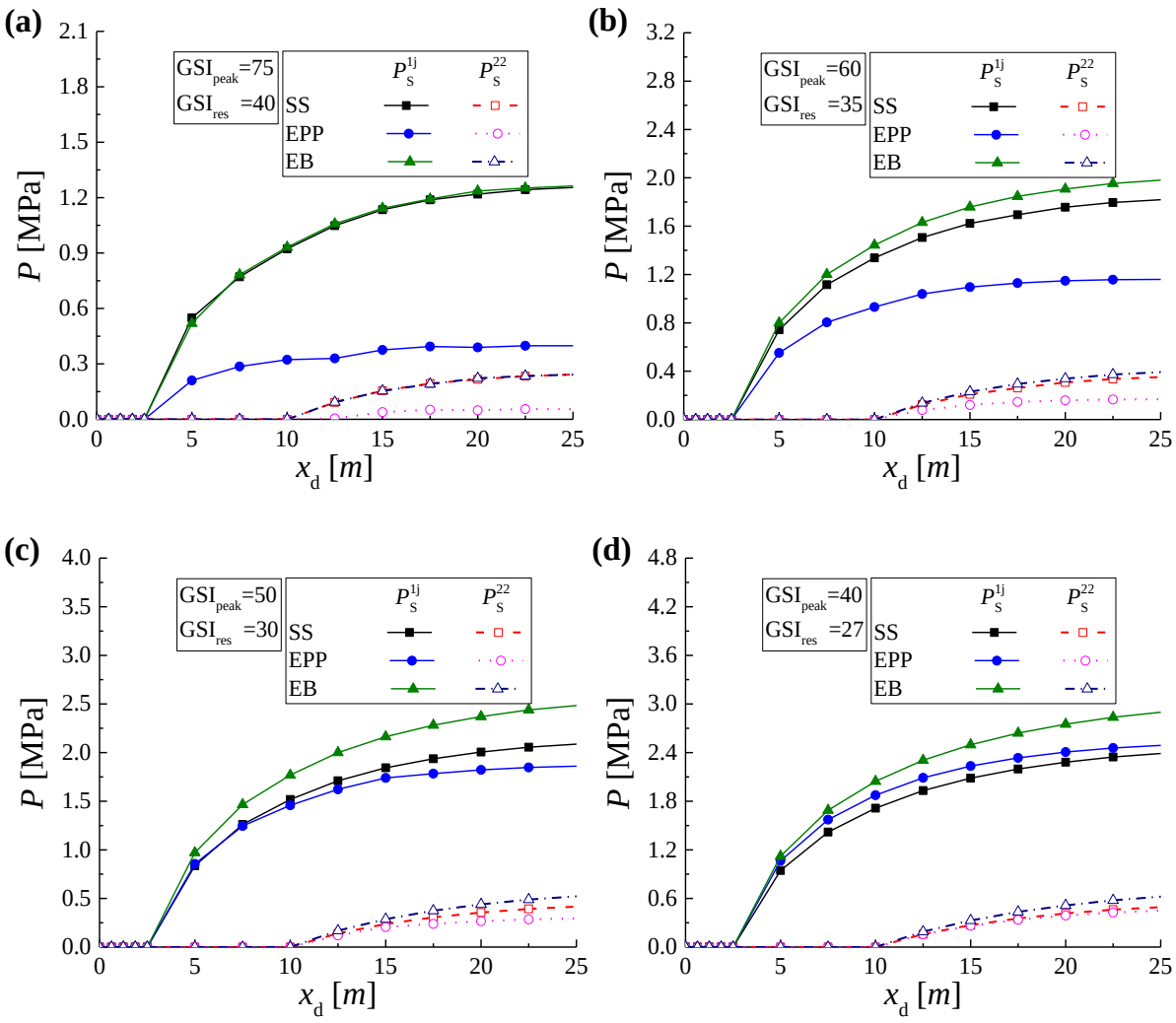

Figure 5.16. Support forces acting on the outer boundary of the primary support system, P_S^{1j}, and support forces acting on the outer boundary of the secondary support system, P_S^{22} (see Figures 5.1 and 5.2), versus the distance to the tunnel face x_d, for four different quality rock masses: **(a)** A2 (GSI_{peak} = 75, GSI_{res} = 40); **(b)** B2 (GSI_{peak} = 60, GSI_{res} = 35); **(c)** C2 (GSI_{peak} = 50, GSI_{res} = 30); and **(d)** D2 (GSI_{peak} = 40, GSI_{res} = 27).

5.6.2. Application in the design of tunnels

Due to the process of tunnel excavation and construction of supports, the final support forces applied on the outer boundary of the secondary support system are significantly affected by the installation distance of support system, as well as the stiffness of the support system (Song et al., 2018a and 2018b). Early installation of the secondary support system leads to larger final support forces acting on the secondary support system and thus, may result in failure of the secondary support system (Song et al., 2018a and 2018b).

In this sub-section, an example is carried out to present the application of our method to tunnel design in terms of installation distance of the secondary support system from the tunnel face (x_2) and thickness of the secondary support system ($d_2 = R_2 - R_3$).

The tunnel is excavated in a strain-softening rock mass with a radius of 7 m. The properties of the rock mass are the same as those in Table 5.1. In all the cases, the elastic modulus of the primary (L1) and secondary (L2) support systems are E_{L1} = 8000 MPa and E_{L2} = 12000 MPa, respectively. The Poisson's ratio of the support systems is $\nu_{L1} = \nu_{L2} = 0.15$. The installation distance of the primary support system is x_1 = 1 m, and the thickness of the primary support system is $d_1 = R_1 - R_2$ = 0.1 m. In this example, the unconfined compressive strength of the secondary support system is assumed as σ_{cL2} = 24 MPa. In the calculation process, the number of annuli n adopted is 500.

The equivalent stress of the secondary support system F^{L2} can be obtained, following Eq. (5.52). We assume that the secondary support system will fail in case $F^{L2} \leq 0$, so as to approximately predict the initial failure in the secondary support system. For the sake of tunnel stability, the secondary support system is not expected to fail, and thus the equivalent stresses (F^{L2}) should be positive in the tunnelling design.

In the application example, Figure 5.17 presents the equivalent stresses (F^{L2}) as a function of the installation distance of the secondary support system to the tunnel face (x_2), and the thickness of the secondary support system (d_2), where the dash lines represent zero equivalent stress. In Figure 5.17(a), the smallest allowable values for the installation distance from the tunnel face (x_2)

of the secondary support system are obtained when the equivalent stress becomes smaller than zero. It should be noted that the bigger is the value of the support thickness, the smaller will be the recommended values of x_2. Moreover, for a constant installation distance to the tunnel face (x_2), increasing the thickness of liners benefits the stability of tunnels although the cost of the support would increase, which is also shown in Figure 5.17(b), where the economic limit regarding the thickness of the secondary support system (d_2) is obtained when the equivalent stress is zero. Note that the aforementioned economic limit corresponds to a safety factor of 1.0. Therefore, with the proposed method, the optimization design on both distance from the tunnel face and thickness of the secondary support system can be conducted conveniently.

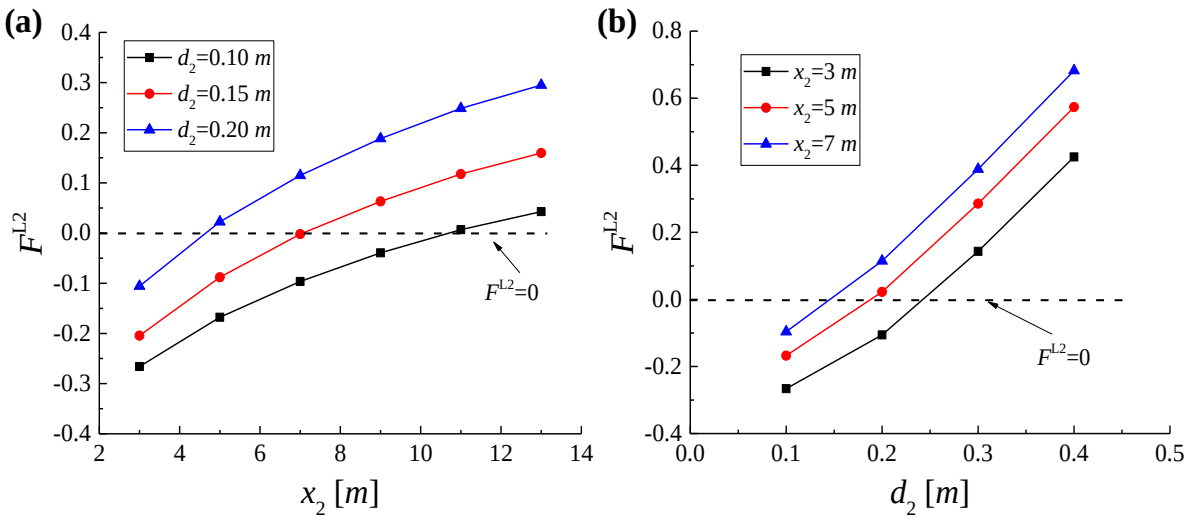

Figure 5.17. Equivalent stresses of the secondary support system, F_{L2}, versus: (a) installation distance of the secondary support system, for various thickness of the support system; (b) thickness of the secondary support system for various installation distances.

5.7. Conclusions

This study provides numerical solutions for supported tunnels excavated in strain-softening rock masses, which can be used in tunnelling for the design of the sequential installation of two different support systems in terms of strength and installation distance. In our approach, primary and secondary support systems are sequentially installed. The fictitious support forces have been

adopted to reflect the three-dimensional face effect. The solutions for displacements and stresses at the whole phases of tunnel excavation and installation of supports have been presented, considering the tunnel advancement and real continuity conditions between rock-support interface and support-support interface are considered. The Finite Difference Method (FDM) has been employed in the derivation of the solutions.

As a verification step, a good agreement between the proposed solutions and the results from the self-similar solutions has been obtained, and the compatibility conditions of the supported tunnels have been checked. Then, the proposed solutions have been compared with the convergence-confinement method (CCM). Unlike the CCM, our method considers the real compatibility conditions at both the rock-support interface and the support-support interface. Consequently, the safety factors obtained using our method are probably closer to reality than those obtained using the CCM, which may be overestimated, leading to an unsafe design of tunnels with combined support systems. Therefore, our proposed method may be used with greater confidence in the design of supported tunnels.

Furthermore, for the sake of comparison, elastic-perfectly-plastic (EPP), strain-softening (SS) and elastic-brittle (EB) material models have been adopted to analyse the effects of the post-failure behaviour model selection on tunnel deformations and support forces. We have observed significant differences in the displacements and the support forces considering the different behaviour models. In general, these differences grow as the quality of the rock mass decreases.

Finally, the proposed solutions have been used for the assessment of the design and optimization of the secondary support system, taking into account the distance from the tunnel face and the thickness of the secondary support system. Therefore, the proposed approach constitutes an alternative method for preliminary tunnel analysis and design, providing a greater confidence and assessment capability.

The obtained solutions are applicable only for the supported circular tunnels, although the solutions are meaningful for a much wider range of non-circular tunnels. In the future research, numerical and analytical solutions for the non-circular tunnels will be considered to improve the applicability of the solutions in real engineering.

Chapter 6. Summary and recommendations

6.1. Summary

This doctoral thesis aims to develop numerical and theoretical approaches for preliminary analysis and design of underground workings, thus providing greater confidence and assessment capability. The main contributions of this thesis are summarized below:

- *Time-dependent plastic mechanical model (chapters 2 and 4)*

  A coupled time-dependent plastic constitutive model has been developed and implemented into the finite element method software CODE_BRIGHT, to be able to simulate the time-dependent behaviour and the plastic behaviour (stress-induced or/and creep-induced) of geomaterials. Firstly, the Burgers model and the viscoplastic model are combined in series. Both the Mohr-Coulomb and Hoek-Brown failure criteria, and the strain-softening post-failure behaviour model are considered. In the programming, the yield surfaces and the viscoplastic potential are smoothed for numerical efficiency. Moreover, the creep deformations are coupled with the strain-softening model to simulate the damage evolution, and hence, the creep-induced failure behaviour can be simulated.

- *A smoothed excavation method (chapter 3)*

  Numerical solutions for coupled non-linear problems may require a high computational effort. Load application or construction of geotechnical structures can be easily smoothed by ramping in time the loads or the weight layers to be constructed. Excavation is more challenging because it is difficult to smooth the removal of pieces of soil or rock that occur instantaneously. Removal of very thin pieces of material can be a solution as it can avoid the sharp changes in stresses and fluid fluxes; however, it can lead to too refined meshes. For the sake of numerical reliability and efficiency, a smoothed excavation (SE) method has been introduced, so it takes place in a smooth way even for relatively coarse layers or pieces of soil or rock. The proposed SE method is a benefit to numerical calculation of the multi-stage excavation problems.

- *Hydro-mechanical modelling of tunnels excavated in saturated time-dependent plastic rock masses (chapters 3 and 4)*

  The hydro-mechanical modelling of tunnels excavated in saturated ground and, at the same time, showing plastic response has been addressed in this thesis. In chapter 3, parametric analyses of longitudinal deformation profiles (LDP) obtained under different hydro-mechanical conditions and different geomechanical qualities (GSI) are performed. In chapter 4, parametric analyses are performed to analyse the effects on tunnelling response of selecting different constitutive models, different standstill times or different excavation rates. Furthermore, empirical solutions have been developed under drained steady-state conditions (chapter 3). The results and conclusions obtained from this thesis are meaningful for the preliminary design of tunnelling in saturated ground with plastic response.

- *Solutions for supported tunnels with a combined support system (chapter 5)*

  Numerical (or semi-analytical) solutions have been developed for supported tunnels excavated in strain-softening rock masses, and the finite difference method has been employed in the derivation of the solutions. The sequential installation of primary and secondary support systems in terms of strength and installation distance are considered. The tunnel advancement and real continuity conditions between rock-support interface and support-support interface are considered. The safety factors obtained using the proposed method are probably closer to reality than those obtained using the convergence-confinement method, which may be overestimated, leading to an unsafe design of tunnels with combined support systems. Therefore, the proposed method may be used with greater confidence in the design of supported tunnels.

6.2. Future research recommendations

Further research topics that may be worth investigating are summarised below:

- *Multi-physics multi-phases modelling*

  Many multi-physical processes (mechanical, hydraulic, thermal and chemical) affect the behaviour of the rock masses in a coupled way, and there are still many aspects of interest to

study, which will require more detailed investigations. This thesis concentrates on the coupled modelling of hydro-mechanical problems; in the future, the research may be extended to a coupled thermal-hydraulic-mechanical-chemical (THMC) framework.

- *Numerical simulations using realistic anisotropic or heterogeneous 3D models*

  Even if the proposed method in this thesis can simulate different cases of tunnels excavated in hydro-mechanical saturated rock masses with time-dependent plastic response, it still has some limitations. For instance, numerical analyses are carried out through homogeneous material models. Actually, geomaterials are frequently anisotropic and inhomogeneous. If an anisotropic geomaterial is assumed to be isotropic, significant errors in stresses and displacements may be introduced in the analysis. In future research, time-dependent plastic responses of tunnelling in anisotropic or/and heterogeneous geomaterials should be analysed using 3D numerical models.

- *Improved longitudinal deformation profiles for time-dependent geomaterials*

  This thesis provides numerical approaches to obtain longitudinal deformation profiles (LDP) in the convergence-confinement method (CCM) framework. However, one of the limitations of the CCM is its application in time-dependent geomaterials. In the future, LDP expressions for tunnels excavated in time-dependent rock masses can be developed and combined with the CCM, to extend its application in time-dependent geomaterials.

Appendix A. FORTRAN scripts

The time-dependent plastic mechanical models presented in chapters 2-4 have been implemented in CODE_BRIGHT. The CODE_BRIGHT program can be downloaded from the official website: https://deca.upc.edu/en/projects/code_bright.

Instead, scripts in this appendix deal with the implementation of tunnelling in strain-softening rock masses (related to chapter 5), considering the longitudinal tunnelling advancement and sequential installation of the primary and secondary support systems.

A.1. Solutions of the ground reaction curves

```
!*************************************************************************
!Determining of the ground reaction curves (GRC)for tunnelling in strain-softening rock masses *
!*************************************************************************
!*********************************************************
!INPUT PARAMETERS                                        *
!P_0: initial stresses                                    *
!E, v: elastic modulus and Poisson's ratio of geomaterials *
!cohesion_0, cohesion_r: peak and residual values of cohesion *
!friction_0, friction_r: peak and residual values of friction angle (deg) *
!dilatancy_0, dilatancy_r: peak and residual values of dilation angle (deg) *
!a_n_p_star: critical values of softening parameter       *
!r: location coordinate                                   *
!n: the number of annuli for the FDM                      *
!radius: the radius of  tunnel wall                       *
!*********************************************************
!*********************************************
!OUTPUT PARAMETERS                           *
!sig_r_i: acting stresses on the tunnel wall *
!u_i*radius/r_i: displacements at the tunnel wall *
!radius/r_i, r_s*radius/r_i: peak and residual plastic radii *
!*********************************************
```

```
PROGRAM MAIN
  IMPLICIT REAL(A-H,O-Z)
  INTEGER I,J,K,L,M,N
 dimension p_i(51)

  READ(222,*) P_0,E,v,cohesion_0,cohesion_r,friction_0,friction_r,dilatancy_0,
.                 dilatancy_r,a_n_p_star,r,n,radius

  Pi=3.141592653
  G=E/(2.0*(1.0+v))
  friction_0=friction_0*Pi/180.0
  friction_r=friction_r*Pi/180.0
  dilatancy_0=dilatancy_0*Pi/180.0
  dilatancy_r=dilatancy_r*Pi/180.0

  do k=1,51
    xk=(k-1)/50.0
    p_i(k)=0.0
    R_p=1.0

    !material parameters for the 1-st annuli
    a_N_0=(1.0+sin(friction_0))/(1.0-sin(friction_0))
    S_0=2.0*cohesion_0*sqrt(a_N_0)

    !radial stress at the plastic-elastic interface
    sig_R_p=(2.0*p_0-s_0)/(1.0+a_N_0)
    delta_sig_r=(P_i(k)-sig_R_p)/N

    !initial values of stresses/strain in the outer boundary of the i-th annulus
    sig_r_0=sig_r_p
    sig_theta_0=2.0*p_0-sig_r_p
    strain_p_r_0=0.0
    strain_p_theta=0.0
    a_n_p_0=0.0
    strain_theta_0=(p_0-sig_r_p)/(2.0*G)
```

```
    U_0=strain_theta_0
    cohesion_i=cohesion_0
    friction_i=friction_0
    dilatancy_i=dilatancy_0
    a_n_p_i=a_n_p_0
    sig_r_i=sig_r_0
    r_i=r_p
    u_i=u_0

  Do i=1,n
     !non-updated material parameters
     r_i_1=r_i
     a_N_i=(1.0+sin(friction_i))/(1.0-sin(friction_i))
     S_i=2.0*cohesion_i*sqrt(a_N_i)
     a_k_dilatancy_i=(1.0+sin(dilatancy_i))/(1.0-sin(dilatancy_i))

     !to update the normalized radial
     r_i=r_i*((sig_r_i+delta_sig_r-S_i/(1.0-a_N_i))/(sig_r_i-S_i/(1.0-a_N_i)))**(1.0/(a_N_i-1.0))

     !stress and displacements in the i-th annulus
     if ((r .gt. r_i) .and. (r .le. r_i_1)) then
        !expression of the stresses
        sig_r=(S_i)/(1.0-a_N_i)+(sig_r_i-S_i/(1-a_N_i))*(r/r_i_1)**(a_N_i-1.0)
        sig_theta=a_N_i*sig_r+S_i
        strain_e_r=(1.0-v*v)/E*((sig_r-P_0)-v/(1.0-v)*(sig_theta-p_0))
        strain_e_theta=(1.0-v*v)/E*((sig_theta-P_0)-v/(1.0-v)*(sig_r-p_0))

        !expression of the displacements
        F_r=strain_e_r+a_k_dilatancy_i*strain_e_theta

        Call INTE(SUM1,r_i_1,r,A_K_dilatancy_i,v,E,S_i,a_N_i,sig_r_i,P_0)
        U=U_i*(r_i_1/r)**a_k_dilatancy_i+SUM1*r**(-a_k_dilatancy_i)
     end if
```

```
    !to update the stresses in the inner boundary of the i-th annulus
    sig_r_i=sig_r_i+delta_sig_r
    sig_theta_i=a_N_i*sig_r_i+S_i

    !to update the elastic strain in the inner boudary of the i-th annulus
    strain_e_r_i=(1.0-v*v)/E*((sig_r_i-P_0)-v/(1.0-v)*(sig_theta_i-p_0))
    strain_e_theta_i=(1.0-v*v)/E*((sig_theta_i-P_0)-v/(1.0-v)*(sig_r_i-p_0))

    !to update u_i
    Call INTE(SUM2,r_i_1,r_i,A_K_dilatancy_i,v,E,S_i,a_N_i,sig_r_i,P_0)
    U_i=U_i*(r_i_1/r_i)**a_k_dilatancy_i+SUM2*r_i**(-a_k_dilatancy_i)

    !to update plastic strain in the inner boundary of the i-th annulus
    strain_p_theta_i=u_i/r_i-strain_e_theta_i
    strain_p_r_i=-a_k_dilatancy_i*strain_p_theta_i

    !to update the plastic parameter a_n_p
    a_n_p_i=strain_p_theta_i-strain_p_r_i

    !to update the material parameters
    if (a_n_p_i .lt. a_n_p_star .and. a_n_p_i .ge. 0.0) then
       cohesion_i=cohesion_0-(cohesion_0-cohesion_r)/(a_n_p_star)*a_n_p_i
       friction_i=friction_0-(friction_0-friction_r)/(a_n_p_star)*a_n_p_i
       dilatancy_i=dilatancy_0-(dilatancy_0-dilatancy_r)/(a_n_p_star)*a_n_p_i
       r_s=r_i
    else
       cohesion_i=cohesion_r
       friction_i=friction_r
       dilatancy_i=dilatancy_r
    end if
end Do

write(111111,*) xk,sig_r_i,u_i*radius/r_i,radius/r_i,r_s*radius/r_i
write(222222,*) r*radius/r_i,U*radius/r_i,sig_r

end do
END
```

```
SUBROUTINE INTE(SUM,A,B,A_K_dilatancy_i,v,E,S_i,a_N_i,sig_r_i,P_0)
N_inte=100000
SUM=0.0
X=A
H=(B-A)/N_inte

sig_r=(S_i)/(1.0-a_N_i)+(sig_r_i-S_i/(1.0-a_N_i))*(B/A)**(a_N_i-1.0)
sig_theta=a_N_i*sig_r+S_i
strain_e_r=(1.0-v*v)/E*((sig_r-P_0)-v/(1.0-v)*(sig_theta-p_0))
strain_e_theta=(1.0-v*v)/E*((sig_theta-P_0)-v/(1.0-v)*(sig_r-p_0))

Fx=strain_e_r+a_k_dilatancy_i*strain_e_theta
F=Fx*X**A_K_dilatancy_i

DO I=1,N_inte
   SI=F*H
   SUM=SUM+SI
   X=X+H

   sig_r=(S_i)/(1.0-a_N_i)+(sig_r_i-S_i/(1.0-a_N_i))*(B/A)**(a_N_i-1.0)
   sig_theta=a_N_i*sig_r+S_i
   strain_e_r=(1.0-v*v)/E*((sig_r-P_0)-v/(1.0-v)*(sig_theta-p_0))
   strain_e_theta=(1.0-v*v)/E*((sig_theta-P_0)-v/(1.0-v)*(sig_r-p_0))

   Fx=strain_e_r+a_k_dilatancy_i*strain_e_theta
   F=Fx*X**A_K_dilatancy_i
END DO
END
```

A.2. Solutions in the primary support stage

```
!************************************************
!Determining of the solutions during the primary support stage *
!************************************************
!*************************************************************************
!INPUT PARAMETERS                                                        *
!P_0: initial stresses                                                   *
!E, v: elastic modulus and Poisson's ratio of geomaterials               *
!cohesion_0, cohesion_r: peak and residual values of cohesion            *
!friction_0, friction_r: peak and residual values of friction angle (deg)*
!dilatancy_0, dilatancy_r: peak and residual values of dilation angle (deg)*
!a_n_p_star: critical values of softening parameter                      *
!r: location                                                             *
!n: the number of annuli in the FDM                                      *
!radius: the radius of  tunnel wall                                      *
!G_L1, v_L1, R_2: material and geometry parameters of the primary support system *
!P_fictitious,ur_x1: the fictitious support forces                       *
!ur_x1: the displacements along tunnel wall at the moment of installation of the primary support *
!*************************************************************************
!*********************************************************************
!OUTPUT PARAMETERS                                                   *
!sig_r_i: acting stresses on the tunnel wall                         *
!u_i*radius/r_i: displacements at the tunnel wall                    *
!radius/r_i, r_s*radius/r_i: peak and residual radii                 *
!p1_xx: support forces at the rock-support interface                 *
!u_L1: displacements of the primary support system at the rock-support interface  *
!*********************************************************************

PROGRAM MAIN
  IMPLICIT REAL(A-H,O-Z)
  INTEGER I,J,K,L,M,N
  READ(111,*) P_0,E,v,cohesion_0,cohesion_r,friction_0,friction_r,dilatancy_0,
 .            dilatancy_r,a_n_p_star,r,n,radius
  READ(222,*) G_L1,R_2,v_L1
  READ(333,*) P_fictitious,ur_x1
```

```
Pi=3.141592653
G=E/(2.0*(1.0+v))
friction_0=friction_0*Pi/180.0
friction_r=friction_r*Pi/180.0
dilatancy_0=dilatancy_0*Pi/180.0
dilatancy_r=dilatancy_r*Pi/180.0

 p1_11=0.0
 p1_22=p_0
10 p1_xx=(p1_11+p1_22)/2.0
 p_i=p1_xx+p_fictitious
 R_p=1.0

!material parameters for the 1-st annulus
a_N_0=(1.0+sin(friction_0))/(1.0-sin(friction_0))
S_0=2.0*cohesion_0*sqrt(a_N_0)

!radial stress at the plastic-elastic interface
sig_R_p=(2.0*p_0-s_0)/(1.0+a_N_0)
delta_sig_r=(P_i-sig_R_p)/N

!initial values of stresses/strain in the outer boundary of the i-th annulus
sig_r_0=sig_r_p
sig_theta_0=2.0*p_0-sig_r_p
strain_p_r_0=0.0
strain_p_theta=0.0
a_n_p_0=0.0
strain_theta_0=(p_0-sig_r_p)/(2.0*G)
U_0=strain_theta_0
cohesion_i=cohesion_0
friction_i=friction_0
dilatancy_i=dilatancy_0
a_n_p_i=a_n_p_0
sig_r_i=sig_r_0
r_i=r_p
u_i=u_0
```

```
Do i=1,n
   !non-updated material parameters
   r_i_1=r_i
   a_N_i=(1.0+sin(friction_i))/(1.0-sin(friction_i))
   S_i=2.0*cohesion_i*sqrt(a_N_i)
   a_k_dilatancy_i=(1.0+sin(dilatancy_i))/(1.0-sin(dilatancy_i))

   !to update the normalized radial
   r_i=r_i*((sig_r_i+delta_sig_r-S_i/(1.0-a_N_i))/(sig_r_i-S_i/(1.0-a_N_i)))**(1.0/(a_N_i-1.0))

   !stress and displacements in the i-th annulus
   if ((r .gt. r_i) .and. (r .le. r_i_1)) then
      !expression of the stresses
      sig_r=(S_i)/(1.0-a_N_i)+(sig_r_i-S_i/(1-a_N_i))*(r/r_i_1)**(a_N_i-1.0)
      sig_theta=a_N_i*sig_r+S_i
      strain_e_r=(1.0-v*v)/E*((sig_r-P_0)-v/(1.0-v)*(sig_theta-p_0))
      strain_e_theta=(1.0-v*v)/E*((sig_theta-P_0)-v/(1.0-v)*(sig_r-p_0))

      !expression of the displacements
      F_r=strain_e_r+a_k_dilatancy_i*strain_e_theta

      Call INTE(SUM1,r_i_1,r,A_K_dilatancy_i,v,E,S_i,a_N_i,sig_r_i,P_0)
      U=U_i*(r_i_1/r)**a_k_dilatancy_i+SUM1*r**(-a_k_dilatancy_i)
   end if

   !to update the stresses in the inner boundary of the i-th annulus
   sig_r_i=sig_r_i+delta_sig_r
   sig_theta_i=a_N_i*sig_r_i+S_i

   !to update the elastic strain in the inner boudary of the i-th annulus
   strain_e_r_i=(1.0-v*v)/E*((sig_r_i-P_0)-v/(1.0-v)*(sig_theta_i-p_0))
   strain_e_theta_i=(1.0-v*v)/E*((sig_theta_i-P_0)-v/(1.0-v)*(sig_r_i-p_0))

   !to update u_i
   Call INTE(SUM2,r_i_1,r_i,A_K_dilatancy_i,v,E,S_i,a_N_i,sig_r_i,P_0)
   U_i=U_i*(r_i_1/r_i)**a_k_dilatancy_i+SUM2*r_i**(-a_k_dilatancy_i)
```

```
      !to update plastic strain in the inner boundary of the i-th annulus
      strain_p_theta_i=u_i/r_i-strain_e_theta_i
      strain_p_r_i=-a_k_dilatancy_i*strain_p_theta_i

      !to update plastic parameter np
      a_n_p_i=strain_p_theta_i-strain_p_r_i

      !to update the material parameters
      if (a_n_p_i .lt. a_n_p_star .and. a_n_p_i .ge. 0.0) then
         cohesion_i=cohesion_0-(cohesion_0-cohesion_r)/(a_n_p_star)*a_n_p_i
         friction_i=friction_0-(friction_0-friction_r)/(a_n_p_star)*a_n_p_i
         dilatancy_i=dilatancy_0-(dilatancy_0-dilatancy_r)/(a_n_p_star)*a_n_p_i
         r_s=r_i
      else
         cohesion_i=cohesion_r
         friction_i=friction_r
         dilatancy_i=dilatancy_r
      end if
   end Do

   residual_1=radius*radius*R_2*R_2/(2.0*G_L1*Radius)/(Radius*radius-R_2*R_2)+(1.0-
  .              2.0*v_L1)*radius*radius*radius/(2.0*G_L1)/(Radius*radius-R_2*R_2)
   residual_xx=(strain_p_theta_i+strain_e_theta_i)*radius-ur_x1-residual_1*(sig_r_i-p_fictitious)
   p_i=p1_11+p_fictitious

   !material parameters for the 1-st annulus
   a_N_0=(1.0+sin(friction_0))/(1.0-sin(friction_0))
   S_0=2.0*cohesion_0*sqrt(a_N_0)

   !radial stress at the plastic-elastic interface
   sig_R_p=(2.0*p_0-s_0)/(1.0+a_N_0)
   delta_sig_r=(P_i-sig_R_p)/N

   !initial values of stresses/strain in the outer boundary of the i-th annulus
   sig_r_0=sig_r_p
   sig_theta_0=2.0*p_0-sig_r_p
```

```
strain_p_r_0=0.0
strain_p_theta=0.0
a_n_p_0=0.0
strain_theta_0=(p_0-sig_r_p)/(2.0*G)
U_0=strain_theta_0
cohesion_i=cohesion_0
friction_i=friction_0
dilatancy_i=dilatancy_0
a_n_p_i=a_n_p_0
sig_r_i=sig_r_0
r_i=r_p
u_i=u_0

Do i=1,n
   !non-updated material parameters
   r_i_1=r_i
   a_N_i=(1.0+sin(friction_i))/(1.0-sin(friction_i))
   S_i=2.0*cohesion_i*sqrt(a_N_i)
   a_k_dilatancy_i=(1.0+sin(dilatancy_i))/(1.0-sin(dilatancy_i))

   !to update the normalized radial
   r_i=r_i*((sig_r_i+delta_sig_r-S_i/(1.0-a_N_i))/(sig_r_i-S_i/(1.0-a_N_i)))**(1.0/(a_N_i-1.0))

   !stress and displacements in the i-th annulus
   if ((r .gt. r_i) .and. (r .le. r_i_1)) then
      !expression of the stresses
      sig_r=(S_i)/(1.0-a_N_i)+(sig_r_i-S_i/(1-a_N_i))*(r/r_i_1)**(a_N_i-1.0)
      sig_theta=a_N_i*sig_r+S_i
      strain_e_r=(1.0-v*v)/E*((sig_r-P_0)-v/(1.0-v)*(sig_theta-p_0))
      strain_e_theta=(1.0-v*v)/E*((sig_theta-P_0)-v/(1.0-v)*(sig_r-p_0))

      !expression of the displacements
      F_r=strain_e_r+a_k_dilatancy_i*strain_e_theta
      Call INTE(SUM1,r_i_1,r,A_K_dilatancy_i,v,E,S_i,a_N_i,sig_r_i,P_0)
      U=U_i*(r_i_1/r)**a_k_dilatancy_i+SUM1*r**(-a_k_dilatancy_i)
   end if
```

```
      !to update the stresses in the inner boundary of the i-th annulus
      sig_r_i=sig_r_i+delta_sig_r
      sig_theta_i=a_N_i*sig_r_i+S_i

      !to update the elastic strain in the inner boudary of the i-th annulus
      strain_e_r_i=(1.0-v*v)/E*((sig_r_i-P_0)-v/(1.0-v)*(sig_theta_i-p_0))
      strain_e_theta_i=(1.0-v*v)/E*((sig_theta_i-P_0)-v/(1.0-v)*(sig_r_i-p_0))

      !to update u_i
      Call INTE(SUM2,r_i_1,r_i,A_K_dilatancy_i,v,E,S_i,a_N_i,sig_r_i,P_0)
      U_i=U_i*(r_i_1/r_i)**a_k_dilatancy_i+SUM2*r_i**(-a_k_dilatancy_i)

      !to update plastic strain in the inner boundary of the i-th annulus
      strain_p_theta_i=u_i/r_i-strain_e_theta_i
      strain_p_r_i=-a_k_dilatancy_i*strain_p_theta_i

      !to update plastic parameter np
      a_n_p_i=strain_p_theta_i-strain_p_r_i

      !to update the material parameters
      if (a_n_p_i .lt. a_n_p_star .and. a_n_p_i .ge. 0.0) then
         cohesion_i=cohesion_0-(cohesion_0-cohesion_r)/(a_n_p_star)*a_n_p_i
         friction_i=friction_0-(friction_0-friction_r)/(a_n_p_star)*a_n_p_i
         dilatancy_i=dilatancy_0-(dilatancy_0-dilatancy_r)/(a_n_p_star)*a_n_p_i
         r_s=r_i
      else
         cohesion_i=cohesion_r
         friction_i=friction_r
         dilatancy_i=dilatancy_r
      end if
   end Do

   residual_1=radius*radius*R_2*R_2/(2.0*G_L1*Radius)/(Radius*radius-R_2*R_2)+(1.0-
  .                2.0*v_L1)*radius*radius*radius/(2.0*G_L1)/(Radius*radius-R_2*R_2)
   residual_11=(strain_p_theta_i+strain_e_theta_i)*radius-ur_x1-residual_1*(sig_r_i-p_fictitious)
```

```
p_i=p1_22+p_fictitious
R_p=1.0

!material parameters for the 1-st annulus
a_N_0=(1.0+sin(friction_0))/(1.0-sin(friction_0))
S_0=2.0*cohesion_0*sqrt(a_N_0)

!radial stress at the plastic-elastic interface
sig_R_p=(2.0*p_0-s_0)/(1.0+a_N_0)
delta_sig_r=(P_i-sig_R_p)/N

!initial values of stresses/strain in the outer boundary of the i-th annulus
sig_r_0=sig_r_p
sig_theta_0=2.0*p_0-sig_r_p
strain_p_r_0=0.0
strain_p_theta=0.0
a_n_p_0=0.0
strain_theta_0=(p_0-sig_r_p)/(2.0*G)
U_0=strain_theta_0
cohesion_i=cohesion_0
friction_i=friction_0
dilatancy_i=dilatancy_0
a_n_p_i=a_n_p_0
sig_r_i=sig_r_0
r_i=r_p
u_i=u_0

Do i=1,n
   !non-updated material parameters
   r_i_1=r_i
   a_N_i=(1.0+sin(friction_i))/(1.0-sin(friction_i))
   S_i=2.0*cohesion_i*sqrt(a_N_i)
   a_k_dilatancy_i=(1.0+sin(dilatancy_i))/(1.0-sin(dilatancy_i))
```

```
!to update the normalized radial
r_i=r_i*((sig_r_i+delta_sig_r-S_i/(1.0-a_N_i))/(sig_r_i-S_i/(1.0-a_N_i)))**(1.0/(a_N_i-1.0))

!stress and displacements in the i-th annulus
if ((r .gt. r_i) .and. (r .le. r_i_1)) then
   !expression of the stresses
   sig_r=(S_i)/(1.0-a_N_i)+(sig_r_i-S_i/(1-a_N_i))*(r/r_i_1)**(a_N_i-1.0)
   sig_theta=a_N_i*sig_r+S_i
   strain_e_r=(1.0-v*v)/E*((sig_r-P_0)-v/(1.0-v)*(sig_theta-p_0))
   strain_e_theta=(1.0-v*v)/E*((sig_theta-P_0)-v/(1.0-v)*(sig_r-p_0))

   !expression of the displacements
   F_r=strain_e_r+a_k_dilatancy_i*strain_e_theta

   Call INTE(SUM1,r_i_1,r,A_K_dilatancy_i,v,E,S_i,a_N_i,sig_r_i,P_0)
   U=U_i*(r_i_1/r)**a_k_dilatancy_i+SUM1*r**(-a_k_dilatancy_i)
end if

!to update the stresses in the inner boundary of the i-th annulus
sig_r_i=sig_r_i+delta_sig_r
sig_theta_i=a_N_i*sig_r_i+S_i

!to update the elastic strain in the inner boudary of the i-th annulus
strain_e_r_i=(1.0-v*v)/E*((sig_r_i-P_0)-v/(1.0-v)*(sig_theta_i-p_0))
strain_e_theta_i=(1.0-v*v)/E*((sig_theta_i-P_0)-v/(1.0-v)*(sig_r_i-p_0))

!to update u_i
Call INTE(SUM2,r_i_1,r_i,A_K_dilatancy_i,v,E,S_i,a_N_i,sig_r_i,P_0)
U_i=U_i*(r_i_1/r_i)**a_k_dilatancy_i+SUM2*r_i**(-a_k_dilatancy_i)

!to update plastic strain in the inner boundary of the i-th annulus
strain_p_theta_i=u_i/r_i-strain_e_theta_i
strain_p_r_i=-a_k_dilatancy_i*strain_p_theta_i
```

```
      !to update plastic parameter np
      a_n_p_i=strain_p_theta_i-strain_p_r_i

      !to update the material parameters
      if (a_n_p_i .lt. a_n_p_star .and. a_n_p_i .ge. 0.0) then
         cohesion_i=cohesion_0-(cohesion_0-cohesion_r)/(a_n_p_star)*a_n_p_i
         friction_i=friction_0-(friction_0-friction_r)/(a_n_p_star)*a_n_p_i
         dilatancy_i=dilatancy_0-(dilatancy_0-dilatancy_r)/(a_n_p_star)*a_n_p_i
         r_s=r_i
      else
         cohesion_i=cohesion_r
         friction_i=friction_r
         dilatancy_i=dilatancy_r
      end if
   end Do

   R_sidual=(radius*radius*R_2*R_2/(2.0*G_L1*Radius)/(Radius*radius-R_2*R_2)+(1.0-
  .              2.0*v_L1)*radius*radius*radius/(2.0*G_L1)/(Radius*radius-R_2*R_2))
   residual_22=(strain_p_theta_i+strain_e_theta_i)*radius-ur_x1-R_sidual*(sig_r_i-p_fictitious)

   if (sign (residual_xx,residual_11) .eq. residual_xx) then
      p1_11=p1_xx
      residual_11=residual_xx
   else
      p1_22=p1_xx
      residual_22=residual_xx
   end if

   if ((abs(residual_11-residual_22).gt.20e-6) .and. abs(residual_xx).gt.20e-6) goto 10
   if(abs(residual_xx).gt.1e-6) p1_xx=(p1_11+P1_22)/2.0
   u_L1=p1_xx*R_sidual

   write(1111111,*) residual_xx,p1_xx,u_L1,u_i*radius/r_i,sig_r_i,radius/r_i,r_s*radius/r_i
   END
```

```
SUBROUTINE INTE(SUM,A,B,A_K_dilatancy_i,v,E,S_i,a_N_i,sig_r_i,P_0)
N_inte=100000
SUM=0.0
X=A
H=(B-A)/N_inte

sig_r=(S_i)/(1.0-a_N_i)+(sig_r_i-S_i/(1.0-a_N_i))*(B/A)**(a_N_i-1.0)
sig_theta=a_N_i*sig_r+S_i
strain_e_r=(1.0-v*v)/E*((sig_r-P_0)-v/(1.0-v)*(sig_theta-p_0))
strain_e_theta=(1.0-v*v)/E*((sig_theta-P_0)-v/(1.0-v)*(sig_r-p_0))

Fx=strain_e_r+a_k_dilatancy_i*strain_e_theta
F=Fx*X**A_K_dilatancy_i

DO I=1,N_inte
   SI=F*H
   SUM=SUM+SI
   X=X+H

   sig_r=(S_i)/(1.0-a_N_i)+(sig_r_i-S_i/(1.0-a_N_i))*(B/A)**(a_N_i-1.0)
   sig_theta=a_N_i*sig_r+S_i
   strain_e_r=(1.0-v*v)/E*((sig_r-P_0)-v/(1.0-v)*(sig_theta-p_0))
   strain_e_theta=(1.0-v*v)/E*((sig_theta-P_0)-v/(1.0-v)*(sig_r-p_0))

   Fx=strain_e_r+a_k_dilatancy_i*strain_e_theta
   F=Fx*X**A_K_dilatancy_i
END DO
END
```

A.3. Solutions in the secondary support stage

```
!*****************************************************
!Determining of the solutions during the secondary support stage *
!*****************************************************
!*************************************************************************************
!INPUT PARAMETERS                                                                    *
!P_0: initial stresses                                                               *
!E, v: elastic modulus and Poisson's ratio of geomaterials                           *
!cohesion_0, cohesion_r: peak and residual values of cohesion                        *
!friction_0, friction_r: peak and residual values of friction angle (deg)            *
!dilatancy_0, dilatancy_r: peak and residual values of dilation angle (deg)          *
!a_n_p_star: critical values of softening parameter                                  *
!r: location                                                                         *
!n: the number of annuli for the FDM                                                 *
!R_1: the radius of  the tunnel wall                                                 *
!G_L1, v_L1: material parameters of the primary support system                       *
!G_L2,v_L2: material parameters of the secondary support system                      *
!R_2, R_3: geometry parameters of supports                                           *
!P_fictitious: the fictitious support forces                                         *
!ur_x1: the displacements along tunnel wall at the moment of installation of the primary support  *
!P_s_11_x2: the support forces on the outer boundary of the primary support         *
!                 at the moment of installation of the secondary support            *
!*************************************************************************************
!*****************************************************************
!OUTPUT PARAMETERS                                                *
!sig_r_i: acting stresses on the tunnel wall                       *
!u_i*R_1/r_i: displacements at the tunnel wall                     *
!R_1/r_i, r_s*R_1/r_i: peak and residual plastic radii             *
!p1_xx: support forces at the rock-support interface               *
!p_s_22: support forces acting on the outer boundary of the secondary support  *
!ur_L1_R1,ur_L1_R2,ur_L2_R2: displacements of supports             *
!*****************************************************************
```

```
PROGRAM MAIN
  IMPLICIT REAL(A-H,O-Z)
  INTEGER I,J,K,L,M,N
  READ(222,*) P_0,E,v,cohesion_0,cohesion_r,friction_0,friction_r,dilatancy_0,
 .            dilatancy_r,a_n_p_star,r,n,R_1
  READ(111,*) G_L1,G_L2,v_L1,v_L2,R_2,R_3,P_fictitious

  cof_A=R_1*R_2*R_2/(2.0*G_L1*(R_1*R_1-R_2*R_2))+(1.0-
 .      2.0*v_L1)*R_1*R_1*R_1/(2.0*G_L1*(R_1*R_1-R_2*R_2))
  cof_B=R_1*R_2*R_2/(2.0*G_L1*(R_1*R_1-R_2*R_2))+(1.0-
 .      2.0*v_L1)*R_1*R_2*R_2/(2.0*G_L1*(R_1*R_1-R_2*R_2))
  cof_C=R_1*R_1*R_2/(2.0*G_L1*(R_1*R_1-R_2*R_2))+(1.0-
 .      2.0*v_L1)*R_1*R_1*R_2/(2.0*G_L1*(R_1*R_1-R_2*R_2))
  cof_D=R_1*R_1*R_2/(2.0*G_L1*(R_1*R_1-R_2*R_2))+(1.0-
 .      2.0*v_L1)*R_2*R_2*R_2/(2.0*G_L1*(R_1*R_1-R_2*R_2))
  cof_E=R_2*R_3*R_3/(2.0*G_L2*(R_2*R_2-R_3*R_3))+(1.0-
 .      2.0*v_L2)*R_2*R_2*R_2/(2.0*G_L2*(R_2*R_2-R_3*R_3))

  Pi=3.141592653
  G=E/(2.0*(1.0+v))
  friction_0=friction_0*Pi/180.0
  friction_r=friction_r*Pi/180.0
  dilatancy_0=dilatancy_0*Pi/180.0
  dilatancy_r=dilatancy_r*Pi/180.0

   p1_11=0.0
   p1_22=p_0
10 p1_xx=(p1_11+p1_22)/2.0
   p_i=p1_xx+p_fictitious
   R_p=1.0

  !material parameters for the 1-st annulus
  a_N_0=(1.0+sin(friction_0))/(1.0-sin(friction_0))
  S_0=2.0*cohesion_0*sqrt(a_N_0)
```

```
!radial stress at the plastic-elastic interface
sig_R_p=(2.0*p_0-s_0)/(1.0+a_N_0)
delta_sig_r=(P_i-sig_R_p)/N

!initial values of stresses/strain in the outer boundary of the i-th annulus
sig_r_0=sig_r_p
sig_theta_0=2.0*p_0-sig_r_p
strain_p_r_0=0.0
strain_p_theta=0.0
a_n_p_0=0.0
strain_theta_0=(p_0-sig_r_p)/(2.0*G)
U_0=strain_theta_0
cohesion_i=cohesion_0
friction_i=friction_0
dilatancy_i=dilatancy_0
a_n_p_i=a_n_p_0
sig_r_i=sig_r_0
r_i=r_p
u_i=u_0

Do i=1,n
   !non-updated material parameters
   r_i_1=r_i
   a_N_i=(1.0+sin(friction_i))/(1.0-sin(friction_i))
   S_i=2.0*cohesion_i*sqrt(a_N_i)
   a_k_dilatancy_i=(1.0+sin(dilatancy_i))/(1.0-sin(dilatancy_i))

   !to update the normalized radial
   r_i=r_i*((sig_r_i+delta_sig_r-S_i/(1.0-a_N_i))/(sig_r_i-S_i/(1.0-a_N_i)))**(1.0/(a_N_i-1.0))

   !stress and displacements in the i-th annulus
   if ((r .gt. r_i) .and. (r .le. r_i_1)) then
      !expression of the stresses
      sig_r=(S_i)/(1.0-a_N_i)+(sig_r_i-S_i/(1-a_N_i))*(r/r_i_1)**(a_N_i-1.0)
      sig_theta=a_N_i*sig_r+S_i
```

```
    strain_e_r=(1.0-v*v)/E*((sig_r-P_0)-v/(1.0-v)*(sig_theta-p_0))
    strain_e_theta=(1.0-v*v)/E*((sig_theta-P_0)-v/(1.0-v)*(sig_r-p_0))

    !expression of the displacements
    F_r=strain_e_r+a_k_dilatancy_i*strain_e_theta

    Call INTE(SUM1,r_i_1,r,A_K_dilatancy_i,v,E,S_i,a_N_i,sig_r_i,P_0)
    U=U_i*(r_i_1/r)**a_k_dilatancy_i+SUM1*r**(-a_k_dilatancy_i)
end if

!to update the stresses in the inner boundary of the i-th annulus
sig_r_i=sig_r_i+delta_sig_r
sig_theta_i=a_N_i*sig_r_i+S_i

!to update the elastic strain in the inner boudary of the i-th annulus
strain_e_r_i=(1.0-v*v)/E*((sig_r_i-P_0)-v/(1.0-v)*(sig_theta_i-p_0))
strain_e_theta_i=(1.0-v*v)/E*((sig_theta_i-P_0)-v/(1.0-v)*(sig_r_i-p_0))

!to update u_i
Call INTE(SUM2,r_i_1,r_i,A_K_dilatancy_i,v,E,S_i,a_N_i,sig_r_i,P_0)
U_i=U_i*(r_i_1/r_i)**a_k_dilatancy_i+SUM2*r_i**(-a_k_dilatancy_i)

!to update plastic strain in the inner boundary of the i-th annulus
strain_p_theta_i=u_i/r_i-strain_e_theta_i
strain_p_r_i=-a_k_dilatancy_i*strain_p_theta_i

!to update plastic parameter np
a_n_p_i=strain_p_theta_i-strain_p_r_i

!to update the material parameters
if (a_n_p_i .lt. a_n_p_star .and. a_n_p_i .ge. 0.0) then
    cohesion_i=cohesion_0-(cohesion_0-cohesion_r)/(a_n_p_star)*a_n_p_i
    friction_i=friction_0-(friction_0-friction_r)/(a_n_p_star)*a_n_p_i
    dilatancy_i=dilatancy_0-(dilatancy_0-dilatancy_r)/(a_n_p_star)*a_n_p_i
    r_s=r_i
else
    cohesion_i=cohesion_r
```

```
        friction_i=friction_r
        dilatancy_i=dilatancy_r
      end if
  end Do

  residual_x=cof_A*(sig_r_i-p_fictitious)-cof_B*cof_C/(cof_D+cof_E)*(sig_r_i-
.                 p_fictitious)+cof_B*cof_C*P_s_11_x2/(cof_D+cof_E)
  residual_xx=(strain_p_theta_i+strain_e_theta_i)*R_1-ur_x1-residual_x
  p_i=p1_11+p_fictitious

  !material parameters for the 1-st annulus
  a_N_0=(1.0+sin(friction_0))/(1.0-sin(friction_0))
  S_0=2.0*cohesion_0*sqrt(a_N_0)

  !radial stress at the plastic-elastic interface
  sig_R_p=(2.0*p_0-s_0)/(1.0+a_N_0)
  delta_sig_r=(P_i-sig_R_p)/N

  !initial values of stresses/strain in the outer boundary of the i-th annulus
  sig_r_0=sig_r_p
  sig_theta_0=2.0*p_0-sig_r_p
  strain_p_r_0=0.0
  strain_p_theta=0.0
  a_n_p_0=0.0
  strain_theta_0=(p_0-sig_r_p)/(2.0*G)
  U_0=strain_theta_0
  cohesion_i=cohesion_0
  friction_i=friction_0
  dilatancy_i=dilatancy_0
  a_n_p_i=a_n_p_0
  sig_r_i=sig_r_0
  r_i=r_p
  u_i=u_0

  Do i=1,n
```

```
!non-updated material parameters
r_i_1=r_i
a_N_i=(1.0+sin(friction_i))/(1.0-sin(friction_i))
S_i=2.0*cohesion_i*sqrt(a_N_i)
a_k_dilatancy_i=(1.0+sin(dilatancy_i))/(1.0-sin(dilatancy_i))

!to update the normalized radial
r_i=r_i*((sig_r_i+delta_sig_r-S_i/(1.0-a_N_i))/(sig_r_i-S_i/(1.0-a_N_i)))**(1.0/(a_N_i-1.0))

!stress and displacements in the i-th annulus
if ((r .gt. r_i) .and. (r .le. r_i_1)) then
   !expression of the stresses
   sig_r=(S_i)/(1.0-a_N_i)+(sig_r_i-S_i/(1-a_N_i))*(r/r_i_1)**(a_N_i-1.0)
   sig_theta=a_N_i*sig_r+S_i
   strain_e_r=(1.0-v*v)/E*((sig_r-P_0)-v/(1.0-v)*(sig_theta-p_0))
   strain_e_theta=(1.0-v*v)/E*((sig_theta-P_0)-v/(1.0-v)*(sig_r-p_0))

   !expression of the displacements
   F_r=strain_e_r+a_k_dilatancy_i*strain_e_theta

   Call INTE(SUM1,r_i_1,r,A_K_dilatancy_i,v,E,S_i,a_N_i,sig_r_i,P_0)
   U=U_i*(r_i_1/r)**a_k_dilatancy_i+SUM1*r**(-a_k_dilatancy_i)
end if

!to update the stresses in the inner boundary of the i-th annulus
sig_r_i=sig_r_i+delta_sig_r
sig_theta_i=a_N_i*sig_r_i+S_i

!to update the elastic strain in the inner boudary of the i-th annulus
strain_e_r_i=(1.0-v*v)/E*((sig_r_i-P_0)-v/(1.0-v)*(sig_theta_i-p_0))
strain_e_theta_i=(1.0-v*v)/E*((sig_theta_i-P_0)-v/(1.0-v)*(sig_r_i-p_0))

!to update u_i
Call INTE(SUM2,r_i_1,r_i,A_K_dilatancy_i,v,E,S_i,a_N_i,sig_r_i,P_0)
U_i=U_i*(r_i_1/r_i)**a_k_dilatancy_i+SUM2*r_i**(-a_k_dilatancy_i)
```

```
      !to update plastic strain in the inner boundary of the i-th annulus
      strain_p_theta_i=u_i/r_i-strain_e_theta_i
      strain_p_r_i=-a_k_dilatancy_i*strain_p_theta_i

      !to update plastic parameter np
      a_n_p_i=strain_p_theta_i-strain_p_r_i

      !to update the material parameters
      if (a_n_p_i .lt. a_n_p_star .and. a_n_p_i .ge. 0.0) then
         cohesion_i=cohesion_0-(cohesion_0-cohesion_r)/(a_n_p_star)*a_n_p_i
         friction_i=friction_0-(friction_0-friction_r)/(a_n_p_star)*a_n_p_i
         dilatancy_i=dilatancy_0-(dilatancy_0-dilatancy_r)/(a_n_p_star)*a_n_p_i
         r_s=r_i
      else
         cohesion_i=cohesion_r
         friction_i=friction_r
         dilatancy_i=dilatancy_r
      end if

   end Do

   residual_1=cof_A*(sig_r_i-p_fictitious)-cof_B*cof_C/(cof_D+cof_E)*(sig_r_i-
  .                p_fictitious)+cof_B*cof_C*P_s_11_x2/(cof_D+cof_E)
   residual_11=(strain_p_theta_i+strain_e_theta_i)*R_1-ur_x1-residual_1

   p_i=p1_22+p_fictitious
   R_p=1.0

   !material parameters for the 1-st annulus
   a_N_0=(1.0+sin(friction_0))/(1.0-sin(friction_0))
   S_0=2.0*cohesion_0*sqrt(a_N_0)

   !radial stress at the plastic-elastic interface
   sig_R_p=(2.0*p_0-s_0)/(1.0+a_N_0)
   delta_sig_r=(P_i-sig_R_p)/N
```

```
!initial values of stresses/strain in the outer boundary of the i-th annulus
sig_r_0=sig_r_p
sig_theta_0=2.0*p_0-sig_r_p
strain_p_r_0=0.0
strain_p_theta=0.0
a_n_p_0=0.0
strain_theta_0=(p_0-sig_r_p)/(2.0*G)
U_0=strain_theta_0
cohesion_i=cohesion_0
friction_i=friction_0
dilatancy_i=dilatancy_0
a_n_p_i=a_n_p_0
sig_r_i=sig_r_0
r_i=r_p
u_i=u_0

Do i=1,n
   !non-updated material parameters
   r_i_1=r_i
   a_N_i=(1.0+sin(friction_i))/(1.0-sin(friction_i))
   S_i=2.0*cohesion_i*sqrt(a_N_i)
   a_k_dilatancy_i=(1.0+sin(dilatancy_i))/(1.0-sin(dilatancy_i))

   !to update the normalized radial
   r_i=r_i*((sig_r_i+delta_sig_r-S_i/(1.0-a_N_i))/(sig_r_i-S_i/(1.0-a_N_i)))**(1.0/(a_N_i-1.0))

   !stress and displacements in the i-th annulus
   if ((r .gt. r_i) .and. (r .le. r_i_1)) then
      !expression of the stresses
      sig_r=(S_i)/(1.0-a_N_i)+(sig_r_i-S_i/(1-a_N_i))*(r/r_i_1)**(a_N_i-1.0)
      sig_theta=a_N_i*sig_r+S_i
      strain_e_r=(1.0-v*v)/E*((sig_r-P_0)-v/(1.0-v)*(sig_theta-p_0))
      strain_e_theta=(1.0-v*v)/E*((sig_theta-P_0)-v/(1.0-v)*(sig_r-p_0))
```

```
    !expression of the displacements
    F_r=strain_e_r+a_k_dilatancy_i*strain_e_theta

    Call INTE(SUM1,r_i_1,r,A_K_dilatancy_i,v,E,S_i,a_N_i,sig_r_i,P_0)
    U=U_i*(r_i_1/r)**a_k_dilatancy_i+SUM1*r**(-a_k_dilatancy_i)
end if

!to update the stresses in the inner boundary of the i-th annulus
sig_r_i=sig_r_i+delta_sig_r
sig_theta_i=a_N_i*sig_r_i+S_i

!to update the elastic strain in the inner boudary of the i-th annulus
strain_e_r_i=(1.0-v*v)/E*((sig_r_i-P_0)-v/(1.0-v)*(sig_theta_i-p_0))
strain_e_theta_i=(1.0-v*v)/E*((sig_theta_i-P_0)-v/(1.0-v)*(sig_r_i-p_0))

!to update u_i
Call INTE(SUM2,r_i_1,r_i,A_K_dilatancy_i,v,E,S_i,a_N_i,sig_r_i,P_0)
U_i=U_i*(r_i_1/r_i)**a_k_dilatancy_i+SUM2*r_i**(-a_k_dilatancy_i)

!to update plastic strain in the inner boundary of the i-th annulus
strain_p_theta_i=u_i/r_i-strain_e_theta_i
strain_p_r_i=-a_k_dilatancy_i*strain_p_theta_i

!to update plastic parameter np
a_n_p_i=strain_p_theta_i-strain_p_r_i

!to update the material parameters
if (a_n_p_i .lt. a_n_p_star .and. a_n_p_i .ge. 0.0) then
    cohesion_i=cohesion_0-(cohesion_0-cohesion_r)/(a_n_p_star)*a_n_p_i
    friction_i=friction_0-(friction_0-friction_r)/(a_n_p_star)*a_n_p_i
    dilatancy_i=dilatancy_0-(dilatancy_0-dilatancy_r)/(a_n_p_star)*a_n_p_i
    r_s=r_i
else
    cohesion_i=cohesion_r
```

```
        friction_i=friction_r
        dilatancy_i=dilatancy_r
      end if
  end Do

  residual_2=cof_A*(sig_r_i-p_fictitious)-cof_B*cof_C/(cof_D+cof_E)*(sig_r_i-
 .              p_fictitious)+cof_B*cof_C*P_s_11_x2/(cof_D+cof_E)
  residual_22=(strain_p_theta_i+strain_e_theta_i)*R_1-ur_x1-residual_2

  if (sign (residual_xx,residual_11) .eq. residual_xx) then
     p1_11=p1_xx
     residual_11=residual_xx
  else
     p1_22=p1_xx
     residual_22=residual_xx
  end if

  if ((abs(residual_11-residual_22).gt.35e-6) .and. abs(residual_xx).gt.35e-6) goto 10
  if(abs(residual_xx).gt.1e-9) p1_xx=(p1_11+P1_22)/2.0

  P_s_22=cof_C*(p1_xx-P_s_11_x2)/(cof_D+cof_E)
  ur_L1_R1=(p1_xx-p_s_22)*R_1*R_1*R_2*R_2/(2.0*G_L1*R_1*(R_1*R_1-R_2*R_2))+((1.0-
 .              2.0*v_L1)*R_1*R_1*p1_xx*R_1- (1.0-2.0*v_L1)*R_2*R_2*p_s_22*R_1)/
 .              (2.0*G_L1*(R_1*R_1-R_2*R_2))
  ur_L1_R2=(p1_xx-p_s_22)*R_1*R_1*R_2*R_2/(2.0*G_L1*R_2*(R_1*R_1-R_2*R_2))+((1.0-
 .              2.0*v_L1)*R_1*R_1*p1_xx*R_2-
 .              (1.0-2.0*v_L1)*R_2*R_2*p_s_22*R_2)/(2.0*G_L1*(R_1*R_1-R_2*R_2))
  ur_L2_R2=p_s_22*R_2*R_2*R_3*R_3/(2.0*G_L2*R_2*(R_2*R_2-R_3*R_3))+((1.0-
 .              2.0*v_L2)*R_2*R_2*p_s_22*R_2)/(2.0*G_L2*(R_2*R_2-R_3*R_3))

  write(111111,*) residual_xx,u_i*R_1/r_i,sig_r_i,R_1/r_i,r_s*R_1/r_i
  write(222222,*) p1_xx,p_s_22,ur_L1_R1,ur_L1_R2,ur_L2_R2
  END
```

```
SUBROUTINE INTE(SUM,A,B,A_K_dilatancy_i,v,E,S_i,a_N_i,sig_r_i,P_0)
N_inte=100000
SUM=0.0
X=A
H=(B-A)/N_inte

sig_r=(S_i)/(1.0-a_N_i)+(sig_r_i-S_i/(1.0-a_N_i))*(B/A)**(a_N_i-1.0)
sig_theta=a_N_i*sig_r+S_i
strain_e_r=(1.0-v*v)/E*((sig_r-P_0)-v/(1.0-v)*(sig_theta-p_0))
strain_e_theta=(1.0-v*v)/E*((sig_theta-P_0)-v/(1.0-v)*(sig_r-p_0))

Fx=strain_e_r+a_k_dilatancy_i*strain_e_theta
F=Fx*X**A_K_dilatancy_i

DO I=1,N_inte
   SI=F*H
   SUM=SUM+SI
   X=X+H

   sig_r=(S_i)/(1.0-a_N_i)+(sig_r_i-S_i/(1.0-a_N_i))*(B/A)**(a_N_i-1.0)
   sig_theta=a_N_i*sig_r+S_i
   strain_e_r=(1.0-v*v)/E*((sig_r-P_0)-v/(1.0-v)*(sig_theta-p_0))
   strain_e_theta=(1.0-v*v)/E*((sig_theta-P_0)-v/(1.0-v)*(sig_r-p_0))

   Fx=strain_e_r+a_k_dilatancy_i*strain_e_theta
   F=Fx*X**A_K_dilatancy_i
END DO
END
```

References

Abbo AJ, Lyamin AV, Sloan SW, Hambleton JP, 2011. A C2 continuous approximation to the Mohr–Coulomb yield surface. International Journal of solids and Structures. 48(21), 3001-3010. https://doi.org/10.1016/j.ijsolstr.2011.06.021

Abbo AJ, Sloan SW, 1995. A smooth hyperbolic approximation to the Mohr-Coulomb yield criterion. Computers & structures. 54(3), 427-441.

https://doi.org/10.1016/0045-7949(94)00339-5

Alejano LR, Alonso E, Rodriguez-Dono A, Fernandez-Manin G, 2010. Application of the convergence-confinement method to tunnels in rock masses exhibiting Hoek–Brown strain-softening behaviour. International Journal of Rock Mechanics and Mining Sciences. 1(47), 150-160. https://doi.org/10.1016/j.ijrmms.2009.07.008

Alejano LR, Rodriguez-Dono A, Alonso E, Manín GF, 2009. Ground reaction curves for tunnels excavated in different quality rock masses showing several types of post-failure behaviour. Tunnelling and Underground Space Technology. 24(6), 689-705.

https://doi.org/10.1016/j.tust.2009.07.004

Alejano LR, Rodríguez-Dono A, Veiga M, 2012. Plastic radii and longitudinal deformation profiles of tunnels excavated in strain-softening rock masses. Tunnelling and Underground Space Technology. 30, 169-182.

https://doi.org/10.1016/j.tust.2012.02.017

Alonso E, Alejano L, Fdez-Manin G, Garcia-Bastante F, 2008. Influence of post-peak properties in the application of the convergence-confinement method for designing underground excavations. 5th International Conference and Exhibition on Mass Mining. Luleå, Sweden.

Alonso E, Alejano LR, Varas F, Fdez‐Manin G, Carranza‐Torres C, 2003. Ground response curves for rock masses exhibiting strain‐softening behaviour.

International journal for numerical and analytical methods in geomechanics. 27(13), 1153-1185. https://doi.org/10.1002/nag.315

Alonso E, Olivella S, Pinyol N, 2005. A review of Beliche Dam. Géotechnique. 55(4), 267-285. https://doi.org/10.1680/geot.2005.55.4.267

Arjnoi P, Jeong JH, Kim CY, Park KH, 2009. Effect of drainage conditions on porewater pressure distributions and lining stresses in drained tunnels. Tunnelling and Underground Space Technology. 24(4), 376-389.

https://doi.org/10.1016/j.tust.2008.10.006

Armand G et al., 2014. Geometry and properties of the excavation-induced fractures at the Meuse/Haute-Marne URL drifts. Rock Mechanics and Rock Engineering. 47(1), 21-41. https://doi.org/10.1007/s00603-012-0339-6

Atkinson KE, 2008. An introduction to numerical analysis. John wiley & sons.

Barla G, Bonini M, Debernardi D, 2010. Time dependent deformations in squeezing tunnels. ISSMGE International Journal of Geoengineering Case Histories. 2(1), 40-65. http://dx.doi.org/10.4417/IJGCH-02-01-03

Barla G, Borgna S, 2000. Numerical modelling of squeezing behaviour in tunnels. Rivista Italiana di Geotecnica. 1(34), 46-52.

Barla G, Debernardi D, Sterpi D, 2011. Time-dependent modeling of tunnels in squeezing conditions. International Journal of Geomechanics. 12(6), 697-710.

https://doi.org/10.1061/(ASCE)GM.1943-5622.0000163

Bobet A, 2009. Elastic solution for deep tunnels. Application to excavation damage zone and rockbolt support. Rock mechanics and rock engineering. 42(2), 147-174.

https://doi.org/10.1007/s00603-007-0140-0

Bonini M, Barla G, 2012. The Saint Martin La Porte access adit (Lyon–Turin Base Tunnel) revisited. Tunnelling and underground space technology. 30, 38-54.

https://doi.org/10.1016/j.tust.2012.02.004

Bonini M, Debernardi D, Barla M, Barla G, 2009. The mechanical behaviour of clay shales and implications on the design of tunnels. Rock mechanics and rock engineering. 42(2), 361. https://doi.org/10.1007/s00603-007-0147-6

Borja RI, Lee SR, Seed RB, 1989. Numerical simulation of excavation in elastoplastic soils. International Journal for Numerical and Analytical Methods in Geomechanics. 13(3), 231-249. https://doi.org/10.1002/nag.1610130302

Brady BGH, Brown ET, 1993. Rock Mechanical for Underground Mining. Springer science & business media.

Brown ET, Bray JW, Ladanyi B, Hoek E, 1983. Ground response curves for rock tunnels. Journal of Geotechnical Engineering. 109(1), 15-39.

https://doi.org/10.1061/(ASCE)0733-9410(1983)109:1(15)

Brown PT, Booker JR, 1985. Finite element analysis of excavation. Computers and Geotechnics. 1(3), 207-220. https://doi.org/10.1016/0266-352X(85)90024-2

Cai M, 2008. Influence of stress path on tunnel excavation response–Numerical tool selection and modeling strategy. Tunnelling and Underground Space Technology. 23(6), 618-628. https://doi.org/10.1016/j.tust.2007.11.005

Careglio C, Canales C, Garino CG, Mirasso A, Ponthot J-P, 2016. A numerical study of hypoelastic and hyperelastic large strain viscoplastic Perzyna type models. Acta Mechanica. 227(11), 3177-3190. https://doi.org/10.1007/s00707-015-1545-6

Carranza-Torres C, 1998. Self-similarity analysis of the elasto-plastic response of underground openings in rock and effects of practical variables. Ph.D. thesis. University of Minnesota.

Carranza-Torres C, Engen M, 2017. The support characteristic curve for blocked steel sets in the convergence-confinement method of tunnel support design. Tunnelling and Underground Space Technology. 69, 233-244.

https://doi.org/10.1016/j.tust.2017.04.003

Carranza-Torres C, Fairhurst C, 1999. The elasto-plastic response of underground excavations in rock masses that satisfy the Hoek–Brown failure criterion. International Journal of Rock Mechanics and Mining Sciences. 36(6), 777-809.

https://doi.org/10.1016/S0148-9062(99)00047-9

Carranza-Torres C, Fairhurst C, 2000. Application of the convergence-confinement method of tunnel design to rock masses that satisfy the Hoek-Brown failure criterion. Tunnelling and Underground Space Technology. 15(2), 187-213.

https://doi.org/10.1016/S0886-7798(00)00046-8

Carranza-Torres C, Rysdahl B, Kasim M, 2013. On the elastic analysis of a circular lined tunnel considering the delayed installation of the support. International Journal of Rock Mechanics and Mining Sciences. 61, 57-85.

https://doi.org/10.1016/j.ijrmms.2013.01.010

Carranza-Torres C, Zhao J, 2009. Analytical and numerical study of the effect of water pressure on the mechanical response of cylindrical lined tunnels in elastic and elasto-plastic porous media. International Journal of Rock Mechanics and Mining Sciences. 46(3), 531-547. https://doi.org/10.1016/j.ijrmms.2008.09.009

Chen FQ, Lin LB, Li DY, 2019. Analytic solutions for twin tunneling at great depth considering liner installation and mutual interaction between geomaterial and liners. Applied Mathematical Modelling. 73, 412-441.

https://doi.org/10.1016/j.apm.2019.04.026

Chen YF, Zheng HK, Wang M, Hong JM, Zhou CB, 2015. Excavation-induced relaxation effects and hydraulic conductivity variations in the surrounding rocks of a large-scale underground powerhouse cavern system. Tunnelling and Underground Space Technology. 49, 253-267.

https://doi.org/10.1016/j.tust.2015.05.007

Chern JC, Shiao FY, Yu CW, 1998. An empirical safety criterion for tunnel construction. Proceedings of the regional symposium on sedimentary rock engineering. 222-227. Taipei, Taiwan.

Christian JT, Wong IH, 1973. Errors in simulating excavation in elastic media by finite elements. Soils and Foundations. 13(1), 1-10.

https://doi.org/10.3208/sandf1972.13.1

Chu ZF, Wu ZJ, Liu BG, Liu QS, 2019. Coupled analytical solutions for deep-buried circular lined tunnels considering tunnel face advancement and soft rock rheology effects. Tunnelling and Underground Space Technology. 94, 103111.

https://doi.org/10.1016/j.tust.2019.103111

Coll A et al.,2018. GiD version 14. Reference Manual. CIMNE. www.gidhome.com

Comodromos E, Hatzigogos T, Pitilakis K, 1993. Multi-stage finite element algorithm for excavation in elastoplastic soils. Computers & structures. 46(2), 289-298.

https://doi.org/10.1016/0045-7949(93)90193-H

Conte E, Donato A, Troncone A, 2013. Progressive failure analysis of shallow foundations on soils with strain-softening behaviour. Computers and Geotechnics. 54, 117-124. https://doi.org/10.1016/j.compgeo.2013.07.002

Corbetta F, Bernaud D, Minh DN, 1991. Contribution à la méthode convergence-confinement par le principe de la similitude. Revue française de géotechnique. 54, 5-11. https://doi.org/10.1051/geotech/1991054005

Cristescu N, Hunsche U, 1998. Time effects in rock mechanics. Wiley New York.

Cui L, Sheng Q, Dong YK, Miao CX, Huang JH, Zhang A, 2020. Two-stage analysis of interaction between strain-softening rock mass and liner for circular tunnels considering delayed installation of liner. European Journal of Environmental and Civil Engineering. 1-26. https://doi.org/10.1080/19648189.2020.1715849

Cui L, Sheng Q, Zheng JJ, Cui Z, Wang A, Shen Q, 2019. Regression model for predicting tunnel strain in strain-softening rock mass for underground openings. International Journal of Rock Mechanics and Mining Sciences. 119, 81-97. https://doi.org/10.1016/j.ijrmms.2019.04.014

Cui L, Zheng JJ, Zhang RJ, Lai HJ, 2015. A numerical procedure for the fictitious support pressure in the application of the convergence–confinement method for circular tunnel design. International Journal of Rock Mechanics and Mining Sciences. 78, 336-349. https://doi.org/10.1016/j.ijrmms.2015.07.001

Damjanac B, Fairhurst C, 2010. Evidence for a long-term strength threshold in crystalline rock. Rock Mechanics and Rock Engineering. 43(5), 513-531. https://doi.org/10.1007/s00603-010-0090-9

de la Fuente M, Sulem J, Taherzadeh R, Subrin D, 2019. Tunneling in Squeezing Ground: Effect of the Excavation Method. Rock Mechanics and Rock Engineering. 1-23. https://doi.org/10.1007/s00603-019-01931-4

Debernardi D, Barla G, 2009. New viscoplastic model for design analysis of tunnels in squeezing conditions. Rock mechanics and rock engineering. 42(2), 259. https://doi.org/10.1007/s00603-009-0174-6

Deng PH, Liu QS, 2020. Influence of the softening stress path on crack development around underground excavations: Insights from 2D-FDEM modelling. Computers and Geotechnics. 117, 103239. https://doi.org/10.1016/j.compgeo.2019.103239

Desai C, Sargand S, 1984. Hybrid FE procedure for soil-structure interaction. Journal of Geotechnical Engineering. 110(4), 473-486. https://doi.org/10.1061/(ASCE)0733-9410(1984)110:4(473)

Desai CS, Zhang D, 1987. Viscoplastic model for geologic materials with generalized flow rule. International Journal for Numerical and Analytical Methods in Geomechanics. 11(6), 603-620. https://doi.org/10.1002/nag.1610110606

Do DP, Tran NT, Mai VT, Hoxha D, Vu MN, 2020. Time-Dependent Reliability Analysis of Deep Tunnel in the Viscoelastic Burger Rock with Sequential Installation of Liners. Rock Mechanics and Rock Engineering. 1-27.

https://doi.org/10.1007/s00603-019-01975-6

Doležalová M, 2001. Tunnel complex unloaded by a deep excavation. Computers and Geotechnics. 28(6-7), 469-493. https://doi.org/10.1016/S0266-352X(01)00005-2

Dong XJ, 2020. Stability Analysis of Rock Masses Subjected to Underground Excavations. Ph.D. thesis. The University of Western Australia.

Dong XJ, Karrech A, Qi CC, Elchalakani M, Basarir H, 2019. Analytical solution for stress distribution around deep lined pressure tunnels under the water table. International Journal of Rock Mechanics and Mining Sciences. 123, 104124.

https://doi.org/10.1016/j.ijrmms.2019.104124

Dubey RK, Gairola VK, 2008. Influence of structural anisotropy on creep of rocksalt from Simla Himalaya, India: An experimental approach. Journal of structural Geology. 30(6), 710-718. https://doi.org/10.1016/j.jsg.2008.01.007

Eberhardt E, Stimpson B, Stead D, 1999. The influence of mineralogy on the initiation of microfractures in granite. 9th ISRM Congress. Paris, France. ISRM-9CONGRESS-1999-200.

El Naggar H, Hinchberger SD, Lo KY, 2008. A closed-form solution for composite tunnel linings in a homogeneous infinite isotropic elastic medium. Canadian geotechnical journal. 45(2), 266-287. https://doi.org/10.1139/T07-055

El Tani M, 2003. Circular tunnel in a semi-infinite aquifer. Tunnelling and underground space technology. 18(1), 49-55. https://doi.org/10.1016/S0886-7798(02)00102-5

Fabre G, Pellet F, 2006. Creep and time-dependent damage in argillaceous rocks. International Journal of Rock Mechanics and Mining Sciences. 43(6), 950-960.

https://doi.org/10.1016/j.ijrmms.2006.02.004

Fahimifar A, Ghadami H, Ahmadvand M, 2015. An elasto-plastic model for underwater tunnels considering seepage body forces and strain-softening behaviour. European Journal of Environmental and Civil Engineering. 19(2), 129-151.

https://doi.org/10.1080/19648189.2014.939305

Fahimifar A, Ranjbarnia M, 2009. Analytical approach for the design of active grouted rockbolts in tunnel stability based on convergence-confinement method. Tunnelling and Underground Space Technology. 24(4), 363-375.

https://doi.org/10.1016/j.tust.2008.10.005

Fahimifar A, Tehrani FM, Hedayat A, Vakilzadeh A, 2010. Analytical solution for the excavation of circular tunnels in a visco-elastic Burger's material under hydrostatic stress field. Tunnelling and Underground Space Technology. 25(4), 297-304. https://doi.org/10.1016/j.tust.2010.01.002

Fahimifar A, Zareifard MR, 2014. A new elasto-plastic solution for analysis of underwater tunnels considering strain-dependent permeability. Structure and Infrastructure Engineering. 10(11), 1432-1450.

https://doi.org/10.1080/15732479.2013.824489

Fenner R, 1938. Untersuchungen zur erkenntnis des gebirgsdrucks. Glückauf.

Galli G, Grimaldi A, Leonardi A, 2004. Three-dimensional modelling of tunnel excavation and lining. Computers and Geotechnics. 31(3), 171-183.

https://doi.org/10.1016/j.compgeo.2004.02.003

Ghaboussi J, Pecknold DA, 1984. Incremental finite element analysis of geometrically altered structures. International journal for numerical methods in engineering. 20(11), 2051-2064. https://doi.org/10.1002/nme.1620201108

Gharti HN, Oye V, Komatitsch D, Tromp J, 2012. Simulation of multistage excavation based on a 3D spectral-element method. Computers & structures. 100, 54-69.

https://doi.org/10.1016/j.compstruc.2012.03.005

Giraud A, Rousset G, 1996. Time-dependent behaviour of deep clays. Engineering Geology. 41(1-4), 181-195. https://doi.org/10.1016/0013-7952(95)00000-3

Guan ZC, Jiang YJ, Tanabashi Y, 2009. Rheological parameter estimation for the prediction of long-term deformations in conventional tunnelling. Tunnelling and Underground Space Technology. 24(3), 250-259.

https://doi.org/10.1016/j.tust.2008.08.001

Guan ZC, Jiang YJ, Tanabashi Y, Huang HW, 2008. A new rheological model and its application in mountain tunnelling. Tunnelling and Underground Space Technology. 23(3), 292-299. https://doi.org/10.1016/j.tust.2007.06.003

Guayacan-Carrillo L-M, Ghabezloo S, Sulem J, Seyedi DM, Armand G, 2017. Effect of anisotropy and hydro-mechanical couplings on pore pressure evolution during tunnel excavation in low-permeability ground. International Journal of Rock Mechanics and Mining Sciences. 97, 1-14.

https://doi.org/10.1016/j.ijrmms.2017.02.016

Günther R-M, Salzer K, Popp T, Lüdeling C, 2015. Steady-state creep of rock salt: improved approaches for lab determination and modelling. Rock Mechanics and Rock Engineering. 48(6), 2603-2613. https://doi.org/10.1007/s00603-015-0839-2

Hoek E, Brown ET, 1980. Underground excavations in rock. CRC Press.

Hoek E, Brown ET, 1997. Practical estimates of rock mass strength. International journal of rock mechanics and mining sciences. 34(8), 1165-1186.

https://doi.org/10.1016/S1365-1609(97)80069-X

Hoek E, Carranza-Torres C, Corkum B, 2002. Hoek-Brown failure criterion-2002 edition. Proceedings of NARMS-Tac. 1(1). 267-273.

Ishihara K, 1970. Relations Between Process of Cutting and Uniqueness of Solutions. Soils and Foundations. 10(3), 50-65. https://doi.org/10.3208/sandf1960.10.3_50

Itasca, 2007. FLAC3D Version 3. Fast Lagrangian Analysis of Continua. 3D Version. Minneapolis, Minnesota, USA.

Itasca, 2008. FLAC version 5. Fast Lagrangian Analysis of Continua. 2D Version. Minneapolis, Minnesota, USA.

Jiang JY, Wang D, Han XP, 2019. Analysis of progressive rupture process in surrounding rock for a deep homogeneous and circular opening. Energy Sources, Part A: Recovery, Utilization, and Environmental Effects. 1-10.

https://doi.org/10.1080/15567036.2019.1645766

Kabwe E, Karakus M, Chanda EK, 2020a. Isotropic damage constitutive model for time-dependent behaviour of tunnels in squeezing ground. Computers and Geotechnics. 127, 103738. https://doi.org/10.1016/j.compgeo.2020.103738

Kabwe E, Karakus M, Chanda EK, 2020b. Proposed solution for the ground reaction of non-circular tunnels in an elastic-perfectly plastic rock mass. Computers and Geotechnics. 119, 103354. https://doi.org/10.1016/j.compgeo.2019.103354

Kabwe E, Karakus M, Chanda EK, 2020c. Time-dependent solution for non-circular tunnels considering the elasto-viscoplastic rockmass. International Journal of Rock Mechanics and Mining Sciences. 133, 104395.

https://doi.org/10.1016/j.ijrmms.2020.104395

Kargar AR, 2019. An analytical solution for circular tunnels excavated in rock masses exhibiting viscous elastic-plastic behavior. International Journal of Rock Mechanics and Mining Sciences. 124, 104128.

https://doi.org/10.1016/j.ijrmms.2019.104128

Kargar AR, Haghgouei H, 2020. An analytical solution for time-dependent stress field of lined circular tunnels using complex potential functions in a stepwise procedure. Applied Mathematical Modelling. 77, 1625-1642.

https://doi.org/10.1016/j.apm.2019.09.025

Kargar AR, Rahmannejad R, Hajabasi MA, 2014. A semi-analytical elastic solution for stress field of lined non-circular tunnels at great depth using complex variable method. International Journal of Solids and structures. 51(6), 1475-1482.

https://doi.org/10.1016/j.ijsolstr.2013.12.038

Karim MR, Oka F, Krabbenhoft K, Leroueil S, Kimoto S, 2013. Simulation of long‐term consolidation behavior of soft sensitive clay using an elasto‐viscoplastic constitutive model. International Journal for Numerical and Analytical Methods in Geomechanics. 37(16), 2801-2824. https://doi.org/10.1002/nag.2165

Kitagawa T, Kumeta T, Ichizyo T, Soga S, Sato M, Yasukawa M, 1991. Application of convergence confinement analysis to the study of preceding displacement of a squeezing rock tunnel. Rock mechanics and rock engineering. 24(1), 31-51.

https://doi.org/10.1007/BF01042717

Kolymbas D, Fellin W, Kirsch A, 2006. Squeezing due to stress relaxation in foliated rock. International journal for numerical and analytical methods in geomechanics. 30(13), 1357-1367. https://doi.org/10.1002/nag.530

Kutter BL, Sathialingam N, 1992. Elastic-viscoplastic modelling of the rate-dependent behaviour of clays. Géotechnique. 42(3), 427-441.

https://doi.org/10.1680/geot.1992.42.3.427

Ladanyi B, Gill D, 1988. Design of tunnel linings in a creeping rock. International Journal of Mining and Geological Engineering. 6(2), 113-126.

https://doi.org/10.1007/BF00880802

Lade PV, 1993. Rock strength criteria: the theories and the evidence. Comprehensive rock engineering. 1, 225-284.

Leca E, Clough GW, 1992. Preliminary design for NATM tunnel support in soil. Journal of geotechnical engineering. 118(4), 558-575.

https://doi.org/10.1061/(ASCE)0733-9410(1992)118:4(558)

Lee I-M, Nam S-W, 2004. Effect of tunnel advance rate on seepage forces acting on the underwater tunnel face. Tunnelling and Underground Space Technology. 19(3), 273-281. https://doi.org/10.1016/j.tust.2003.11.005

Lee SW, Jung JW, Nam SW, Lee IM, 2007. The influence of seepage forces on ground reaction curve of circular opening. Tunnelling and Underground Space Technology. 22(1), 28-38. https://doi.org/10.1016/j.tust.2006.03.004

Lee YK, Pietruszczak S, 2008. A new numerical procedure for elasto-plastic analysis of a circular opening excavated in a strain-softening rock mass. Tunnelling and Underground Space Technology. 23(5), 588-599.

https://doi.org/10.1016/j.tust.2007.11.002

Li SC, Wang MB, 2008. An elastic stress–displacement solution for a lined tunnel at great depth. International Journal of Rock Mechanics and Mining Sciences. 45(4), 486-494. https://doi.org/10.1016/j.ijrmms.2007.07.011

Li XP, 1999. Stress and displacement fields around a deep circular tunnel with partial sealing. Computers and Geotechnics. 24(2), 125-140.

https://doi.org/10.1016/S0266-352X(98)00035-4

Lin LB, Chen FQ, Huang Z, 2019. An analytical solution for sectional estimation of stress and displacement fields around a shallow tunnel. Applied Mathematical Modelling. 69, 181-200. https://doi.org/10.1016/j.apm.2018.12.012

Lin LB, Chen FQ, Lu YP, Li DY, 2020. Complex variable solutions for tunnel excavation at great depth in visco-elastic geomaterial considering the three-dimensional effects of tunnel advance. Applied Mathematical Modelling. 82, 700-730. https://doi.org/10.1016/j.apm.2020.01.070

Lisjak A, Garitte B, Grasselli G, Müller H, Vietor T, 2015. The excavation of a circular tunnel in a bedded argillaceous rock (Opalinus Clay): short-term rock mass response and FDEM numerical analysis. Tunnelling and Underground Space Technology. 45, 227-248. https://doi.org/10.1016/j.tust.2014.09.014

Lo KY, Yuen CMK, 1981. Design of tunnel lining in rock for long term time effects. Canadian Geotechnical Journal. 18(1), 24-39. https://doi.org/10.1139/t81-004

Lu AZ, Chen HY, Qin Y, Zhang N, 2014a. Shape optimisation of the support section of a tunnel at great depths. Computers and Geotechnics. 61, 190-197.

https://doi.org/10.1016/j.compgeo.2014.05.011

Lu AZ, Zhang LQ, Zhang N, 2011. Analytic stress solutions for a circular pressure tunnel at pressure and great depth including support delay. International journal of rock mechanics and mining sciences. 48(3), 514-519.

https://doi.org/10.1016/j.ijrmms.2010.09.002

Lu AZ, Zhang N, Kuang L, 2014b. Analytic solutions of stress and displacement for a non-circular tunnel at great depth including support delay. International Journal of Rock Mechanics and Mining Sciences. 70, 69-81.

https://doi.org/10.1016/j.ijrmms.2014.04.008

Lu AZ, Zhang N, Qin Y, 2015. Analytical solutions for the stress of a lined non-circular tunnel under full-slip contact conditions. International Journal of Rock Mechanics and Mining Sciences. 79, 183-192. https://doi.org/10.1016/j.ijrmms.2015.08.008

Maghous S, Bernaud D, Couto E, 2012. Three-dimensional numerical simulation of rock deformation in bolt-supported tunnels: a homogenization approach. Tunnelling and underground space technology. 31, 68-79.

https://doi.org/10.1016/j.tust.2012.04.008

Malan DF, 2002. Manuel Rocha medal recipient simulating the time-dependent behaviour of excavations in hard rock. Rock Mechanics and Rock Engineering. 35(4), 225-254. https://doi.org/10.1007/s00603-002-0026-0

Mánica MÁ, 2018. Analysis of underground excavations in argillaceous hard soils - weak rocks. Ph.D. Thesis. Technical University of Catalonia.

Mason DP, Abelman H, 2009. Support provided to rock excavations by a system of two liners. International Journal of Rock Mechanics and Mining Sciences. 46(7), 1197-1205. https://doi.org/10.1016/j.ijrmms.2009.01.006

Ming HF, Wang MS, Tan ZS, Wang XY, 2010. Analytical solutions for steady seepage into an underwater circular tunnel. Tunnelling and Underground Space Technology. 25(4), 391-396. https://doi.org/10.1016/j.tust.2010.02.002

Moon J, Fernandez G, 2010. Effect of excavation-induced groundwater level drawdown on tunnel inflow in a jointed rock mass. Engineering Geology. 110(3-4), 33-42. https://doi.org/10.1016/j.enggeo.2009.09.002

Nam SW, Bobet A, 2007. Radial deformations induced by groundwater flow on deep circular tunnels. Rock mechanics and rock engineering. 40(1), 23. https://doi.org/10.1007/s00603-006-0097-4

Nogueira CdL, Azevedo RFd, Zornberg JG, 2011. Validation of coupled simulation of excavations in saturated clay: Camboinhas case history. International Journal of Geomechanics. 11(3), 202-210. https://doi.org/10.1061/(ASCE)GM.1943-5622.0000077

Nomikos P, Rahmannejad R, Sofianos A, 2011. Supported axisymmetric tunnels within linear viscoelastic Burgers rocks. Rock mechanics and rock engineering. 44(5), 553-564. https://doi.org/10.1007/s00603-011-0159-0

Olivella S, 1995. Nomsothermal multiphase flow of brine and gas through saline media. Ph.D. thesis. Technical University of Catalonia.

Olivella S, Gens A, 2002. A constitutive model for crushed salt. International journal for numerical and analytical methods in geomechanics. 26(7), 719-746. https://doi.org/10.1002/nag.220

Olivella S, Gens A, Carrera J, Alonso EE, 1996. Numerical formulation for a simulator (CODE_BRIGHT) for the coupled analysis of saline media. Engineering Computations. 13(7), 87-112. https://doi.org/10.1108/02644409610151575

Olivella S, Jean V, Alfonso RD, 2020. CODE_BRIGHT USER'S GUIDE. Barcelona, Spain, Division of Geotechnical Engineering and Geosciences, Department of Civil and Environmental Engineering, Technical University of Catalonia (UPC). https://deca.upc.edu/en/projects/code_bright.

Oreste P, 2008. Distinct analysis of fully grouted bolts around a circular tunnel considering the congruence of displacements between the bar and the rock. International Journal of Rock Mechanics and Mining Sciences. 45(7), 1052-1067.

https://doi.org/10.1016/j.ijrmms.2007.11.003

Oreste P, 2015. Analysis of the Interaction between the Lining of a TBM Tunnel and the Ground Using the Convergence-Confinement Method. American Journal of Applied Sciences. 12(4), 276.

Oreste PP, 2003. Analysis of structural interaction in tunnels using the covergence–confinement approach. Tunnelling and Underground Space Technology. 18(4), 347-363. https://doi.org/10.1016/S0886-7798(03)00004-X

Pan YW, Dong JJ, 1991. Time-dependent tunnel convergence—I. Formulation of the model. International journal of rock mechanics and mining sciences & geomechanics abstracts. 6, 469-475.

https://doi.org/10.1016/0148-9062(91)91122-8

Panet M, 1993. Understanding deformations in tunnels. Comprehensive rock engineering. 1, 663-690.

Panet M,1995. Le calcul des tunnels par la méthode convergence-confinement. Presses ENPC.

Paraskevopoulou C, 2016. Time-dependency of rocks and implications associated with tunnelling. Ph.D. Thesis. Queen's University.

Paraskevopoulou C, Diederichs M, 2018. Analysis of time-dependent deformation in tunnels using the Convergence-Confinement Method. Tunnelling and Underground Space Technology. 71, 62-80.

https://doi.org/10.1016/j.tust.2017.07.001

Paraskevopoulou C, Perras M, Diederichs M, Loew S, Lam T, Jensen M, 2018. Time-Dependent Behaviour of Brittle Rocks Based on Static Load Laboratory Tests. Geotechnical and Geological Engineering. 36(1), 337-376.

https://doi.org/10.1007/s10706-017-0331-8

Park KH, Owatsiriwong A, Lee JG, 2008a. Analytical solution for steady-state groundwater inflow into a drained circular tunnel in a semi-infinite aquifer: a revisit. Tunnelling and Underground Space Technology. 23(2), 206-209.

https://doi.org/10.1016/j.tust.2007.02.004

Park KH, Tontavanich B, Lee JG, 2008b. A simple procedure for ground response curve of circular tunnel in elastic-strain softening rock masses. Tunnelling and Underground Space Technology. 23(2), 151-159.

https://doi.org/10.1016/j.tust.2007.03.002

Pellet F, Hajdu A, Deleruyelle F, Besnus F, 2005. A viscoplastic model including anisotropic damage for the time dependent behaviour of rock. International journal for numerical and analytical methods in geomechanics. 29(9), 941-970.

https://doi.org/10.1002/nag.450

Perzyna P, 1966. Fundamental problems in viscoplasticity. Advances in applied mechanics. 9, 243-377.

PLAXIS 2D, CONNECT Edition V20.04, 2020. Material models mannual. Bentley.

Prassetyo SH, 2017. Hydro-mechanical analysis of tunneling in saturated ground using a novel and efficient sequential coupling technique. Ph.D. thesis. Colorado School of Mines.

Prassetyo SH, Gutierrez M, 2018a. Designing Tunnel Support Systems based on Ground Reaction Curve and Equilibrium Strain Approach. 10th Asian Rock Mechanics Symposium, the ISRM International Symposium for 2018. Singapore.

Prassetyo SH, Gutierrez M, 2018b. Effect of transient coupled hydro-mechanical response on the longitudinal displacement profile of deep tunnels in saturated ground. Tunnelling and Underground Space Technology. 75, 11-20.

https://doi.org/10.1016/j.tust.2018.02.003

Prassetyo SH, Gutierrez M, 2020. Hydro-mechanical response of excavating tunnel in deep saturated ground. International Journal of Geo-Engineering. 11(1), 1-18.

https://doi.org/10.1186/s40703-020-00128-x

Ramírez Oyanguren P, 1966. A study of longwall mining in potash. Master's thesis. University of Newcastle.

Ramoni M, Anagnostou G, 2011. The effect of consolidation on TBM shield loading in water-bearing squeezing ground. Rock mechanics and rock engineering. 44(1), 63-83. https://doi.org/10.1007/s00603-010-0107-4

Rodriguez-Dono A, 2011. Studies on undergrond excavations in rock masses. Ph.D. thesis. Universidade de Vigo.

Sainoki A, Tabata S, Mitri HS, Fukuda D, Kodama J-i, 2017. Time-dependent tunnel deformations in homogeneous and heterogeneous weak rock formations. Computers and Geotechnics. 92, 186-200.

https://doi.org/10.1016/j.compgeo.2017.08.008

Sakurai S, 2010. Modeling strategy for jointed rock masses reinforced by rock bolts in tunneling practice. Acta Geotechnica. 5(2), 121-126.

https://doi.org/10.1007/s11440-010-0117-0

Sandrone F, Labiouse V, 2010. Analysis of the evolution of road tunnels equilibrium conditions with a convergence–confinement approach. Rock mechanics and rock engineering. 43(2), 201-218. https://doi.org/10.1007/s00603-009-0056-y

Sastry SS, 2012. Introductory methods of numerical analysis. PHI Learning Pvt. Ltd. New Delhi, India.

Serrano A, Olalla C, Reig I, 2011. Convergence of circular tunnels in elastoplastic rock masses with non-linear failure criteria and non-associated flow laws. International Journal of Rock Mechanics and Mining Sciences. 48(6), 878-887.

https://doi.org/10.1016/j.ijrmms.2011.06.008

Seyedi DM, Armand G, Noiret A, 2017. “Transverse Action”–A model benchmark exercise for numerical analysis of the Callovo-Oxfordian claystone hydromechanical response to excavation operations. Computers and Geotechnics. 85, 287-305. https://doi.org/10.1016/j.compgeo.2016.08.008

Sharifzadeh M, Tarifard A, Moridi MA, 2013. Time-dependent behavior of tunnel lining in weak rock mass based on displacement back analysis method. Tunnelling and Underground Space Technology. 38, 348-356.

https://doi.org/10.1016/j.tust.2013.07.014

Shen Q, Zheng JJ, Cui L, Pan Y, Cui B, 2019. A procedure for interaction between rock mass and liner for deep circular tunnel based on new solution of longitudinal displacement profile. European Journal of Environmental and Civil Engineering. 1-19. https://doi.org/10.1080/19648189.2019.1657960

Shin JH, Addenbrooke TI, Potts DM, 2002. A numerical study of the effect of groundwater movement on long-term tunnel behaviour. Geotechnique. 52(6), 391-403. https://doi.org/10.1680/geot.2002.52.6.391

Shin YJ, Kim BM, Shin JH, Lee IM, 2010. The ground reaction curve of underwater tunnels considering seepage forces. Tunnelling and Underground Space Technology. 25(4), 315-324. https://doi.org/10.1016/j.tust.2010.01.005

Song F, Rodriguez-Dono A, 2021. Numerical solutions for tunnels excavated in strain-softening rock masses considering a combined support system. Applied Mathematical Modelling. 92, 905-930. https://doi.org/10.1016/j.apm.2020.11.042

Song F, Rodriguez-Dono A, Olivella S, Zhong Z, 2020. Analysis and modelling of longitudinal deformation profiles of tunnels excavated in strain-softening time-dependent rock masses. Computers and Geotechnics. 125, 103643.

https://doi.org/10.1016/j.compgeo.2020.103643

Song F, Wang HN, Jiang MJ, 2018a. Analytical solutions for lined circular tunnels in viscoelastic rock considering various interface conditions. Applied Mathematical Modelling. 55, 109-130. https://doi.org/10.1016/j.apm.2017.10.031

Song F, Wang HN, Jiang MJ, 2018b. Analytically-based simplified formulas for circular tunnels with two liners in viscoelastic rock under anisotropic initial stresses. Construction and Building Materials. 175, 746-767.

https://doi.org/10.1016/j.conbuildmat.2018.04.079

Starfield AM, Cundall P, 1988. Towards a methodology for rock mechanics modelling. International journal of rock mechanics and mining sciences & geomechanics abstracts. 3, 99-106. https://doi.org/10.1016/0148-9062(88)92292-9

Sterpi D, Gioda G, 2009. Visco-plastic behaviour around advancing tunnels in squeezing rock. Rock Mechanics and Rock Engineering. 42(2), 319-339.

https://doi.org/10.1007/s00603-007-0137-8

Sulem J, Panet M, Guenot A, 1987. An analytical solution for time-dependent displacements in a circular tunnel. International journal of rock mechanics and mining sciences & geomechanics abstracts. 3, 155-164.

https://doi.org/10.1016/0148-9062(87)90523-7

Timoshenko SP, Goodier JN, 1970. Theory of elasticity. McGraw-Hill, New York,

Tomanovic Z, 2006. Rheological model of soft rock creep based on the tests on marl. Mechanics of Time-Dependent Materials. 10(2), 135-154.

https://doi.org/10.1007/s11043-006-9005-2

Unlu T, Gercek H, 2003. Effect of Poisson's ratio on the normalized radial displacements occurring around the face of a circular tunnel. Tunnelling and Underground Space Technology. 18(5), 547-553.

https://doi.org/10.1016/S0886-7798(03)00086-5

Vlachopoulos N, Diederichs MS, 2009. Improved longitudinal displacement profiles for convergence confinement analysis of deep tunnels. Rock mechanics and rock engineering. 42(2), 131-146. https://doi.org/10.1007/s00603-009-0176-4

Vrakas A, Anagnostou G, 2014. A finite strain closed‐form solution for the elastoplastic ground response curve in tunnelling. International Journal for Numerical and Analytical Methods in Geomechanics. 38(11), 1131-1148.

https://doi.org/10.1002/nag.2250

Vu MT, Sulem J, Subrin D, Monin N, 2013. Semi-analytical solution for stresses and displacements in a tunnel excavated in transversely isotropic formation with non-linear behavior. Rock mechanics and rock engineering. 46(2), 213-229.

https://doi.org/10.1007/s00603-012-0296-0

Wang HN, Chen XP, Jiang MJ, Song F, Wu L, 2018a. The analytical predictions on displacement and stress around shallow tunnels subjected to surcharge loadings. Tunnelling and Underground Space Technology. 71, 403-427.

https://doi.org/10.1016/j.tust.2017.09.015

Wang HN, Gao X, Wu L, Jiang MJ, 2020a. Analytical study on interaction between existing and new tunnels parallel excavated in semi-infinite viscoelastic ground. Computers and Geotechnics. 120, 103385.

https://doi.org/10.1016/j.compgeo.2019.103385

Wang HN, Gong H, Liu F, Jiang MJ, 2017a. Size-dependent mechanical behavior of an intergranular bond revealed by an analytical model. Computers and Geotechnics. 89, 153-167. https://doi.org/10.1016/j.compgeo.2017.04.015

Wang HN, Jiang MJ, Zhao T, Zeng GS, 2019. Viscoelastic solutions for stresses and displacements around non-circular tunnels sequentially excavated at great depths. Acta Geotechnica. 14(1), 111-139. https://doi.org/10.1007/s11440-018-0634-9

Wang HN, Li Y, Ni Q, Utili S, Jiang MJ, Liu F, 2013. Analytical solutions for the construction of deeply buried circular tunnels with two liners in rheological rock. Rock mechanics and rock engineering. 46(6), 1481-1498.

https://doi.org/10.1007/s00603-012-0362-7

Wang HN, Nie GH, 2010. Analytical expressions for stress and displacement fields in viscoelastic axisymmetric plane problem involving time-dependent boundary regions. Acta mechanica. 210(3-4), 315-330.

https://doi.org/10.1007/s00707-009-0208-x

Wang HN, Song F, Zhao T, Jiang MJ, 2020b. Solutions for lined circular tunnels sequentially constructed in rheological rock subjected to nonhydrostatic initial stresses. European Journal of Environmental and Civil Engineering.

https://doi.org/10.1080/19648189.2020.1737576

Wang HN, Utili S, Jiang MJ, 2014. An analytical approach for the sequential excavation of axisymmetric lined tunnels in viscoelastic rock. International Journal of Rock Mechanics and Mining Sciences. 68, 85-106.

https://doi.org/10.1016/j.ijrmms.2014.02.002

Wang HN, Utili S, Jiang MJ, He P, 2015. Analytical solutions for tunnels of elliptical cross-section in rheological rock accounting for sequential excavation. Rock mechanics and rock engineering. 48(5), 1997-2029.

https://doi.org/10.1007/s00603-014-0685-7

Wang HN, Wu L, Jiang MJ, 2018b. Viscoelastic ground responses around shallow tunnels considering surcharge loadings and effect of supporting. European Journal of Environmental and Civil Engineering. 1-23.

https://doi.org/10.1080/19648189.2018.1505662

Wang HN, Wu L, Jiang MJ, Song F, 2018c. Analytical stress and displacement due to twin tunneling in an elastic semi‐infinite ground subjected to surcharge loads. International Journal for Numerical and Analytical Methods in Geomechanics. 42(6), 809-828. https://doi.org/10.1002/nag.2764

Wang HN, Xiao G, Jiang MJ, Crosta GB, 2018d. Investigation of rock bolting for deeply buried tunnels via a new efficient hybrid DEM-Analytical model. Tunnelling and Underground Space Technology. 82, 366-379.

https://doi.org/10.1016/j.tust.2018.08.048

Wang HN, Zeng GS, Jiang MJ, 2018e. Analytical stress and displacement around non-circular tunnels in semi-infinite ground. Applied Mathematical Modelling. 63, 303-328. https://doi.org/10.1016/j.apm.2018.06.043

Wang HN, Zeng GS, Utili S, Jiang MJ, Wu L, 2017b. Analytical solutions of stresses and displacements for deeply buried twin tunnels in viscoelastic rock. International Journal of Rock Mechanics and Mining Sciences. 93, 13-29.

https://doi.org/10.1016/j.ijrmms.2017.01.002

Wang MB, Li SC, 2009. A complex variable solution for stress and displacement field around a lined circular tunnel at great depth. International journal for numerical and analytical methods in geomechanics. 33(7), 939-951.

https://doi.org/10.1002/nag.749

Wang SL, Wu ZJ, Guo MW, Ge XR, 2012a. Theoretical solutions of a circular tunnel with the influence of axial in situ stress in elastic–brittle–plastic rock. Tunnelling and Underground Space Technology. 30, 155-168.

https://doi.org/10.1016/j.tust.2012.02.016

Wang SL, Yin SD, 2011. A closed-form solution for a spherical cavity in the elastic–brittle–plastic medium. Tunnelling and Underground Space Technology. 26(1), 236-241. https://doi.org/10.1016/j.tust.2010.06.005

Wang SL, Yin SD, Wu ZJ, 2012b. Strain‐softening analysis of a spherical cavity. International journal for numerical and analytical methods in geomechanics. 36(2), 182-202. https://doi.org/10.1002/nag.1002

Wang SL, Yin XT, Tang H, Ge XR, 2010. A new approach for analyzing circular tunnel in strain-softening rock masses. International journal of rock mechanics and mining sciences. 47(1), 170-178.

Wang Y, 1996. Ground response of circular tunnel in poorly consolidated rock. Journal of Geotechnical Engineering. 122(9), 703-708.

https://doi.org/10.1061/(ASCE)0733-9410(1996)122:9(703)

Weng MC, Tsai LS, Liao CY, Jeng FS, 2010. Numerical modeling of tunnel excavation in weak sandstone using a time-dependent anisotropic degradation model. Tunnelling and underground space technology. 25(4), 397-406.

https://doi.org/10.1016/j.tust.2010.02.004

Yang XL, Huang F, 2010. Influences of strain softening and seepage on elastic and plastic solutions of circular openings in nonlinear rock masses. Journal of Central South University of Technology. 17(3), 621-627.

https://doi.org/10.1007/s11771-010-0531-3

Yi CK, Senent S, Jimenez R, 2019. Effect of advance drainage on tunnel face stability using Limit Analysis and numerical simulations. Tunnelling and Underground Space Technology. 93, 103105. https://doi.org/10.1016/j.tust.2019.103105

Yu HS, 1992. Expansion of a thick cylinder of soils. Computers and Geotechnics. 14(1), 21-41. https://doi.org/10.1016/0266-352X(92)90022-L

Yuan SC, Harrison JP, 2005. Development of a hydro-mechanical local degradation approach and its application to modelling fluid flow during progressive fracturing of heterogeneous rocks. International Journal of Rock Mechanics and Mining Sciences. 42(7-8), 961-984. https://doi.org/10.1016/j.ijrmms.2005.05.005

Zareifard MR, 2018. An analytical solution for design of pressure tunnels considering seepage loads. Applied Mathematical Modelling. 62, 62-85.

https://doi.org/10.1016/j.apm.2018.05.032

Zareifard MR, Fahimifar A, 2014. Effect of seepage forces on circular openings excavated in Hoek–Brown rock mass based on a generalised effective stress principle. European journal of environmental and civil engineering. 18(5), 584-600. https://doi.org/10.1080/19648189.2014.891470

Zareifard MR, Fahimifar A, 2015. Elastic–brittle–plastic analysis of circular deep underwater cavities in a Mohr-Coulomb rock mass considering seepage forces. International Journal of Geomechanics. 15(5), 04014077.

https://doi.org/10.1061/(ASCE)GM.1943-5622.0000400

Zeng GS, Wang HN, Jiang MJ, 2019. Analytical study of ground responses induced by the excavation of quasirectangular tunnels at shallow depths. International Journal for Numerical and Analytical Methods in Geomechanics. 43(13), 2200-2223.

https://doi.org/10.1002/nag.2980

Zhang JZ, Zhou XP, Yin P, 2019a. Visco-plastic deformation analysis of rock tunnels based on fractional derivatives. Tunnelling and Underground Space Technology. 85, 209-219. https://doi.org/10.1016/j.tust.2018.12.019

Zhang K, Zhang GM, Hou RB, Wu Y, Zhou HQ, 2015. Stress evolution in roadway rock bolts during mining in a fully mechanized longwall face, and an evaluation of rock bolt support design. Rock Mechanics and Rock Engineering. 48(1), 333-344.

https://doi.org/10.1007/s00603-014-0546-4

Zhang Q, Jiang BS, Lv HJ, 2016. Analytical solution for a circular opening in a rock mass obeying a three-stage stress–strain curve. International Journal of Rock Mechanics and Mining Sciences. 100(86), 16-22.

Zhang Q, Jiang BS, Wang SL, Ge XR, Zhang HQ, 2012a. Elasto-plastic analysis of a circular opening in strain-softening rock mass. International Journal of Rock Mechanics and Mining Sciences. 50, 38-46.

https://doi.org/10.1016/j.ijrmms.2011.11.011

Zhang Q, Jiang BS, Wu XS, Zhang HQ, Han LJ, 2012b. Elasto-plastic coupling analysis of circular openings in elasto-brittle-plastic rock mass. Theoretical and applied fracture mechanics. 60(1), 60-67. https://doi.org/10.1016/j.tafmec.2012.06.008

Zhang Q, Wang HY, Jiang YJ, Lu MM, Jiang BS, 2019b. A numerical large strain solution for circular tunnels excavated in strain-softening rock masses. Computers and Geotechnics. 114, 103142. https://doi.org/10.1016/j.compgeo.2019.103142

Zhang Q, Zhang CH, Jiang BS, Li N, Wang YC, 2018. Elastoplastic coupling solution of circular openings in strain-softening rock mass considering pressure-dependent effect. International Journal of Geomechanics. 18(1), 04017132.

https://doi.org/10.1061/(ASCE)GM.1943-5622.0001043

Zhao K, Bonini M, Debernardi D, Janutolo M, Barla G, Chen G, 2015. Computational modelling of the mechanised excavation of deep tunnels in weak rock. Computers and Geotechnics. 66, 158-171. https://doi.org/10.1016/j.compgeo.2015.01.020

Zhou ZL, Cai X, Li XB, Cao WZ, Du XM, 2019. Dynamic response and energy evolution of sandstone under coupled static–dynamic compression: insights from experimental study into deep rock engineering applications. Rock Mechanics and Rock Engineering. 1-27. https://doi.org/10.1007/s00603-019-01980-9

Zhu HH, Ye B, Cai YC, Zhang F, 2013. An elasto-viscoplastic model for soft rock around tunnels considering overconsolidation and structure effects. Computers and Geotechnics. 50, 6-16. https://doi.org/10.1016/j.compgeo.2012.12.004

Zienkiewicz O, Taylor R, 2000. The finite element method fifth edition volume 2: Solid Mechanics. Massachusetts: Butterworth-Heinemann.

Zienkiewicz OC, Taylor RL, 2005. The finite element method for solid and structural mechanics. Elsevier.

Zou JF, Li C, Wang F, 2017a. A new procedure for ground response curve (GRC) in strain-softening surrounding rock. Computers and Geotechnics. 89, 81-91.

https://doi.org/10.1016/j.compgeo.2017.04.009

Zou JF, Li SS, 2015. Theoretical solution for displacement and stress in strain-softening surrounding rock under hydraulic-mechanical coupling. Science China Technological Sciences. 58(8), 1401-1413.

https://doi.org/10.1007/s11431-015-5885-1

Zou JF, Xia MY, Xu Y, 2017b. Nonlinear Visco-Elasto-Plastic Model for Surrounding Rock Incorporating the Effect of Intermediate Principal Stress. Geotechnical and Geological Engineering. 35(1), 403-423.

https://doi.org/10.1007/s10706-016-0116-5

Zou JF, Xia ZQ, Xu Y, 2017c. Nonlinear visco-elasto-plastic solution of surrounding rock considering seepage force and 3-D Hoek–Brown failure criterion. International Journal of Geotechnical Engineering. 11(3), 302-315.

https://doi.org/10.1080/19386362.2016.1216662